

**OPTICAL EMISSION DIAGNOSTICS OF
LASER PRODUCED PLASMA FROM
GRAPHITE AND $\text{YBa}_2\text{Cu}_3\text{O}_7$**

HARILAL. S.S.

**THESIS SUBMITTED
IN PARTIAL FULFILMENT OF THE REQUIREMENTS
FOR THE DEGREE OF**

DOCTOR OF PHILOSOPHY

**LASER DIVISION
INTERNATIONAL SCHOOL OF PHOTONICS
COCHIN UNIVERSITY OF SCIENCE AND TECHNOLOGY
COCHIN - 682 022
INDIA**

1997

Preface

Powerful laser beams are capable of producing several spectacular effects. High power laser pulses focused onto a solid target not only vapourizes the material at the focal spot but also generates bright luminous plasma along with ejection of material in different forms from this point. Laser induced plasmas are currently a topic of considerable interest in fundamental and applied areas of scientific research. The subject has made significant progress in its application to many fields of basic research and material technology such as thin film deposition, production of clusters, lithography, etching, annealing, and in the fabrication of micro-electronic devices. The interaction of high power laser beams with matter is a very complex phenomenon and it gives rise to a number of exotic processes. When the laser pulses of moderate power densities are focused on an opaque surface they can produce high heating rates and extremely high temperatures. At lower laser irradiances heating without phase change occurs while at higher irradiances, ionization occurs which leads to the plasma formation. Spectroscopic studies of optical emission of a laser produced plasma is the most effective method for characterizing both the laser target interaction and the resulting plasma.

Optical emission spectroscopy is a technique which analyzes the light emitted from the plasma. The optical spectroscopic studies of laser produced plasma are very convenient method to identify different excited species like neutrals, ionic, diatomic molecules, molecular clusters etc.. The light essentially originates from transitions from excited states to lower energy levels in atoms and molecules due to many kinds of decay processes. By means of this technique, the types of excited species in the plasma can be determined. Estimations of temperatures for such species can also be made from the analysis of their energy distribution and their respective populations. Because of the highly transient behaviour of laser produced plasma (LPP), it is important to characterize the LPP in a time and space resolved manner.

The work presented in this thesis covers the experimental results on the plasma produced with moderately high power laser with irradiance range in between 10 GW cm^{-2} to 100 GW cm^{-2} . The characterization of laser produced plasma from solid targets viz. graphite and high temperature superconducting material like $\text{YBa}_2\text{Cu}_3\text{O}_7$ have been carried out. The fundamental frequency from a Q - switched Nd: YAG laser with 9 ns pulse duration is used for the present studies. Various optical emission diagnostic techniques were employed for the the characterization of the LPP which include emission spectroscopy, time resolved studies, line broadening method etc.. In order to understand the physical nature of the LPP like recombination, collisional excitation and the laser interaction with plasma, the time resolved studies offer the most logical approach.

The thesis is divided into nine chapters, and a chapter wise summary of the same is given below.

Chapter I contains a brief general introduction of the plasma and the basic theory underlying the process of interaction of laser beam with materials. This chapter is subdivided into three sections. The first section deals with elementary plasma physics, second gives a brief account of laser matter interaction. The last section includes different methods for the plasma diagnostics and their applications.

Chapter II presents the general experimental methods followed in the present study. Details of the experimental set up used for the spectroscopic as well as time resolved studies are discussed separately. The various subsystems like laser source, the plasma chamber, monochromator, light detectors, boxcar averager, and digital storage oscilloscope used for the present experimental studies and their specific features are also discussed in this chapter.

Results obtained from space resolved spectroscopic study of light emission from molecular C_2 in laser produced carbon plasma form **Chapter III**. It is found that when graphite target is vapourized by intense laser pulses in a helium atmosphere of moderate pressure, remarkably stable carbon clusters are produced. Although

considerable progress has been achieved in studying carbon clusters (C_n) with $n \geq 10$, little effort has been spent for the characterization and production of low mass carbon clusters C_n with $n \leq 10$. We have made the spatially resolved analysis of C_2 Swan bands in the spectrum in the laser induced plasma from graphite target in helium atmosphere. These investigations demonstrate that the emission intensities from C_2 species are sensitive to laser irradiance, pressure of the background gas and spatial separation from the target. From the spectroscopic studies of the emission bands, vibrational temperature of the C_2 species in the plasma has been estimated.

Chapter IV gives the time resolved analysis of various species present in the graphite plasma. The emission features of laser ablated graphite plume generated in a helium ambient atmosphere have been investigated with time and space resolved plasma diagnostic technique. Time resolved optical emission spectroscopy is employed to reveal the velocity distribution of different species ejected during ablation. The different formation mechanisms for the C_2 along with the expansion dynamics of these species are discussed in detail. Analysis of data collected provides a fairly complete picture of the evolution and dynamics of C_2 species in the laser induced plasma from graphite.

Chapter V deals with the dynamics of graphite plasma in presence of various background gases like helium, argon and air. Plasmas are usually characterized by their density and temperature. We determined the electron density and electron temperature of the laser generated plasma by spectroscopic means. Relative line intensity measurements of successive stages of ionized carbon are used for these measurements. The electron temperature and its variation with air, argon and helium ambient gas pressures are studied. We also employed Stark broadened profile of singly ionized carbon species for the evaluation of electron density. The variation of electron density and electron temperature with numerous experimental parameters like ambient gas pressure, laser irradiance, spatial variation from the target are given in detail.

Chapter VI gives time and space resolved studies of spectral emission from CN molecules. These molecules are formed when the plasma produced during the Nd:YAG

laser ablation of graphite target under partial vacuum conditions or in air. Depending on the laser pulse energy, time of observation and position of the sampled volume of the plasma, the features of the emission spectrum are found to change drastically. The vibrational temperature and population distribution in the different vibrational levels have been studied as functions of distance, time, laser energy and ambient gas pressure. Nonlinear effects of the plasma medium like self-focusing are also observed.

Chapter VII discusses dynamics of Nd:YAG laser ablated high temperature superconducting material viz. $\text{YBa}_2\text{Cu}_3\text{O}_7$ plasma. Electron temperature and electron density measurements are made from spectral data. The Stark broadening of emission lines has been used to determine the electron density and the ratio of line intensities has been exploited for the determination of electron temperature. The dependence on electron temperature and density on different experimental parameters like distance from the target, delay time after the initiation of the plasma and laser irradiance is also discussed.

Chapter VIII outlines the time resolved investigations made on the $\text{YBa}_2\text{Cu}_3\text{O}_7$ plasma. $\text{YBa}_2\text{Cu}_3\text{O}_7$ target was laser ablated, and the time of flight (TOF) distributions of various species present in the resultant plasma are investigated as functions of distance from the target and laser energy density using emission spectroscopy. Up to a short distance from the target ($\sim 1.5\text{cm}$), TOF distributions show twin peaks for Y and YO, while only single peak distribution is observed for YII. At greater distances ($> 1.5\text{cm}$) all of them exhibit single peak distribution. The twin peaks are assigned to species corresponding to those generated directly/in the vicinity of target surface and those generated from collisional/recombination process.

The concluding **Chapter IX** gives a summary and assessment of the scientific results presented in the previous chapters.

Most of the results to be included in the thesis has been published or accepted/communicated for publication, details of which are given below.

- [1] Temporal and spatial evolution of laser ablated plasma from $\text{YBa}_2\text{Cu}_3\text{O}_7$
S S Harilal, P Radhakrishnan, V P N Nampoore & C P G Vallabhan
Applied Physics Letters **64** 3377 (1994)
- [2] Temporal and spatial evolution of C_2 in laser induced plasma from graphite
S S Harilal, R C Issac, C V Bindhu, V P N Nampoore & C P G Vallabhan
Journal Applied Physics **80** 3561 (1996)
- [3] Emission and expansion dynamics of C_2 species from laser produced carbon plasma
S S Harilal, R C Issac, C V Bindhu, V P N Nampoore & C P G Vallabhan
Journal of Applied Physics **81** (in press) 1997
- [4] Electron density and temperature measurements in laser produced graphite plasma
S S Harilal, R C Issac, C V Bindhu, V P N Nampoore & C P G Vallabhan
Journal of Applied Physics (communicated)
- [5] Time resolved analysis of C_2 emission from a laser induced graphite plasma in helium atmosphere
S S Harilal, R C Issac, C V Bindhu, V P N Nampoore & C P G Vallabhan
Japaneese Journal of Applied Physics **36** 134 (1997)
- [6] Optical emission studies of C_2 from laser produced carbon plasma
S S Harilal, R C Issac, C V Bindhu, V P N Nampoore & C P G Vallabhan
Journal of Physics D: Applied Physics (in press) (1997)
- [7] Spatial analysis of C_2 band emission from laser produced graphite plasma
S S Harilal, R C Issac, C V Bindhu, V P N Nampoore & C P G Vallabhan
Plasma Sources Science & Technology (in press) (1997)
- [8] Time resolved study of CN band emission from plasma generated by laser irradiation of graphite
S S Harilal, R C Issac, C V Bindhu, P. Gopinath, V P N Nampoore & C P G Vallabhan
Spectrochimica Acta A (in press) (1997)
- [9] Spatial and time resolved analysis of CN bands in the laser induced plasma from graphite
S S Harilal, R C Issac, C V Bindhu, G K Varier, V P N Nampoore & C P G Vallabhan
Pramana - Journal of Physics **46** 145 (1996)
- [10] Fine structure in the time of flight distribution of C_2 in laser produced plasma from graphite.
S S Harilal, R C Issac, C V Bindhu, V P N Nampoore & C P G Vallabhan
Pramana - Journal of Physics (under consideration)
- [11] Electron density and temperature measurements of laser induced $\text{YBa}_2\text{Cu}_3\text{O}_7$ plasma
S S Harilal, C V Bindhu, R C Issac, V P N Nampoore & C P G Vallabhan
Journal Physics B: At. Mol.Opt. Phy. (Communicated)

- [12] Time evolution of electron density and temperature of laser produced $\text{YBa}_2\text{Cu}_3\text{O}_7$ plasma
S S Harilal, R C Issac, C V Bindhu, V P N Nampoori & C P G Vallabhan
Pramana - Journal of Physics (communicated)
- [13] Effect of ambient gas on the dynamics of laser produced carbon Plasma
S S Harilal, C V Bindhu, R C Issac, V P N Nampoori & C P G Vallabhan
 To be communicated to *Physical Review E*
- [14] Stark broadening measurements of electron density in laser produced carbon plasma
S S Harilal, C V Bindhu, R C Issac, V P N Nampoori & C P G Vallabhan
 Communicated to *Modern Physics Letters B*
- [15] Influence of ambient gas on the temperature of laser produced $\text{YBa}_2\text{Cu}_2\text{O}_7$ plasma.
S S Harilal, C V Bindhu, R C Issac, V P N Nampoori & C P G Vallabhan
 To be communicated to *Physica Scripta*
- [16] Study of laser ablation in liquids using pulsed photoacoustic technique
S. S. Harilal, R. C. Issac, C. V. Bindhu, V. P. N. Nampoori & C. P. G. Vallabhan
Modern Physics Letters B 10 1053 (1996)
- [17] Observation of multiphoton process in liquid CS_2 using pulsed photoacoustic technique
S S Harilal, R C Issac, C V Bindhu, G K Varier, V P N Nampoori & C P G Vallabhan
Modern Physics Letters B 9 871 (1995)
- [18] Pulsed photoacoustic study of toluene
S S Harilal, R C Issac, G K Varier, C V Bindhu, V P N Nampoori & C P G Vallabhan
Journal of Pure and Applied Ultrasonics 17 72 (1995)
- [19] Measurement of collision cross-section and line broadening coefficient for $2p-4d$ transition in neon
P R Sasikumar, S S Harilal, V P N Nampoori and C P G Vallabhan
Technical Digest Series (Optical Society of America), 1 WB2-2 (1993)
- [20] High resolution optogalvanic spectrum of N_2 rotational structure of (11,7) band in the first positive system
P R Sasikumar, S S Harilal, V P N Nampoori and C P G Vallabhan
Pramana - Journal of Physics 42 232 (1994)
- [21] Electron density determination of laser induced plasma from Poly Methyl Methacrylate using phaseshift detection technique
G K Varier, S S Harilal, C V Bindhu, R C Issac, V P N Nampoori & C P G Vallabhan
Modern Phys. Letts. B 10 235 (1996)

- [22] Investigations in nanosecond laser produced plasma in air from $\text{YBa}_2\text{Cu}_3\text{O}_7$
G K Varier, R C Issac, C V Bindhu, **S S Harilal**, V P N Nampoore & C P G Vallabhan
Spectrochimica Acta B (in press) (1997)
- [23] Observation of two photon induced photoemission optogalvanic effect using Copper target
K A Prasad, P R Sasikumar, **S S Harilal**, V P N Nampoore & C P G Vallabhan
Modern Physics Letters B **8** 1917 (1994)
- [23] Measurement of absolute fluorescence quantum yield of Rhodamine B solution using dual beam thermal lens technique
C V Bindhu, **S S Harilal**, R C Issac, G. K. Varier, V. P. N. Nampoore & C. P. G. Vallabhan
Journal Physics D - Applied Physics **29** 1074 (1996)
- [24] Anomalous variation of thermal lens signal with concentration from rhodamine B in methanol solution
C V Bindhu, **S S Harilal**, R C Issac, G. K. Varier, V P N Nampoore & C P G Vallabhan
Pramana - Journal Physics **44** 225 (1995)
- [25] Thermal lens study of rhodamine B in methanol : Signature of resonance two photon absorption
C V Bindhu, **S S Harilal**, R C Issac, G K Varier, V P N Nampoore & C P G Vallabhan
Modern Physics Letters B **9** 1471 (1995)
- [26] Photoacoustic and optical limiting studies in C70
R C Issac, **S S Harilal**, G K Varier, C V Bindhu, V P N Nampoore & C P G Vallabhan
Optical Engineering (in press) (1997)
- [27] Determination of Fluorescence quantum yield of Rh B laser dye by pulsed photoacoustic calorimetry
C V Bindhu, **S S Harilal**, R C Issac, V P N Nampoore & C P G Vallabhan
Modern Physics Letters B **10** 1103 (1996)
- [28] Pulsed photoacoustic technique to study nonlinear process in liquids : Results in toluene
C V Bindhu, **S S Harilal**, R C Issac, G K Varier, V P N Nampoore and C. P. G. Vallabhan
Pramana - Journal of Physics **44** 221 (1995)
- [29] A study of photoacoustic effect and optical limiting in the solution of C60 in toluene
R C Issac, C V Bindhu, **S S Harilal**, G K Varier, V P N Nampoore & C P G Vallabhan
Modern Physics Letters B **10** 61 (1996)
- [30] Application of laser beam deflection technique for the study of diffusion process in electrolyte solutions
A Kurien, C V Bindhu, **S S Harilal**, R C Issac, V P N Nampoore & C P G Vallabhan
Pramana - Journal of Physics **43** 401 (1994)

- [31] Time of flight behaviour of molecular species generated from laser ablated $\text{YBa}_2\text{Cu}_3\text{O}_7$ using emission spectroscopy
S S Harilal, R C Issac, P Radhakrishnan, V P N Nampoori & C P G Vallabhan
Proc. of Trombay sym. on Rad. and Photochem. (BARC, Bombay) 2 352 (1994)
- [32] Time resolved studies of Ba and Ba^+ spectral emission from laser ablated $\text{YBa}_2\text{Cu}_3\text{O}_7$
S S Harilal, R C Issac, P Radhakrishnan, V P N Nampoori & C P G Vallabhan
Proc. of National Laser Symposium (CAT Indore) 159 (1994)
- [33] Spatial analysis of CN bands in the laser induced plasma from graphite
R C Issac, **S S Harilal**, P Radhakrishnan, V P N Nampoori & C P G Vallabhan
Proc. of Trombay sym. on Rad. and Photochem. (BARC Bombay) 2 355 (1994)
- [34] Investigations on behaviour of Ba and Ba^+ in the plasma of laser ablated $\text{YBa}_2\text{Cu}_3\text{O}_7$
S S Harilal, R C Issac, P Radhakrishnan, V P N Nampoori & C P G Vallabhan
Proc. of Current trends in Atm. and Mol. Phys. (BARC Bombay) 112 (1993)
- [35] Spectral features of laser induced fluorescence emission from C70
S S Harilal, R C Issac, G K Varier, C V Bindhu, V P N Nampoori & C P G Vallabhan
Proc. of National Laser Sym. (IRDE Dehradun) 235 (1995)
- [36] Laser induced plasma from graphite : Time dependence of vibrational temperature
S S Harilal, R C Issac, C V Bindhu, G K Varier, V P N Nampoori & C P G Vallabhan
Proc. of National Laser Sym. (IRDE Dehradun) 265 (1995)
- [37] Temporal and spatial evolution of laser ablated carbon clusters from graphite plasma
S S Harilal, R C Issac, C V Bindhu, G K Varier, V P N Nampoori & C P G Vallabhan
Proc. International Conf. on Spectroscopy : Perspectives & Frontiers (INCONS) (BARC Bombay) 146 (1996)
- [38] Laser ablation in liquids using pulsed photoacoustic technique
S S Harilal, R C Issac, C V Bindhu, G K Varier, V P N Nampoori & C P G Vallabhan
Proc. of Trombay sym. on Rad. and Photochem. (BARC, Bombay) 191 (1996)
- [39] Time resolved studies of C_2 emission spectrum in the laser induced plasma from graphite
R C Issac, **S S Harilal**, C V Bindhu, G K Varier, V P N Nampoori & C P G Vallabhan
Proc. of National Laser Sym. (BARC Bombay) H13 (1996)
- [40] Characterisation of C_2 emission from laser ablated carbon plasma
S S Harilal, R C Issac, C V Bindhu, G K Varier, V P N Nampoori & C P G Vallabhan
Proc. of National Laser Sym. (BARC Bombay) H15 (1996)
- [41] Self-reversal and anomalous line profile of the $4554 \text{ \AA}^0 \text{ Ba}^+$ resonance line in the laser produced plasma of $\text{YBa}_2\text{Cu}_3\text{O}_7$ in air
S S Harilal, R C Issac, C V Bindhu, G K Varier, V P N Nampoori & C P G Vallabhan
Proc. of National Laser Sym. (CAT, Indore) 283 (1997)

ontents

General Introduction	1
1.1 Fundamental Concepts about Plasma	2
1.1.1 Basic Plasma Phenomena	2
1.1.2 Characteristics of Plasma Behaviour	4
1.1.3 Classification of Plasma	9
1.1.4 Reactions in Plasmas	12
1.1.5 Transport Phenomena	16
1.1.6 Emission Processes in a Plasma	18
1.1.7 Equilibrium in Plasmas	21
1.2 Laser - Matter Interaction	23
1.2.1 Laser excitation of Matter	25
1.2.2 Heating without melting	28
1.2.3 Melting without vapourization	30
1.2.4 Laser induced vapourization	31
1.2.5 Ionization of the vapour and electron cascade growth	33
1.2.6 Plasma production	34
1.2.7 Plasma Expansion Models	35
1.3 Plasma diagnostics	39
1.3.1 Mass Spectroscopy	41
1.3.2 Ion Probes	42
1.3.3 Laser induced fluorescence spectroscopy	43
1.3.4 Optical Absorption Spectroscopy	44
1.3.5 Optogalvanic Spectroscopy	44
1.3.6 Coherent Anti-Stokes Raman Spectroscopy	45
1.3.7 Thomson Scattering	45
1.3.8 Interferometry	46
1.3.9 Optical emission spectroscopy	46
1.3.10 Photography and Imaging	49
1.4 References	51
Experimental Aspects of Laser Plasma Studies	56
2.1 Introduction	57
2.2 Sub-systems used for the present studies	58
2.2.1 Laser Source	58
2.2.2 Plasma Chamber and vacuum system	59
2.2.3 Target Holder	61
2.2.4 Monochromators	61
2.2.5 The Photomultiplier Tube	62
2.2.6 Energy Meter	64
2.2.7 Digital Storage Oscilloscope	64
2.2.8 Boxcar averager/integrator	65
2.2.9 Chart Recorder	66

2.3	Emission Spectroscopy	66
2.3.1	Space Resolved Studies	67
2.4	Time resolved studies	68
2.4.1	Time of flight (TOF) spectroscopic studies	69
2.5	References	71
3	Optical Emission Studies of C₂ Species in Laser Produced Plasma from Carbon	73
3.1	Introduction :	74
3.2	Experimental Details	78
3.3	Results and Discussion	79
3.3.1	Spectroscopy of the Swan Band Emission	79
3.3.2	Spatial Dependence	83
3.3.3	Laser Intensity Dependence	88
3.3.4	Time Dependence	89
3.3.5	Effect of Helium Gas Pressure	91
3.4	Conclusions	93
3.5	References	95
4	Temporal and Spatial Evolution of Laser Induced Plasma from Graphite Target	100
4.1	Introduction	101
4.2	Experimental Setup	103
4.3	Results and Discussion	104
4.3.1	Salient Features of the Double Peaks Observed in the Present Study	106
4.3.2	Formation Mechanisms	111
4.3.3	Effect of Helium gas	115
4.3.4	Plume Dynamics	118
4.3.5	Spatial Analysis at Greater Distances - Triple Peak Structure in TOF Distribution	120
4.3.6	Time Resolved Studies of Ionized Species	126
4.3.7	Expansion Dynamics	130
4.4	Conclusions	132
4.5	References	134
5	Dynamics of Laser Produced Carbon Plasma	139
5.1	Introduction	140
5.2	Experimental	143
5.3	Relative line intensity measurements	143
5.3.1	Spatial dependence	145
5.3.2	Time dependence	148
5.3.3	Dependence on Laser Irradiance	150
5.3.4	Pressure dependence	156
5.4	Condition for LTE	164

5.5	Determination of Electron Density using Stark Broadening method	165
5.5.1	Spatial dependence	168
5.5.2	Dependence on Laser Irradiance	168
5.5.3	Time Dependence	170
5.6	Comparison between the two ways to determine the electron density . . .	171
5.7	Conclusions	172
5.8	References	174
6	Spectroscopic Studies on Cyanogen Bands from Laser Produced Carbon Plasma	180
6.1	Introduction	181
6.2	Experimental Details	182
6.3	Results and Discussion	183
6.3.1	Emission Spectra	183
6.3.2	Spatial Dependence	184
6.3.3	Time Dependence	190
6.3.4	Effect of Laser Irradiance	192
6.3.5	Effect of Ambient Nitrogen	193
6.3.6	Time of Flight Analysis	194
6.4	Conclusions	196
6.5	References	198
7	Dynamics of laser produced plasma from $\text{YBa}_2\text{Cu}_3\text{O}_7$	201
7.1	Introduction	202
7.2	Experimental	205
7.3	Results and Discussion	206
7.3.1	Time Resolved Spectra	206
7.3.2	Electron Density Measurements	209
7.3.3	Electron Temperature Measurements	214
7.3.4	Local Thermodynamic Equilibrium	220
7.4	Conclusions	221
7.5	References	222
8	Temporal and spatial evolution of laser ablated plasma $\text{YBa}_2\text{Cu}_3\text{O}_7$	227
8.1	Introduction	228
8.2	Experimental	229
8.3	Results and Discussion	230
8.4	Conclusion	241
8.5	References	242
9	Summary and Conclusions	246

Chapter 1

General Introduction

This thesis presents the results of the spectroscopic investigations made on laser produced plasma from Graphite and $\text{YBa}_2\text{Cu}_3\text{O}_7$. In this chapter a brief description of the Plasma, Laser-matter interaction and plasma diagnostic techniques is given. These aspects are discussed in three sections. In the first section the basic concepts of elementary plasma are given. In the following section, the different processes underlying the laser-matter interaction are discussed. In the last section, different types of plasma diagnostic techniques are dealt in possible detail.

1.1 Fundamental Concepts about Plasma

A **Plasma** is a collection of charged and neutral particles that satisfies certain special criteria. Due to the presence of free electrical charges, a plasma differs fundamentally from ordinary gases and it is subject to electric and magnetic forces at macroscopic level. Plasma has been called the "fourth state of matter", after solid, liquid, and gas. Ordinarily, we hardly come into contact with plasma in our daily life. Matter in its normal forms is seen to exist in the solid, liquid, or gaseous phase. However, the conducting gas in a fluorescent tube or in a neon sign is in the plasma state. Lightning and aurora appearing in the polar regions are plasmas in nature. All the stars, including the sun, are masses of high-temperature plasmas. The interstellar matter and nebulae are also in the plasma state. Consequently, perhaps 99 % of all matter in the universe are plasmas. On Earth, however, the temperatures and atmospheric densities that are conducive for the existence of life forms cannot support plasmas, and these can be studied only in laboratory vacuum chambers.

Plasmas are more complicated than ordinary fluids for several reasons. First, they are subject to long-range electromagnetic forces. Second, plasmas have a particulate nature, unlike fluids, which are continuous media. At high temperatures, collisions in plasmas are so rare that it can be treated as collisionless fluids; and in the absence of randomizing collisions, the individual particles of the fluid must be taken into account. Third, since the charged-particle motions are greatly affected by magnetic fields, the plasma is a highly anisotropic, dielectric and supports a rich variety of possible wave motions.

1.1.1 Basic Plasma Phenomena

A. Fluid Description

At the simplest level, a plasma can be treated as an electrified fluid, without regard for its particulate nature. A common approach is to consider the positive ions and negative electrons of the plasma to be two interpenetrating fluids, which interact via electric and magnetic field that they each generate in their motions [1]. The equation of motion for fluid elements of each species j can be written

$$m_j n_j \left[\frac{\partial v_j}{\partial t} + v_j \cdot \nabla v_j \right] = q_j n_j (E + v_j \times B) - \nabla p_j - m_j n_j \nu_{jk} (v_j - v_k) \quad (1.1)$$

where q_j and m_j are the charge and mass of species j ; n_j , p_j and v_j are the fluid density, pressure, and velocity of that species; and ν_{jk} is its average collision frequency with species k . The pressure p_j is given by $p_j = \gamma_j n_j k T_j$, where k is Boltzmann's constant, T_j is the temperature of the fluid in kelvin, and γ_j is an adiabatic constant equal to 3, 2, or 5/3 for one-, two-, or three-dimensional plasmas respectively. For constant T_j , γ_j is unity. A plasma can have a different temperature and even a different value of γ for each species. Each species also follows the equation of continuity,

$$\frac{\partial n_j}{\partial t} + \nabla \cdot (n_j \mathbf{v}_j) = 0 \quad (1.2)$$

A set of eqns. (1.1) and (1.2) can be written for each species of positive or negative ions. The electric and magnetic fields E and B are governed by the vacuum Maxwell's equations:

$$\epsilon_0 \nabla \cdot E = \sigma \quad (1.3)$$

$$\nabla \times E = \frac{\partial B}{\partial t} \quad (1.4)$$

$$\nabla \cdot B = 0 \quad (1.5)$$

$$\nabla \times B = \mu_0 (J + \epsilon_0 \frac{\partial E}{\partial t}) \quad (1.6)$$

Together with the equation of state for p_j given above, the system of equations is closed by defining the plasma charge and current as

$$\sigma = \sum n_j q_j, \quad (1.7)$$

$$J = \sum n_j q_j v_j \quad (1.8)$$

The charged-particle motions generate the internal electromagnetic fields, and the fields move the particles; thus eqns. 1.1 to 1.8 must be solved self-consistently. It is also possible to describe the plasma as a dielectric medium with a susceptibility χ and a permittivity $\epsilon = \epsilon_0(1 + \chi)$ that incorporates the effects of the plasma charges and currents, as given by eqns. (1.1) and (1.2). The terms J and σ are then omitted from eqns. (1.3) and (1.6), and ϵ_0 replaced by ϵ . Plasmas in a magnetic field are anisotropic, and ϵ is then a rather complicated dielectric tensor. It is a characteristic of plasmas that χ is often negative. The electromagnetic quantities D and H need not be defined and are generally not used in plasma physics.

B. Kinetic Description

The fluid description is valid when collisions are frequent enough to maintain a Maxwell-Boltzmann velocity distribution for each species, so that a temperature T can be defined. Fluid theory is also a good approximation for motions perpendicular to a strong magnetic field even when collisions are rare. In the general case, deviations from a Maxwellian distribution are possible, and one has to solve for the distribution function $f_j(r, v, t)$ for each species. A function of seven independent scalar variables, $f_j(r, v, t)$ is governed by the Boltzmann equation

$$\frac{\partial f}{\partial t} + v \cdot \nabla f + \frac{q}{m}(E + v \times B) \cdot \frac{\partial f}{\partial v} = \left[\frac{\partial f}{\partial t} \right]_c \quad (1.9)$$

where $(\partial f / \partial t)_c$ is a collision term. "Collisionless" plasmas are hot enough that this term can be set equal to zero, in which case eqn. (1.9) is called the Vlasov equation. Such "Vlasov plasmas" have been intensively studied by plasma theorists [2]. Since the integral of $f(v)$ over all velocities is just the density, the continuity eqn. (1.2) can be recovered by integrating the Vlasov equation.

Though plasmas can often be treated as fluids, plasma physics differs from hydrodynamics because non-Maxwellian distributions sometimes occur, which require the kinetic treatment described above; it differs from electromagnetism because the details of the dielectric tensor ϵ are treated from the particulate point of view. Indeed, the complex motions of charged particles in electric and magnetic fields support a rich variety of wave phenomena that do not occur in ordinary fluids or dielectrics.

1.1.2 Characteristics of Plasma Behaviour

Electrical discharges have commonly been used to generate plasmas in the laboratory. This is accomplished by using a gas discharge tube in which two metal electrodes are installed, evacuating the discharge tube to a pressure range between 10^{-1} to 1 torr and applying the voltage between the two electrodes. As the voltage gradually increases, only a very small electrical current flows. When the voltage has reached a few hundred volts, electric current through the tube shows an abrupt increase, and the tube begins to emit visible orange-red light. This condition in the discharge tube is called plasma. The gas becomes electrically conductive due to its ionization. Generally in such a plasma positively charged ions and negatively charged electrons move with statistically distributed

random velocities. Positive and negative particles drift in opposite directions according to the electric field.

A. The Temperature of the Plasma

Random motion of particles, such as gas molecules, atoms or electrons, can be described by the Maxwell distribution, if the system is in thermal equilibrium. The one-dimensional Maxwellian distribution is given by

$$f(u)du = A \exp \left[-\frac{mu^2}{2kT} \right] du \quad (1.10)$$

where $f(u) du$ is the number of particles per m^3 with velocity between u and $u + du$, $\frac{1}{2}mu^2$ is the kinetic energy, and k is Boltzmann's constant. The density n , or number of particles per m^3 , is given by

$$n = \int_{-\infty}^{+\infty} f(u) du \quad (1.11)$$

The constant A is related to the density n by [1]

$$A = n \left(\frac{m}{2\pi kT} \right)^{1/2} \quad (1.12)$$

The width of the distribution is characterized by the constant T , which we call the temperature. The average kinetic energy of particles in this distribution:

$$E_{ave} = \frac{\int_{-\infty}^{+\infty} \frac{1}{2}mu^2 f(u) du}{\int_{-\infty}^{+\infty} f(u) du} = \frac{1}{2}kT \quad (1.13)$$

For three dimensional case the average kinetic energy is $\frac{3}{2} kT$.

The mean kinetic energies of electrons, ions, and excited molecules in a plasma are different, in contrast to gas molecules in a system of ordinary mixed gases, which have identical mean kinetic energies regardless of species. Therefore the temperature of the plasma should be described according to the temperature of the respective particle: the electron temperature T_e , ion temperature T_i , and gas temperature T_g . In addition, since the gas molecule itself has an internal structure of its own, the energy ϵ of the desired system is

$$\epsilon = \epsilon_{trans} + \epsilon_{rot} + \epsilon_{vib} + \epsilon_{elect} \quad (1.14)$$

where ϵ_{trans} , ϵ_{rot} , ϵ_{vib} and ϵ_{elect} express energies associated with translation, rotation, vibration and the electronic states respectively. The value of the translational energy ϵ_{trans} subtracted from the total energy ϵ is called the internal energy.

When the system is at thermal equilibrium, the distribution of internal energies of the gas particles in an ensemble is given by the Boltzmann distribution law, i.e.,

$$n_i = \frac{Ng_i \exp(-\epsilon_i/kT)}{\sum g_i \exp(-\epsilon_i/kT)} \quad (1.15)$$

where n_i is the number of particles at the energy level ϵ_i , N the total number of particles, and g_i the statistical weight. Consequently, for molecules, energies due to rotation, vibration and the electronic states must also be considered. These energies are described in terms of the rotational temperature T_{rot} , vibrational temperature T_{vib} , and electronic temperature T_{elect} . On the other hand, the energy of electrons is described only by T_e since the electron, unlike a molecule, has no internal structure.

Thus, the energy of a plasma can be represented using several temperatures and normally each of them are different. This indicates that thermal equilibrium is not applicable among particles in a plasma or for energy states of a desired particle. However, it often happens that the electrons and the ions have separate Maxwellian distributions characterized by different temperatures T_e and T_i , and the electrons or the ions themselves may be at thermal equilibrium. This is caused by larger collision rates among electrons or among ions than the collision rates between an electron and an ion.

B. Quasineutrality and Debye Shielding

A plasma is a collection of particles consisting of electrons, ions, neutrals and excited molecules. Of these the charged particles are the electrons and ions. Ions are normally positively charged, except for plasmas that contain gases with large electron affinities such as oxygen or halogen gases. Plasmas are characterized by an overriding tendency to be neutral. The numbers of positive and negative charges per unit volume cannot be exactly equal, of course; else there would be no electric fields at all. Since the opposing charge densities need differ only by, say, one part per million to create the electric fields normally observed in a plasma, for all intents and purposes these densities can be treated as being equal. This approximation known as "quasineutrality", is an important concept in plasma physics. "Quasineutrality" is thus a criterion for the existence of a plasma and can be written as

$$n_i \cong n_e \quad (1.16)$$

where n_e is the electron number density and n_i is the ion density.

The dominance of collective phenomena may be regarded as the basic plasma criterion. To quantify the concept we introduce a characteristic distance known as the Debye length, λ_D . Any individual charge in plasma will act on its immediate neighbours with a definite Coulomb force: at greater distances its influence is counterbalanced by the other surrounding charged species, particularly those of the opposite sign. A plasma shields itself from external fields by Debye shielding. When a positively charged object is placed in a plasma, the mobile electrons are attracted to it and form an electron cloud covering the charge; similarly, a negative object will repel electrons, leaving an ion cloud for shielding. The thickness of these clouds is of the order of the Debye length λ_D , defined by

$$\lambda_D = (\epsilon_0 kT / ne^2)^{1/2} \quad (1.17)$$

where k is the Boltzmann constant and T is the effective temperature (in K) of the particles of charge e of which there are n per unit volume. The Debye length does provide a measure of the distances over which the influence of an individual charged particle is dominant. Beyond λ_D the electric field, and hence the influence, of the individual particle is nil, and collective effects dominate.

The Debye length is an important physical parameter for a plasma. If a piece of charged matter is inserted into a plasma, a cloud of positively charged ions will surround the object when the object is negatively charged, and a cloud of electrons will surround a positively charged object. No electric field will be present in the bulk of plasma outside of these clouds. The clouds are called the sheaths. The Debye length gives the thickness of the sheath in which the shielding is almost complete. Thus only over the outside of the sheath can macroscopic electrical neutrality hold. However, the shielding is not perfect, since electrons near the edge of the cloud can escape because of their thermal energies, consequently, electric potentials of order $\frac{1}{2}kT_e$ can exist in the plasma. Debye shielding also occurs at the walls confining a plasma, where an ion-rich sheath of about $5\lambda_D$ thickness forms to repel electrons. The Coulomb barrier of the sheath is just high enough to make the escaping electron flux equal to the ion flux, so that no net charge is lost. Unless the plasma is extremely tenuous, these sheaths are much thinner than the dimensions of the plasma, so that the interior is quasineutral.

It is only beyond the Debye length that collective phenomena are of primary importance; hence if they are to dominate the behaviour of the system, the dimensions of the

latter, characterized by L , must satisfy:

$$L \gg \lambda_D \quad (1.18)$$

The concept of Debye length would require that the number of particles inside a sphere of radius λ_D should be considerably greater than unity, i.e.

$$\frac{4\pi n_e}{3} \lambda_D^3 \gg 1 \quad (1.19)$$

The Debye length was introduced originally in the theory of electrolytes and its application to plasmas should be made with caution.

C. Plasma Oscillations

Generally the density distribution of gas which is in the equilibrium state is macroscopically uniform as a whole. However, by means of fluctuations the uniformity can be broken at a given time and position. Also in a plasma, the particle density distribution has fluctuations. This is evidenced through oscillations built up by the charge of the particles. One of the fastest and most important of the collective motions is the bulk oscillation of the plasma electrons with respect to the ions. If the electron density at a certain point happens to become larger than the uniform background, the electrons will be pulled back to their original positions by Coulomb forces. This keeps the plasma neutral. However, because of their inertia, electrons overshoot their equilibrium positions and, once again, the electrons are subjected to Coulomb forces, but now in the opposite direction. Therefore electrons will oscillate by moving back and forth across an equilibrium position with a characteristic frequency ω_p , called the plasma frequency, which depends on the density of electrons as well as their charge and mass:

$$\omega_p = \left[\frac{n_e e^2}{m_e \epsilon_0} \right]^{1/2} \quad (1.20)$$

Collisions between ions and electrons will tend to damp these collective oscillations. In order for the oscillations to be only slightly damped, the collision frequency ω_c must be so small that

$$\omega_p \gg \omega_c \quad (1.21)$$

Other resonant-type phenomena with their own characteristic frequencies can however occur. Thus analogous with eqn. (1.20) there is a corresponding frequency for ionic

oscillation which is obtained by simply replacing the electron mass m_e by the ionic mass m_i . Again in the presence of a magnetic field both the electrons and ions may spiral around the field lines with characteristic frequencies, called cyclotron frequencies, ω_{ec} and ω_{ic} respectively. These natural frequencies determine the response to radiation incident on the plasma. If the frequency, ω , of the incoming waves matches one of the characteristic frequencies, or some combination of them, a resonance interaction may occur and the transfer of energy from the electromagnetic wave to the plasma may be greatly enhanced. The dispersion relationship (i.e. the dependence of ω on the propagation constant $k = 2\pi/\lambda$) for an electromagnetic wave travelling through a plasma is given by

$$\omega^2 = \omega_p^2 + c^2 k^2 \quad (1.22)$$

where ω_p is the plasma frequency and c is speed of light. Clearly if an electron density gradient exists, as it does in laser produced plasma, ω_p varies according to eqn. (1.20). For $\omega_p < \omega$, k is real and the wave propagates; for $\omega_p > \omega$, k is imaginary and the wave is not transmitted. In fact reflection occurs at the density, called the critical density n_c , for which $\omega_p = \omega$; thus

$$n_c = \frac{\epsilon_0 m_e \omega^2}{e^2} \quad (1.23)$$

A well-known example of this is provided by the reflection of electromagnetic waves by the ionosphere - the phenomenon which makes long-range radio communication possible. The ionosphere is relatively dilute plasma and hence reflects waves in the radio frequency range. Very dense plasmas on the other hand will reflect radiation at optical frequencies and this proves to be a factor of considerable importance in the generation of laser-produced plasmas.

1.1.3 Classification of Plasma

Plasmas are characterized by their electron energy kT_e and their electron density n_e . Several kinds of plasmas in nature and in laboratories are shown in fig. 1.1. [3]. Plasmas can be broadly classified into cold plasmas and thermal plasmas based on the electron energy and electron density.

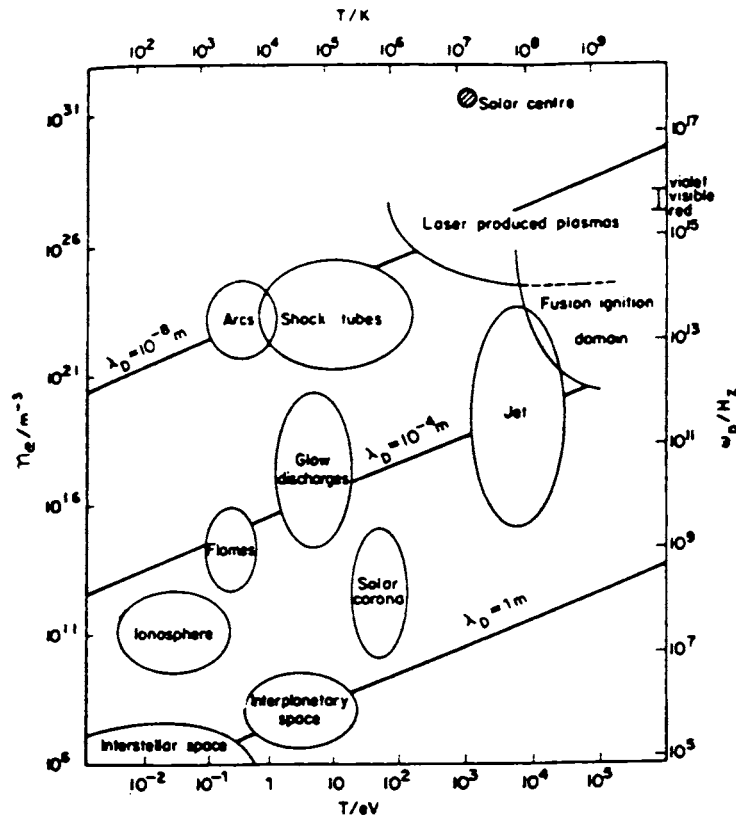


Figure 1.1: Approximate range of conditions in some typical laboratory and astrophysical plasmas

A. Cold Plasma

Cold Plasma such as that which can be obtained by a direct current glow discharge, can also be generated by a high frequency or a microwave discharge at low pressure. In this plasma, the degree of ionization is typically only 10^{-4} , so the gas consists mostly of neutral but excited species. A characteristic feature of this plasma is the lack of thermal equilibrium between the electron temperature and the gas temperature. Hence, this type of plasma is called a nonequilibrium plasma. In plasmas generated by discharge under a pressure of less than several tens of torr, the electron temperature becomes high but the gas particles remain at relatively low temperature. This is because the collision frequency between electrons and gas particles is small.

The relative temperatures in a cold plasma are considered as

$$T_e > T_{elect} > T_{vib} \geq T_{rot} > T_g \quad (1.24)$$

It is often observed that rotational and translational energies of gas molecules obey the Boltzmann distribution, however, the energies based on the vibration and electronic states deviate from the Boltzmann distribution.

B. Thermal plasma

In the plasma generated by an arc discharge, the energy distribution of electrons (characterized by T_e) and gas molecules (characterized by T_g) are nearly the same, because the collision frequency between electrons and gas molecules becomes large. The plasma is at thermal equilibrium, therefore $T_e \cong T_g$. Thermal equilibrium is also reached within each category of energy states of the gas molecules. A plasma composed of high-temperature gas particles is called a thermal plasma.

When a plasma is in thermal equilibrium, the density of particles can be calculated as functions of temperature and pressure, provided that the reaction



is at equilibrium where u_i is the ionization potential of gas molecule A. The degree of ionization α is defined using densities n_A and n_{A^+} for A and A^+ as

$$\alpha = \frac{n_{A^+}}{n_A + n_{A^+}} \quad (1.26)$$

The relation between α , temperature T, and pressure P is given using internal partition functions Q_A and Q_{A^+} for A and A^+ , respectively

$$\frac{\alpha^2}{1 - \alpha^2} P = \left[\frac{2\pi m_e kT}{h^2} \right]^{3/2} kT \frac{2Q_{A^+}}{Q_A} \exp \left[\frac{u_i}{kT} \right] \quad (1.27)$$

where m_e is the electron mass, and h is the Plancks constant. This is known as the Saha equation, which is applied to the ionization of neutral molecule A to a singly charged ion A^+ .

1.1.4 Reactions in Plasmas

In a plasma, electrons acquire energy from the electric field and collide with gas molecules. Electron collisions cause excitation and ionization of the gas molecules. Excited molecules and ions produce various kinds of reactions in the plasma.

A. Collision Phenomena

In a plasma there are charged particles (electrons and ions) and neutral particles (gas atoms and molecules). Collisions are continuously occurring among these particles. Collisions with no change of internal energy are termed elastic collisions, and those with an

exchange of internal energy between the particles are termed inelastic collisions. Consider a particle of mass m with initial kinetic energy E_i colliding head-on with a particle of mass M at rest. The energy transfer coefficient, i.e., the ratio of transferred energy E_t to kinetic energy E_i is given by

$$\frac{E_t}{E_i} = \frac{4mM}{(m+M)^2} \quad (1.28)$$

Thus, the internal energy of a particle of mass M increases by inelastic collisions according to

$$\frac{\Delta U}{E_i} = \frac{M}{m+M} \quad (1.29)$$

For collisions between electrons and gas molecules, E_t/E_i is 0.01% and $\Delta U/E_i$ is about 99%. The kinetic energy transferred by elastic collisions between electrons and gas molecules is extremely small.

The various kinds of inelastic collisions between particles lead to reactions such as excitation, dissociation, or ionization of gas molecules. Various reaction cross-sections can be obtained for each reaction. The total collision cross-section is expressed as the sum of cross sections for each reaction process:

$$\sigma = \sigma_1 + \sigma_2 + \sigma_3 + \sigma_4 + \dots \quad (1.30)$$

Excitation processes include many kinds of excitations between energy levels, such as electronic excitation, vibrational excitation and rotational excitation. Thus, occasionally, the sum of several kinds of excitation cross-sections is called the total excitation cross-section.

When the reaction cross-sections $\sigma_r(\epsilon)$ of an excitation, a dissociation or an ionization are given, a macroscopic reaction rate constant can be calculated by a combination of $\sigma_r(\epsilon)$ with the electron energy distribution function $f(\epsilon)$. Combining the velocity of random motion of electrons $v_e(\epsilon)$, the electron density n_e , and the particle density of the gas n_g , the reaction rate per unit volume is

$$\frac{dn_e}{dt} = n_e n_g \int_0^\infty \sigma_r(\epsilon) v_e(\epsilon) f(\epsilon) d\epsilon \quad (1.31)$$

Electron-electron collisions do not produce radiation except at relativistic velocities. In a hot plasma the important collisions are those between electrons and ions; in a slightly ionized gas the more numerous, though less effective, collisions between electrons and neutral atoms are more important.

B. Excitation and Ionization

As atoms or molecules receive energy, translational energy increases and the internal energy undergo a transition to a higher state. This process is excitation. Given further energy, most loosely bound electrons are removed from an atom. This is ionization and the minimum energy required for the ionization process is known as the ionization energy. Regarding the excitation and ionization processes for an atom or a molecule, the following reactions are known:

- 1) Excitation and ionization by an electron collision.
- 2) Excitation and ionization by an ion collision.
- 3) Excitation and ionization by a neutral particle collision.
- 4) Excitation and ionization by radiation.

The probability that these reactions occur is given by the cross-section for each reaction.

Collisional excitation involves a collision between an electron and a neutral species or ion, resulting in the conversion of kinetic energy into excitation energy in the atomic system. In collisional de-excitation, the inverse process in which excitation energy is converted into kinetic energy in the collision. Electrons, because of their high mean velocity and the long range nature of their interaction, can dominate the collisional excitation and de-excitation processes.

Collisional ionization can occur when the kinetic energy in an electron encounter is sufficient to remove another electron from an atomic species. Collisional recombination occurs when electrons encounter an ion and one electron recombines with a gain in the kinetic energy of the system.

In cold plasmas, it is possible that atoms or molecules are ionized through collisions with metastable excited particles that have small kinetic energy but high internal energy. When the gas reaches high temperatures, the kinetic energy of the neutral atoms and molecules is high enough to cause ionization by collision. Such a collision process resulting in ionization by thermal movement of particles is called *thermal ionization*. This ionization is observed in arc plasmas or burning flames when the gas temperature exceeds several thousand degrees. Such conditions are considered to be nearly in thermal equilibrium.

Penning ionization is the ionization process caused by the collision between metastable particles at excited states, and neutral particles which have a lower ionization

energy than the excitation energy of the metastable particles. It is expressed as



where B^* is the excited atom or molecule. The difference between the excitation energy of B^* and the ionization energy of A is transferred to the kinetic energy of the electron. If A is a molecule, a dissociative ionization of the molecule is possible as well. Penning ionization is significant in the longer mean free-path pressure regime.

Photoexcitation corresponds to the absorption of a photon as a result of which the atomic system is raised to a higher state. Photodeexcitation is simply the converse emission process. The absorption of light and the subsequent transition between the energy levels of a gas particle obey the selection rules. Homonuclear diatomic molecules do not have electric dipole moments, and no transition occurs between the vibrational energy levels of a particular electronic energy level. Therefore visible light which in most cases corresponds approximately to the energy difference between the vibrational levels, is not absorbed. However, by irradiating with UV light, which has higher energy, electronic energy states can be excited.

Photo-ionization can occur when an incident photon has sufficient energy to have an electron removed from an atomic system thus leaving it in a higher stage of ionization. The photoionization cross-section is about an order of magnitude smaller than the ionization cross-section caused by electron collisions. The difference between the energy of light and the ionization energy of a gas appears as kinetic energy of the released electron.

C. Recombination

The charged particles generated by various processes can be neutralized in the gas phase or on a solid surface. This relaxation to a neutral atom or molecule by combining a positive ion with an electron, or a positive ion with a negative ion, is termed recombination. In both cases, the vanishing rate of a charged particle due to recombination dn/dt is given as

$$\frac{dn}{dt} = \frac{dn_+}{dt} = \frac{dn_-}{dt} = -\alpha n_+ n_- \quad (1.33)$$

where n_+ and n_- are the densities of particles with positive charge and negative charge. α is called recombination coefficient.

In a radiative recombination process, electrons are caught by ions. As a result, excited neutral atoms or molecules are produced and the excess energies are radiated as photons.

When the electrons' energy spreads, a continuous spectrum is radiated.

In the three-body recombination involving an electron, there are two cases. The third body is either an electron or an atom or a molecule. Since the three-body recombination coefficient in the former case is proportional to $n_e(kT_e/e)^{-9/2}$, [4] when the electron temperature is low and its density is low, the coefficient increases. In the latter case, the recombination coefficient is proportional to $p(kT_e/e)^{-5/2}$ where p is the gas pressure in units of torr. In order to explain the pressure dependence of the three-body recombination coefficient, quite a number of models have been proposed [4].

In photo-recombination the electron recombines with an ion with the emission of a photon. The optical spectrum associated with the latter process is a continuum which falls off monotonically in intensity above the ionization limit.

1.1.5 Transport Phenomena

A. Drift

When an ion moves in its own gas in a uniform and relatively weak electric field, only elastic collisions between ions and gas molecules occur, i.e. no excitation and ionization. After an impact the initial velocity of an ion is supposed to be the same as if it collides with a neutral gas molecule. The electric field however, tends to drive the particle along the field direction, so that in the velocity - time graph the ion moves along a parabola. Fig. 1.2 show the imaginary path of an ion which starts its journey with a certain random velocity in a general direction.

When the ion has moved along a path whose average length equals a mean-free path, it collides with another gas atom and rebounds at random. Though it may happen that the ion starts moving against the electric field, it proceeds on the average in the field direction. This is the picture which conforms to Langevin's first mobility theory [5]. The ionic mobility is defined as the drift velocity, i.e. the velocity component in the field direction, in unit field (X). In a plasma, electrons and ions which frequently make collisions with neutral or ionized gas molecules, having random velocity by thermal motion, are moved collectively by the electric field in specific directions. The motion of these charged particles is characterized by drift velocity v_d .

$$v_d = \mu E \tag{1.34}$$

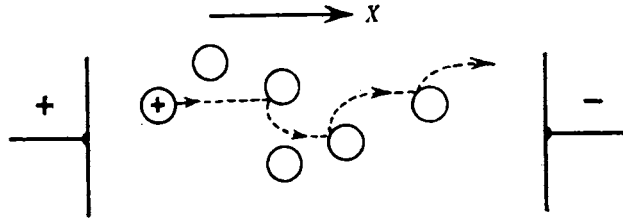


Figure 1.2: Motion of a positive ion through a gas in an electric field

where

$$\mu = \frac{e/m}{i\omega + \nu_m} \quad (1.35)$$

is called the mobility of the charged particle, where \mathbf{E} = the alternating electric field ($\mathbf{E} = \mathbf{E}_0 e^{i\omega t}$), m the mass of the particle, e , the charge of the particle and ν_m the collision frequency of ions with neutral particles.

In the case that the charged particle is subject to a constant electric field, i.e. $\omega = 0$, or in the case of $\nu_m \gg \omega$, the mobility simplifies to

$$\mu = \frac{e}{m\nu_m} \quad (1.36)$$

The above formula is applicable when the energy which the charged particle obtains from the electric field is small in comparison to its thermal energy. If the electric field is strong, the charged particle loses some portion of the thermal energy by elastic collisions with neutral particles and gains an equivalent amount of energy from the electric field. In this case

$$v_d = \left(\frac{c e^2}{2 m^2} \right)^{1/4} (E\lambda)^{1/2} \quad (1.37)$$

where $v/\lambda = \nu_m$.

B. Diffusion

Charged or uncharged particles are said to diffuse in a gas if they move from points of high concentration to those of low concentration. The origin of this motion is a purely thermal one; thus the actual path of an individual particle is a zig-zag line [6]. If the

mean-free paths of electrons and ions in a plasma are short compared to the size of the chamber, the computational procedure is the same as for diffusion of gas molecules.

When the density n of the particles changes only with position, the diffusion velocity v is $v = -(D/n) \text{ grad } n$, where D is the diffusion coefficient. The diffusion coefficient D is

$$D = \frac{kT}{m\nu_m} = \frac{1}{3}\lambda\bar{v}_r \quad (1.38)$$

where ν_m is the collision frequency, λ is the mean-free path, and \bar{v}_r is the root mean square (rms) velocity for the gas molecule.

The diffusion coefficient of electrons in a plasma is much greater than that of ions. This causes a charge separation in the plasma and gives rise to an electric field. Therefore the diffusion of electrons is suppressed and ions are accelerated by the electric field. In the steady state it is considered that the movements of electrons and ions are not independent; both diffuse together in the same direction with a common velocity. This phenomenon is called ambipolar diffusion. The ambipolar diffusion coefficient D_a is given by the weighted coefficients of electrons and ions in the ratio of their mobilities,

$$D_a = \frac{D_+\mu_e + D_e\mu_+}{\mu_e + \mu_+} \quad (1.39)$$

where D_+ , μ_+ , and D_e , μ_e are the diffusion coefficients and the mobilities of positive ions and electrons respectively. If the ion temperature T_i is about the same as the electron temperature T_e , the drift velocity of the electrons will be larger than that of the ions, and hence

$$D_a = \frac{2D_+\mu_e}{\mu_e + \mu_+} \cong 2D_+ \quad (1.40)$$

If T_e is much higher than T_i , then

$$D_a = \frac{D_e\mu_+}{\mu_e} \quad (1.41)$$

Since the relation between the diffusion coefficient, mobility and temperature is written by Einstein's relation

$$\frac{D}{\mu} = \frac{kT}{e} \quad (1.42)$$

the ambipolar diffusion coefficient in the latter case can also be written as

$$D_a = \frac{kT_e\mu_+}{e} \quad (1.43)$$

1.1.6 Emission Processes in a Plasma

Thermal ionization of an atom implies a high temperature, and under conditions approaching complete ionization, laboratory plasmas are difficult to contain and are unstable. An investigation of the physical properties of such a system can be undertaken by the study of the radiation emitted from or absorbed by a plasma. In this field of plasma diagnostics, plasma spectroscopy has evolved and provides information on the temperature, particle density and life history of the plasma.

In contrast to conventional spectroscopy, where one is mainly concerned with the structure of the isolated atom or molecule, the radiation from a plasma also depends on the properties of the plasma in the immediate environment of the atomic or molecular radiator. This dependence on the plasma properties is a consequence of the long-range Coulomb potential effects which dominate the interactions of ions and electrons with each other and with the existing neutral particles. These interactions are reflected in the details of the radiation in several ways. They can control the population densities of the discrete atomic states, shift and broaden energy levels by the Stark effect, lower the ionization potentials of the atomic species, cause continuum radiation emissions and the emission of normally forbidden lines. The propagation of electromagnetic radiation is prohibited for frequencies less than the plasma characteristic frequency and in the region just above the cut-off, the spectrum of continuous radiation is considerably modified by collective plasma effects.

The radiation emitted from a self-luminous plasma can be divided into bound-bound (discrete), bound-free (photoelectric absorption) and free-free (bremsstrahlung emission and absorption) transitions and are briefly discussed each in turn. Free-free and bound-free transitions result in continuous absorption and emission spectra. Bound-bound transitions in atoms result in line spectra while in molecules they result in the formation of band spectra. Under certain conditions the individual lines are so close to one another that they even partially overlap and the resulting spectrum is almost continuous (quasi-continuous).

A. Bound-Bound Transitions

When an atom or an ion makes a transition from one bound state to another of lower energy, the energy of the emitted photon is well defined. In the absence of perturbations

the transition gives rise to a spectral line whose profile depends upon the spontaneous life time of the upper state, and on the distribution of velocities of the emitting atoms, which causes a distribution of Doppler shifts. Collisions, electric fields and magnetic fields may all perturb the initial and final states of the emitting atoms: the perturbations affect the spectral line profile, which thus contains much information about conditions existing in the plasma, though often in an indecipherable form.

Collisional excitation by energetic electrons is a very important process, and the spectrum of the line radiation depends on the electron temperature (or velocity distribution) and density. In a cool partially-ionized gas ($T_e = 1$ eV) much of the line radiation is in the infrared and visible regions of the spectrum. As the temperature rises, atoms can be raised to more energetic excited states and thus tend to emit lines of shorter wavelengths. When $T_e \sim 10$ eV nearly all the atoms will be ionized and multiple ionization of many-electron atoms occurs. The reduced screening of the nuclear charges in multiply-ionized atoms leads to larger energy differences between bound states, so that line radiation emitted mostly at shorter wavelengths in the far ultraviolet and X-ray regions of the spectrum. At sufficiently high temperatures, when virtually all the ions are reduced to bare nuclei, bound-bound transitions giving line radiation ceases.

B. Bound-Free Transitions

Transfers between different ionic states for both atomic and molecular species are classified under the name of bound-free transitions. Thus the absorption of radiation from a discrete atomic state, such that the photon has enough energy to extend above the next ionization threshold, results in the removal of an electron and gives rise to the process of photoionization. The reverse process of recombination occurs when an ion and an electron recombine with the emission of a photon to form an ion in the next lowest ionic state (or in the neutral atomic state. Since the upper state is continuous, the energy above the ionization threshold is that of the kinetic energy of the ion and the free electron, the emitted or absorbed radiation in the two processes, recombination and photoionization respectively, is also continuous. However, the lower states which being discrete give rise to absorption or emission edges in the otherwise continuous spectra.

A complex ion may have two or more ionization potentials corresponding to different configurations of the bound electrons. A free electron may thus be captured without the emission of radiation, into a bound state 's' of a configuration with a higher ionization

potential. This transition is generally balanced by the inverse ‘autoionization’ process: however, the recombination may be stabilized by a radiative transition from ‘s’ to another bound state of lower energy which is not subject to autoionization. This process is known as ‘dielectronic’ recombination.

C. Free-Free transitions

Free-free or Bremsstrahlung involves an encounter between an electron and an ion of charge ze so that the two particles may be regarded as being in a continuum state of the system of charge $(z-1)e$; a transition to a lower continuum state of the system may occur with the emission of a photon, which have energies of the order of thermal electron energies [7]. In plasmas with kT_e in the 100-10000 eV range, Bremsstrahlung is in the soft X-ray regime and passes readily through the plasma. The major part of the Bremsstrahlung is due to electron-ion collisions and, since the initial and final states are continuous, the spectrum associated with the process is continuous. In a plasma sufficiently hot for most of the ions to be stripped of all their orbital electrons, electron-ion Bremsstrahlung is the dominant mechanism.

In the inverse process a photon is absorbed by the ion-electron system and the electron is raised from a lower level in the continuum to a higher one. Essentially the energy of the incoming photon is converted into an increase in the kinetic energy of the free electron. Inverse Bremsstrahlung is of basic importance as a mechanism for plasma heating by laser light of all wavelengths. Both Bremsstrahlung and inverse Bremsstrahlung are of major importance in laser produced plasmas.

D. Cyclotron Radiation

In Cyclotron radiation, the acceleration is due to the gyration of charged particles in a magnetic field. Although the particles are free, the spectrum of the radiation is a kind of line spectrum composed of frequencies which are harmonics of the cyclotron frequency ω_c . Thus the plasma radiates like a black body at ω_c and its first few harmonics but is transparent to the high harmonics. For relativistic particles, the radiation becomes truly continuous - synchrotron radiation. The process is sometimes known as magnetic Bremsstrahlung, but it is quite unlike collisional Bremsstrahlung. It is anisotropic and usually of much longer wavelength and it consists of lines, although these may be smeared

out by perturbations.

1.1.7 Equilibrium in Plasmas

Consider a plasma in an ideal thermodynamic enclosure at a temperature T . In such a system the following conditions are satisfied: (a) all particles, electrons, neutral species and ions obey the Maxwell velocity distribution law; (b) the population distributions over the states of any atom or ion are given by the Boltzmann formula; (c) the number of ions in stage z relative to the number in stage $(z-1)$ is given by the Saha equation; (d) the density distribution of the radiation in the cavity as a function of frequency and temperature is given by the Planck's formula.

A system described above is said to be in complete thermodynamic equilibrium at the temperature appearing in the equations which describe conditions (a) to (d) has a unique value. Furthermore, every atomic process occurring in the plasma is balanced by an equal and opposite process: thus for example in electron-atom encounters the rate of collisional excitation is equal to the rate of collisional de-excitation.

It is hard to find a plasma in complete thermodynamic equilibrium. Various excitation, de-excitation, and particle loss processes prevent such an equilibrium from occurring. Nevertheless, other, less complete, conditions of equilibrium may obtain. The commonest plasma model is that which conforms to the local thermodynamic equilibrium (LTE). In LTE it is assumed that collisional events, particularly the events involving electrons, determine the behaviour of the system. These collisions are assumed to be governed by the same laws as hold in total thermodynamic equilibrium. Thus an electron temperature, T_e , is defined and in terms of this temperature the electron velocity distribution, the populations in excited levels and various stages of ionization are given by Maxwell velocity distribution, the Boltzmann formula and Saha ionization equation. The radiation distribution however is not given by Planck's equation and radiative effects are assumed to play an insignificant role in determining the equilibrium in the plasma. Furthermore it is not assumed that the temperature T_i , which describes the velocity distribution of ions and neutral atoms is necessarily the same as the electron temperature T_e , describing the velocity distribution of electrons.

Clearly for LTE to hold the electron density must be sufficient high. The condition for n_e , the number of electrons per cm^3 : [8]

$$n_e \geq 1.4 \times 10^{14} T_e^{1/2} \chi^3 \quad (1.44)$$

where T_e is in eV and χ is the excitation potential (in eV) of the transition under consideration. At low energy densities a second limiting type of equilibrium may be attained *viz.* coronal equilibrium (so called because it describes conditions in the solar corona). In this case the excitation and ionization occur as the result of electron collisions whereas de-excitation and recombination occur by the emission of radiation. The plasma is assumed to be optically thin so that re-absorption of the emitted radiation is negligible. Conditions in a coronal system depend strongly on the details of the atomic processes involved and their cross-sections.

1.2 Laser - Matter Interaction

The laser, as a source of 'pure' energy in the form of monochromatic and coherent photons, is enjoying ever increasing popularity in diverse and broad applications from drilling micron-sized holes on semiconductor devices to guidance system used in drilling a mammoth tunnel under English Channel. The reason for this is that the radiation emitted by lasers has unusual properties that distinguish it from ordinary sources of light. The main properties of interest that are different in laser radiation as compared to radiation from conventional light sources are the intensity, directionality, monochromaticity, and coherence of the laser radiation. The effects produced by interaction of high-power laser beams with matter is of considerable interest. These high-power effects include heating, melting and vapourization of solid materials, emission of charged particles and plasmas, electrical discharges in gases, and applications of these effects in such areas as material processing.

Laser processing research activities started in the early 1960s soon after the first high-power lasers became available. Shortly after the demonstration of the first laser (ruby laser), the most intensely studied theoretical topics dealt with laser beam-solid interactions. Experiments were undertaken to verify theoretical models for these processes. Later, these experiments became the pillars of many practical applications. The early work was mainly motivated by the prospect of using laser beams as machining tools. Most of the phenomena governing evaporation by laser beams were understood by 1975 although, of course, important insights and refinements have been made in the meantime and continue to be made.

Industry can now exploit the results of two major research areas which are continuously providing new contribution: laser physics and the physics of the interaction of the radiation with matter. Machining (surface modification, hardening, cutting, welding, milling, drilling, etc.) is the first area in which laser processing is presently in widespread industrial use. Other applications are in the domain of quantitative and qualitative chemical analyses; surface removal treatment in ambient gas; compound synthesis from binary layered structures and from irradiation of material in ambient gas; material deposition etc. Generally these applications are achieved in an ambient gas, except for ultra-trace chemical analysis. Concentrating industrial laser metal-working processes, low power densities are used for transformation hardening and surface alloy-

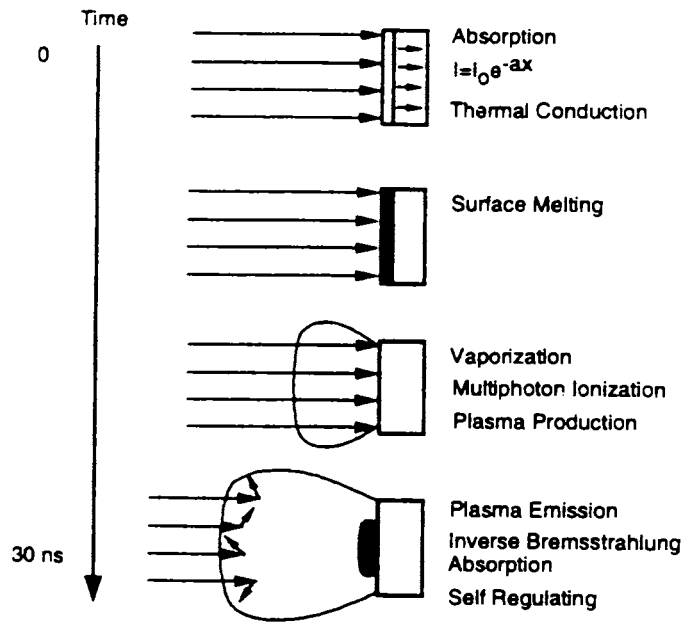


Figure 1.3: Schematic representation for the laser target interactions

ing and cladding. High irradiance levels are required for deep penetration welding and cutting. Higher power densities and shorter interaction times are used for drilling. The production of ultra dense plasma capable of sustaining thermonuclear fusion for energy sources needs larger laser power density. Such hot and dense laser produced plasmas can be used as sources of X-ray radiation.

Some of the most interesting phenomena associated with lasers involve the effects produced when a high-power laser beam is absorbed at an opaque surface. The phenomenon of laser-target interaction has been studied by several workers [9-17]. Ready [11] gave a comprehensive description of melting and evaporation at metal surfaces. Mc Mordie and Roberts [15] measured the pressure generated from an aluminium alloy in vacuum. Measures and Cardinal [13] developed a simple model for laser ionization. Pert [16] investigated the role of thermal conduction in the laser solid interaction. Sneddon and co-workers [18-20] have made quantitative studies of plasma emission during excimer laser interaction with copper as the target material.

A schematic representation of the laser-target, laser-plasma interactions is shown in fig. [1.3]. This representation illustrates several steps of the process, including absorption of photon energy, surface melting, vapourization and multiphoton ionization,

plasma emission and plasma heating by inverse Bremsstrahlung absorption, and finally, supersonic expansion of plumes owing to the pressure differences [21]. Laser irradiance and thermo-optical properties of the material are critical parameters that influence these processes.

1.2.1 Laser excitation of Matter

Laser radiation from the ultraviolet to the infrared interacts primarily with the electrons of an atom or atom system. Furthermore, the frequencies and energies associated with this reasonably extensive band of electromagnetic radiation do not induce nuclear disturbances, or even affect the energy levels of the inner core electrons of an atom. These photons do however readily interact with the outer (bound or free) valence electrons of the atoms. Clearly, the optical properties of any material will be mainly affected by the nature of its outermost electrons.

The primary process in light absorption is electronic excitation by the absorption of a photon. In metals the dominant absorption mechanism involves free-free transitions (inverse Bremsstrahlung). The absorption causes the temperature of the conduction electron gas to rise. By electron-phonon interaction, the absorbed energy is transferred in part to the motion of the atoms or ions making up the metallic lattice. Typical transfer times between hot electrons and the lattice are of the order of one picosecond for most materials. The heating by free-free transitions is usually well described by a Drude model. Thermal conduction will carry heat deeper into the metal. The penetration depth by heat conduction is of the order of $\sqrt{Dt_p}$, where D is the thermal diffusivity and t_p is the duration of the irradiation.

In semiconductors the photon energy must exceed the band gap in order to have significant absorption. The basic process is the creation of an electron-hole pair, corresponding to a transition of an electron from the valence to the conduction band. The electrons and holes may have a considerable kinetic energy $h\nu - E_g$. This energy is rapidly shared with the lattice vibrations and leads again to heating of the semiconductor material, on a time scale of picoseconds. In intense laser pulses the density of electrons may become so high, that rapid electron-hole recombination occurs via Auger process, [14] in which the recombination energy is given to a third carrier rather than to the lattice.

Insulating materials, with $h\nu \ll E_g$, are optically transparent. At very high radiation intensities multiphoton absorption processes and impact ionization become sufficiently

probable, that significant concentrations of conduction electrons are created. In multi-photon interband transition, n photons, the combined energy of which exceeds E_g , are absorbed simultaneously. Impact ionization is the inverse process of Auger recombination. Upon colliding with a lattice atom an energetic carrier is slowed down while creating an additional low-energy carrier pair (an extra electron being knocked off the atom, leaving behind a hole). Thus free-carriers are generated at high irradiance due either multiphoton transitions or impact ionization. When this happens the subsequent heating mechanisms become again rather similar to those described for metals and semiconductors.

When a laser pulse is incident on an opaque solid target two extreme situations may be identified. At very low irradiances the light causes only a rise in temperature by conduction below the surface with no change of phase. If the irradiance is very high, multi-photon ionization takes place at the surface during a few cycles of the electric field. Between these extremes there is a wide variety of intermediate situations in which changes of phase, the pressure due to vapourization, thermionic emission and shock wave generation may be important. Not only the time dependence of the irradiance of the laser pulse but also the many thermal, optical and mechanical properties of the target material and their temperature and pressure dependence must be taken into consideration in any complete theoretical treatment of the interaction. To utilize the advantages of laser processing and to achieve appropriate results, it is necessary to understand the physical processes involved.

In the following sections the physical phenomena that occur when high-power laser radiation interacts with a target will be discussed.

A. Reflection:

Reflection and absorption coefficients determine the amount of beam power absorbed within the material. Reflection of part of the energy of an incident laser beam is an important consideration in determining the fraction of laser energy absorbed by a sample, especially at low irradiances, during the beginning of the laser pulse. For metals, a model based on the Drude-Zener free-electron theory predicts a linear decrease in reflectivity of the metal as its temperature increases, because the apparent electron-lattice collision time shortens [22]. Consequently more laser energy would be expected to be absorbed by a hot, laser heated solid surface than that predicted using room temperature reflectivity.

Experimentally the reflectivities of copper and steel samples decrease to 25 % of their initial values during the first half of a Nd:glass laser pulse [23]. The change in reflectivity may be due in part to the result of phase changes that occur during intense heating. In any case these measurements indicate that laser energy can be coupled effectively into a target that is initially highly reflective, if the irradiance is very high.

B. Photoelectrons

The optical coupling of a metal is dominated by the conduction electrons. Only electrons in states close to the Fermi level, referred to as ‘free electrons’, contribute to the optical properties. Before the laser irradiance reaches the level where a sample begins to vapourize, photoelectrons may be ejected by multiphoton absorptions, which involves simultaneous absorption by an electron of a sufficient number of photons to be ejected from the conduction band. For Q-switched pulses the effect may be relatively weak compared to thermionic emission of the electrons, but the photoelectric effect is assumed to play an important role in the generation of plasma plume using ultraviolet (UV) lasers. Photoelectric electrons are coincident with the laser pulse and do not involve a thermally related delay. Two and three photon photoelectric effects have been observed and studied by several authors [24-26]. At still higher irradiances the electron pulse is delayed by several nanoseconds and is produced mainly by thermionic emission.

C. Thermionic emission

Thermionic emission of positive ions from heated metallic surfaces have long been recognized [27-29]. A sample heated to a temperature of the order of 2000 K or higher will emit ions of the materials present as impurities on the surface and also of the parent metal itself. Laser heating will produce the same type of positive ion emission. Thermionic emission can be produced by free running laser pulses as well as Q-switched pulses at irradiances lower than those that destroy the surface. The only requirement is that the surface temperature be raised sufficiently to allow significant escape of thermal electrons. The electron yield is greater for higher sample temperatures T and can be fitted by the Richardson law describing the thermionic electron flux as a function of the surface temperature.

$$j = AT^2 e^{-\phi/kT} \quad (1.45)$$

where j is the current density (A cm^{-2}); ϕ is the work function (eV); k is Boltzmann constant and A is a proportionality constant. Current densities obtained from calculated surface temperatures caused by free-running and Q-switched laser pulses agree quite well with measured current densities for irradiances low enough to prevent surface destruction [30, 31].

Thermionic emission of ions and molecules are related by the Langmuir - Saha equation,

$$\frac{j_+}{j_0} = \frac{g_+}{g_0} e^{(\phi - I)/kT} \quad (1.46)$$

provided equilibrium conditions exist about the surface (a condition that may not be reached during laser interactions). j_+ and j_0 are the positive ion and neutral particle flux leaving the surface at temperature T , g_+ and g_0 are the statistical weights of the ionic and neutral states, and I and ϕ are the ionization potential and electron work functions, respectively.

Thermionic ejection of electrons, ions and neutral molecules show that important species are ejected from the surface of the sample material prior to the onset of melting and major vapourization of the sample material during a laser pulse. These species add to the complexity of the laser interaction with the surface. For instance, as the free electrons absorb more laser energy (inverse Bremsstrahlung) they may become energetic enough to initiate a breakdown of the gas above the sample surface. A breakdown at a sufficiently high irradiance then initiates a radiation-supported atmospheric shock wave, which precedes the expansion into the atmosphere of the major portion of the vapourized sample [32].

1.2.2 Heating without melting

The basic and dominant physical mechanism of laser interaction on absorbing media is heating. Heat treatments serve as a wide range of purposes in material technology such as softening or hardening of metals, annealing of crystals, dopant diffusion in semiconductors, compound formation in mixtures, oxide layer growth, polymerization of plastics etc. The main advantage of laser induced heating is that heating can be done in a localized fashion, both in space and time. By matching the wavelength and the beam power to the optical and thermal material properties, the amount of heating can be chosen accurately to suit the needs of a process. Sharply delimited areas can be heated to high temperature while the remainder of the workpiece stays virtually cold. Rapid cooling

of the heated material can be achieved by using short pulses or rapidly moving beams. Laser beams are chemically pure and free of inertia and can be moved easily and passed through windows to reach remote or inaccessible parts of a work piece.

The temperature rise is determined by the laser power, pulse duration, absorption coefficient, specific heat and thermal diffusivity. The phase of the material may or may not change depending upon the strength of the laser radiation incident on it. Heat transfer equations have been used to predict the temperature at various depths in the sample for cases where a phase change does not occur in the material. When the incident laser intensity is low the material will not undergo phase transformation; the only effect of the irradiation is raising the temperature of the material. The irradiances in the laser pulse for such studies are thus restricted so that no significant evaporation or boiling takes place. Dielectric breakdown by avalanche ionization or multiphoton absorption is also excluded.

In order that a single instantaneous temperature may be defined at every point, the light must not cause a substantial change in the internal energy of the region where absorption occurs during the relaxation times involved, which are of the order of 10^{-12} to 10^{-13} seconds [33]. Provided this condition is satisfied it is possible to discuss classically the effects of thermal conductivity on the temperature distribution in the solid. This assumption may break down for the case of picosecond and femtosecond pulses. During the absorption of a picosecond duration pulse, there will not be time for the energy to be distributed among many particles in the collision processes. The energy received by the electron which absorbs a quantum may be coupled into the lattice relatively slowly on a picosecond time scale. Therefore, observations of heating effects produced by a single picosecond pulse will probably require a different treatment.

· Ready [11] carried out detailed calculations of the temperature rise due to the absorption of laser pulse using a one-dimensional model. A one-dimensional model of thermal diffusion is valid only provided the diameter of the laser beam at the surface is much greater than the penetration depth during the laser pulse. For most of the laser pulses used in plasma production this condition is obeyed. In most cases the optical absorption coefficient of the absorbing material will be large. The absorption coefficient for metals is high enough ($10^5 - 10^6 \text{ cm}^{-1}$) that the laser energy can be considered to be deposited at the surface, and then transferred into the metal by conduction. If the laser pulse is

flat in time and is uniform over the x-y plane we have [11]

$$T(0, t) = \frac{2F_0}{K} \left(\frac{Dt}{\pi} \right)^{1/2} \quad (1.47)$$

The above equation has great utility in estimating approximate surface temperature rises for a broad variety of cases.

1.2.3 Melting without vapourization

The next stage in heating a solid target begins when the target temperature is raised to the melting point. Melting of surfaces occurs at a higher regime of absorbed flux densities. In many applications, such as welding, this transition is of course very important. Regarded as a step towards the production of the plasma, however, the transient liquid phase is not of great significance. The latent heat of fusion is small compared with the latent heat of vapourization or the ionization energy. Also, within the short duration of a high power laser pulse the molten target material will not be displaced significantly. The most important consideration may well be the change in the optical characteristics of the surface. Bonch-bruevich *et al* [23]. measured the time dependence of the reflectivities of several metal surfaces heated by laser pulses, and deduced the relationship between the surface temperature and the absorptance of silver.

This situation of optimum melting without vapourization is produced only over a fairly narrow range of laser parameters. For welding applications one desires effective melting of the surface without excessive vapourization. The flux density must be high enough to raise the surface above the melting point. If it is too high, the surface will begin to vapourize before the interface between molten and solid material has progressed far into the sample. Q-switched lasers are not suitable for melting applications, since the pulse durations are too short and the flux densities too high to produce effective melting. Generally the flux density must be kept below some critical value and the pulse width stretched as long as possible to produce effective melting. In fact, the optimum pulse length for melting is longer than the pulse length that are conveniently produced by most lasers. With continuous high power lasers, any desired duration of exposure can be attained by shuttering, and effective melting can be produced.

If the spatial profile of the laser beam is Gaussian of radius d and if the absorbed flux density at the surface is a constant F_0 for times less than the pulse duration t_p , the temperature as a function of radial distance r from the centre of the heated spot, depth

z from the surface, and time t is given by

$$T(\tau, z, t) = \frac{d^2 D^{1/2} F_0}{K \pi^{1/2}} \int_0^t \frac{dt' \exp(-z^2/4Dt') \exp[-\tau^2/(4Dt' + d^2)]}{t'^{1/2}(4Dt' + d^2)} \quad (1.48)$$

The thermal time constant represents the time at which the rear surface of a pulse reaches a temperature of the same order of magnitude as the front surface where heat is absorbed. For a plate of thickness d and thermal diffusivity D , the thermal time constant τ can be defined [11]

$$\tau = \frac{d^2}{4D} \quad (1.49)$$

The significance of the thermal time constant is that it gives an order of magnitude estimate for the time for heat to penetrate through a sheet and thus an approximate estimate of the time required to melt through the sheet. If the laser pulse length is much shorter than the thermal time constant of the workpiece, good fusion through the workpiece will not be attained.

The maximum depth that may be melted without surface vapourization may be expressed by [11]

$$X_{\max} = \frac{G}{F} \quad (1.50)$$

where G is a numerical factor characteristic of the metal. Q-switched lasers drive metals past their vapourization temperatures before much melting can proceed. The limited depths available for melting pose a problem in laser welding, where maximum melting without vapourization is desired.

1.2.4 Laser induced vapourization

When the temperatures are high enough to cause a phase change in the material, some of the incident energy is used to produce the phase change. A one-dimensional model that includes surface heating and the presence of a solid-liquid boundary is presented in Masters [34]. The thermal conductivity and specific heats of the liquid phase differ from those of the solid phase. When temperatures near the boiling point are reached, a significant part of the material begins to vapourize. Laser vapourization of solid samples has received a great interest of attention due to its potential applications in material coating, its use as a sample introduction method for solid samples in atomic spectroscopy, and the use of the laser generated plume or plasma for analytical measurement [18].

For materials with lower thermal conductivities, the absorbed heat remains nearer the focal region, causing higher temperatures to be reached and greater amounts of material

to be vapourized, than for materials that conduct heat away more quickly. As the laser flux density increases, the heat is supplied too quickly to be conducted away; a larger fraction of the heat is used to vapourize the material and the latent heat of vapourization becomes the dominant factor in determining the amount of material vapourized during a laser pulse. Experimental results show less copper than Type 18-8 stainless steel vapourized by a free-running laser pulse at low laser output, while more copper than stainless steel is vapourized at higher laser energies [11]. The flux density F_c for which the crossover from the region in which the thermal conductivity is dominant to the region in which the effect of the thermal conductivity is negligible is given approximately by

$$F_c \geq 2L\rho D^{1/2}t^{-1/2} \quad (1.51)$$

where L is the latent heat per unit mass, ρ the density, D the thermal diffusivity and t the laser pulse length. At very low laser powers, the materials exhibiting the largest amount of material removal will be those with the lowest thermal conductivity.

The heat capacity is an important variable in determining the time t_v , that it takes the surface to reach the vapourization temperature, or boiling point. This time can be estimated from a one-dimensional heat flow equation, assuming a constant laser flux density F absorbed at the surface [35]

$$t_v = \frac{\pi K \rho c}{4F^2} \Delta T \quad (1.52)$$

In this equation K is the thermal conductivity, c the heat capacity per unit mass, and ΔT the temperature rise necessary to reach the vapourization temperature. After the material reaches a state of steady vapourization, the rate of vapourization V ($\text{gcm}^{-2}\text{s}^{-1}$) can be estimated by

$$V = \frac{F}{c\Delta T + L_v} \quad (1.53)$$

The first term in the denominator represents the heat used to raise the temperature of an amount of the material to the vapourization temperature, and the second term the heat required to vapourize the amount.

In the case of vapourization with normal pulse lasers it was assumed that the vapourized material does not interact further with the incident laser radiation. But with Q-switched laser vapourization the presence of the blowoff material *i.e.* the material emitted from the target surface interacts with the incident laser radiation. It exerts a high pressure on the surface and absorbs light and shield the surface from the incident laser

light. Also as the material becomes very hot, it can produce an impulse reaction on the surface.

The threshold laser irradiance to reach superficial vapourization of the target can be determined from temperature estimation. Particles escaping from the hot surface have a velocity distribution corresponding to the surface temperature, their velocity vectors all pointing away from the surface. This anisotropic velocity distribution is transformed into an isotropic one by collisions between the vapour particles. This happens within a mean-free path from the surface, a region known as the Knudsen layer. Beyond Knudsen layer the vapour reaches a new internal equilibrium with a temperature different from the surface temperature.

The influence of the laser parameters on the mass removed has been studied by several authors [17,36]. For many solids, the power density required for evaporation is in the range 10^4 to 10^9 W cm^{-2} . In the range 10^4 to 10^7 W cm^{-2} , the resulting vapour consists of polyatomic particles. At power densities below 7×10^7 W cm^{-2} , no atoms were in the vapour, whereas above 5×10^8 W cm^{-2} , the evaporated material was partially ionized. Mitchell et al [37] found that the higher the repetition rate, the higher the atomic emission signal and, subsequently, the greater the mass ablated.

When considering vapourization it is important to remember that the boiling point of a material is pressure-dependent. The radiation pressure due to a focused laser beam absorbed or reflected by a surface can be very great due to the recoil on the surface from departing particles. If I is the effective irradiance, v the final velocity of the vapour flow and W the energy of vapourization and acceleration per unit mass, the recoil pressure, known as the ablation pressure is given approximately by [33]

$$p = \frac{Iv}{W} \quad (1.54)$$

A detailed discussion of the dynamics of the vapourization process has been given by Krokhin [38].

1.2.5 Ionization of the vapour and electron cascade growth

At the temperature with which the vapour leaves the irradiated surface the thermal ionization degree of the vapour is relatively high (10^{-5} - 10^{-4}), which means that the development of the electron cascade growth is significantly improved. This is the pre-breakdown state of the vapour. The threshold for avalanche depends on the vapour

ionization.

Electrons will gain energy in the field through inverse Bremsstrahlung absorption and lose energy by elastic and inelastic collisions with neutral particles. Richter [39] has shown that the electron temperature is largest with the CO₂ laser (10.6 μm) compared to the case of excimer laser (0.308 μm), because the inverse Bremsstrahlung process heating the electrons is more efficient in the infrared region. Indeed the laser radiation absorption coefficient is inversely proportional to λ². If the laser irradiance is high enough, primary electrons will gain an energy larger than the ionization energy. These electrons will generate new electrons by impact ionization of atoms of the vapour, thereby leading to cascade growth.

The minimum laser intensity required for breakdown in the metal vapour and/or in the ambient gas is given by [40]

$$I_i(MWcm^{-2}) > 2 \times 10^3 \frac{\Delta}{\lambda^2 M} \quad (1.55)$$

where Δ is the ionization potential of neutral particles (in eV), λ in μm and M (amu) the atomic mass. This process is dominated by the inverse Bremsstrahlung process favoured for large laser wavelengths. The dependence of I_i with 1/λ² means that it is easier to obtain a breakdown with an IR laser than with UV, as observed by Richter [39]. Nevertheless, the amount of ablated matter is larger using an UV laser than with an IR laser.

1.2.6 Plasma production

When the radiation from a Q-switched laser with sufficient energy is focused on a solid target, a characteristic form of plasma is generated. Its salient features are high density, high temperature and transience - it lasts essentially only the same length of time as the exciting laser pulse. This process of laser induced optical breakdown involves the radiative heating of free electrons within the solid by the intense laser pulse. These initial electrons are thought to be present because of thermionic and photoelectric emission. The electrons couple very strongly to the incident radiation, and by absorbing the energy, they are strongly accelerated, and collide with ions and neutral atoms and molecules (inverse Bremsstrahlung). In this way more atoms are ionized and they in turn provide more electrons which further increase the rate of ionization. The whole process of plasma formation can be divided into three distinct phases; firstly initiation, secondly formative

growth and the onset of breakdown and thirdly plasma formation with the generation of shock waves and their propagation.

Although the basic processes of initial breakdown are different in the cases of conductors and dielectrics, once the priming plasma is formed the physics of the subsequent events is essentially the same. The incoming laser radiation is now absorbed in the primary plasma by inverse bremsstrahlung. The absorption coefficient for this process is [41, 33]

$$\alpha_{ib}(cm^{-1}) = 3.69 \times 10^8 \frac{Z^3 n_e^2}{T^{1/2} \nu^3} (1 - \exp(-h\nu/kT)) \quad (1.56)$$

where λ is the wavelength of the laser photons in μm . The rate of absorption depends on n_e^2 . The absorbed energy causes an increase in the kinetic energy of the electrons, i.e. an increase in electron temperature, and this in turn produces further ionization with a consequent increase in n_e . Hence, the rate of absorption, and with it the rate of ionization escalates so that n_e increases further and eventually approaches n_c at which stage the critical density is established across the plane surface some distance into the plasma. The most important modifications arise at high fluences from the fact that the plasma in front of the target surface becomes sufficiently dense and ionized, such that the laser radiation is significantly absorbed by the plasma [42]. When the plasma becomes opaque laser radiation can no longer reach the surface of the target to generate new plasma by evaporation and ionization. The target material becomes decoupled from the laser radiation. Plasma growth however does not cease. Because of the heating which follows the absorption energy by inverse Bremsstrahlung, the plasma is driven rapidly away from the target surface; consequently the electron density decreases and the laser radiation again reaches the target. These processes merge into a smooth self-regulating regime with the generation, heating and expansion of plasma taking place throughout the length of the laser pulse.

1.2.7 Plasma Expansion Models

A. Effusion model of transient plasma expansion

The effusion model [43-45] assumes that the particles of the target material fly freely from the target surface. When the density of released particles is high enough, they collide with each other and form Knudsen layer (KL). In the KL particle velocities are thermalized although the resulting velocity distribution is anisotropic in space, having

large forward peaking. At the outer edge of the KL, particle flow is transformed into unstable adiabatic expansion (UAE). The particle release occurs in the time interval $(0, \tau_r)$. This phase of laser produced plasma expansion is known as flow phase. The flow velocity (u_k) of particles leaving the KL boundary is found to be

$$u_k = a_k = \sqrt{\frac{\gamma k T_k}{m}} \quad (1.57)$$

where a_k is the speed of sound at the KL boundary, T_k is the temperature at the KL boundary, $\gamma = C_p/C_v$ and m is the particle mass.

Eqn (1.57) is used as a boundary condition for a planar UAE which is, for the ideal gas, described by Navier-Stokes flow equations. These equations were solved in the 1-dimensional case by Kelly for the case of flow into vacuum with the following results:

$$\frac{a}{u_k} = 1 - \frac{\gamma - 1}{\gamma + 1} \frac{z}{u_k t} \quad (1.58)$$

$$\frac{u}{u_k} = 1 + \frac{2}{\gamma + 1} \frac{z}{u_k t} \quad (1.59)$$

$$\frac{\rho}{\rho_k} = \left(\frac{a}{u_k} \right)^3 \quad (1.60)$$

$$v_{EF} = \frac{\gamma + 1}{\gamma - 1} u_k \quad (1.61)$$

Here, a is the local velocity of sound, u is the local flow velocity, z is the distance from the outer KL boundary, ρ is the local particle density, ρ_k is the particle density at the KL boundary, and v_{EF} is the velocity of the expansion front.

At the end of the release process particles cease to flow out of the target. The flow phase is finished and the phase of UAE begins. The recondensation of the particles is neglected in this phase. In front of the target there are now three different regions with different flow conditions. In the region nearer to the target surface, abrupt ending of particle flow into the KL produces a rarefaction wave which spreads out from the target surface. The solutions of the Navier-Stokes equations for this region

$$x = ut \quad (1.62)$$

$$\frac{a}{u_k} = \frac{\gamma + 1}{4} \frac{t}{\tau_r}^{-(\gamma-1)/2} \quad (1.63)$$

The abrupt change of the boundary condition at $t = \tau_r$ leads to a catastrophic fall in density at the surface. After that, the density at the surface decreases slowly with time.

The first region extends from the surface ($z = 0$) up to the first line of contact (LOC) located at ($z = z_1$). This LOC is easily understood as the position of the disturbance triggered by the abrupt change in the density of released particles at the surface. The position of the first LOC is given by

$$z_1 = \frac{\gamma + 1}{2(\gamma - 1)} u_k \tau_r \left[\frac{t}{\tau_r} - \left(\frac{t}{\tau_r} \right)^{(3-\gamma)/2} \right] \quad (1.64)$$

Outside the first LOC, the second region which joins region 1 to the remanant of the flow phase, region 3, the junction being at the second LOC at $z = z_2$. This second LOC is visualized as the position of the disturbance triggered by the impingement of the region 2 with its reduced density on the region 3. The position of the second LOC is found to be

$$z_2 = \frac{\gamma + 1}{\gamma - 1} u_k \tau_r \left[\frac{t}{\tau_r} - \left(\frac{t}{\tau_r} \right)^{(3-\gamma)/(\gamma+1)} \right] \quad (1.65)$$

By comparing eqn. 1.64 with 1.65, $t \gg \tau_r$ we have $z_2 = 2z_1$.

The third region is just a remnant of the flow phase, and physical conditions in it are described by eqn. 1.58 to 1.61. This regions begins at $z = z_2$ and ends at z_{EF} .

Also, it should be pointed out that these are one-dimensional solutions of the Navier-Stokes flow equations. Due to the extreme complexity of the problem, no analytical solutions are known for 2-D or 3-D cases.

B. Plasma Expansion in the presence of an ambient gas

Ambient gases present during pulsed laser ablation scatter, attenuate and thermalize the plume, changing the spatial distribution and kinetic energy distribution of the plume species. Different diagnostics of the background gas interaction indicate that the plume interacts hydrodynamically with the background gas, undergoing a transition to a stable shock front as the plume material scatters off the background becomes delayed, and coalesces with the slower moving material.

For high background pressures a blast wave model has been used to describe the luminous shock front caused by the expansion of laser ablation plasmas. This model was developed to describe the propagation of a shock wave through a background gas (density ρ_0) caused by the sudden release of energy, E_0 , in an explosion. The propagation of spherical shock front through a background gas follows the distance - time relation

$$R = \xi_0 \left(\frac{E_0}{\rho_0} \right)^{1/5} t^{2/5} \quad (1.66)$$

where ξ_0 is a constant (for a planar shock wave $R(t) \propto (E_0/\rho_0)^{1/3}t^{2/3}$). This model strictly applies when the mass of the ejected products is small compared with the mass of the background gas set in motion by the shock.

A classic drag-model shows better agreement at low pressures and early times. The ejected pulse of ablation products is regarded as an ensemble that experiences a viscous force proportional to its velocity through the background gas. The equation of motion $a = -\beta v$, giving

$$v = v_0 e^{-\beta t} = v_0 - \beta z \quad (1.67)$$

$$x = x_f(1 - e^{-\beta t}) \quad (1.68)$$

where β is the slowing coefficient and $x_f = v_0/\beta$ is the stopping distance of the plume.

The drag model predicts that the plume will eventually come to rest, due to resistance from collisions with the background gas, while the shock model (neglecting viscosity) predicts continued propagation $R \propto t^{0.4}$. Experimentally, laser ablated plumes are travelling a path that can be described by a composite of these two models, the overlap occurring during the transition region when viscous slowing of the leading edge of the plume coalesces to form a stable shock structure.

1.3 Plasma diagnostics

Viewing a laser produced plasma as a physical system, the experimentalist is immediately confronted with a range of challenging and intriguing questions.

1. How does the plasma evolve and decay in time ?
2. What is the electron temperature and electron density and how do they vary in space and time ?
3. What are the variations of these fundamental parameters of the laser produced plasma at different ambient atmospheres and at different irradiance levels ?
4. What species of ions are present and how are they distributed over states of ionization?
5. Are these species at equilibrium ?
6. What are the characteristics of the spectrum emitted from the plasma ?
7. What are the different particles present in the ablation products ?

8. How does the plasma behave under the influence of applied electric and magnetic fields? In order to answer these questions, wide range of experiments have been carried out over the past two decades. Many of the techniques used have been taken from classical plasma physics but they have had to be adapted and improved to deal with the peculiar difficulties encountered in laser produced plasma. The particular features that present new problems are its short life time, i.e. transient nature and its high temperature. In connection with the last point it should be noted that if any reasonable degree of equilibrium exists in the plasma, then from considerations of equipartition of energy, one would expect $h\nu = kT$ where ν is the frequency of the emitted radiation. Hence at high temperatures involved the most important and interesting radiative processes will be expected in the vacuum ultraviolet and X-ray regions [46, 75, 48].

Many models have been developed to describe the processes involved in laser-matter interaction but each pertains only to a separate component of the interaction and is applicable only under limited conditions. There are several mechanisms happening inside a laser produced plume. The classification of these mechanisms is simplified and phenomenological; the power densities given for vaporization and ablation are merely approximate. Power densities above 10^6 W cm^{-2} cause vaporization, ablation, both of these processes simultaneously or additional mechanisms that have not yet been identified. Some of the mechanisms that have to be studied are given in table 1. The existence of shock waves is easily confirmed by the sonic boom heard by any one who has witnessed

a focused short-pulse laser exploding target materials at atmospheric pressure.

Table 1. Laser ablation mechanisms

- * Absorption (single, multiphoton, defect initiated)
- * Reflection (time-dependent)
- * Thermodynamics (melting, latency, phase change.)
- * Photoelectric, thermionic emissions
- * Plasma ignition
- * Shock waves (gas)
- * Stress waves (solid)
- * Laser plasma interaction (inverse bremsstrahlung)
- * gas dynamic expansion
- * Hydrodynamic expansion
- * ?????

The physics of laser ablated plasmas limits the applicability of the different diagnostic techniques. For example, some of the most sensitive diagnostics are overwhelmed by the robust environment of dense laser plasmas, while rugged diagnostics are insensitive in low density plasmas. The diagnostic methods themselves should not disturb the plasma. If it is necessary to actively perturb the plasma with electromagnetic waves or an electric field, the disturbance to the plasma should be minimum. Sensitivity, time and space resolutions must also be considered. Unfortunately, information obtained by each diagnostic tool is limited. Results obtained within the physical range of one technique may not apply at higher or lower laser energies. Generally, more complicated experimental arrangements have simpler diagnostics interpretations, while more applicable and simple experimental arrangements require more complicated interpretations. Finally each diagnostic tool usually allows one or two components of the plasma plume such as excited as well as ground state monoatomic atoms and ions, molecules, clusters, or particles to be identified. Total characterization of the pulsed laser ablated plume therefore requires an understanding of the advantages and limitations of several techniques, as well as their results which provide complementary information.

Despite the variety of diagnostic experiments designed to study laser produced plasmas, a number of major questions remain to be solved, including:

- (a) The role of nonthermal (electronic) and thermal (evaporation) ejection mechanisms in the ablation of material amounts necessary for film growth.

- (b) The extent and explanation of laser absorption by the initial ejectants.
- (c) The etching effects of the laser plasma on the target.
- (d) The expansion mechanism(s) responsible for the high kinetic energy of the ejectants: the competition between adiabatic expansion and space charge acceleration models.
- (e) The fractional ionization of the plasma plume and the range of distances over which it can be electromagnetically steered.
- (f) The role of clusters and particulars in the mass transfer to the substrate during thin film growth.
- (g) The collision kinetics within the plume in the collisionless regime. The roles of scattering, diffusion and hydrodynamics in the slowing and thermalization of the plume by background gases.
- (h) The major factors (ie. kinetic energy, deposition rate etc.) determining the optimal film growth distance for various materials.
- (i) The role of chemistry with the background gas.
- (j) The role of target surface morphology and phase on ejecta.

For the characterization of plasmas, many diagnostic tools are used including optical emission spectroscopy, laser induced fluorescence spectroscopy, mass spectroscopy, optical absorption spectroscopy, ion probe method, interferometry, Thomson scattering etc. Probably the most accurate, local, and unambiguous way to determine fundamental parameters of the plasma is Thomson Scattering and the spectroscopy as far as instrumentation is concerned. In the following sections, a brief report is made on the different diagnostic techniques.

1.3.1 Mass Spectroscopy

Laser vapourization is rapidly gaining popularity as a method of sample introduction for mass spectrometry [49-51]. The mass spectrometry has been used with multi channel deflection in time of flight (TOF) techniques and also in Fourier transform spectrometers. Time of flight mass spectrometry (TOFMS) [52] is very sensitive to the fast ions ejected from the laser irradiated surface. Ions with charge Ze , are collected using electric fields and then accelerated by a potential, V , down a field-free drift tube, each acquiring energy ZeV . The ions travel at different velocities $v = (2ZeV/m)^{1/2}$ and arrive at a high gain detector such as multichannel plate (MCP) or channeltran, at different times, from which the mass-to-charge ratio (m/z) is derived. The actual velocity with which the ions

travel to the collection region is convoluted with the drift velocity. Careful timing and mathematical stimulation are required to extract actual kinetic energy distribution of the photoejected species.

In quadrupole mass spectrometer (QMS) [53], the plume can be directed through an aperture and the ion's velocity can carry them directly into the quadrupole mass filter that can be tuned to select ions of different mass. Assuming the velocity of the particles does not change when passing through the quadrupole, the kinetic energy can be directly inferred from their arrival time. The QMS has a mass throughput function that must be known for quantitative ratios of the different ions. Pulse counting electronics can be used statistically to record the TOF for ions at a selected mass. An ionizer stage in front of the quadrupole input is used to ionize neutrals by electron impact. Retarding grids are placed in front of the QMS inputs to verify the kinetic energies and screening of the ions in the plume.

Alternatively, neutrals can be photoionized by a time delayed pulsed laser and the resulting ions extracted into a TOF-MS for laser ionization mass spectrometer (LIMS) [54]. Mass spectrometry involving nonresonant single photon ionization (REMPI) [55] can be used in this step. In general, because these mass spectrometric techniques rely on steering the ions in the plume with electromagnetic fields, they are most useful in vacuum at low plasma densities.

1.3.2 Ion Probes

Electric probes have widely been used to determine electron and ion densities, electron temperature and potentials in plasmas [56-58]. These plasma parameters can be determined by inserting a small metallic electrode or probe into the plasma; and by measuring electric current *vs* voltage applied to the small metal electrode as a function of plasma space potential. Several types of probes have been designed, these include the single probe (Langmuir probe) applied to discharges which have one electrode in the plasma, the double or triple probe, which has been used principally for the electrodeless discharges, and the emissive probe in which the plasma potential can be clearly observed by abrupt changes in the probe current at the plasma potential because of overlap of the thermionically emitted electron from the probe with the current carried by electrons already existing in the plasma. Other designs of ion probes are plane discs, parallel plate probes and multi grid retarding potential probes.

There are a number of assumptions made when the probe characteristics are analyzed; the plasma is collisionless, the electron density distribution is Maxwellian, the electron temperature is much higher than the ion temperatures, the ions are singly charged, and ion and electron densities are equal.

Electrostatic ion probes have got several advantages compared to other diagnostic techniques. They are inexpensive and rugged, and have the advantage of providing local information on plasma conditions, unlike most spectroscopic or imaging techniques that average along the line of sight. They can be immersed into dense plasmas and higher background pressures than other diagnostics, such as mass spectrometers, can tolerate.

The probe method can be effectively used for the determination of the ion density and electron density of a plasma by keeping the negative or positive potential respectively. Fast (~ 5 ns) electrical circuit response can be achieved, but attention must be paid to the design of the bias/detection circuit and unwanted points of grounding on chamber feedthroughs and in power supplies. The magnitude and velocity of the ion probe signal combine to serve as a very sensitive *in-situ* monitor of ablation reproducibility during pulsed laser deposition. Loss of ablation effectiveness, due to attenuation of the laser beam by window deposits or by cratering of the target surface, becomes evident as a loss of signal and velocity at the probe.

1.3.3 Laser induced fluorescence spectroscopy

Laser induced fluorescence (LIF) is the technique in which the laser frequency ν is tuned to match a transition of a group of atoms or molecules, whose energy difference is E_{12} , by a relation $h\nu = E_{12}$, and the resultant fluorescence is observed [59,60]. By resonant nature of the excitation, the fluorescence intensity in many orders of magnitude larger than other sources of scattering, such as Rayleigh, Raman or Thomson scattering, if the relevant number densities are in the same order of magnitude. Therefore, the LIF technique is very selective of species to be detected, sensitive and/or yields high spatial and temporal resolution. In LIF spectroscopy, laser photons are absorbed by atoms or molecules which are then excited from lower energy levels to higher levels, and spontaneous decay to lower levels is observed as fluorescence. In principle, atoms, molecules and ions in the ground state as well as in the metastable or excited states can be detected.

Usually a tunable dye laser pulse is used to pump the ground state species to a selected excited state. The absorption is followed by spontaneous emission of the excited

state to lower energy levels. An interference filter or spectrometer tuned to one of these wavelengths is used to record the laser induced fluorescence signal intensity. LIF is most useful in determining local vibrational and rotational temperatures of the molecules in a laser plumes. Often it is found that three different temperatures will be measured for a molecule in plasma plumes, translational, vibrational and rotational. From the time of flight (TOF) data of the molecules, translational temperature can be measured. Rotational and vibrational temperatures are estimated by comparison between the measured occupation of rotational or vibrational manifold using LIF, and that calculated from a Boltzmann distribution [61].

Tuning of the wavelength of dye laser slightly off-line center results in Doppler shifted absorption ($\Delta\lambda = \lambda v_z/c$) by species travelling with a specific velocity v_z along the probe beam axis. The small region in the LIF in the plasma plume can be moved about by tuning the dye laser to provide a spatial map of the species' angular velocity distribution.

1.3.4 Optical Absorption Spectroscopy

Optical absorption spectroscopy is a technique for analyzing the absorption of light which is radiated into a plasma from the outside [57, 62]. Since the absorption is caused by species existing in the plasma, it is possible to identify species and to determine their densities. If the low particle density causes difficulty in obtaining sufficient signal strength, the light path that passes through the plasma may be made longer by utilization of multireflection with the help of mirrors. By using laser with narrow band as a radiation source, space and time resolved spectra can be obtained at high sensitivity. The degree and rate of dissociation for a molecule can be determined by observing that specific species in the plasma.

Similar to LIF spectroscopy absorption spectroscopy has the advantage that species can also be detected at ground state. However, absorption spectra in the visible or infrared regions are frequently hidden by the emission from the plasma. It should be noted that results on concentration of species obtained by absorption spectroscopy are an average over the whole length of the absorption path.

1.3.5 Optogalvanic Spectroscopy

This type of diagnostic technique usually applies to discharge plasma [63, 64]. When the wavelength of the incident light applied to the plasma correspond to the optical

transition wavelength of atoms or molecules, the light is absorbed. Consequently, the plasma impedance, that is the discharge current/voltage undergoes a change. This fact is called the optogalvanic (OG) effect. Recently laser induced optogalvanic spectroscopy (LOGS) has come into use for plasma diagnostics. Both DC and RF discharges have been studied by the OGS technique. The magnitude and the sign of the OG signal depend upon many factors including incident laser power, absorption coefficient, radiative life time and the effect of collisional interactions between the laser coupled levels and those of the remaining discharge species. Compared to other diagnostic techniques, OGS has an extremely high sensitivity, therefore, radicals and ions that cannot be detected by other spectroscopic technique can be observed relatively easily.

1.3.6 Coherent Anti-Stokes Raman Spectroscopy

When two laser beams of angular frequency, ω_1 and ω_2 are radiated into a plasma from the same direction, light containing components of $2\omega_2 - \omega_1$ and $2\omega_1 - \omega_2$ are produced in addition to incident laser light and harmonic waves. The intensity of the Anti-Stokes line is proportional to the square of the nonlinear third order susceptibility for gas molecules. The spectrum shape depends entirely on rotational energy distribution for molecules. The technique is based on the CARS has been used to measure densities and rotational temperatures for gas species in plasma [65].

1.3.7 Thomson Scattering

Thomson scattering is the scattering of electromagnetic radiation of free electrons in a plasma. Probably the most accurate, the local and unambiguous way to determine electron density is Thomson scattering [66-68]. Accuracies of 3 % can be achieved using this diagnostic; the tradeoffs are price and complexity.

A laser beam incident on a medium can be scattered by inhomogeneities in the medium. In a plasma, such scattering is mainly due to electron density fluctuations. Every charged particle in the plasma is capable of scattering light, but because the scattering cross section is inversely proportional to the square of the particle mass, the contribution from ions is negligible compared with that from the electrons. The spectrum of the electron density fluctuation in the plasma is impressed on the scattered light, thus providing information about the collective motion of the electrons as well as the noncollective motion (velocity distributions). These features make Thomson scattering

a powerful diagnostic, providing direct information about these two aspects of electron fluctuations. Thomson scattering can be effectively used for the determination of electron density, electron temperature as well as neutral particle densities.

Scattering from a collection of charged particles occurs only if there are spatial fluctuations in electron density. Conservation of momentum tells that the wave number of the density fluctuation must satisfy the condition $k = k_s - k_i$ where k_i and k_s are the wavenumbers of the incident and scattered beam respectively. The magnitude k is given $k = \frac{4\pi}{\lambda} \sin \frac{\theta}{2}$, where θ is the angle between k_s and k_i . The vector k is fixed by selecting a laser wavelength and a scattering angle. The quantity k^{-1} is the scale length for scattering, and represent the length on which the plasma fluctuations are viewed.

1.3.8 Interferometry

Optical interferometric techniques can be used to probe the laser produced plasma material in real time. It is a well established technique for measuring the refractivity of plasma. Interferometry can also be used to determine the electron density distribution because in highly ionized plasmas, the refractive index is related to the free-electron density [69, 70]. In the interferometric technique, usually the laser produced plasma is allowed to expand into one leg of a Mach-Zehnder or Michelson interferometer. A He-Ne laser can be used as the light source for the interferometer. When the plasma was formed, the optical path length in the active leg changed, leading to a shift in the interference pattern. The interferometric data yields both the absorption coefficient of the plasma and the phase change due to plasma density. The density is related to the phase difference due to the presence of plasma using the equation [70].

$$n_e = 1.788 \times 10^{12} \frac{\gamma(t)}{\lambda l} \quad (1.69)$$

where $\gamma(t)$ is the phase difference, λ , wavelength of the probe beam and l , path length of the plasma.

1.3.9 Optical emission spectroscopy

In a plasma, matter breaks apart into atoms, ions and electrons, producing a visible flash and are audible popping sound due to the acoustical shock wave generated by the sudden, high velocity expansion of matter outward from the plasma plume. Useful information about the elemental composition of the target material can be obtained from analysis

of the emissions emanating from the plasma volume. Optical emission spectroscopic technique is concerned with the light emitted by electronically excited species in laser produced plasma in front of the target surface. The light originates from transitions from electronically excited states decaying to lower energy levels in atoms and molecules due to many kinds of processes. By means of this technique, the types of excited species in the plasma can be determined [71,72].

A typical set-up for optical emission spectroscopy essentially consists of a monochromator, wavelength scanner, photomultiplier tube and recorder [73]. The transitions between electronic energy levels correspond to the wavelength of light in the ultra-violet to visible range. This necessitates that the monochromator and the photomultiplier are sensitive over a range of about 200 - 900 nm. The resolution required for the monochromator depends on its task. Normally it is sufficient to be able to resolve the vibrational structure of the emission spectra of molecules, that is, about 0.1 nm resolution. The Multi-Channel Analyzer (MCA), using a photodiode array instead of photomultiplier, allows the simultaneous measurement of time resolved spectra over the entire range of wavelength.

The window through which the emission light passes should be made of quartz, which absorbs little in the ultraviolet region. This should be placed away from the plasma reaction zone to avoid depositing films onto the window's surface, which might prevent the transmission of light. If it is difficult to admit the light directly into the monochromator, the path can be bent using a quartz glass fibre. To determine the temperatures of atoms or molecules from the emission spectra, a comparison at different wavelengths among observed emission intensities, even if only relative, is required. Spectral intensities must be corrected against wavelength by taking into account the absorption of windows and glass fibres, the efficiency of the monochromator and the sensitivity characteristics of the photomultiplier or the photodiode which is used.

Spectral lines and bands can be identified from the coincidence of wavelengths of the observed emission lines and bands with those calculated from energy level transitions of the atoms and molecules concerned, if energies at each level are known. It is also possible to refer to publications which describe energy levels, wavelengths at which the absorption or emission occur, or transition probabilities for atoms and atomic ions or molecules and molecular ions.

Recently time and space resolved emission spectra have been measured in a laser

produced plasma [74, 75]. In order to achieve time and space resolved spectroscopy, different sections of the plasmas are imaged onto the monochromator slit, and these signals are sampled by a gate which is triggered by a delay circuit. The time delay in the optical channel is negligible in comparison with the sampling time of the gate. Spatial resolution can be obtained by using suitable optical system made up of slits and lenses.

The energy distribution for the ensemble of gas particles is expressed by Maxwell-Boltzmann equation concerned with some internal energy. For molecules, the energies associated with rotation, vibration and electronic state have to be taken into consideration. However, even when rotational spectra are not resolved in an emission spectrum, the vibrational temperature T_{vib} can be estimated by comparing the intensities of each band in the a given sequence. The sum of the band strength $I_{v'v''}$ resulting from the transition between vibrational energy level $v' - v''$ is given by

$$I_{v'v''} = A_{v'v''} \nu_{v'v''}^4 \exp\left(\frac{-G(v')hc}{kT_{vib}}\right) \quad (1.70)$$

where $A_{v'v''}$ is the Frank-Condon factor, $\nu_{v'v''}$ is the transition frequency, $G(v')$ is the energy of the vibrational level v' , and c is the velocity of the light, h is the Planck's constant. Therefore T_{vib} can be estimated from the slope of the straight line drawn by plotting $\ln(I_{v'v''}/A_{v'v''}\nu_{v'v''}^4)$ against $G(v')$. If the transition probabilities are unknown, the T_{vib} can be evaluated by using the equation [76]

$$\ln \sum_{v'} (\lambda^4 I_{v'v''}) = C_1 - G(v') \left[\frac{hc}{kT_{vib}} \right] \quad (1.71)$$

where λ is the wavelength corresponding to each transition ($v'v''$), C_1 is a constant. The T_{vib} is obtained by from the slope of the Boltzmann plot between $\ln \sum_{v'} (\lambda^4 I_{v'v''})$ and $G(v')$. The advantage of using sum of the vibrational band heads for the determination of T_{vib} is that the information regarding the transition probability is not essential in this case.

The emission intensity of atoms is given by

$$I = \frac{c}{4\pi} \ln_n A h \nu \quad (1.72)$$

where c is the speed of light, l is the length of the light path, n_n is the particle density of atoms in the initial state at energy levels n , A is the Einstein transition probability, and ν is the wave number of light emitted at the time of transition. According to Maxwell-

Boltzmann relation, n_n can be written as

$$n_n = n_0 \frac{g_n}{Z} \exp\left(\frac{E_n}{kT}\right) \quad (1.73)$$

where g_n is the statistical weight and Z is the partition function. Using the above two equations the atomic temperature T can be obtained.

A simpler technique, the so-called two-line radiance ratio method, has also been used for the determination of temperature. Taking the ratios of intensities of two lines in an emission spectrum, we obtain [77]

$$\frac{I_1}{I_2} = \frac{g_1 A_1 \lambda_2}{g_2 A_2 \lambda_1} \exp\left(\frac{-(E_1 - E_2)}{kT}\right) \quad (1.74)$$

where E_1 and E_2 are the energy levels corresponding to these two lines. In using the above methods to determine temperatures, it must be carefully considered whether the assumption that the Boltzmann distribution is applicable for the distribution of internal energy states for the gas particles is valid. In fact, the Boltzmann energy distribution function between internal energies or within one internal energy distribution is sometimes not satisfactory.

Optical emission spectroscopy is an extremely useful technique for diagnosing a plasma without disturbing the plasma. However, species for which the optical transitions are forbidden by the selection rule and have a very small transition probability are not detected, even if they exist in the plasma.

1.3.10 Photography and Imaging

The simplest experiment one can do with a laser-produced plasma is to photograph it. Photography and other imaging techniques add another dimension to ablation diagnostics by providing two-dimensional snapshots of the three-dimensional plume propagation. This capability becomes essential for a hydrodynamic understanding of the plume propagation and reactive scattering. High speed cameras with electronic gates and image converters can be used to image the plume emission, as in high-speed framing photography, streak photography, and intensified-CCD array (ICCD) photography. Ultrafast imaging techniques are now allowing investigations of molecular energy transfer ablation processes [78, 79]. Imaging techniques are thus extremely useful for studies of ablation plumes in vacuum.

Improvements in the sensitivity and application of diagnostics continue to reveal new features of the ablation process, plume propagation, and plume-film interaction. Each technique provides a different perspective of the plume, given its detection limitations. Only through the overlap of results from several techniques can a comprehensive picture of the plume be revealed.

1.4 References

- [1] F. F. Chen, in *Physics of Laser Plasmas* A. Rubenchik, S. Witkowski(eds.) **3** (North Holland, Amsterdam 1991).
- [2] D. R. Nicholson, *Introduction to Plasma Theory*, (Wiley, New York 1983).
- [3] F. I. Boley, *Plasmas - Laboratory and Cosmic*, (Van Nostrand Reinhold Company, New York, 1966).
- [4] P. T. Rumsby and J. W. M. Paul, *Plasma Physics*, **16** 247 (1974).
- [5] A. V. Engel, *Ionized Gases*, (Oxford Press, London, 1965) Chp. 5.
- [6] W. Jost, *Diffusion*, (Academic Press, New York, 1952).
- [7] G. Bekefi, *Radiation Processes in Plasmas* Wiely, New York, 1966 .
- [8] G. Bekefi, *Principles of Laser Plasmas* (John Wiley & Sons, New York, 1976).
- [9] J. F. Ready, *Appl. Phys. Lett.* **3** 11 (1963).
- [10] J. F. Ready, *J. Appl. Phys.* **36** 462 (1965).
- [11] J. F. Ready, *Effects of High Power Laser Radiation*, (Academic, New York, 1971).
- [12] Yu. V. Afanas'ev and O. N. Krokhin, *Sov. Phys. JEPT* **25** 639 (1967).
- [13] R. M. Measures and P. G. Cardinal, *Phys. Rev. A*, **23** 804 (1981).
- [14] M. von Allmen, *Laser-Beam Interactions with Materials: Physical Principles and Applications* (Springer - Verlag, New York, 1987).
- [15] J. A. McMordie and P.D. Roberts, *J. Phys. D*, **8** 788 (1975).
- [16] G. J. Pert, *Plasma Physics*, **16** 1019 (1974).
- [17] K. P. Selter and H. J. Kunze, *Phys. Scripta*, **25** 929 (1982).
- [18] Z. Hwang, Y. Teng, K. Lee and J. Snedden, *Appl. Spectrosc.* **45** 435 (1991).

- [19] Y. Lee, S. P. Sawan, T. L. Thiem, Y. Teng and J. Snedden, *Appl. Spectrosc.* **46** 436 (1992).
- [20] Y. :Lee, T. L. Thiem, Y. Teng, G. Kim and J. Snedden, *Appl. Spectrosc.* **46** 1597 (1992).
- [21] A. A. Voevodin and M. S. Donley, *Sur. Coat. Tech.* **82** 199 (1996).
- [22] M. N. Libenson, G. S. Romanov and Y. A. Imas *Sov. Phys.-Tech. Phys* **13** 925 (1969).
- [23] A. M. Bonch-Bruevich, S. E. Potanov and Y. A. Imas, *Sov. Phys.-Tech. Phys* **13** 640 (1968).
- [24] I. Adawi, *Phys. Rev.*, **134** A788 (1964).
- [25] M. C. Teich and G. J. Wolga, *Phys. Rev.*, **171** 809 (1968).
- [26] H. Sonnerberg, H. Heffner and W. Spicer, *Appl. Phys. Letts.*, **5** 95 (1964).
- [27] S. H. Khan, F. A. Richards and D. Walsh, *IEEE J. Quantum Electron.*, **QE - 1** 359 (1965).
- [28] D. M. Stevenson, *Proc. IEEE*, **54** 1471 (1966).
- [29] E. Bernal, J. F. Ready and L. P. Levin, *Phys. Lett*, **19** 645 1966)
- [30] C. M. Verber and A. H. Adelman, *J. Appl. Phys.*, **36** 1522 (1965).
- [31] J. F. Ready, *Phys. Rev.* **137** A620 (1965)
- [32] E. H. Piepmeir and D. E. Austin, *Appl. Spectrosc.*, **25** 642 (1971).
- [33] T. P. Hughes, *Plasmas and Laser Light* (Adam Hilger, England, 1975).
- [34] J. I. Masters, *J. Appl. Phys.*, **27** 477 (1956).
- [35] H. G. Landau, *Quart. J. Appl. Math.* **8** 81 (1950).
- [36] C. D. Allemand, *Spectrochim. Acta* **27B** 185 (1973).
- [37] P. G. Mitchell and J. Sneddon and L. J. Radziemski, *Appl. Spectrosc.*, **41** 141 (1987).

- [38] O. N. Krokin, *Physics of High Energy Density* (Academic, New York, 1971).
- [39] A. Richter, *Thin Solid Films*, **188** 275 (1990).
- [40] C. Boulmer-Leborgne, J. Hermann and B. Dubreuil, *Plasma Sour. Sci. Tech.*, **2** 219 (1993).
- [41] D. B. Chrisey and G. K. Hubler (eds.) *Pulsed Laser Deposition of Thin Films* (John Wiley and sons, New York, 1994) Chapter 5.
- [42] R. W. Dreyfus, *J. Appl. Phys.*, **69** 1721 (1991).
- [43] R. Kelly and B. Braren, *Appl. Phys.* **B53** 160 (1991).
- [44] R. Kelly, *J. Chem. Phys.* **92** 5047 (1990).
- [45] R. Kelly, *Nucl. Instr. Meth. Phys. Res.* **B46** 441 (1990).
- [46] P. E. Young and P. R. Bolton, *Phy. Rev. Letts.* **77** 4556 (1996).
- [47] U. Teubner, T. Missalla, I. Uschmann, E. Forster, W. Theobald and C. Walker, *Appl. Phys. B*, **62** 213 (1996).
- [48] W. Theobald, C. Wulker, J. Jasny, S. Szatmari and F. P. Schafar, *Phys. Rev. E* **49** R4799 (1994).
- [49] W. R. Creasy and J. T. Brenna, *J. Chem. Phys.* **92** 2269 (1990).
- [50] E. A. Rohlfing, D. M. Cox and A. Kaldor, *J. Chem. Phys.* **81** 3322 (1984).
- [51] C. P. Safvan, F. A. Rajgara, V. Bhardwaj, G. R. Kumar and D. Mathur, *Chem. Phys. Lett.* **255** 25 (1996).
- [52] A. Namiki, T. Kawai and K. Ichize, *Sur. Sci.* **166** 129 (1986).
- [53] L. Wiedeman and H. Helvajian, *J. Appl. Phys.* **70** 4513 (1991).
- [54] T. Venkatesan, X. D. Wu, A. Inam, Y. Jeon, M. Croft, E. W. Chase, C. C. Chang, J. B. Wachtman, R. W. Odom, F. R. di Brogolo and C. A. Mazer, *Appl. Phy. Lett.* **53** 1437 (1988).

- [55] S. G. Nakhate, S. A. Ahmad, A. A. N. Razvi and G. D. Saksena, *J. Phys. B* **24** 4973 (1991).
- [56] J. M. Hendron, R. A. Al-Wazzan, C. Mahony, T. Morrow and W. G. Graham, *Appl. Sur. Sci.* **96-98** 112 (1996).
- [57] D. B. Geohegan and A. A. Puretzky, *Appl. Sur. Sci.* **96-98** 126 (1996).
- [58] J. G. Lunney, J. F. Lawler and R. Aratari, *J. Appl. Phys.* **74** 4277 (1993).
- [59] K. Muraoka and M. Maeda, *Plas. Phys. Control. Fusion* **35** 633 (1993).
- [60] Y. Nakata, H. Kaibara, T. Okada and M. Maeda, *J. Appl. Phys.* **80** 2458 (1996).
- [61] R. W. dryfus, R. Kelly and R. E. Walkup, *Nucl. Instru. Meth. Phys. Res.* **B23** 557 (1987).
- [62] R. A. Al-Wazzan, J. M. Hendron and T. Morrow, *Appl. Sur. Sci.* **96-98** 170 (1996).
- [63] P. R. Sasikumar, S. S. Harilal, V. P. N. Nampoori and C. P. G. Vallabhan *Technical Digest Series (OSA)*, **1** WB2-2 (1993).
- [64] P. R. Sasikumar, S. S. Harilal, V. P. N. Nampoori and C. P. G. Vallabhan *Pramana - J. Phys.* **42** 232 (1994).
- [65] N. Hata, A. Matsuda, K. Tanaka, K. Kajiyama, N. Moro and K. Sajiki, *Jpn. J. Appl. Phys.* **22** L1 (1983).
- [66] S. M. Cameron, M. D. Tracy and J. F. Camacho, *IEEE Trans. Plas. Sci.* **24** 45 (1996).
- [67] J. M. de. Regt, J. A. M. Vander Mullen and D. C. Schram, *Phys. Rev. E.* **52** 2982 (1995).
- [68] J. M. de. Regt, R. A. H. Engeln, F. P. J. de. Groote, J. A. M. Vander Mullen and D. C. Schram, *Rev. Sci. Instrun.* **66** 3228 (1995).
- [69] G. K. Varier, S. S. Harilal, C. V. Bindhu, R. C. Issac, V. P. N. Nampoori and C. P. G. Vallabhan *Mod. Phys. Letts. B* **10** 235 (1996).

- [70] G. K. Varier, R. C. Issac, C. V. Bindhu, S. S. Harilal, V. P. N. Nampoori and C. P. G. Vallabhan *Spectrochim. Acta B* (in press) (1997)
- [71] P. Heszler, J. O. Carlsson and P. Demirev, *Phy. Rev. B* **53** 12541 (1996).
- [72] P. R. Bolton, A. B. Bullock, C. D. Decker, M. D. Feit, A. J. P. Megofna and P. E. Young, *J. Opt. Soc. Am. B* **13** 336 (1996).
- [73] See Chapter 2 of this Thesis.
- [74] S. S. Harilal, R. C. Issac, C. V. Bindhu, V. P. N. Nampoori and C. P. G. Vallabhan, *Spectrochim. Acta A* (in press) (1997).
- [75] S. S. Harilal, R. C. Issac, C. V. Bindhu, V. P. N. Nampoori and C. P. G. Vallabhan, *J. Phys. D* (in press) (1997).
- [76] See Chapter 3 of this Thesis.
- [77] H. R. Griem, *Plasma spectroscopy* (McGraw-Hill Book Company, NewYork, 1964).
- [78] H. Kim, J. C. Postlewaite, T. Zyung and D. Dlott, *Appl. Phys. Letts.*, **22** 2274 (1989).
- [79] H. Kim, J. C. Postlewaite, T. Zyung and D. Dlott, *J. Appl. Phys.*, **65** 4548 (1989).

Chapter 2

Experimental Aspects of Laser Plasma Studies

This chapter deals with the general experimental methods followed in the study of laser produced plasma. Details of the experimental setup used for the spectroscopic as well as time resolved studies are discussed separately. The details of the various subsystems like laser source, plasma chamber, monochromator, photomultiplier tube, boxcar averager and storage oscilloscope used for the above measurements are also presented.

2.1 Introduction

The high power laser-material interaction initiates a luminous plasma in front of the solid surface [1-3]. For the characterization of the photofragmented species in a plasma, many spectroscopic tools are used including Laser Induced Fluorescence [4], Absorption Spectroscopy [5], Mass Spectroscopy [6], Optical Emission Spectroscopy [7], Time Resolved Spectroscopy [8] etc.. Of these the nonrestrictive methods to study the the laser plasmas are mass spectrometry and optical emission spectroscopy. Compositional analysis of the sample can be obtained directly by measuring the optical emission spectra of the laser induced plasma (LIP). Optical emission spectroscopy technique is concerned with the light emitted by electronically excited species in LIP produced in front of a target surface. Also optical emission measurements are useful for species identification and *in situ* monitoring during deposition [3]. Useful information about the elemental composition of the target material can be obtained from the analysis of the emissions emanating from the plasma plume.

In the present work, studies on plasma formed by the interaction of a focused Nd:YAG laser beam on the graphite and $\text{YBa}_2\text{Cu}_3\text{O}_7$ targets are described. LIP emission spectra consist of neutral atom and ionic lines superimposed on a spectrally broad band continuum of radiation. The goal of the work was to obtain some understanding of the processes occurring in the generation and expansion of the plasma. The plasma was characterized by emission spectra through space and time resolved techniques. The spectra emitted by the laser ablated plasma vary depending upon the location of the region of observation as well as the period of time after the impact of the laser pulse [9]. Thus time and space resolved analysis of the LIP offer an excellent means to investigate their evolution and dynamics.

In this chapter a comprehensive account of experimental technique for the optical emission spectroscopic analysis of the laser produced plasma and the various subsystems needed for the experiments are given. These experimental details are divided into two sections. In the first section, the description of the various sub-systems like excitation source, plasma chamber, detection and other setup for the recording the plasma spectrum are described. In the second section, the experimental set-up for the space and time resolved studies are mentioned.

2.2 Sub-systems used for the present studies

2.2.1 Laser Source

The laser used in our experiment is an electro-optically Q-switched Nd:YAG laser (Quanta Ray DCR 11) having a fundamental out put of $1.06 \mu\text{m}$.

The optical cavity in the DCR-11 is an unstable resonator. In a stable resonator the ray of light is traveling close to the optical axis and is reflected toward the optical axis by its cavity mirrors, so it is always contained along the primary axis of the laser. By contrast, a ray traveling in an unstable resonator can be reflected away from the axis by one of the cavity mirrors. Stable resonators can only extract energy from a small volume near the optical axis of the resonator, which limits the energy of the output. Conversely, unstable resonators can have large beam diameters. Thus they can efficiently extract energy from active media whose cross-sectional area is large, like that of typical Nd:YAG laser rods. The output coupler in an unstable resonator is a small high reflector mounted on a clear substrate which lies on the optical axis of the resonator. Energy escapes from the resonator by diffracting around this dot, which gives the "diffraction coupled resonator" (DCR) its name [10]. The diffraction coupled resonator delivers a 'doughnut' shaped beam profile at 9 ns pulse width (FWHM) with a power stability of $\pm 4\%$. The laser beam has a typical lie width of $< 1 \text{ cm}^{-1}$ with 220 MHz spacing between the longitudinal modes and a beam divergence of $< 0.5 \text{ mrad}$. Fig. 2.1 show the schematic diagram of the Nd:YAG laser with beam profile. The high peak power of the Q-switched pulses permit frequency conversion in nonlinear crystals like KD^*P . By introducing appropriate crystals in the beam path, higher order harmonics can be obtained. The 1064 nm fundamental interacts with the crystal to produce 532 nm wavelength. The resultant 532 nm wave can be doubled again by passing it through a second crystal, which yields a 266 nm wave. It can also be mixed in KD^*P with the residual 1064 nm to produce a 355 nm wave.

When the fundamental wavelength $1.06 \mu\text{m}$ is emitted in 9 ns pulses with pulse energies up to 275 mJ is focused on a solid target, it produces power densities of the order of 10^{10} Wcm^{-2} at the focal spot. This enormous amount of power density creates transient plasma from the target surface. The laser provides trigger outputs to synchronize oscilloscope, energy meter, boxcar etc..

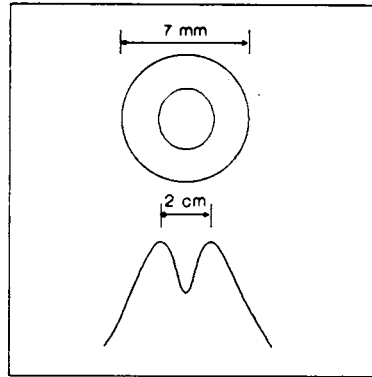
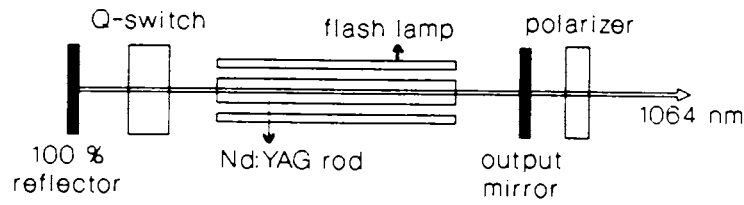


Figure 2.1: The schematic diagram of the Nd:YAG laser with beam profile.

Beam parameters of the Nd:YAG laser used for these studies.

Wavelength	1064 nm
Pulse width	9 ns
Pulse energy	275 mJ
Maximum light intensity	30 MW
Maximum repetition rate	16 Hz
Maximum repetition rate at maximum pulse energy	10 Hz
Radius of the laser beam	3.2 mm
Spatial Mode	Diffraction coupled
Line width	$< 1.0 \text{ cm}^{-1}$
Beam Divergence	$< 0.5 \text{ mrad}$
Calculated minimum spot size	$5 \times 10^{-3} \text{ mm}^2$
Estimated spot size	$31.4 \times 10^{-3} \text{ mm}^2$
Maximum laser irradiance	$9.6 \times 10^{10} \text{ W cm}^{-2}$

2.2.2 Plasma Chamber and vacuum system

For studying laser produced plasmas at reduced pressure, a vacuum apparatus was procured which include a rotary vacuum pump and diffusion pump. Ambient pressure as low as $\sim 10^{-8}$ mbar can be achieved by using these pumps. The plasma chamber was designed and fabricated using a cylindrical stainless steel tube with diameter 25 cm and

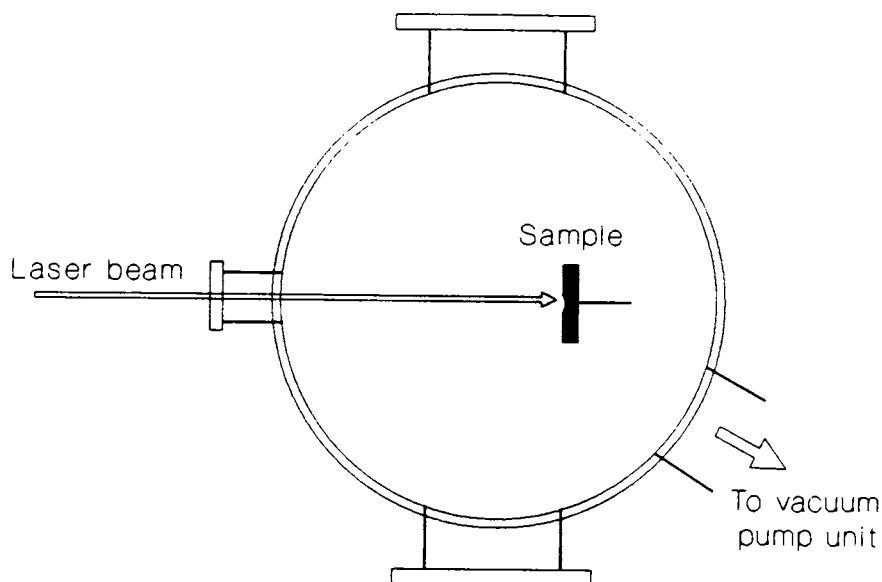


Figure 2.2: The schematic diagram of the plasma chamber.

and is provided with appropriate windows for laser beam entrance and light collection. The chamber has three basic units : (1) the base plate, (2) a main chamber with windows and (3) top plate. The base plate is a stainless steel disc having thickness 1.5 cm and diameter 35 cm. A central hole in the base plate with diameter 10 cm allows the plasma chamber to be in contact with the rotary and diffusion pumps. The schematic diagram of the plasma chamber is shown in fig. 2.2. The height of the chamber is 20 cm. It contains mainly three windows, one for the entrance of the excitation laser and other two for the collection of the light emitted by the plasma. Two quartz windows are used for the collection of emission from the plasma in a direction perpendicular to the plasma expansion axis. The optical emission from the plasma is allowed to fall on the entrance slit of a monochromator for spectral analysis. The vacuum system consists of a rotary pump followed by a diffusion pump. The system is fitted with a needle valve and the chamber can be maintained at pressures ranging from atmospheric pressure (760 torr) to 1×10^{-5} mbar. The chamber is also provided with feed through (needle valve) for the admission of the buffer gases in the chamber. In the present case we used He, Ar as well as air as buffer gases. For the accurate measurement of pressure inside the plasma chamber, gauges viz., pirani and penning, are used.

2.2.3 Target Holder

The solid target used in the present investigations were glued onto a sample holder which itself is mounted on to a externally controlled DC motor. The rotation of the sample about an axis parallel to the laser beam avoid errors due to local heating and drilling by providing fresh surface for ablation.

2.2.4 Monochromators

Monochromators are widely used for analyzing the light emitted from another device or process, and for observing the effects of specific wavelengths of light transmitted through various materials. The specifications for the performance of a monochromator include the dispersion and the stray light levels. Generally the dispersion is given in nm/mm, where the slit width is expressed in mm. In selecting monochromator for emission spectroscopy, one looks for low stray light levels to avoid problems due to scattered stray light. Stray light is defined as any light which passes through the monochromator besides that of the desired wavelength. In addition, monochromators are chosen for high efficiency to maximize the ability to detect low light levels. The slit widths are generally variable and a typical monochromator will have both an entrance and an exit slit. The light intensity which passes through a monochromator is approximately proportional to the square of the slit width. Larger slit widths yield increased signal levels, and therefore higher signal to noise (S/N) ratios. Smaller slit widths yield higher resolution, but at the expense of light intensity. A small slit width is used to increase precision of the wavelength determination and to decrease the light intensity. Grating monochromators may have planar or concave gratings. Planar gratings are usually produced mechanically and may contain imperfections in some of the grooves. Concave gratings are usually produced by holographic and photoresist methods, and imperfections are rare. Imperfections of the gratings are major source of stray light transmission by the monochromators, and of ghost images from the grating. For this reason the holographic gratings are preferable for emission spectroscopy. Another important characteristic of the grating monochromators is that the transmission efficiency depends upon polarization of the light. Therefore the emission spectrum of the sample can be shifted in wavelength and altered in shape, depending upon the polarization conditions chosen to record. In the present work we used the following two monochromators:

2.2.4.1. Spex

Spex Model 1704 is a 1 meter scanning spectrometer having a maximum resolution $\sim 0.05 \text{ \AA}^0$ [11]. The monochromator covers a spectral range 350 - 950 nm using a grating with 1200 grooves per mm blazed at 500 nm and spectral band pass 0.1 \AA^0 . The entrance and exit slits on the front of the spectrometer are controlled by micrometer type knob above the slits. The scan rate of the monochromator is adjusted by using microprocessor controlled Spex compudrive (CD2A) arrangement. Spex compudrive has got a key board control over the spectrometer which not only provides repeat scan over the spectral regions but also gives the scan status and spectrometer position. So using this system one can easily tie into a dialog with the detector electronics system. The main advantages of CD2A compudrive are, we can programme the start and end positions of the scan, rate, repetitions, delay between repetitions, recorder scale and marker frequency [12].

The output of the Spex monochromator is coupled to a thermoelectrically cooled photomultiplier tube (Thorn EMI, model KQB 9863, rise time 2 ns).

2.2.4.2. Jarrell Ash

Jarrell-Ash 82-000 is a 0.5 meter Ebert scanning monochromator having a maximum resolution of 0.02 nm [13]. The monochromator covers a spectral range of 200 nm to 1600 nm with three interchangeable grating blazed at 180 nm, 500 nm and 750 nm respectively. This instrument provides a smooth scanning motion in eight speeds ranging from 0.2 nm/minute to 50 nm/min. The output from the Jarrell-Ash monochromator is detected by an EMI, model 9683 KQB photomultiplier tube that can be directly mounted at the exit face of the monochromator. Model 9683 is a head-on type PMT having an S-20 cathode, and performs well in the 300-800 region.

2.2.5 The Photomultiplier Tube

The photomultiplier tube (PMT) is a very versatile and sensitive detector of radiant energy in the ultra-violet, visible, and near-infrared regions of the electromagnetic spectrum. Among the oldest detector technologies (first developed in the mid 1930s), PMTs use vacuum rather than solid-state techniques to multiply electrons generated by photons. They are widely used in research activities ranging from biomedicine to astronomy as well as in medical diagnostic technology, environmental monitoring and aerospace.

For a large number of applications the PMT is the most practical sensitive detector available. The basic reason for the superiority of the PMT is the secondary-emission amplification which makes them uniquely sensitive among photosensitive devices currently used. The basic radiation sensor is the photocathode which is located inside a vacuum envelope. Light passes through an input window and strikes the photocathode, leading to the emission of photoelectrons into an evacuated tube. Photoelectrons are emitted and directed by an appropriate electric field to an electrode or dynode within the envelope. A number of secondary electrons are emitted at this dynode for each impinging primary photoelectron. These secondary electrons in turn are directed to a second dynode and so on until a final gain of perhaps 10^6 is achieved [14]. The electrons from the last dynode are collected by an anode which provides the signal current that is read out.

The PMT has a photocathode in either a side-on or a head-on configuration. The side-on type receives incident light through the side of the glass bulb, while, in the head-on type, it is received through the end face of the glass bulb. The head-on type has a semitransparent photocathode (transmission-mode photocathode) and it provides better uniformity than the side-on type having a reflection-mode photocathode. A schematic representation and its operation of a typical photomultiplier tube is given in fig. 2.3. We have used the following Thron EMI PMTs with S-20 cathode in our works. The

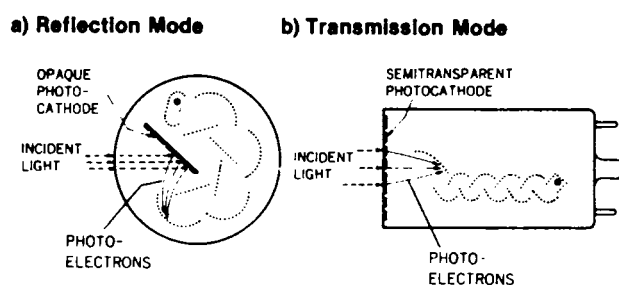


Figure 2.3: A schematic representation and operation of a typical photomultiplier tube.

exit slit of the Jarrall-Ash monochromator was coupled to a Thorn EMI PMT (Model 9683-KQB) with S-20 cathode. This Thorn EMI PMT was operated in the range 1-1.3 kV. It has a fairly good quantum efficiency in the 300-800 nm spectral range. For the maintenance of a constant output voltage across the terminals, a highly stabilized power

supply (Thron EMI PM 28B) was fed to the PMT. The tube has an air-cooled, RF shielded housing.

The Spex monochromator was coupled to a thermoelectrically cooled ($-50\text{ }^{\circ}\text{C}$) Thron EMI photon counting PMT with S20 cathode (quantum efficiency 22 %). The operating voltage for this PMT was 1.7-2.1 kV.

2.2.6 Energy Meter

It is important to measure the energy incident on the target surface accurately. The Energy meter used in the present work is the Delta Developments Pulsed Laser Energy Monitor. This on-line energy monitor uses a polarization compensated beam splitter to sample the beam, 90 % of which is transmitted [15]. The sampled beam strikes a retro-reflecting diffuser and reaches the photo-diode via a "Range Plate" which attenuates the light appropriately for the range of energies being measured. The geometry of the energy meter is such that all positions on the diffuser give equal signals. Different Range Plates can be used for different energies or laser wavelengths. Each range plate gives a factor of 30 in the energy giving full scale deflection. A switch allows readings to be referred to either the energy entering or the energy leaving the instrument. BNC sockets provide pulse shape, pulse energy, trigger input, trigger output etc.. The energy meter can be triggered externally with laser pulses or internally. The wavelength response of the energy meter is from 200 nm to 1100 nm.

2.2.7 Digital Storage Oscilloscope

A digital storage oscilloscope (DSO, 200 MHz, Iwatsu Model DS-8621) was used to monitor the signal from the photomultiplier tube. The oscilloscope can be triggered both internally and externally. In the present work it was triggered externally using Nd:YAG laser pulses. It is provided with averaging facility. The pulse shapes can be digitally stored and plotted. The oscilloscope is necessary for measuring time delays of different species in the laser produced plasma. The oscilloscope trace of the PMT response of the plasma emission from the target shows a definite time delay between the incident laser pulse and the onset of emission from a particular species. The storage oscilloscope is also required while setting the gate width and delay of the gated integrator. The DSO has facilities to capture and store the pulse shapes for later analysis and to obtain a hard copy using a plotter/printer [16].

2.2.8 Boxcar averager/integrator

In some experiments, it might be essential to recover a part or the whole of an output signal pulse so that the signal can be analyzed. To recover such a signal buried in noise, some form of averaging process is required and for that, some kind of multi-point averager or a Fourier transform analyzer is necessary. Signals of such transient nature, triggered by repetitive pulses from the excitation source can be analyzed in this fashion. This is achieved by a boxcar integrator, which essentially is an instrument used to recover complex repetitive signals hidden in noise.

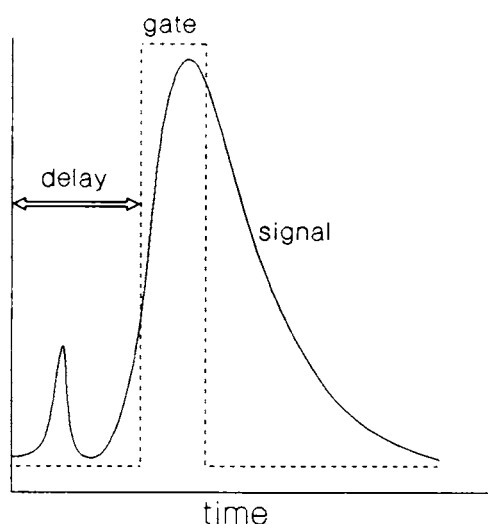


Figure 2.4: The typical PMT signal, the time delay and the gate width of the boxcar.

The boxcar used here is a Stanford Research Systems (SR 250) module. It essentially has a fast gated integrator and an averager. Triggered by the pulse from the laser, the gate provides an adjustable delay from few ns to 100 ms, before it generates a continuously adjustable gate of 2 ns to 15 ms [17]. The signal at the gate is integrated by the fast gated integrator and is normalized by the gate width to provide a voltage proportional to the part of the input signal pulse level at the gate. By fixing the delay and the gate width so that only the voltage from the part of the signal pulse alone is measured, it is possible temporally separate out the PMT signal due to the emission of the particular species from the other unwanted signal components contained in the signal pulse, thus improving the signal to noise (S/N) ratio of the detection. The sensitivity control of the boxcar averager provides further amplification of the signal. The typical

PMT signal, the time delay and the gate width of the boxcar are shown in fig. 2.4.

A moving exponential average over 1 to 10,000 samples is available at the averaged output. This traditional averaging technique is useful for pulling out small signals from noisy backgrounds. Typically the signals are averaged over 10 pulses. Averaging over very large number of pulses does increase S/N ratio, but makes the system very sluggish in response to fast variation in the signal. In addition to the traditional technique, the averaging circuitry may be used to actively subtract a baseline drift or background from the signal.

2.2.9 Chart Recorder

The Analog - Digital X - Y plotter used in these experiments was manufactured by Rikadenki Kogyoco Ltd., Japan. This is a high performance DC Servo system X-Y recorder with added digital plotter function [18]. In digital mode, title, scale, data etc. can be added to this recording. We used the Chart recorder with its analog mode. In analog mode, the input analog signal is recorded directly by a pen writing.

In analog mode, the Chart recorder provides high performance, high-speed X-Y recorder function. The X-output and the averaged output sockets of the boxcar averager/integrator were connected to the X and Y terminals of the chart recorder respectively for recording the plasma emission spectrum.

2.3 Emission Spectroscopy

When high intensity laser light is focused on a solid target surface, the target surface will get vapourized and a plasma is formed at the surface. The distribution of the plasma is due to the shock wave propagation. The shock wave is created initially at the sample surface and propagated along the axial direction [19]. A block diagram of the experimental arrangement for the emission spectroscopy is shown in fig. 2.5. The laser pulse used in the experiment was produced by a Q-switched Nd:YAG laser system with a pulse duration (FWHM) of 9 ns. By focusing the laser pulses onto the sample surface, it is possible to get a transient plasma above the sample surface. The target in the form of a disc is placed in an evacuated chamber provided with optical windows for laser irradiation and spectroscopic observation of the plasma produced from the target. The target was continuously rotated with an external motor so that the fresh solid surface

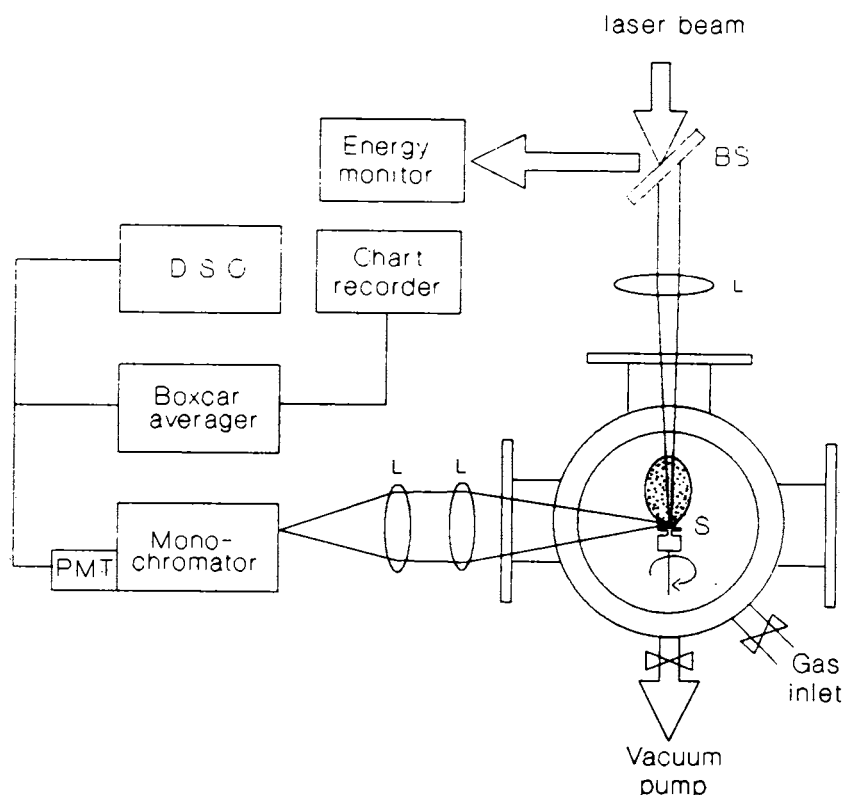


Figure 2.5: A block diagram of the experimental arrangement for the emission spectroscopy.

faces the laser pulses every time. The bright plasma emission was viewed through a side window at right angles to the plasma expansion direction. The section of the plasma was imaged onto the slit of a monochromator (with entrance and exit slits are parallel to the target surface) using appropriate collimating and focusing lenses so as to have one to one correspondence with the sampled area of the plasma and the image. The recording was done by using a photomultiplier tube, which was coupled to a boxcar averager/gated integrator. The averaged output from the boxcar averager was fed to a chart recorder and to an oscilloscope for monitoring. We have made space and time resolved studies on laser plasma.

2.3.1 Space Resolved Studies

Space resolved studies of plasma emission from the laser ablated plasma give information about the spatial composition and ionized state of the plasma at different distances from the target surface [20]. Also knowledge of the spatial distribution of plasma emission might afford some insight into the space resolved technique for the improvement of analytic detection in atomic spectroscopy. Spatially resolved information in two directions:

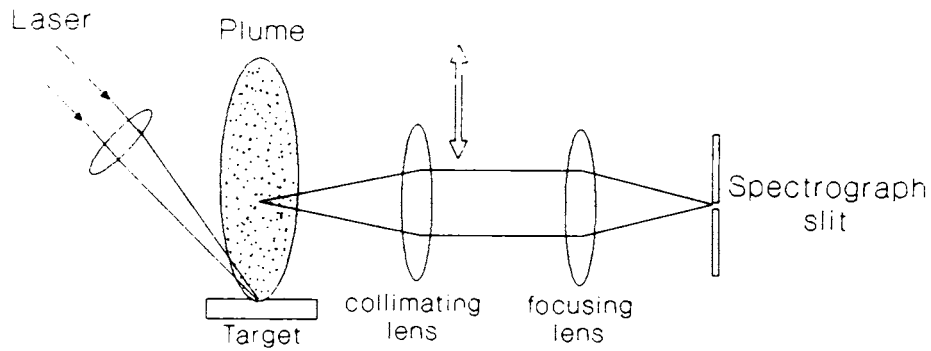


Figure 2.6: The schematic view of the spatial imaging of the plasma on to the monochromator slit.

axially (*i.e.*, along the plasma expansion axis (z)) and radially (*i.e.*, perpendicular to z and parallel to the spectrograph entrance slit) can be easily obtained when using a normal incidence grating spectrograph. A map of the expanding plasma plume should provide a good picture of the basic processes controlling the plasma kinetics and may provide insights into the mechanisms of the film growth. We have made spatially resolved analysis of the plasma by concentrating strictly along the expansion direction of the plasma. The direction of expansion of the plasma is always perpendicular to the target surface irrespective of the angle of the incident beam. The schematic view of the spatial imaging of the plasma on to the monochromator slit is given in the fig. 2.6. The spatially resolved studies were carried out by using a collimating and focusing lenses. The collimating lens could be translated continuously in the horizontal plane in the direction of the axis of the expansion of the plasma to examine different parts of the plasma plume at different distances from the target surface. The wavelength of the emission lines can be directly read from the display on the monochromator which is calibrated against standard spectral lines. Using this set-up, one can record the emission spectra of laser ablated plasma at different distances from the target surface.

2.4 Time resolved studies

In the photoablation of solid targets knowledge of the time evolution of the ablation process is of considerable significance since it may, in conjunction with theoretical models

[21] helps to resolve uncertainties in the interaction mechanism and thus lead to improved understanding of this phenomenon which has importance in practical applications [22]. The results throw much light on the complex recombination process in a laser ablated plasma. Time resolved emission spectroscopy can be used to measure the expansion velocities of atomic, molecular and ionic species. Measurement of the number density and internal energy as well as the kinetic energy distributions of the evaporants is important in understanding the fundamental physics of the epitaxial film formation process.

In the present studies, time resolved analysis of the plasma emission spectra were carried out by scanning the gate of the boxcar averager through the required temporal regions by adjusting the delay.

2.4.1 Time of flight (TOF) spectroscopic studies

The experimental set-up for the time of flight study is given in fig. 2.7. For these studies, the output from the PMT is directly connected to a digital storage oscilloscope with 50Ω termination. In order to study the time evolution of a particular species produced during the laser ablation process, the characteristic lines were easily selected using a monochromator and the PMT output was fed to a fast storage oscilloscope. This setup essentially provides delay as well as decay times for emission from constituent species at a specific point within the plasma and these are extremely important parameters related to the evolution of laser ablated materials in a direction normal to the target surface. The time resolved studies of the plasma give vital information regarding the time taken for a particular state of the constituent to evolve after the plasma is formed. Thus this measurement is important for obtaining knowledge of complicated ablation and transport processes occurring in the plasma produced by the laser ablation technique [22]. The oscilloscope trace of the PMT response of the emission from different species in the plasma shows a noticeable time delay between the incident laser pulse on the target and the onset of emission from a particular species. All time delays are measured with respect to the laser trigger pulse which coincides with the incident laser pulse. Each temporal profile represents a complex convolution of different factors that govern the temporal history of the emitting species viz. its production mechanism and rate, its flight past the viewing region and its radiative and collisional decay rates. With the knowledge of spatial separation from the target surface, one can directly convert the time of flight distribution of any species into velocity distribution from which translation temperature

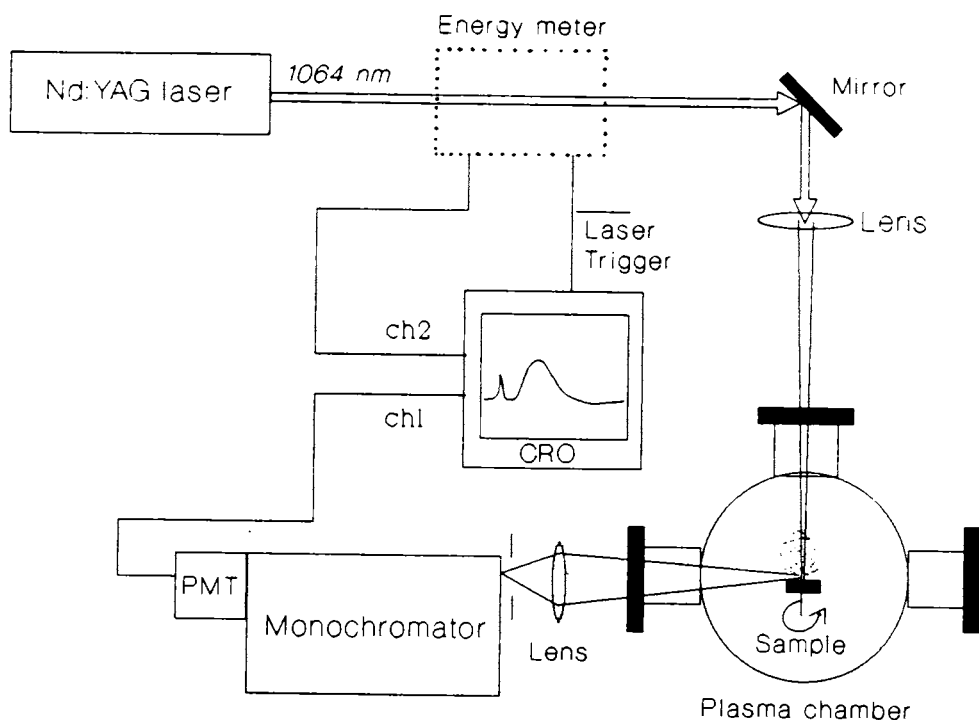


Figure 2.7: The experimental set-up used for the time of flight (TOF) study.

can be determined. The delay times for the plasma production is very critical on different experimental parameters like, spatial position, pressure of the ambient gas, laser irradiance used etc.

The exact reason for the existence of time delays for the after the elapse of laser pulse is some what controversial. There are many reasons for the occurrence of a time delay for emission from any species in the plasma plume which includes: (1) Time of Flight (TOF) of the species, (2) thermal processes leading to generation of plasma from the target (3) recombination and/or dissociation of the species.

The above sections describe the salient aspects of the experimental systems utilized for the measurements presented in this thesis. However, depending on the actual measurements conditions one or several of the experimental parameters have to be suitably altered. For eg., to measure the effect of ambient gases on the features of the plasma and their variations with pressure of the gas one has obviously need to alter the pressure of the gas in the plasma chamber. Hence, what is described in the above sections can be considered as a typical arrangement for a standard examination of laser induced plasma.

2.5 References

- [1] J. F. Ready, *Effect of High Power Laser Radiation* (Academic press, New York, 1971).
- [2] L. J. Radziemski and D. A. Cremers, *Laser-Induced Plasmas and Applications* (Marcel Decker, Inc., New York, 1989).
- [3] T. P. Hughes, *Plasmas and Laser Light* (Adam Hilger, England, 1975).
- [4] K. Muraoka and M. Maeda, *Plasma Phys. Control. Fusion*, **35** 633 (1993).
- [5] R. Mitzner, A. Rosenfeld and R. Konig, *Appl. Surf. Sci.*, **69** 180 (1993).
- [6] R. C. Estler and N. S. Nogar, *J. Appl. Phys.*, **69** 1654 (1991).
- [7] S. S. Harilal, P. Radakrishnan, V. P. N. Nampoori and C. P. G. Vallabhan, *Appl. Phys. Lett.* **63** 3377 (1994).
- [8] S. S. Harilal, R. C. Issac, C. V. Bindhu, V. P. N. Nampoori and C. P. G. Vallabhan, *Jpn. J. Appl. Phys.* **36** 134 (1997).
- [9] S. S. Harilal, R. C. Issac, C. V. Bindhu, V. P. N. Nampoori and C. P. G. Vallabhan, *Spectrochimica Acta A*, (in press) (1997).
- [10] Instruction Manual, Quanta Ray DCR 11, Nd:YAG laser
- [11] Instruction Manual, Spex 1704 Spectrometer (Spex, USA)
- [12] Instruction Manual, Spex CD 2A CompuDrive (Spex, USA)
- [13] Instruction Manual, Jarrell-Ash monochromator
- [14] Photomultiplier tubes, Construction and operating characteristics (Hamamatsu, Japan)
- [15] Instruction Manual, Delta Developments Laser Energy Meter
- [16] Instruction Manual, Iwatsu DS 8651 Oscilloscope, (Iwatsu, Japan).
- [17] Instruction Manual, Stanford Research Systems Boxcar Averager and Gated Integrator.

- [18] Instruction Manual, Rikadenki Chart Recorder.
- [19] Y. B. Zeldovich and Y. P. Raizer, *Physics and Shock Waves and High-Temperature Phenomena* (Academic, New York, 1966).
- [20] S. S. Harilal, R. C. Issac, C. V. Bindhu, V. P. N. Nampoori and C. P. G. Vallabhan, *J. Appl. Phys.* **80** 3561 (1996).
- [21] Z. W. Gortel, H. J. Kreuzer, M. Schaff and G. Wedler, *Sur. Sci.*, **134** 577 (1983).
- [22] D. B. Chrisey and G. K. Hubler (eds.) *Pulsed laser deposition of thin films* (John Wiley and sons, New York, 1994).

Chapter 3

Optical Emission Studies of C₂ Species in Laser Produced Plasma from Carbon

Optical emission studies of C₂ molecules in plasma obtained by Nd:YAG laser ablation of graphite in a helium atmosphere are studied at irradiance in the range 10 GW cm⁻² to 92 GW cm⁻². The characteristics of the spectral emission intensity of Swan bands from the C₂ species have been investigated as functions of distance from the target, ambient helium pressure, time after the elapse of laser pulse and laser irradiance. The estimates of vibrational temperature of C₂ species at various irradiance conditions are made. Results of measurements performed under different ambient helium gas pressures are also discussed.

3.1 Introduction

C_2 occurs in a variety of chemical reactions and in a wide range of astrophysical environments. Energetic treatment of hydrocarbons, either by radiation, by highly exothermic stripping reactions, or by exposure to high temperatures, invariably produces C_2 which is often in an emissive excited state [1-4]. C_2 appears in the atmospheres of carbon stars and in sun as well as in comets and diffuse interstellar clouds [5]. The C_2 molecule possesses seven known triplet and six known singlet electronic states giving rise to nine band systems which lie across vacuum ultraviolet (VUV), the visible and infrared (IR) regions [6]. The prominent C_2 band systems are Swan system ($d^3\Pi_g \rightarrow a^3\Pi_u$), Phillips system ($A^1\Pi_u \rightarrow X^1\Sigma_g^+$), Mulliken system ($D^1\Sigma_u^+ \rightarrow X^1\Sigma_g^+$) and Deslandres-d'Azambuja system ($C^1\Pi_g \rightarrow A^1\Pi_u$) [7]. Rohlfing [8] has observed direct emission in three band systems *viz.* Swan, Deslandres-d'Azambuja and Mulliken from free jet expanded C_2 formed by laser vapourization of graphite into pulsed helium flow. These experiments extended to those of Anselment et al [9] into UV and VUV. Rohling [8], in addition to emission from C_2 formed from vapourization of graphite into a confined helium flow, has observed a long-lived continuum attributed to the incandescence of hot carbon particles.

The C_2 bands, which were discovered in 1856 in a study of flames with carbon components, naturally appear in various types of discharges. Therefore, eventhough the chemical processes in the plasma are unknown, they are often used as a 'thermometer' to estimate the gas temperature in the corresponding emission region [10]. The strongest and most easily excited C_2 band system is the Swan system which lies between 420 nm and 770 nm. Potential curves for the C_2 Swan system [11, 12] are shown in fig. 3.1. It is prominent in flame spectra [13] and in the spectra of electrical discharges through carbon-bearing materials [14]. The surfaces of space vehicles during atmosphere reentry are subjected to intense radiation heating from the hot gas cap behind the bow shock wave which often emits the Swan bands arising from carbon contained in carbonaceous heat shields [15]. Laser excitation of the Swan bands has been used in several flame studies, first relying on accidental coincidence between the 514 nm line from argon ion laser and the transition in the (0-0) Swan band [16], and then using a tunable dye laser [17]. The exact mechanism responsible for the Swan band emission are difficult to determine which vary with wavelength of excitation. Their convenient wavelengths have been exploited for a variety of laser based measurements [18]. C_2 Swan band emission seems to be ubiquitous

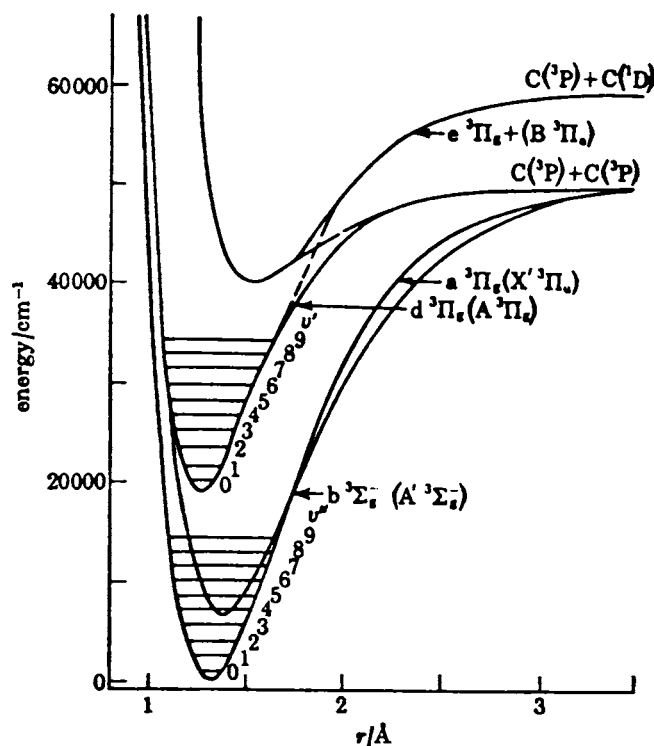


Figure 3.1: Potential curves for the C₂ Swan system ($d^3\Pi_g \rightarrow a^3\Pi_g$)

in many environments, appearing almost any time that intense laser pulses, with any wavelengths, irradiate carbon containing compounds.

Pesic et al [19] observed the Swan bands of $^{13}\text{C}_2$ and $^{12}\text{C}^{13}\text{C}$ and determined isotope effects upon band origins and molecular vibrational and rotational parameters. A series of high resolution Fourier transform spectroscopy studies of $^{12}\text{C}_2$, $^{13}\text{C}_2$ and $^{12}\text{C}^{13}\text{C}$ were made by Amiot and co-workers [20, 21]. Review of experimentally determined lifetimes (τ_v), oscillator strengths ($f_{v'v''}$) and/or electronic transition moments of the important systems of C₂ is available in literature [22]. The lifetime measurement of these species using laser techniques has presumably yielded more accurate data [23]. The reported values of lifetime for C₂ swan band system is $\tau_v = 102$ ns obtained by using laser induced fluorescence decay of supersonically cooled C₂($d^3\Pi_g$) [23].

Plasma generation by laser induced dielectric breakdown at a gas solid interface has attracted considerable attention in recent times [24, 25]. Lasers have been used to produce high-temperature and high density plasmas by vapourizing a small amount of material with high-powered picosecond or nanosecond pulses. In addition to applications in basic research, pulsed laser ablation has well established uses in materials technology like de-

position of diamond-like carbon thin films [26-38]. Pulsed laser deposition is increasingly being utilized for thin film preparation, in which a laser beam is focused onto a solid target and the resulting vapour is made to condense onto the substrate of interest. Diamond-like carbon (DLC) thin films which are successfully prepared using laser ablation have wide applications owing to their interesting characteristics like extreme hardness, electrical insulation, high thermal conductivity, optical transparency etc. With pulsed laser evaporation of carbon targets hydrogen free films with improved characteristics may be grown [35]. Several types of laser have been used for the preparation of DLC films which include excimer lasers [28-30], Nd:YAG laser [31-37], CO₂ [38] with laser intensities varying from 0.1 to 100 GW cm⁻². Recently, a critical review of the pulsed laser deposition of amorphous DLC films is performed by Voevodin and Donley [39].

Laser ablated carbon plasmas have also been extensively studied for production of carbon clusters [40]. Further laser ablation is a convenient method for the production of C₆₀ and higher fullerenes [40-46]. When graphite surface is vapourized by intense laser pulses in a helium atmosphere of moderate pressure, remarkably stable carbon clusters are produced. Experiments with these sources provide information on fullerene formation in the presence of carbon alone, with no possible interference from species containing other atoms. A typical time of flight (TOF) mass spectrum of carbon clusters in the range of 1-100 atoms obtained with frequency doubled Nd:YAG (532 nm) vapourizing laser and with unfocussed ArF ionizing laser (193 nm) is shown in the fig. 3.2 [41]. The dimer molecule, C₂, has not been seen as an abundant species in any of the studies involving mass spectroscopic detection, which is doubtless due to high ionizing potential of C₂ which is 12 eV. Creasy and Brenna [47] have reported fullerene ions from laser ablation of DLC films demonstrating that C₆₀ ions can be formed in a variety of systems. Carbon molecules (C_n) are particularly interesting due to their unique and fascinating structural and spectroscopic properties, their importance in astrophysical processes and due to their role in combustion and soot formation. Laser ablation has the unique advantage that most of these molecules are formed in their excited states and hence spectroscopic measurements offer an excellent means to investigate their evolution and dynamics. The general nature and outcome of interaction of intense laser radiation with solid matter depends very much on the parameters of incident laser beam, material properties and environmental conditions. Laser - solid interaction causes several processes to occur simultaneously and these include energy transfer, evaporation of solid material,

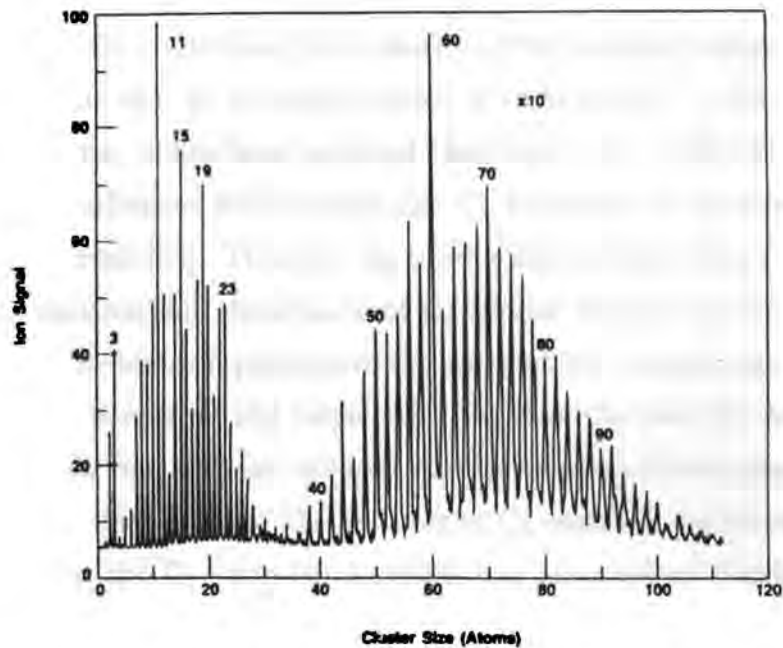


Figure 3.2: Typical time of flight mass spectra (TOF - MS) for carbon clusters obtained with doubled Nd:YAG vapourizing laser and unfocussed ArF ionizing laser. The spectrum is a combination of two different spectra. The gain in the later section was increased by a factor 10.

generation of a dense plasma, formation of charged and neutral particles. Obviously the theoretical models based on local thermodynamic equilibrium (LTE) can give only a qualitative explanation of these processes taking place during laser deposition [48]. There were several techniques used for the characterization of laser produced carbon plasma such as emission spectroscopy [49-55], time resolved spectroscopy [56-61], laser induced fluorescence [18], mass spectroscopy [40, 41], electronic probe method [62, 63] etc. Measurements of space and time dependent emission of the species present in the plasma plume provide a means to understand the dynamics and reaction kinematics of the ablated materials. Recently time resolved measurements have been made on C_2 species in a laser induced plasma generated on a graphite surface with laser irradiance and ambient helium pressure [56-58] as the varying parameters and these studies have yielded many interesting results. Against this background it was thought worthwhile to investigate the dynamics of laser induced plasma from a graphite target in a helium atmosphere.

Despite considerable experimental and theoretical progress, the studies on laser produced carbon plasma have not yet yielded a clear-cut picture on plasma dynamics of

the cluster formation and such a situation arises mainly due to the complexity of the phenomena involved. By controlling the intensity of the incident radiation it is possible to obtain high ionic as well as molecular states of carbon [64]. In the context of laser deposition of DLC films, it has been reported that high quality DLC films are obtained at moderate laser irradiances where molecular C_2 formation is prominent as revealed by its emission spectrum [65]. Thus for the production of DLC films it is necessary to understand the formation and dominance of C_2 species and its dependence on various parameters like laser irradiance, pressure of the ambient gas, concentration of the species at different distances normal to the target etc.. We describe here the details of a series of experiments carried out on laser induced plasma produced from graphite in helium atmosphere. We have here studied the features of C_2 emission spectrum under various conditions specifically, the C_2 Swan band system was analyzed as function of laser irradiance, distance from the target surface and helium pressure in different regions of the plasma.

3.2 Experimental Details

The details of the experimental set-up used in this work are given in chapter 2. Briefly, a Q - switched Nd:YAG laser at its fundamental wavelength with a pulse repetition frequency of 10 Hz is used to produce the carbon plasma. A lens of focal length 20 cm is used to focus the laser beam onto the rotating graphite target. The plasma chamber is evacuated to a pressure $\sim 10^{-3}$ mbar and then filled with helium gas at desired pressures. Under these experimental conditions intense emission from plasma in the visible region appears on irradiation of the target surface. The bright optical emission from the laser produced carbon plasma is imaged right angles to the expansion direction to produce a 1:1 image on the entrance slit of a calibrated 1 m Spex scanning monochromator equipped with thermoelectrically cooled Thorn EMI photomultiplier tube. The output from the PMT is then fed to a boxcar averager/gated integrator coupled with a chart recorder and this arrangement averages out emission intensities for ten consecutive pulses. Using a series of slits and apertures it is possible to record the emission spectrum from a segment of the plasma plume situated a definite distance from the target. For spatially resolved studies, different regions of the plasma plume were focused on to the monochromator slit. The spatial resolution available here is better than 0.2 mm.

3.3 Results and Discussion

The experimental arrangement described above enables one to obtain the spectra from different vertical slices of the plasma plume generated by laser irradiation of a target. As seen in many earlier studies, beyond a threshold laser irradiance, the target gets ablated with the emission of light caused by a variety of processes occurring in the ablated products. However the various features of the emission spectra depend strongly on the laser irradiance incident on the target surface.

In the present case, the emission spectra of laser generated carbon plasma were recorded at low as well as high levels of laser irradiances in a helium ambient atmosphere from sections at various distances from the target. The intensities of the spectral lines from the plasma plume were found to be sensitive to different experimental parameters like laser irradiance, ambient gas pressure and perpendicular distance from the target. The apparent length of the plasma plume was around 25 mm in vacuum and it got reduced considerably with increasing pressure of the helium gas. The presence of helium gas helps faster cooling of plasma so as to reduce the plume length and causes changes in the colour of the plasma. Under low irradiance conditions the recorded spectra were found to be dominated by band emission from C_2 molecules (Swan bands), whereas at high irradiance, strong line emission from atomic and ionic species occur. In these experiments, emission from multiply ionized species up to C IV (triply ionized Carbon) has been recorded along with those from the molecular C_2 species. Surprisingly emission originating from excited carbon atoms is relatively difficult to detect in the wavelength region under study because of its weak concentration within the plasma plume in our experimental conditions.

3.3.1 Spectroscopy of the Swan Band Emission

The Swan bands arise from transition between the $d^3\Pi_u$ and $a^3\Pi_u$ electronic states of the C_2 molecules. Swan band emission is a likely result when intense laser pulses of almost any wavelength are focused onto carbon containing solids or gases. Swan bands are clear signature of C_2 species, a detailed study of these bands offers the best method to trace the evolutionary history of C_2 molecules generated in the laser ablation of graphite.

In the present case when graphite target is irradiated with a Nd:YAG laser beam at $1.06 \mu m$ wavelength the emission spectrum in the presence of helium gas contained

well defined Swan band heads in the $\Delta v = -2, -1, 0, 1, 2$ sequences. In addition to C_2 bands there are lines from some neutral and lower ionic carbon species which are very prominent at points closer to the target surface even at low levels of laser irradiance. But at higher laser irradiance the multiply ionized species up to C IV have been observed. Swan band heads corresponding to (0,0), (1,1), (2,2), (3,3) and (4, 4) are seen for $\Delta v = 0$ sequence (fig. 3.3) and for $\Delta v = -1$ sequence (fig. 3.4), Swan band heads up to (4,5) are observed at low laser irradiances. The bands (0,2), (1,3), (2,4), (3,5), (4,6), even though very weak, are also observed at low laser irradiances for $\Delta v = -2$. All the band heads corresponding to $\Delta v = 1$ (up to (6,5) at 467 nm, (fig. 3.5) and for $\Delta v = 2$ (up to (4,2) at 437 nm) have been recorded (fig. 3.6). The spectra are partially rotationally resolved. The overall uncertainty expected in the intensity tabulation is expected to be less than 10 %. At low irradiances we further observed, though less intense, the high pressure band of the Swan system which originates from $v' = 6$ level centered at 589.9 nm. These bands have been seen in the *in vacuo* laser vapourization of graphite [66]. The presence of C_2 high pressure bands ($d^3\Pi_g \rightarrow a^3\Pi_u$) could be due to the possibility that the upper level of these bands are populated via a potential-energy curve crossing by the metastable state which is populated preferentially during the formation of C_2 from free carbon atoms [67]. The cometary band centered around 405 nm was not identifiable in the recorded spectra.

The detection of band emission originating from C_2 is of particular interest since it provides an estimation of the plume temperature. The Swan band emission intensities are analyzed in order to calculate molecular vibrational temperature T_{vib} . The variation in diamond-like character in DLC films is mainly due to different temperature of various species in the laser plasmas. An estimate of temperature of dominating species of the film helps to optimize the film properties. Molecules in a certain vibrational state v' of the upper electronic state can decay to different vibrational levels v'' of the lower electronic state giving subsequently the emission intensities $I_{v',v''}$. According to the vibrational sum rule for intensities of different bands in a progression, the sums of the band strengths of all bands with the same upper or lower states are proportional to the number of molecules in the respective states [68], *ie.*

$$\sum_{v''} \frac{I(v', v'')}{\nu^4} \propto N_{v'} \quad (3.1)$$

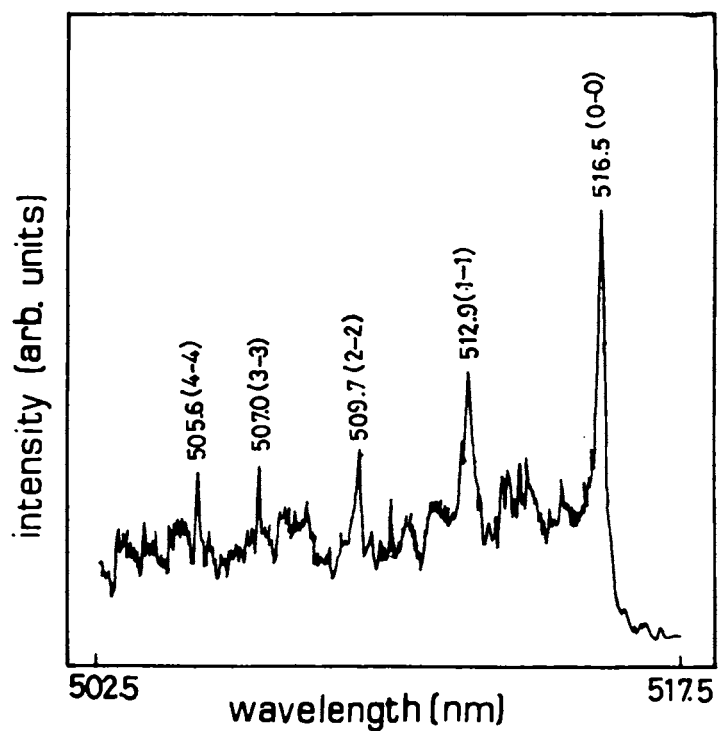


Figure 3.3: Spectrum of the resolved C_2 Swan band emission for $\Delta v = 0$

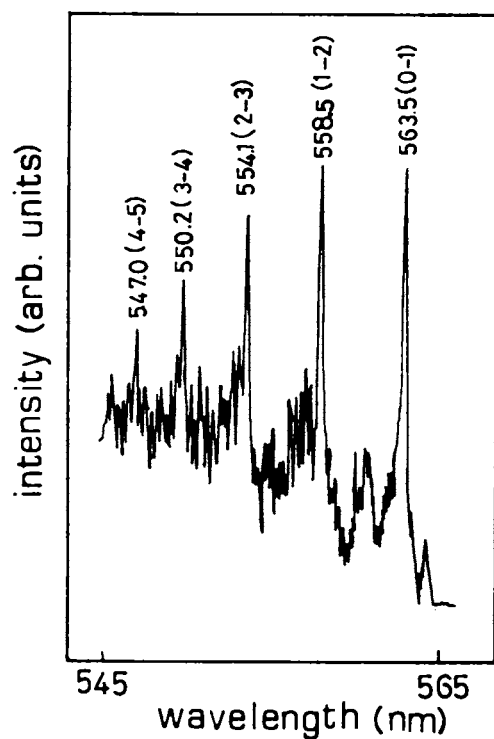


Figure 3.4: Spectrum of the resolved C_2 Swan band emission for $\Delta v = -1$

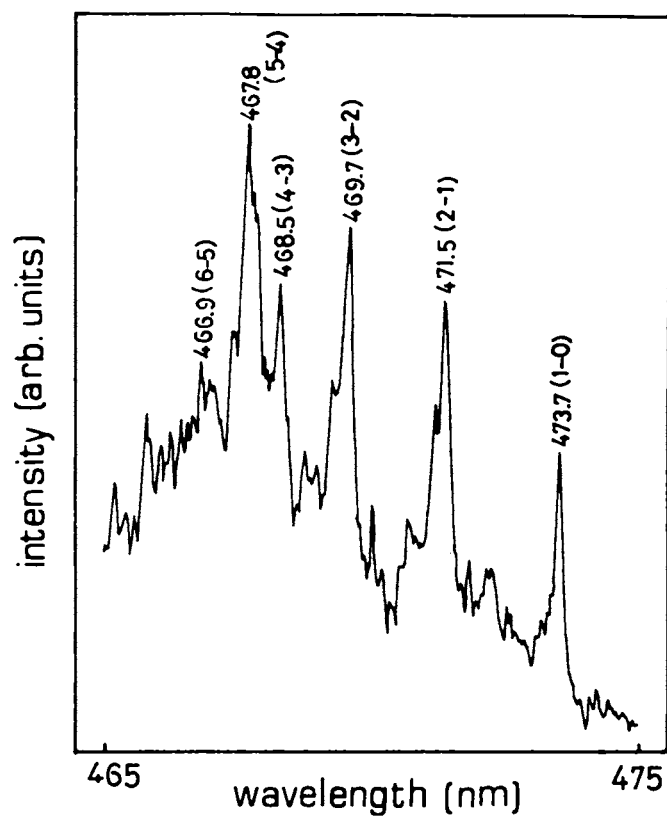


Figure 3.5: Spectrum of the resolved C_2 Swan band emission for $\Delta v = 1$

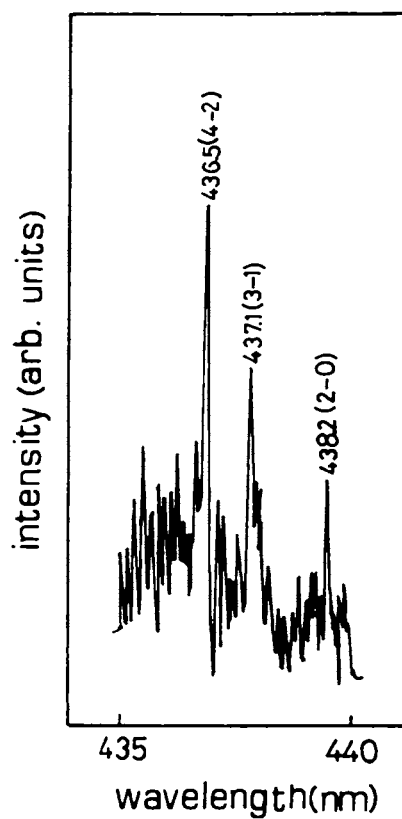


Figure 3.6: Spectrum of the resolved C_2 Swan band emission for $\Delta v = 2$

$$\sum_{\nu'} \frac{I(\nu', \nu'')}{\nu^4} \propto N_{\nu'} \quad (3.2)$$

where ν is the frequency in cm^{-1} , N_{ν} and $N_{\nu'}$ the numbers of the molecules in the corresponding vibrational levels of the electronic states respectively.

For a plasma at local thermodynamic equilibrium (LTE) [68],

$$\ln \sum_{\nu'} (\lambda^4 I_{\nu\nu'}) = C_1 - G(\nu') \left[\frac{hc}{kT_{vib}} \right] \quad (3.3)$$

where λ is the wavelength corresponding to the emission, h the Planck's constant, c the velocity of light, C_1 a constant, $G(\nu')$ the term value corresponding to the vibrational level in the upper electronic state and T_{vib} the vibrational temperature. The vibrational temperature for C_2 bands is obtained from the plot of the sums of the band strengths measured in various ν' or ν'' progressions against the vibrational term values $G(\nu)$. Since the intercept C_1 has no significance, the slope is a direct measure of the vibrational temperature. The advantage of using Boltzmann distribution is that the information regarding the transition probability is not essential in this case. Typical Boltzmann plots of the band intensities against vibrational energy was made for different laser irradiances and are given in fig. 3.7.

The vibrational distribution of the excited states of C_2 molecules at distance 5 mm away from the target surface and at a laser irradiance of 70 GW cm^{-2} is given in fig. 3.8. The calculated values of N_{ν} are to be regarded as relative values. The population in different vibrational levels showing an inverse distribution for $\nu < 1$ is in accordance with the Frank-condon principle. Similar inverse distributions are also observed in certain other molecules [69-71]. Please note that these values of N_{ν} are to be regarded as relative values and not as absolute values. However the calculated orders of magnitude are in good agreement with that of the reported values [53, 72].

3.3.2 Spatial Dependence

One of the important results of the present series of studies is that the spectral features are distinctly different for the emission from different sections of the plasma plume. The spectra contain a strong continuum background emission close to the target surface. At distances less than 1 mm from the target surface, irrespective of the level of laser irradiance, we cannot distinguish any line or broad band spectra. One can observe in this case just an intense continuum emission due to free - free transitions. Rohling [8]

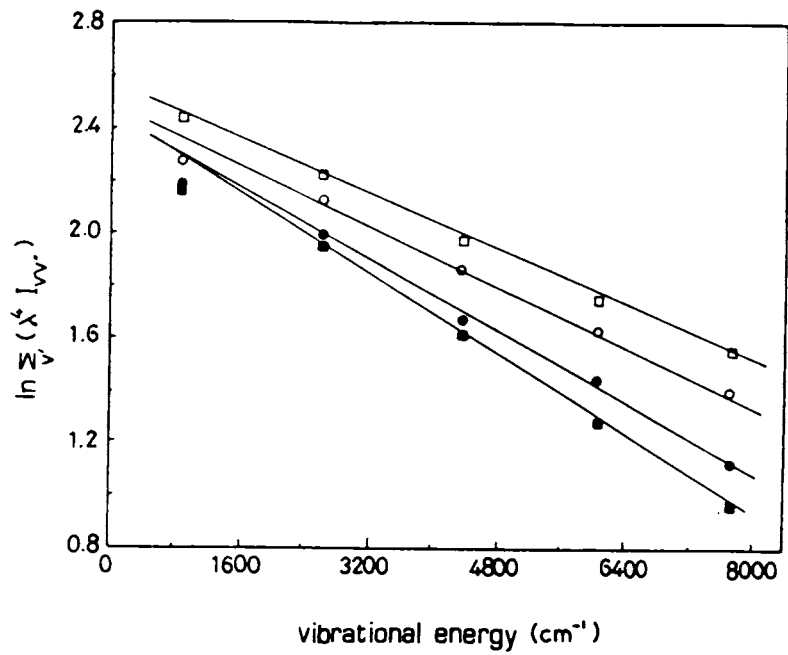


Figure 3.7: Boltzmann plots of vibrational band intensity vs vibrational energy for different laser irradiances at a distance 10 mm from the target. (\square - 45 GW cm^{-2} , \circ - 42. GW cm^{-2} , \bullet - 35 GW cm^{-2} and \blacksquare - 2.5 GW cm^{-2}). The slope of the fitted line is used to calculate the vibrational temperature

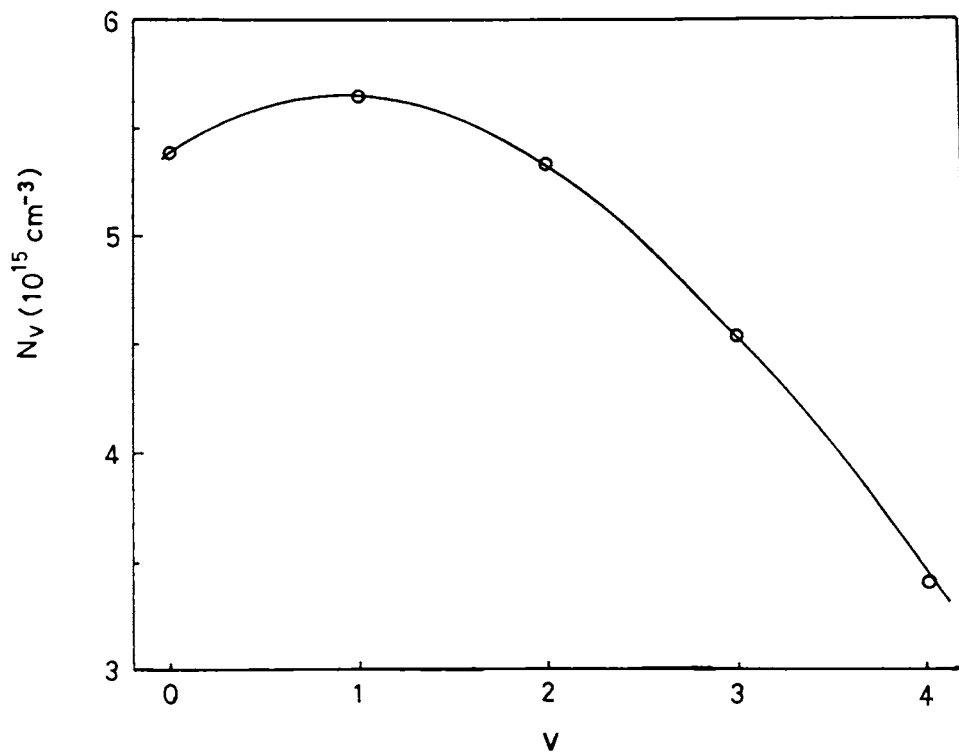


Figure 3.8: The vibrational distribution of C_2 molecules (distance 5 mm, laser irradiance 70 GW cm^{-2})

also observed such a continuum emission, in addition to emission from C_2 formed from vapourization of graphite into a confined helium flow, and attributed the long-lived continuum to the incandescence of hot carbon particles. Fig. 3.9 shows typical Swan band sequence corresponding to $\Delta v = -1$ at different distances from the target surface. Fig. 3.10 shows the variation of vibrational temperature with spatial separation from the target surface for 5 μs after the laser pulse at laser irradiances 20 GW cm^{-2} . For these studies the gate width of the boxcar is set at 100 ns. It is observed that the vibrational temperature of the C_2 molecules attain maximum values (7600 K) at an optimal distance (a typical distance being 4 mm at 20 GW cm^{-2}), and then decreases with further increase in distance. The spatial dependence of vibrational temperature of C_2 molecules at higher irradiance of 70 GW cm^{-2} for 2 and 5 μs delays after the evolution of plasma are given in fig. 3.11. The peculiar nature of the vibrational temperature with distance at different laser irradiances results from the fact that excited state C_2 formation is controlled by different interaction processes like electron capture, collisional excitation and ionization, recombination processes and fragmentation of higher clusters. The dominant mechanism for the production of C_2 molecules at low laser irradiance is likely to be the electron collision with higher clusters of carbon followed by photofragmentation where one of the emitted product species is an excited C_2 molecule while at higher irradiance Swan band emission is mainly due to excitation resulting from electron-ion, ion-ion recombination [29]. It may in this connection, be noted that high quality DLC films are obtained at laser irradiance $\sim 10 \text{ GW cm}^{-2}$ for $1.06 \mu m$ pulsed laser deposition [27, 73]. Peeler and Murray [74] have shown that low energy carbon clusters form graphite films while small, fast carbon atoms/molecules produce DLC films.

It is well known that graphite exhibits a large difference between the inter-layer and the intra-layer bond strengths. It is expected that at low laser irradiances graphite will be ablated layer by layer producing large clusters which in turn get dissociated due to high temperature to form C_2 molecules near the target surface [40]. Such dissociative mechanism can further be supported by the observation of comparatively longer duration of Swan band emission. The spatial dependence of vibrational temperature of C_2 molecules can be explained as follows. The temperature near the target surface is so high that collision induced nonradiative processes predominate and cause a reduction in the effective vibrational temperature due to fast de-excitation of the higher vibrational levels as well as due to quenching. As we move away from the target, due to reduced collisional

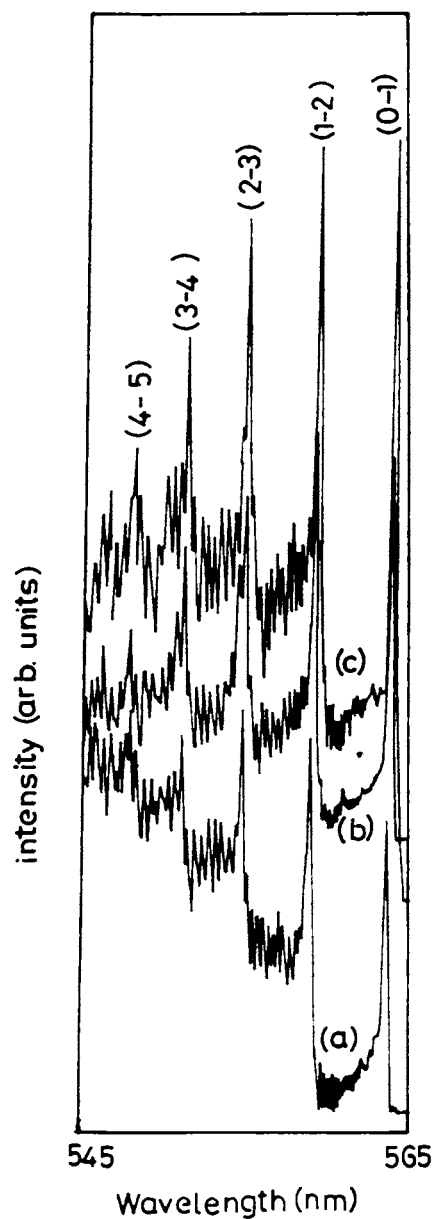


Figure 3.9: C₂ d-a Swan band sequence $\Delta v = -1$ recorded at different distances from the target surface (a) 3 mm, (b) 5mm, and (c) 7 mm.

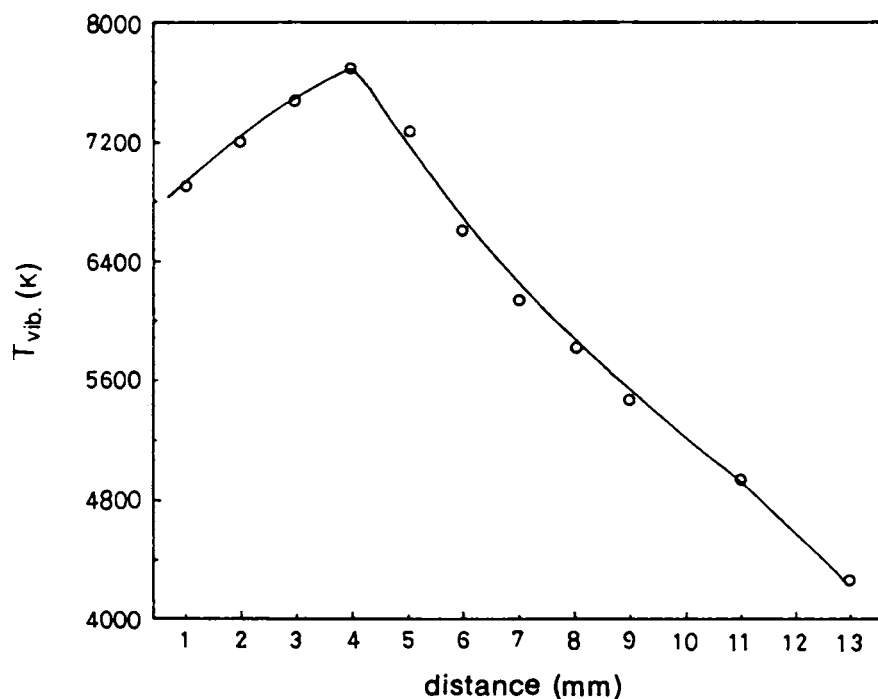


Figure 3.10: The variation of vibrational temperature (T_{vib}) of the C_2 molecules with distance from the target at a laser irradiance 20 GW cm^{-2} (time delay $5 \mu\text{S}$).

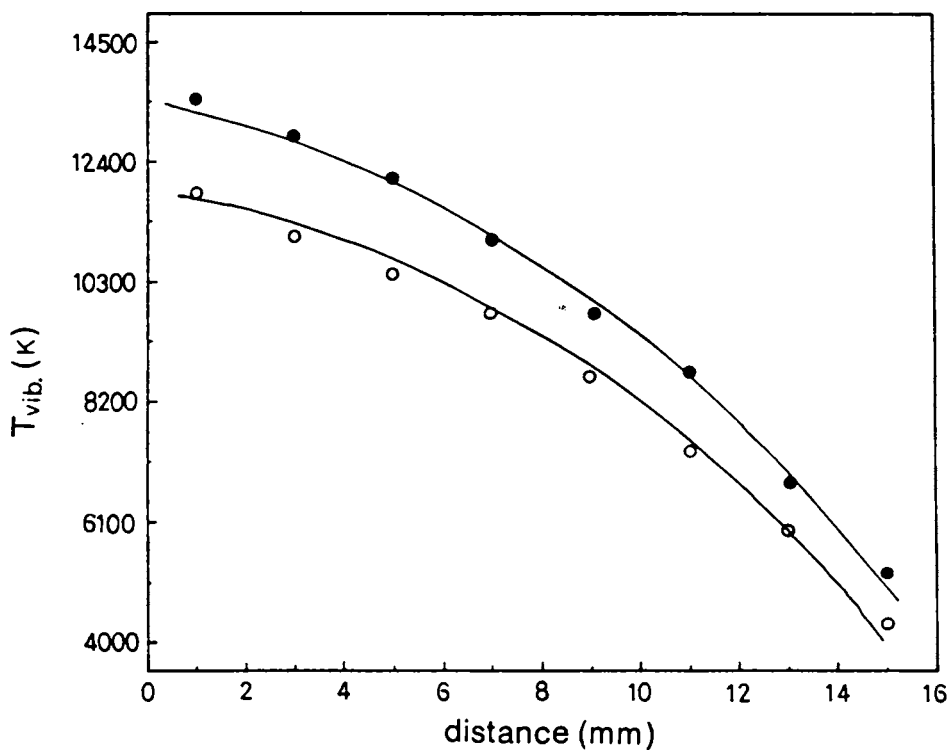


Figure 3.11: Spatial dependence of vibrational temperature of the C_2 molecules for different time delays (\bullet - $2 \mu\text{s}$ \circ - $5 \mu\text{s}$) at high irradiances (70 GW cm^{-2})

energy transfer processes, the population of excited C_2 species increases which in turn increases the vibrational temperature. At distances farther than an optimal distance the decrease in plasma temperature will cause a reduction in vibrational temperature for these species due to lack of excitation processes. But at higher irradiance (70 GW cm^{-2}) it is observed that the vibrational temperature of the C_2 species decreases steadily with increasing distance from the target. This variation is quadratic in separation (z) from the target surface and can be written as

$$T_{vib}(z) = T_0 - az^2 \quad (3.4)$$

with T_0 as the vibrational temperature at $z = 0$. At higher laser irradiance energy absorbed exceeds the energy required for the breakage of intra-layer and the inter-layer carbon bonds. The presence of the ambient helium atmosphere which acts as coolant and creates a denser plasma improves the dissociative mechanism. This causes a decrease in particle size at higher irradiance. This may be the reason for the quadratic dependence of the vibrational temperature at higher laser irradiances from the target surface.

3.3.3 Laser Intensity Dependence

It has already been reported that the diamond-like character of the films deposited on substrates is strongly dependent upon the variation of temperature in the laser plasma which in turn depends upon laser irradiance [40]. The properties of the carbon films grown by the ablation of graphite are dependent on the kinetic energy of the carbon species striking on the surface of the grown film and these varies widely with laser irradiance. Estimates of the velocities of different species obtained by time of flight measurements have been reported earlier [57, 58]. These were found to depend strongly on laser irradiance levels. Here we have measured the intensities of emission bands from C_2 molecules as a function of incident laser irradiance for the calculation of vibrational temperature. At low laser irradiances the spectrum is dominated by the emission band of C_2 molecules originating from the Swan system; but at higher laser irradiances, emission originating from C II, CIII, CIV etc. are detected along with C_2 molecular bands. The variation of vibrational temperature with laser irradiance corresponding to C_2 molecules at distances 5 and 10 mm are given in fig. 3.12. Such variation of vibrational temperature with laser irradiance occurs essentially due to the fact that comparatively larger number of molecules are excited into higher vibrational levels with increasing laser irradi-

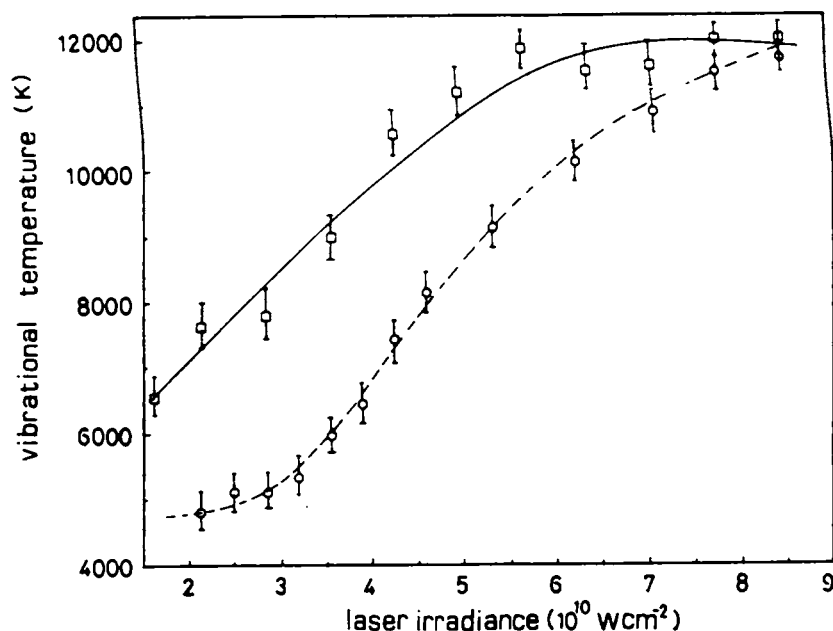


Figure 3.12: Vibrational temperature calculated from C_2 swan bands as a function of laser irradiance at different distances (\square - 5 mm and \circ - 10 mm)

ance. At higher irradiances the enhancement in the production of carbon clusters which get photofragmented into C_2 molecules. The saturation in vibrational temperature at high irradiance could be mainly due to the fact that at high laser irradiances plasma temperature is so high that the depletion of excited states could occur not only because of excitation to higher levels leading dissociation or ionization but also by deexcitation to lower levels (quenching). This could produce energetic and/or excited fragments and the excess energy could be converted into kinetic energy of the C_2 vapourized species via gas phase collisions. The saturation in emission intensity at higher laser irradiances is also due to a change in the efficiency of laser coupling to the target by increased absorption and/or reflection from the laser induced plasma, a process known as plasma shielding [75]. The absorption by the fragments heats the plume to higher temperatures by which further fragmentation into small components including atoms and ions occurs.

3.3.4 Time Dependence

For the time resolved, C_2 swan band emission spectra were recorded by varying delay times, *ie.*, by setting the gate with 100 ns duration at different times after the elapse of the laser pulse, in the range 100 ns to 40 μs . All the spectra were recorded at a distance 5

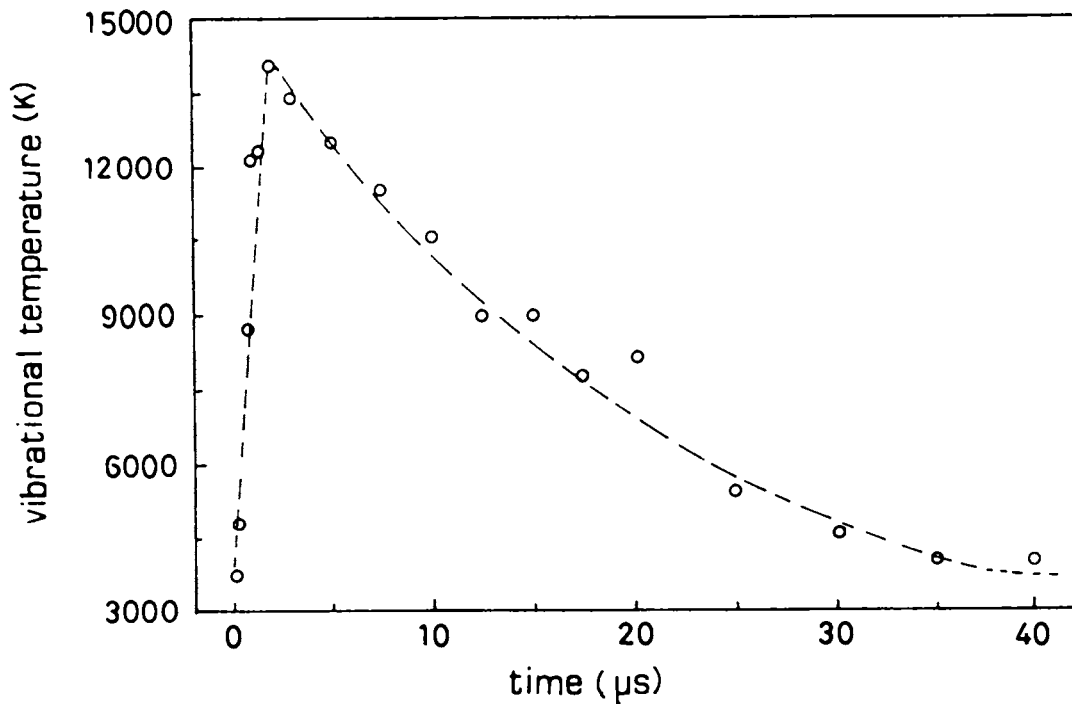


Figure 3.13: Time dependence of vibrational temperature of C_2 molecules at a laser irradiance 70 GW cm^{-2} (distance 5 mm).

mm away from the target and at a laser irradiance 70 GW cm^{-2} . For an integration time of 100 ns, the spatial distance travelled by the C_2 species is 0.4 mm, taking the average expansion velocity being $4 \times 10^5 \text{ cms}^{-1}$ at a laser irradiance 70 GW cm^{-2} , which is much smaller than the successive spatial steps of 1 mm. Hence there will not be any significant mixing of spatial and temporal aspects of plasma and an effective separation of spatial and temporal effects can be achieved. It is observed that the emission characteristics of the plasma varied drastically with time. At shorter times, the dominant radiation was a continuum mixed with ionic lines. The continuum emission is due to bremsstrahlung radiation and radiative recombination or due to incandescence of hot carbon particles [8]. But at times $> 1 \mu\text{s}$ the radiation from the continuum emission are absent leaving neutral lines and molecular bands which were seen up to $40 \mu\text{s}$ or longer. It has been observed that during the shorter times, due to high electron density the individual emission lines from different atomic and ionic lines are highly stark broadened [76, 77]. The time dependence of vibrational temperature of C_2 species is shown in fig. 3.13. As it is clear from the figure there is a maximum vibrational temperature ($14.2 \times 10^3 \text{ K}$) after an elapse of $2 \mu\text{s}$ at a distance of 5 mm away from the target.

3.3.5 Effect of Helium Gas Pressure

The emission characteristics of the laser produced plasma are influenced to a large extent by the nature and composition of the surrounding atmosphere. The interaction between laser plasma and the ambient gas is of interest because it provides information on collisional, collective and electromagnetic processes in astrophysical and laboratory plasmas produce several observable effects and that can help in the solution of various practical problems [29]. Mass spectroscopic studies reveal that higher carbon clusters are predominant when the laser evaporation takes place in a helium ambient atmosphere [8]. The presence of helium atmosphere helps to confine the plasma by collisions to allow increased absorption of the laser energy by inverse bremsstrahlung [78-80]. Therefore a denser plasma is formed in the presence of helium gas. The C₂ Swan band spectra were recorded from a section at a distance of 5 mm away from the target surface with ambient helium pressure as the varying parameter. With the addition of helium pressure, the plume boundary is slowed by collisions with the background gas which intern attenuate the amount of material penetrating the background gas.

The presence of helium ambient atmosphere cools the hot electrons by collisions leading to a more efficient electron impact excitation and plasma recombination, which also lead to plasma confinement near the target thereby enhancing the emission from this region. In general increase in helium ambient pressure gives rise to an enhancement in the emission intensity from all the species due to collisions on the expansion front and subsequent intraplume collisions, sharpening of the plume boundary and slowing down of the plume relative to the propagation in vacuum, all leading to the spatial confinement of the plasma.

The dependence of vibration temperature of C₂ molecules on helium ambient is given in fig. 3.14. It is seen that the increase in helium pressure decreases the vibrational temperature of the C₂ species. This is due to the fact that helium ambient atmosphere cools the hot electrons as well as excited states in molecules by collisions leading to a more efficient thermalization thereby decreasing the vibrational temperature. The helium atoms possess metastable triplet states, from which radiative decay to the singlet ground state is forbidden by the selection rules for electronic transitions [81]. The two lowest triplet state for helium lie at 19.73 and 20.53 eV. Because these metastable states are relatively high and their lifetimes are quite long ($10^6 - 10^7$ times longer than other states)

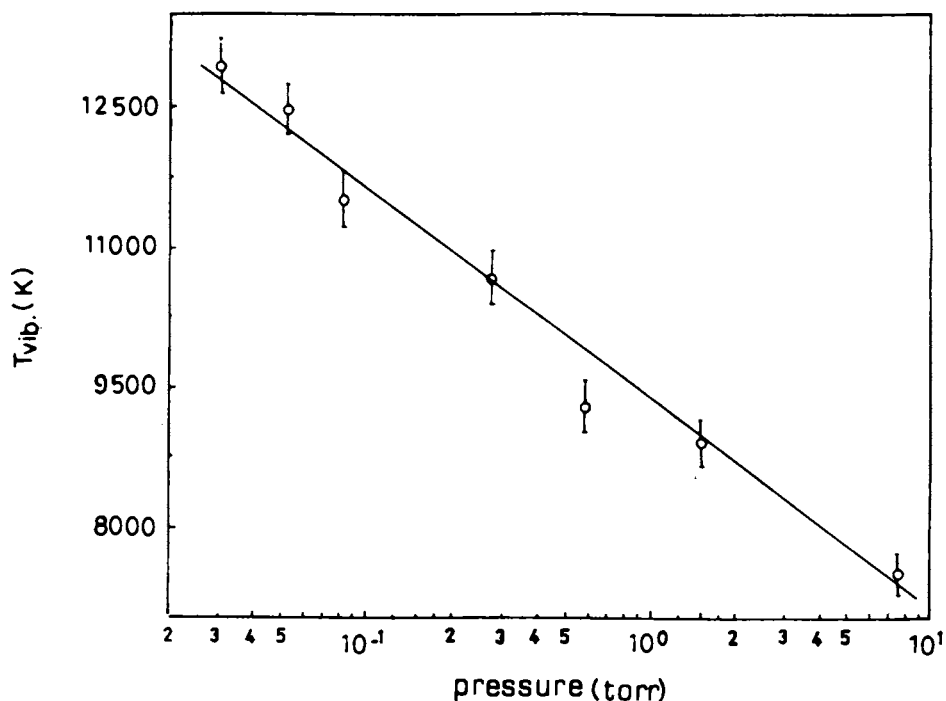


Figure 3.14: The change in vibrational temperature for C_2 molecules with respect to ambient helium gas pressure inside the plasma chamber (distance 5 mm, laser intensity 70 GW cm^{-2})

they can function as energy reservoirs. When significant population of the metastable states occurs, these species can become instrumental in exciting emissions via collisions with other species present in the plasma [82]. This can occur also by the enhancement in the intensities of C_2 bands on increasing helium pressure (fig. 3.15). This result implies that the distribution of vibrationally excited states is not in equilibrium with the plasma at low pressures, which is normal. An estimation of the translational temperature from expansion velocity of the C_2 species was attempted using the relation [83, 84]

$$k_B T = \frac{1}{\eta} \left(\frac{1}{2} m v^2 \right) \quad (3.5)$$

where v is the velocity of the C_2 species, k is the Boltzmann's Constant, m is the mass of the species, T is the translational temperature and η is the number of internal degrees of freedom which varies from 2.53 to 3.28. Using the above equation at a laser irradiance of 60 GW cm^{-2} , it is found that the translational temperature is $\sim 26000 \text{ K}$ [57]. But the maximum molecular vibrational temperature for C_2 molecules is $\sim 12000 \text{ K}$. Thus the translational temperature obtained are significantly greater than vibrational temperature of C_2 molecules. Collisional energy transfer occurring within the plasma might be responsible for the higher kinetic energy distribution of the C_2 molecules. The

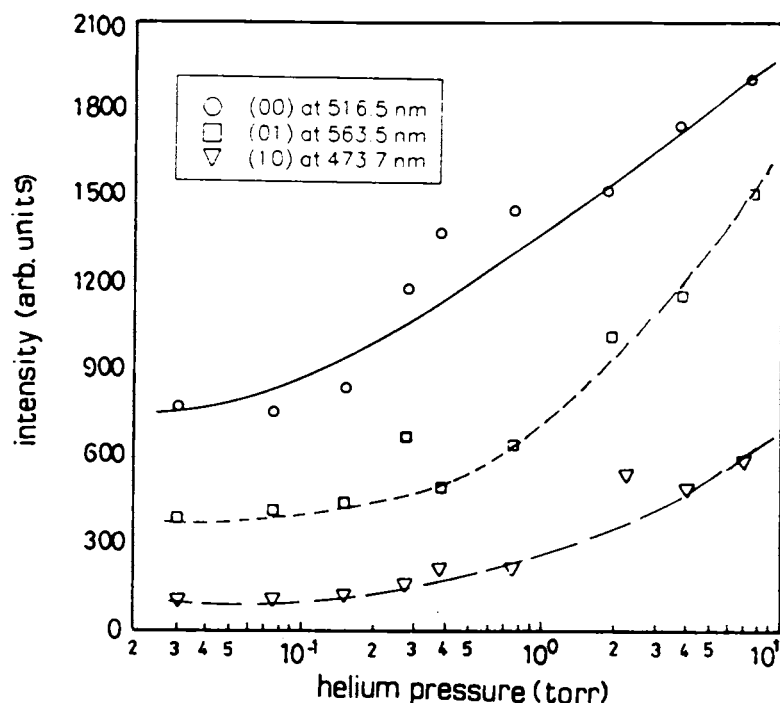


Figure 3.15: The change in intensity of band heads with respect to helium ambient pressure (distance 5 mm, laser intensity 70 GW cm^{-2}).

additional nonthermal processes like photofragmentation may contribute to the high kinetic energies. It is possible that some of the higher clusters are photofragmented during laser ablation.

3.4 Conclusions

In this chapter we describe a detailed spectroscopic study of C_2 emission from laser produced carbon plasma. We have made the spatially resolved analysis of C_2 Swan bands in the spectrum at emissions of laser induced plasma from graphite target in helium atmosphere. These investigations demonstrate that the emission intensities from C_2 species are sensitive to laser irradiance, pressure of the background gas, time after the elapse of the laser pulse and spatial separation from the target. It also demonstrates different possible routes for the formation of C_2 molecules. At low incident irradiance the emission bands due to C_2 predominates while at higher irradiance the multiply ionized species of carbon up to C IV have been observed along with C_2 species. The formation of C_2 emission could be observed at low irradiance due to plasma excitation and at high irradiance due to recombination processes. The presence of helium ambient atmosphere causes the line emission enhancement of the band heads of the C_2 species.

This enhancement in the emission intensity from C_2 is due to collisions on the expansion front and subsequent intraplume collisions

From the spectroscopic studies of the emission bands, vibrational temperature of the C_2 species in the plasma have been estimated. The vibrational temperature is found to increase with increase in laser irradiance and saturates at higher irradiance levels. The increase in laser irradiance causes an increase in degree of ionization and vibrational temperature of C_2 molecules in the plasma. The saturation at higher laser irradiances is mainly due to the change in efficiency of the laser beam coupling to the target because of plasma shielding. It is also confirmed that vibrational temperature of the C_2 molecules decreases with increase in helium pressure. The addition of helium apparently cools and confines the plasma causing reduction in the vibrational temperature. In summary, the present work throws some light on the production and kinetics of C_2 molecules in a laser generated plasma from graphite target.

3.5 References

- [1] M. Nicol, M. L. Johnson and N. C. Holmes, *Physica B* **139** 140 (1986).
- [2] A. M. Wodtke and Y. T. Lee, *J. Phys. Chem.*, **89** 4744 (1985).
- [3] D. Winicur and J. L. Hardwick, *Chem. Phys.*, **94** 157 (1985).
- [4] M. C. Curtis and P. J. Sarre, *J. Mol. Spectrosc.*, **114** 427 (1985).
- [5] William Weltner Jr. and R. J. Van Zee, *Chem. Rev.*, **89** 1713 (1989).
- [6] G. Herzberg, A. Lagerquist, and C. Malberg, *Can. J. Phys.*, **47** 2734 (1969).
- [7] R. W. B. Pearse and A.G.Gaydon, *The Identification of Molecular Spectra*, (Chapman & Hall Ltd, London 1965) P94.
- [8] E. A. Rohlfing, *J. Chem. Phys.*, **89** 6103 (1988).
- [9] M. Anselment, R.S. Smith, E. Daykin and L.F. Dimauro, *Chem. Phys. Letts.* **134** 444 (1987).
- [10] S. Pellerin, K. Musiol, O. Motret, B. Pokrzywka and J. Chapelle, *J. Phys. D* **29** 2850 (1996).
- [11] L. L. Danylewych and R. W. Nicholls, *Proc. Roy. Soc. Lond. A.* **339** 197 (1974).
- [12] L. L. Danylewych and R. W. Nicholls, *Proc. Roy. Soc. Lond. A.* **339** 213 (1974).
- [13] A.G.Gaydon, *The Spectroscopy of Flames* (Chapman and Hall, London 1974).
- [14] M. I. Savadatti and K. S. Kini, *Ind. J. Pure. Appl. Phys.*, **10** 890 (1972).
- [15] V. H. Reiss, *J. Quant. Spectr. Rad. Transf.* **4** 783 (1964).
- [16] C. J. Vear, P. J. Hendra and J. J. Macfarlane, *J. Chem. Soc. Chem. Commn.* **7** 381 (1972).
- [17] K. H. Bekker, D. Haaks and T. Tatarczyk, *Z. Naturforsch.* **29a** 829 (1974).
- [18] J. E. M. Goldsmith and D. T. B. Kearsley, *Appl. Phys. B* **50** 371 (1990).

- [19] D. S. Pesic, B. R. Vujisic, D. Rakotoarijimy and S. Weniger, *J. Mol. Spectrosc.*, **100** 245 (1983).
- [20] C. Amiot, J. Chauville and J. P. Maillard, *J. Mol. Spectrosc.*, **75** 19 (1979).
- [21] C. Amiot, and J. Verges, *Astrophys. J.* **263** 933 (1982)
- [22] T. Tatarczyk, T. Fink and E. H. becker, *Chem. Phys. Letts.*, **40** 126 (1976).
- [23] C. Naulin, M. Costes and G. Dorthe, *Chem. Phys. Letts.*, **143** 496 (1988).
- [24] T. P. Hughes *Plasmas and Laser Light* (England : Adam Hilger, IOP, 1975).
- [25] J. C. Miller and D. B. Geohegan (eds) *Laser ablation : Mechanisms and Applications* (New York, AIP, 1993).
- [26] S. S. Wagal, E. M. Juengerman and C. B. Collins *Appl. Phys. Lett.* **53** 187 (1988).
- [27] A. A. Voevodin, S. J. P. Laube, S. D. Walck, J. S. Solomon, M. S. Donley and J. S. Zabinski, *J. Appl. Phys.* **78** 4123 (1995).
- [28] T. Sato, S. Furuno, S. Iguchi and M. Hanabusa, *Jpn. J. Appl. Phys.*, **26** L1487 (1987).
- [29] D. L. Pappas, K. L. Saenger, J. J. Cuomo, and R. W. Dreyfus, *J. Appl. Phys.* **72** 3966 (1992).
- [30] D. L. Pappas, K. L. Saenger, J. Bruley, W. Krakow, J. J. Cuomo, T. Gu and R. W. Collins, *J. Appl. Phys.* **71** 5675 (1992).
- [31] J. A. Martin, L. Vazquez, P. Bernard, F. Comin and F. Ferrer *Appl. Phys. Lett.* **57** 1742 (1990).
- [32] C. B. Collins and F. Davanloo in *Pulsed Laser Deposition of Thin Films*, D. B. Chrisey and G. K. Hubler (eds) (John Wiley & Sons, New York, 1994).
- [33] F. Davanloo, E. M. Juengerman, J. D. Jander, T. J. Lee and C. B. Collins, *J. Appl. Phys.*, **67** 2081 (1990).
- [34] G. Dollinger, C. M. Frey and P. Maier-Komor, *Nucl. Inst. Meth. A*, **334** 167 (1993).

- [35] G. Dollinger and P. Maier-Komor, *Nucl. Inst. Meth. A*, **303** 50 (1991).
- [36] R. K. Dwivedi and R. K. Thareja, *Phys. Rev. B*, **51** 7160 (1995).
- [37] R.K. Dwivedi and R. K. Thareja, *Sur. Coat. Tech.* **73** 170 (1995).
- [38] S. Fujimori, T. Kasai and T. Inamura, *Thin Solid Films*, **92** 71 (1982).
- [39] A.A. Voevodin and M.S. Donley, *Surf. Coat. Technol.*, **82** 199 (1996)
- [40] E. R. Bernstein, *Atomic and Molecular Clusters* (Amsterdam: Elsevier 1990).
- [41] E. A. Rohlfing, D. M. Cox and A. Kaldor *J. Chem. Phys.* **81** 3322 (1984).
- [42] P. P. Radi, T. L. Bunn, P. R. Kemper, M. E. Molchan and M. T. Bowers *J. Chem. Phys.* **88** 2809 (1988).
- [43] H. W. Kroto and K. G. Mikay, *Nature* **331** 328 (1988).
- [44] W. Kratschmer, L. D. Lamb, K. Fostiropoulos and D.R.Huffmann, *Nature* **347** 354 (1990).
- [45] P.S.R.Prasad, Abhilasha and R.K.Thareja, *Phys.Stat.Sol.* **139** K1 (1993).
- [46] S. W. McElvany, M. M. Ross and J. H. Callahan, *Acc. Chem. Res.* **25** 162 (1992).
- [47] W. R. Creasy and J. T. Brenna, *J. Chem. Phys.*, **92** 2269 (1990).
- [48] M. Busquet, *Phys. Fiu. B* **5** 4191 (1993).
- [49] R. K. Thareja, Abhilasha and R. K. Dwivedi, *Laser and Particle Beams*, **13** 481 (1995).
- [50] Abhilasha and R. K. Thareja, *Appl. Phys. B* **61** 67 (1995).
- [51] Abhilasha and R. K. Thareja, *Phys. Letts. A* **184** 99 (1993).
- [52] Abhilasha, R. K. Dwivedi, R. K. Thareja, *J. Appl. Phys.* **75** 8237 (1994).
- [53] X.Chen, J.Mazumcker and A.Purohit, *Appl. Phys. A* **52** 328 (1991)
- [54] X.Chen and J.Mazumcker *Appl. Phys. Letts.* **57** 2178 (1990)

- [55] S. S. Harilal, R. C. Issac, C. V. Bindhu, V. P. N. Nampoori and C. P. G. Vallabhan, *Pramana - J. Phys.* **46** 145 (1996).
- [56] S. S. Harilal, R. C. Issac, C. V. Bindhu, V. P. N. Nampoori and C. P. G. Vallabhan, *Jpn. J. Appl. Phys.* **36** 134 (1997).
- [57] S. S. Harilal, R. C. Issac, C. V. Bindhu, V. P. N. Nampoori and C. P. G. Vallabhan, *J. Appl. Phys.* **80** 3561 (1996).
- [58] S. S. Harilal, R. C. Issac, C. V. Bindhu, V. P. N. Nampoori and C. P. G. Vallabhan, *J. Appl. Phys.* **81** (in press) (1997).
- [59] G. Korn and J. T. C. Yeh, *J. Appl. Phys.*, **56** 2120 (1984)
- [60] Y. Tasaka, M. Tanaka and S. Usami, *Jpn. J. Appl. Phys.* **34** 1673 (1995).
- [61] Y. Tasaka, M. Tanaka and S. Usami, *Appl. Sur. Sci.*, **79/80** 141 (1994).
- [62] D. H. Lowndes, D. B. Geohegan, A. A. Puretzky, D. P. Norton and C. M. Rouleau, *Science* **273** 898 (1996).
- [63] C. Germain, C. Girault, J. Aubreton and A. Catherinot, *Appl. Sur. Sci.*, **69** 359 (1993).
- [64] Abhilasha, P. S. R. Prasad, R. K. Thareja, *Phy Rev E* **48** 2929 (1993).
- [65] Iida and E. S. Yeung *Appl. Spect.* **48** 945 (1994).
- [66] M. Jeunehomme and R. P. Schwenker, *J. Chem. Phys.*, **42** 2406 (1965).
- [67] C. E. Little and P. G. Browne *Chem. Phys. Letts.* **134** 560 (1987).
- [68] G. Herzberg, *Spectra of Diatomic Molecules (Molecular Spectra and Molecular Structure)* (New York: Van Nostrand 1950).
- [69] M. A. MacDonald, S. J. David and R. D. Coombe *J. Chem. Phys.* **84** 5513 (1986).
- [70] R. L. Stephen, W. B. Charles and P. R. Alistair, *J. Chem. Phys.* **92** 300 (1990).
- [71] S. S. Harilal, R. C. Issac, C. V. Bindhu, V. P. N. Nampoori and C. P. G. Vallabhan, *Spectrochimica Acta A*, (in press) (1997).

- [72] G. Padmaja, A. V. R. Kumar, P. Radhakrishnan, V. P. N. Nampoori and C. P. G. Vallabhan, *J. Phys. D*, **26** 35 (1993).
- [73] C. L. Marquardt, R. T. Williams and D. J. Nagel *Mater. Res. Soc. Symp. Proc.* **38** 325 (1985).
- [74] D. T. Peeler and P. T. Murray in *Laser ablation : Mechanism and applications II* (American Institute of Physics, New York 1993).
- [75] D. B. Geohegan in *Pulsed laser deposition*, D. B. Chrisey and G. K. Hubler (eds) (John Wiley & Sons, Inc., New York, 1994).
- [76] G. R. Griem, *Plasma Spectroscopy* (McGraw-Hill Book Company, New York, 1964).
- [77] See Chapter 5.
- [78] Y. Iida *Spectrochim. Acta* **45B** 1353 (1990).
- [79] G. Bekfi, *Principles of Laser Plasmas* (John Wiley & Sons, New York, 1976).
- [80] G. V. Marr, *Plasma Spectroscopy* (Elsevier Publishing Company, Amsterdam, 1968).
- [81] G. Herzberg, *Atomic Spectra and Atomic Structures* (Prentice Hall, New York, 1937).
- [82] M. R. Joseph, Ning Xu and V. Majidi, *Spectrochim. Acta* **49B** 89 (1994).
- [83] R. W. Dreyfus, R. Kelly and R. E. Walkup *Nucl. Instru. and Meth. B* **23** 557 (1987).
- [84] R. Kelly A. and Miotello in *Pulsed laser deposition of thin films* D. B. Chrisey and G. K. Hubler (eds.) (New York : John Wiley and Sons, 1994).

Chapter 4

Temporal and Spatial Evolution of Laser Induced Plasma from Graphite Target

The emission features of laser ablated graphite plume generated in a helium ambient atmosphere have been investigated with time and space resolved plasma diagnostic technique. Time resolved optical emission spectroscopy is employed to reveal the velocity distribution of different species ejected during ablation. At low laser irradiance levels only a slowly propagating component of C_2 is seen. At high irradiance levels emission from C_2 shows a twin peak distribution in time. The formation of an emission peak with diminished time delay giving a more energetic peak indicating higher velocity component at enhanced laser irradiance levels is attributed to many body recombination. It is also observed that these double peaks get modified into triple peaks for the time of flight distribution at distances greater than 16 mm from the target. The occurrence of multiple peaks in the C_2 emission is mainly due to the delays caused from the different formation mechanism of C_2 species. The velocity distribution of the faster peak exhibits an oscillating character with distance from the target surface.

4.1 Introduction

As indicated in chapter 3, pulsed laser ablation of graphite has become well established as a reliable method for preparation of newly found materials like fullerenes [1-4], carbon clusters and diamond-like carbon (DLC) films [5-12]. However, the underlying physics and chemistry of the processes such as carbon cluster formation or their dissociation are less than well understood. Further, the details of the dynamics of laser interaction with materials are extremely important in the context of optimizing the conditions for depositing good quality thin films. The preparation of DLC film was first reported in 1985 by Nagel and co-workers [13] who determined a critical threshold density of 50 GW cm^{-2} on the carbon feed stock, above which DLC was condensed from the carbon plasma and below which only soft graphitic layers were deposited. A good understanding of the physics involved in the interaction of laser light with solid targets at these intensities was achieved through theoretical [14] and experimental [15] studies as early as two decades ago. However, only few authors have considered the subsequent expansion of the laser produced plasma over several millimeters on the length scale. A characteristic feature of such adiabatic expanding plasma is the persistence of ions in high charge states in the cold region. Stevefelt and Collins [16] reported a modeling of the free expansion of a carbon plasma produced at moderate intensities, which includes the dominant constituent mechanisms of electron-ion recombination through both three body collisional and radiative processes.

Comparatively, the pulsed laser deposition (PLD) technique is used mainly for producing multicomponent oxides and other dielectric oxides and superconducting materials [17]. It has received less attention in DLC production, partially owing to the high initial cost of high power lasers and related equipment, and mainly owing to the success of other DLC deposition techniques, e.g. ion-beam and magnetron sputtering. However, the decreasing cost of powerful lasers and success in the development of PLD technology for large-area deposition [18], which is currently 100-150 mm in diameter [19], provide the basis for introducing PLD into general engineering fields. One very promising application of PLD is to produce DLC coatings for reducing friction and wear [20] and the capability to produce both hydrogen-free and hydrogenated DLC films allow good control over the mechanical properties important for tribology applications [21]. A comparison of selected properties of DLC films produced by various techniques is presented

in the review article by Voevodin and Donley [22].

Based on the widely accepted theory of the pulsed laser evaporation [23, 24], the physical model of the laser ablation can be explained as follows. In the initial stage the interaction of the laser beam with the bulk target results in the evaporation of the surface layer. Following this, the interaction of the laser beam with evaporating material leads to the formation of isothermally expanding plasma and this persists until the termination of the laser pulse. In the final stage, adiabatic expansion of the plasma in the forward direction takes place when the target is irradiated under vacuum. Several spectroscopic studies of graphite plasma have been carried out using a variety of laser wavelengths such as 193, 248, 308, 532 and 1064 nm [25]. It has been shown that shorter wavelengths are more effective for penetration into the sample, mainly because of large ablation rates possible at these wavelengths [26]. However, the main advantage in the use of NIR low energy photons is that, they are less likely to invoke photochemistry into the ablation phenomenon.

High quality DLC films are obtained at low laser irradiances where the molecular C_2 emission is most dominant [27]. The relative population of the carbon clusters produced in the laser ablation of graphite has been found to depend on different experimental parameters like laser irradiance, nature of background gas and its pressure, relative position of the plasma volume with respect to target surface etc.. The composition and energetic characteristics of the laser-produced carbon plumes depend also on which form of carbon is used as the target material. Plume characteristics in the laser ablation of pressed diamond powder [28], amorphous and glassy carbon [29] or polymer carbon [30] may differ from that of graphite. However, high-purity graphite targets are most commonly used in PLD of DLC films.

In pulsed laser deposition as the amount of ablated material increases, gas dynamic effects are thought to play a leading role in determining the spatial and velocity distribution of the vapourized material. Collisions between the ejectants during the initial expansion are theorized to cause a Knudsen layer (KL) or unstable adiabatic expansion (UAE) zone which results in stopped or backward moving material closed to the target and strongly forward peaked velocity distributions away from the target surface [31-33].

Optical emission spectroscopic technique is concerned with the light emitted by electronically excited species in laser induced plasma produced in front of the target surface. Also optical emission measurements are useful for species identification and in-situ mon-

itoring during deposition. Useful information about the elemental composition of the target material can be obtained from the analysis of the emissions emanating from the plasma plume. Laser ablation has the unique advantage that most of these species are formed in their excited states and hence spectroscopic measurements offer an excellent means to investigate their evolution and dynamics. The carbon clusters like C_{60} and higher fullerenes are well known to be formed as a product of the laser ablation of graphite in an ambient helium atmosphere. Although considerable progress has been achieved in studies involving ablation of large carbon clusters $C_n (n \geq 10)$, including fullerenes from laser irradiated carbon targets, relatively little effort has been expended to study the production and characterization of C_n clusters with $n \leq 10$.

In this chapter, a comprehensive study of spatial characteristic emission from C_2 using time resolved spectroscopy is presented. In these experiments time resolved spectroscopic observations of the plasma plume from graphite under helium ambient atmosphere were carried out to determine the velocities of the different ablated species inside the plasma. Such temporally and spatially resolved high resolution spectroscopic studies are helpful to optimize parameters of DLC film deposition and to correlate the carbon clusters with plasma dynamics. To the best of our knowledge this is the first report regarding the existence of triple peak in the temporal evolution of C_2 emission from laser produced carbon plasma. Our results also indicate that the temporal profile of C_2 species produced during laser ablation of graphite exhibits a triple peak structure only beyond a certain spatial separation from the target (16 mm) and thereafter these propagate with three different expansion velocities.

4.2 Experimental Setup

The experimental setup used for the present study is similar to the one described in chapter 2. Briefly, the $1.06 \mu m$ laser beam from a Q-switched Nd:YAG laser with repetition rate 10 Hz was focused onto a graphite target contained in a vacuum chamber. The graphite target was rotated by a small electric motor so that the laser pulses are made to fall at a new spot every time on the graphite surface. The emission from the carbon plasma was focused at right angles to its expansion direction to produce a 1:1 image on the entrance slit of a monochromator (Jarrel Ash 0.5 m) coupled to a photomultiplier tube. Using a number of apertures and slits emission features from various

vertical segments of the plasma plume can be studied. The characteristic emission lines were selected using the monochromator and the output from the PMT was monitored using a digital storage oscilloscope with a maximum sampling rate of 200 MHz with 50 Ω termination to record the emission pulse shapes. In these experiments spatially resolved studies were carried out for distances up to 25 mm normal to the target surface with an accuracy better than 0.2 mm.

4.3 Results and Discussion

The time resolved studies of emission lines from various species are carried out from the oscilloscope traces which show definite time delays for emission with respect to the incidence of the laser pulse. The time of flight (TOF) measurements provide excellent technique to determine the velocity distribution of the plasma. Our observations show that the emission lines from different emitting species within the plasma possess distinctly different temporal profiles. Each temporal profile represents a complex convolution of different factors that govern the temporal history of the emitting species *viz.* its production mechanism and rate, its flight past the viewing region and its radiative and collisional decay rates. Time resolved studies of various species are made at irradiance in the range of 10 GW cm⁻² to 95 GW cm⁻². Typical TOF distributions of C₂ species obtained by monitoring the spectral emission from C₂ in electronic excited state ($d^3\Pi_g$) [34, 35] (at $\lambda = 516.5$ nm corresponding to the (0, 0) transition $d^3\Pi_g \rightarrow a^3\Pi_u$ of C₂ Swan system) at distances 5 mm and 10 mm from the target for different laser irradiances are given in figs. 4.1a and 4.1b (helium pressure 0.05 mbar). The initial spike in the figure is due to scattering and/or prompt emission and can be used as a time marker. The interesting feature in TOF pattern of C₂ species is its double peak structure which becomes prominent beyond a threshold laser irradiance. Below this threshold laser irradiance only single peak distribution is observed. It is also noted that these double peak structure gets modified into a triple peak distribution at distances greater than 16 mm and these results are discussed in the preceding section. For simplicity, this section contains spatial studies up to 16 mm from the target. In what follows the first peak is designated as P1 and delayed peak P2. Such double peak structure has already been reported by a few of the earlier workers [36-38] even though no detailed analysis have been attempted.

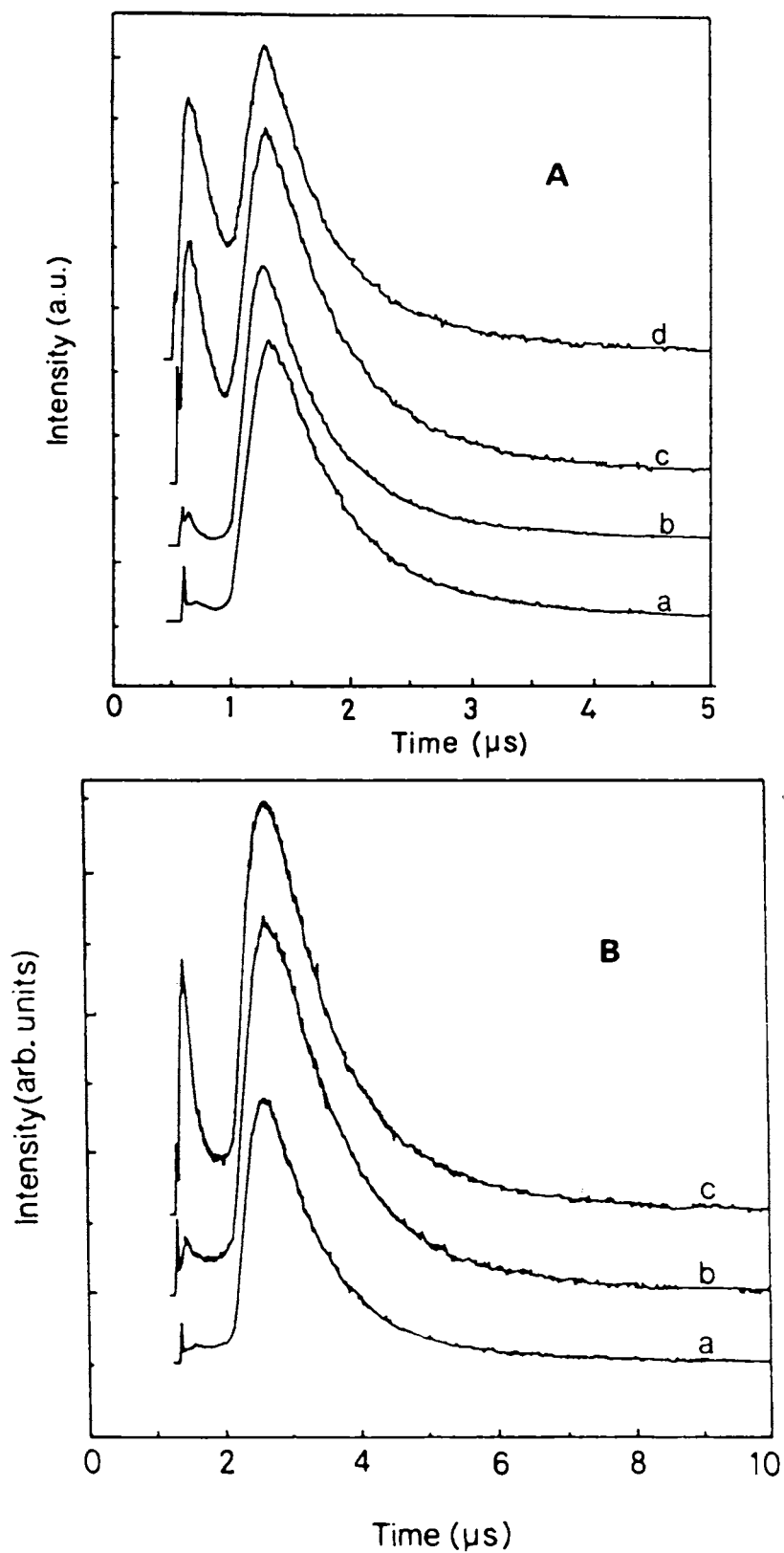


Figure 4.1: Intensity variation with time for 516.5 nm spectral emission from C₂ observed at different distances from the target surface (A) 5 mm, laser irradiance used (a) 35.4 GW cm⁻² (b) 74.3 GW cm⁻², (c) 77.8 GW cm⁻² and (d) 81.4 GW cm⁻² and (B) 10 mm, laser irradiance used (a) 74.2 GW cm⁻² (b) 76 GW cm⁻² and (c) 77.8 GW cm⁻².

4.3.1 Salient Features of the Double Peaks Observed in the Present Study

1. Appearance of P1 occurs only beyond a threshold laser irradiance about 74.2 GW cm^{-2} at 5 mm away from the target ($z = 5 \text{ mm}$) and this threshold value increases with increasing distance from the target. (for eg. at $z = 10 \text{ mm}$ the threshold irradiance is increased to 75.7 GW cm^{-2}).
2. The time delay for P1 with respect to the separation between the point of observation and the target surface varies in a nonlinear manner; the nonlinearity being more pronounced at lower laser irradiances. As is evident from fig.4.2, the delay of P1 is almost constant up to 10 mm separation which is paradoxical while the delay of P2 varies almost linearly (fig.4.3) with such separation. We do observe a pulsating nature in the time delays for P1 with distance greater than 16 mm.
3. The intensity for P1 is maximum at a point around $z = 12 \text{ mm}$ (fig.4.4) for all values of irradiances while that of P2 attains maximum around $z = 5 \text{ mm}$ (fig.4.5).
4. The delay of P1 increases with laser irradiance (fig.4.6) while that of P2 (fig.4.7), decreases sharply after being constant up to a certain value of irradiances.
5. The intensity of P1 increases from zero (at irradiances about 74.2 GW cm^{-2}) and saturates at higher irradiances ($> 84.8 \text{ GW cm}^{-2}$) (fig.4.8) while that of P2 increases up to an optimum laser irradiance and begins to decrease thereafter (fig.4.9). This behaviour is predominant at points having smaller separation from the target.
6. It is noted that the delay time for the P1 decreases with increasing ambient helium pressure, whereas the delay time corresponding to P2 has been found to increase with respect to helium pressure. Also the first peak gets narrowed while the second peak becomes broadened as the helium pressure is increased.
7. Intensity for the P1 increases steadily with increasing helium pressure and a sudden enhancement is observed at higher helium pressures, while for P2, it is being constant up to a particular helium gas pressure and an enhancement in intensity is observed at high pressures.

The above observations indicate that the plasma apparently develops fast and slow components above a threshold laser irradiance. There are only a few reports available in the literature which describe twin peak TOF distribution in laser generated plasma from graphite target. Abhilasha *et al* [39] reported a peculiar double peak structure in the temporal profile of C II species at 426.8 nm in a laser produced carbon plasma at various

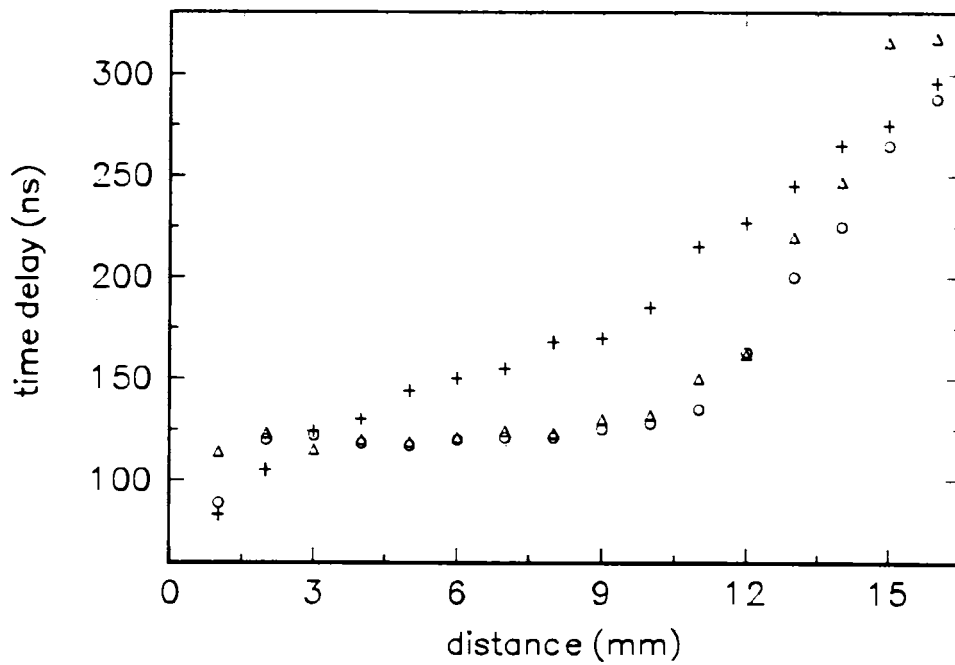


Figure 4.2: Variation of time delays with distance of P1 for different laser irradiances (o) 81.34 GW cm^{-2} , (Δ) 88.42 GW cm^{-2} and (+) 95.5 GW cm^{-2}

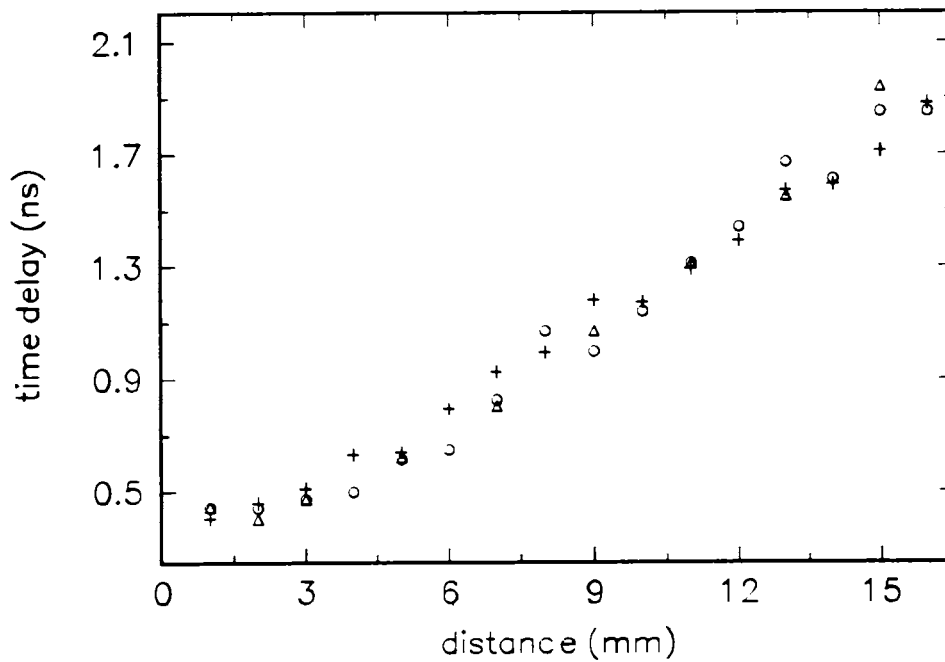


Figure 4.3: Variation of time delays with distance of P2 for different laser irradiances (o) 81.34 GW cm^{-2} , (Δ) 88.42 GW cm^{-2} and (+) 95.5 GW cm^{-2}

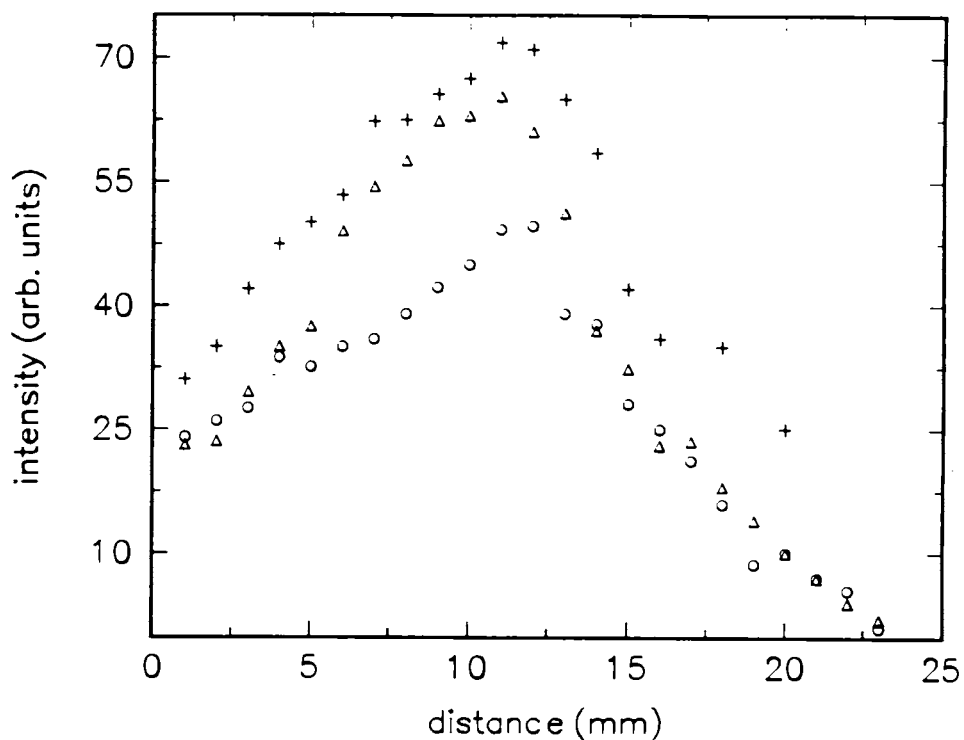


Figure 4.4: Change in intensity with distance for different laser irradiances for the peak P1 (○) 81.34 GW cm⁻², (Δ) 88.42 GW cm⁻² and (+) 95.5 GW cm⁻²

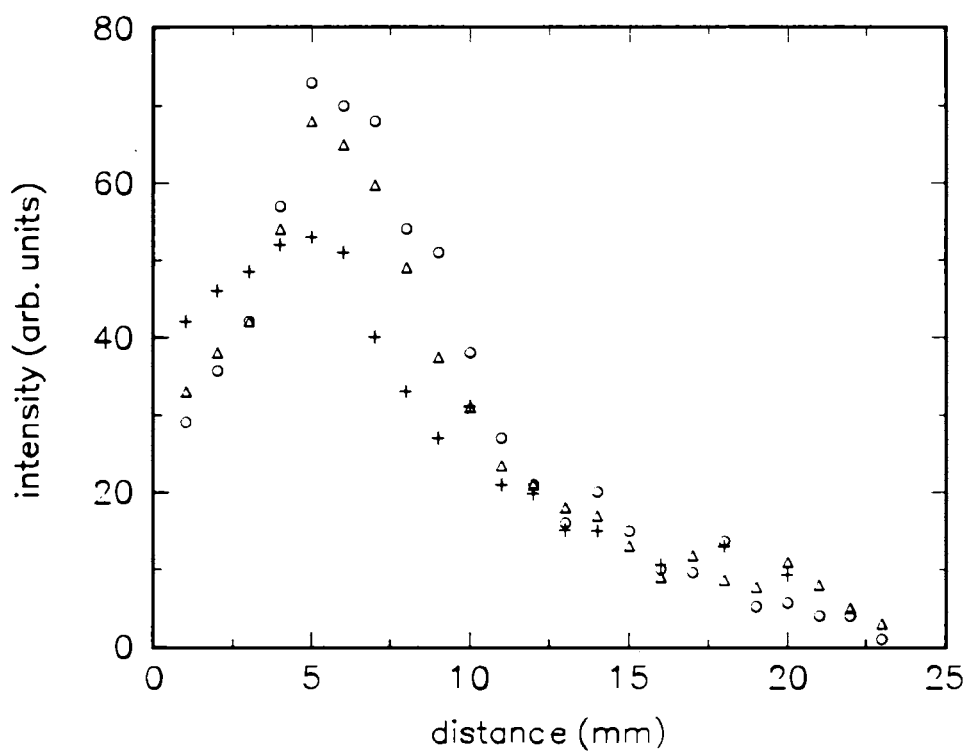


Figure 4.5: Change in intensity with distance for different laser irradiances for the peak P2 (○) 81.34 GW cm⁻², (Δ) 88.42 GW cm⁻² and (+) 95.5 GW cm⁻²

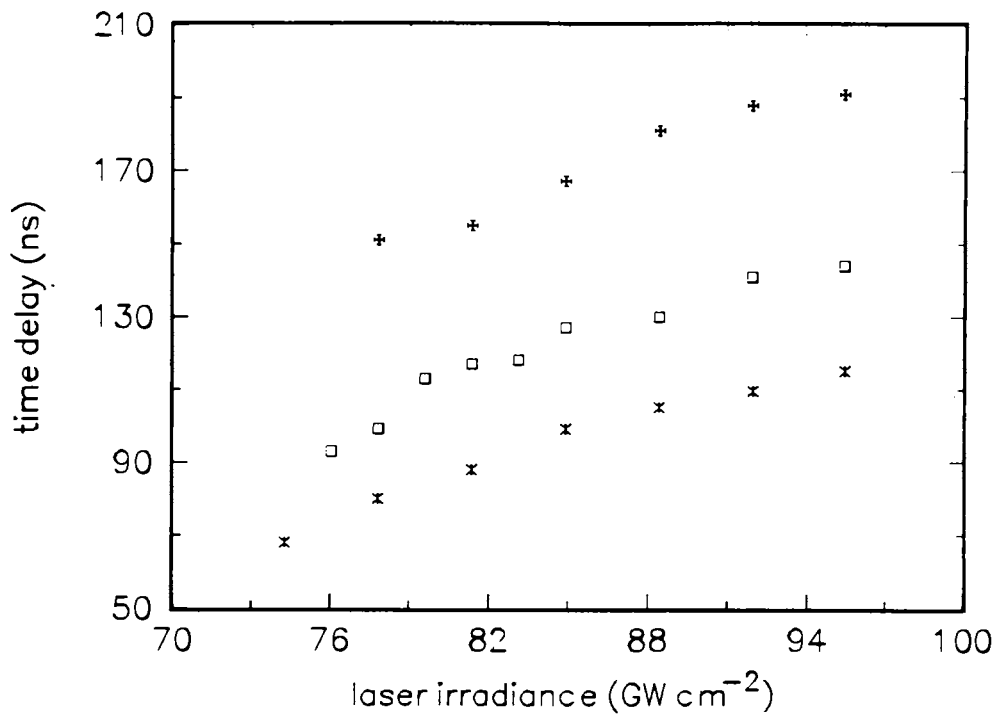


Figure 4.6: Plot of time delays on laser irradiance of P1 for different distances (x) 5 mm, (□) 10 mm and (+) 15 mm

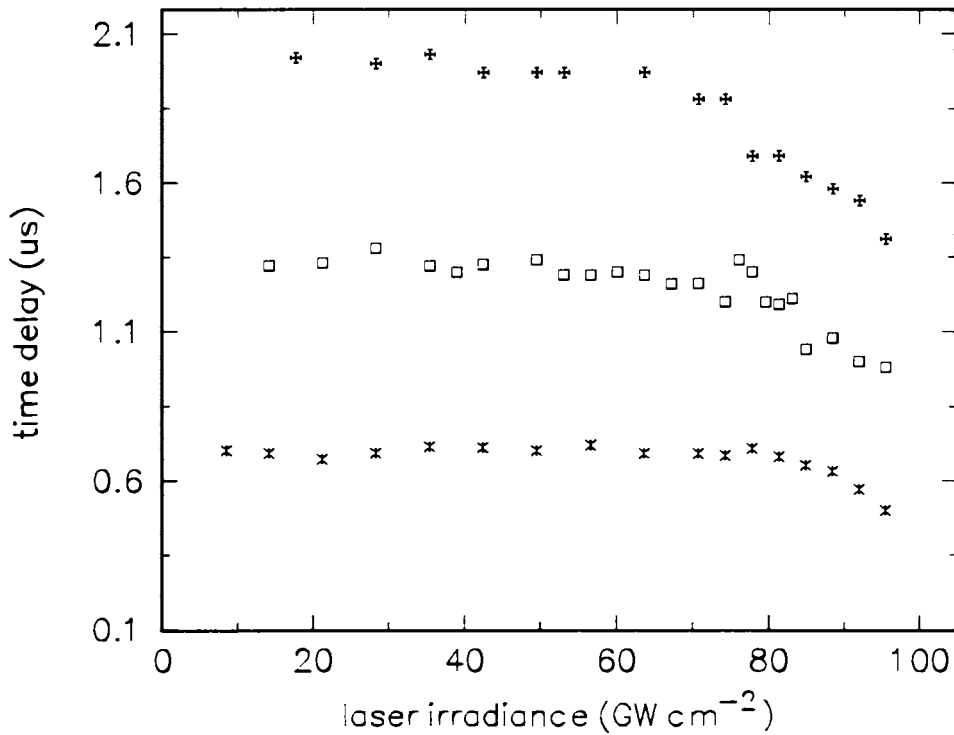


Figure 4.7: Plot of time delays on laser irradiance of P2 for different distances (x) 5 mm (□) 10 mm and (+) 15 mm

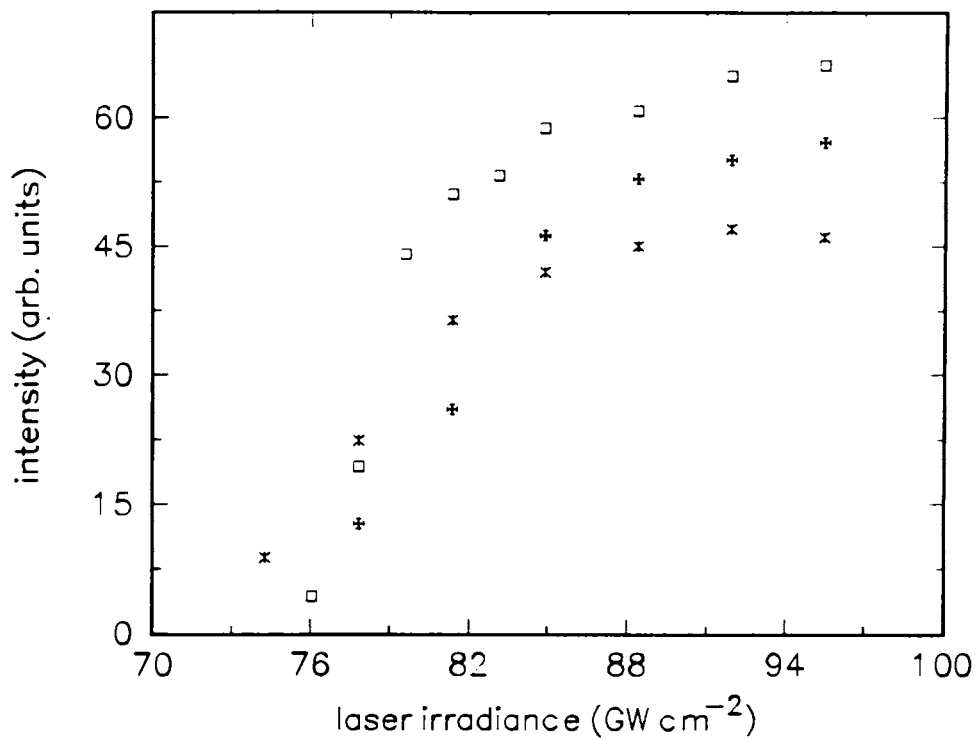


Figure 4.8: Variation of intensity of P1 with laser irradiance for (x) 5 mm, (□) 10 mm and (+) 15 mm.

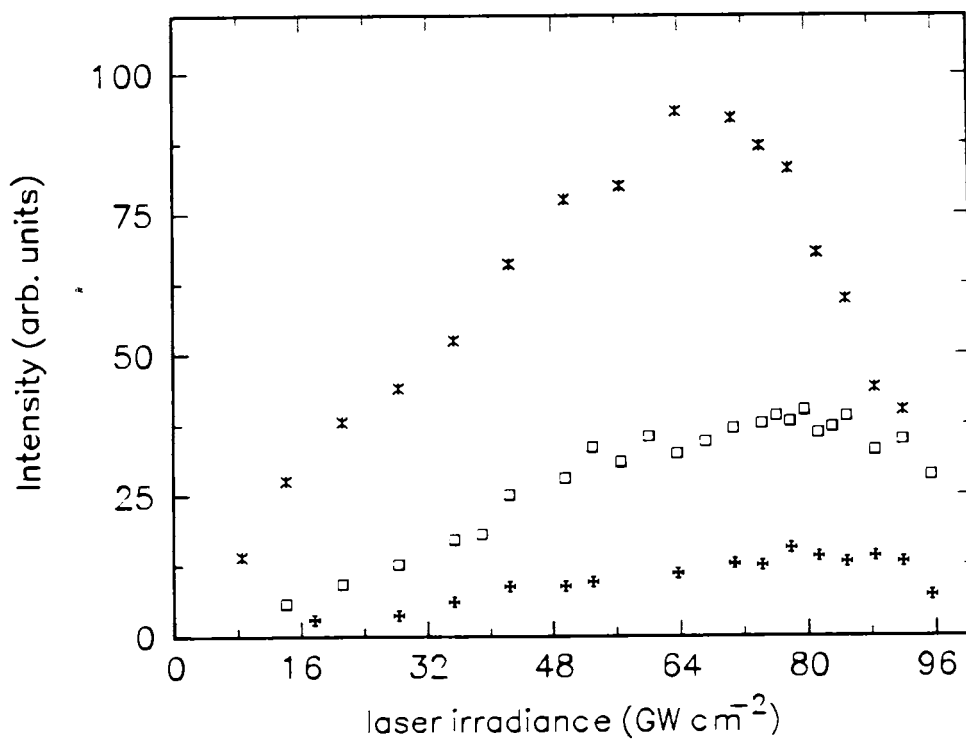


Figure 4.9: Variation of intensity of P2 with laser irradiance for (x) 5 mm, (□) 10 mm and (+) 15 mm.

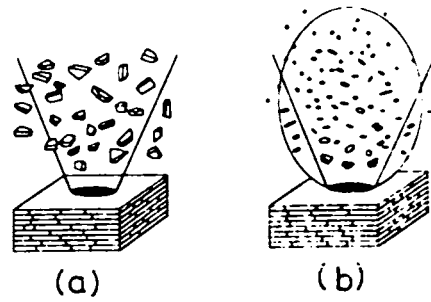


Figure 4.10: Schematic representation of laser ablation of graphite target (a) at low irradiance levels (b) at high irradiance levels

air pressures and they proposed that, this may be due to stratification of the plasma into fast and slow ion components at the interface where the occurrence of Rayleigh - Taylor instability causes deceleration of the plasma front by ambient gas (In fact we also observed the same double peak structure in the time profile of C II species at 426.8 nm). Dixon and Seely [37,38] also observed a double peak structure in C II species and they explain it as due to collisional interaction like resonance charge transfer which has been shown to be a velocity dependent one. In fact the existence of twin peak structure for the C_2 species from the laser induced plasma observed previously has been explained as due to emission from the 'shell' (fast) and the 'core' (slow) components [36]. Attributing peaks P1 and P2 solely to fast and slow components will not explain the unusual spatial dependence of time delays as depicted in figures 4.2 and 4.3 respectively. We have also observed a twin peak structure for Y I and YO emission in the laser produced plasma from $YBa_2Cu_3O_7$ and the twin peaks were assigned as due to species corresponding to those generated directly/in the vicinity of the target surface and to those generated from collisional and recombination processes [40].

4.3.2 Formation Mechanisms

The schematic diagram of the laser ablation of graphite target at low and high irradiance levels is shown in fig. 4.10. This figure also exhibits the effect of laser irradiance on the size of the ablated particles. Two mechanisms could exist for the particle formation, *viz.*, dissociative and recombinational. Harano et al [41] have suggested the strip-off mechanism for the formation of carbon clusters by considering the balance between the total mass of the carbon particles and the laser irradiance used for the ablation. Most

of the models of fullerene formation are based on the recombination mechanism, i.e, the formation by nucleation from carbon vapour consisting of carbon atoms and very small carbon molecules [42]. It is well known that graphite exhibits a large difference between the inter-layer and the intra-layer bond strengths. It is expected that at low laser irradiance levels, graphite will be ablated layer by layer producing large particles which in turn get dissociated to form C_2 species [43]. The dissociative mechanism can further be supported by the observation of long duration of Swan band emission at low irradiances. At low laser irradiance levels only a slowly propagating component with low kinetic energy is observed. The larger masses of C_n will result in longer delays which are observed in the C_2 emission (P2) occurring at the lower laser irradiances. Above a distance $\simeq 6$ mm from the target, the plasma is colder compared with the same in core region and collisional effects become insufficient to cause dissociation of C_n . The dominant mechanism for the production of C_2 Swan band emission at low irradiances is the electron collision with C_n cations and neutrals ($n > 2$) followed by dissociation where one of the fragments is an ejected C_2 molecule [43]. As the laser irradiance is increased, clusters with lower values of n will be ejected directly from the target. Above a threshold laser irradiance, temperature of the plasma becomes so large so as to dissociate C_n to neutral and ionized carbon atoms just outside the target. At higher irradiance levels Swan band formation is mainly due to electron-ion and ion-ion recombination. It is observed here that at high laser irradiances, after a threshold, an emission peak showing a faster component with higher kinetic energy for C_2 molecules begins to appear.

Spectral analyses show that at low irradiance levels, the emission spectrum is dominated by C_2 molecules whereas at higher irradiance levels the plasma emission is mainly due to ionic species of carbon up to C IV along with C_2 species. It is also observed that the ions have higher velocity as compared to neutrals and molecules because of the Coulomb fields which are generated by negatively charged electrons escaping from the plume. It is in fact observed that the emission intensity of the ionized species does increase drastically above this threshold laser irradiance. Once ions and electrons are produced, one can have neutral carbon atoms by three body collision processes like



Collisional ionization is also possible through processes like



In the vicinity of the target, (4.2) may be predominant over (4.1) so that we get excited state C_2 formation slightly away from the target, giving emission peak P1. The threshold like phenomenon in the case of P1 also shows the initiation of production of ionized species so as to open the channels (4.1) and (4.2) at higher laser irradiances. As the laser intensity is increased beyond 74.2 GW cm^{-2} , the probability of cluster formation of the type C_n ($n > 2$) in the plasma diminishes, thereby causing a drastic decrease in the intensity of P2. Moreover, as the laser irradiance is increased, the trailing edge of the laser pulse will enhance the dissociation of C_n by multiphoton absorption through laser plasma interaction. This could cause the formation of C_2 nearer the target surface. Koren and Yeh [37] also have observed such double peaks in the case of C_2 from polyimide target and their interpretation in terms of the fast and slow components does not completely explain our observations. We are therefore compelled to attribute the double peak formation due to the delays inherent in the distinctly different formation mechanisms of C_2 in the plasma.

Figs. 4.6 and 4.7 give respectively the variation in time delay for P1 and P2 with laser irradiance for different distances from the target. From fig. 4.6, we see that the time delay for P1 increases with respect to increase in laser irradiance which is against the normal observation where velocity usually increases with the intensity of the incident laser pulse. By considering the velocity distribution, this anomaly can be explained only if one can have some type of a "negative diffusion" or anomalous diffusion of C_2 towards the target. Similar observations by one of the previous workers have been explained as due to selective depletion of high velocity C_2 species [44]. However, one can have slightly different scenario as explained below. As the laser irradiance increases, the electron, atom and ion number densities of the plasma and plasma temperature are also increased. This may cause larger probability for events (4.1) and (4.2) indicated in the previous paragraph. It is also believed that ions are accelerated by Coulomb fields generated by fast moving electrons escaping from the plume. One should also consider the multiphoton dissociation of C_n by the trailing edge of the laser pulse so as to produce C_2 nearer to the target surface. Due to these processes C_2 may thus be formed at points nearer to the target surface by recombination processes, but with more than usual delay in the appearance of P1. In other words, decrease in delay with laser irradiance compete

with the increase in delay due to shift of "formation site" of C_2 nearer to the target surface. Therefore, as far as P1 is concerned, delay due to the location of formation site is more predominant in the range of laser irradiances considered here thereby causing the observed enhancement in the delay on increasing the laser irradiance. This is further born out by the fact that there is a perceptible increase in the half width of peak P1 as the intensity of the laser pulse is increased.

Similar arguments can be made in the case of the measured time delays corresponding to P2. Contrary to the case of P1, delay of P2 remains almost constant up to a threshold laser irradiance and thereafter it decreases. As noted earlier P2 is found to be formed due to dissociation of carbon clusters C_n ($n > 2$). As the laser irradiance is increased the formation of C_2 through dissociation of C_n will occur nearer to the target surface, thereby causing an increase in the delay as opposed to its decrease due to enhancement of kinetic energy of the species with laser irradiance. Up to a threshold laser irradiance, these two time delays are more or less balanced to give an effectively constant time delay as observed in fig. 4.7. Above this threshold irradiance, enhancement in kinetic energy becomes so large that there will be a notable decrease in time delay for P2.

The nature of variation of delay with distance also exhibit certain peculiarities in terms of the behaviour of peaks P1 and P2 (figs. 4.2 and 4.3). Beyond a distance of 8 mm there is a sudden enhancement in delay for P1 especially at comparatively lower levels of irradiances but well above the threshold. The unusual spatial dependence of time delay is observed only for P1 and the variation differs widely as the laser irradiance is changed. However for P2 the nearly linear spatial dependence of the delay is observed. The intensity variation for the peaks P1 and P2 with respect to distance is shown in figs. 4.4 and 4.5. The spatial maximum (the distance at which the intensity of the peak is maximum) of P1 is at about 12 mm while that for P2 is at 6 mm. It is also clear from fig. 4.9 that the intensity of P2 decreases after the threshold laser irradiance whereas intensity of P1 increases from zero (at 74.2 GW cm^{-2} for $z = 5 \text{ mm}$) and saturates at higher irradiance levels (fig. 4.8). It indicates a decrease in the population of C_n ($n > 2$) when irradiance is increased (fig. 4.9). The saturation effect of plasma emission can be explained as due to the absorption of the trailing part of the laser radiation by the plasma. This absorption will be more pronounced at higher plasma densities so that effective laser power reaching the target will be reduced. Such "shielding effect" of target from the laser radiation will result in the observed saturation effect.

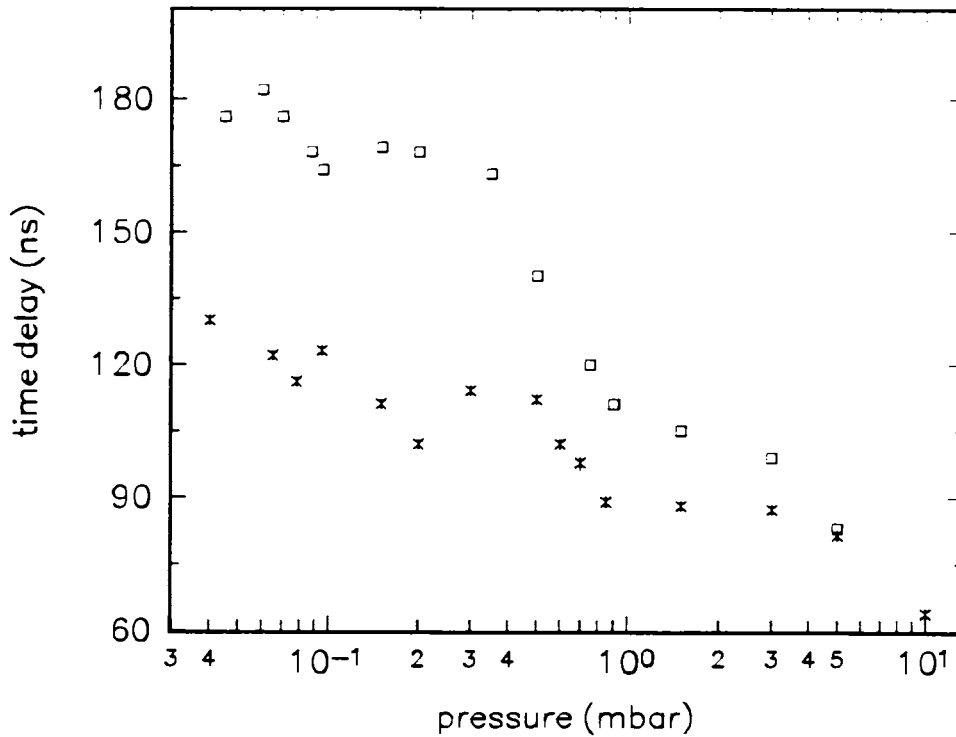


Figure 4.11: Dependence of time delays of first peak on ambient helium pressure (\times) 5 mm and (\square) 8 mm (laser irradiance 81.34 GW cm^{-2})

4.3.3 Effect of Helium gas

In order to understand the mechanism more clearly, experiments were carried out by varying the helium gas pressure in the plasma chamber. Variation of time delay for the peaks P1 and P2 with respect to helium ambient gas pressure is shown in figs. 4.11 & 4.12 respectively. It is interesting to note that the delay for the first peak decreases and for the second peak it is increased with increasing helium pressure. The presence of helium gas helps cooling of plasma so as to reduce the plasma temperature. It is also supported by the fact that the increase of helium pressure decreases vibrational temperature of C_2 species [45]. The enhancement of delay time with the increase in gas pressure for P2 in the temporal profile is, therefore, due to the reduction in the velocity of C_2 species. However, the time delay dependence on helium pressure corresponding to P1 cannot be explained easily as in the case of P2. Decrease in time delay of P1 with increase in pressure can be understood, at least qualitatively, as follows. Presence of helium gas reduces the plasma temperature [46] so that the formation of bulk of C_2 through recombination process shifts towards the target surface. This reduction in time

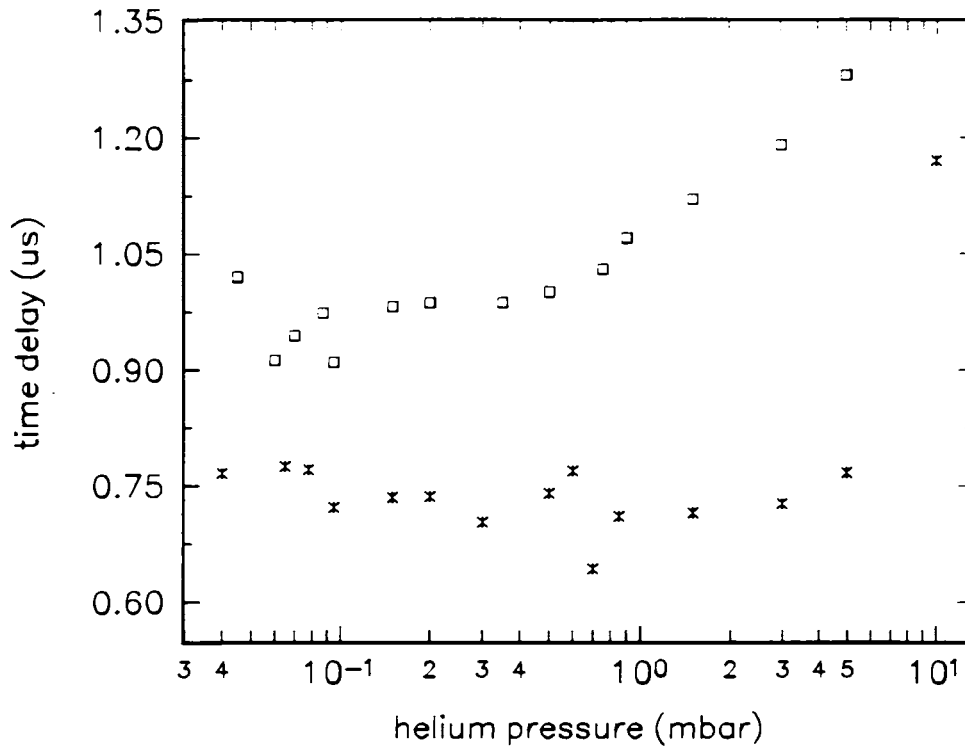


Figure 4.12: Dependence of time delays of second peak on ambient helium pressure (x) 5 mm and (□) 8 mm (laser irradiance 81.34 GW cm^{-2})

delay due to shift in formation site will exceed the enhancement in time delay due to reduction in velocity of C_2 species. This is in conformity with the observation of increase in delay with laser irradiance.

Figs. 4.13 and 4.14 give the intensity variation for the P1 and P2 respectively with helium gas pressure. From fig. 4.13, it is clear that the intensity of the P1 increases steadily with increase in helium pressure. But in the case of P2, the intensities are almost constant up to a pressure of 1.3 mbar, then it enhances. The helium serves to cool the hot electrons by collisions leading to a more efficient electron impact excitation and plasma recombination, leading also to the plasma confinement near to the target which enhances the emission from these species. Fig. 4.15 gives the temporal profile of C_2 species for different helium ambient pressures, from which it is clear that with increasing pressure P1 becomes more and more narrow with decreasing time delay, while P2 broadens with increasing time delay. The increase in helium pressure improves the spatial confinement of the plasma which in turn increases the collisions. The kinetic energy distributions are more sensitive to collisions because elastic scattering cross-sections are usually considerably larger than the cross-sections for rotational or vibrational energy transfer [47].

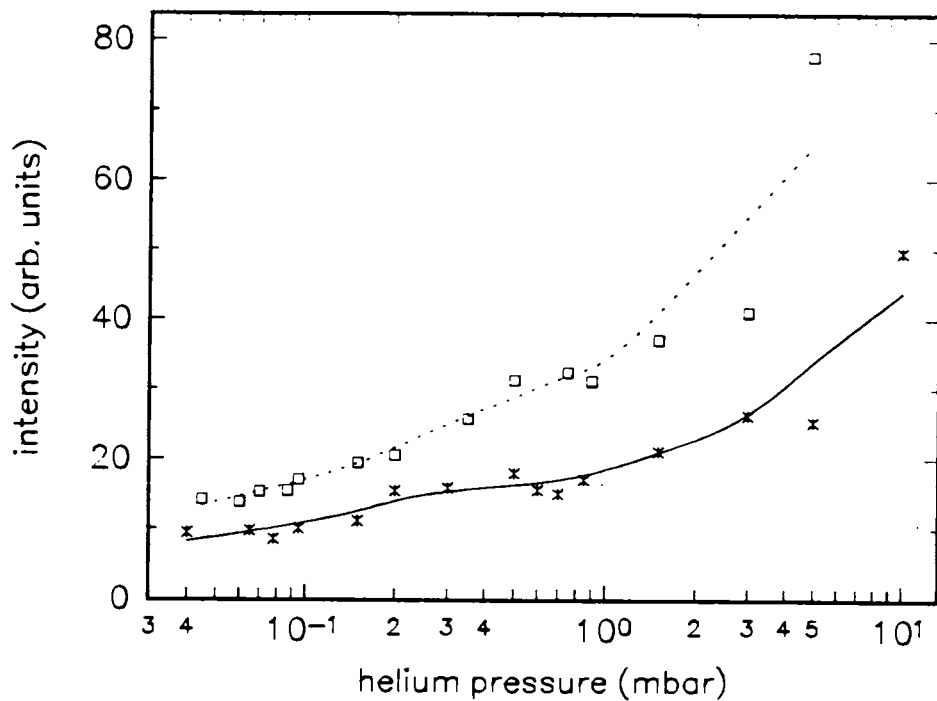


Figure 4.13: Change in intensity of P1 with ambient helium gas pressure (x) 5 mm and (□) 8 mm (laser irradiance 81.34 GW cm^{-2})

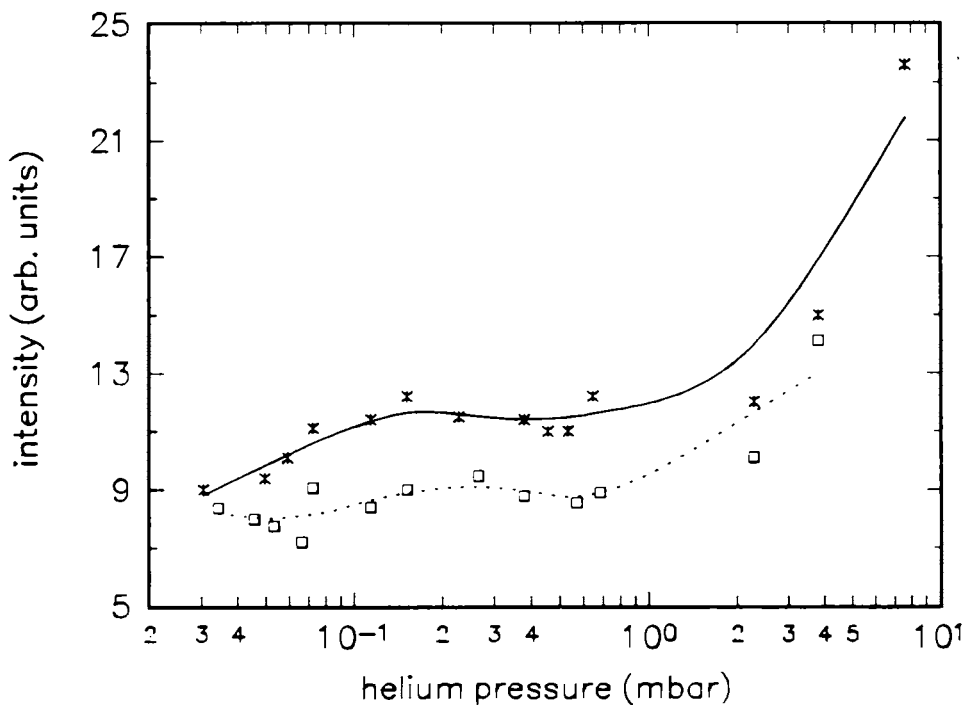


Figure 4.14: Change in intensity of P2 with ambient helium gas pressure (x) 5 mm and (□) 8 mm (laser irradiance 81.34 GW cm^{-2})

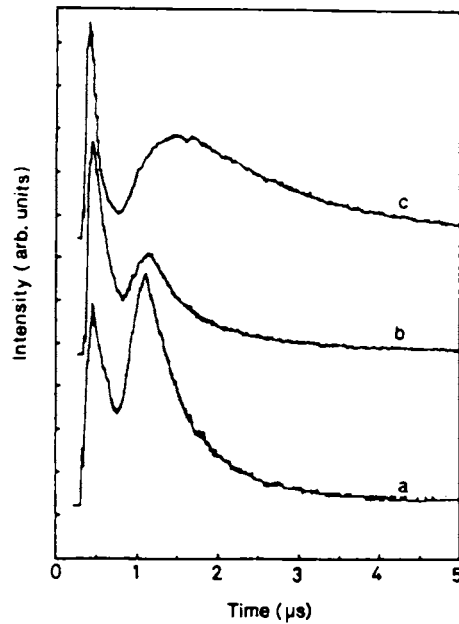


Figure 4.15: Intensity variation of spectral emission with time for C_2 observed at 8 mm away from the target at different ambient helium pressures (laser irradiance 81.34 GW cm^{-2}) (a) 0.065 mbar, (b) 1 mbar and (c) 10 mbar

Collisions make kinetic energy distributions more narrow, but with large peak velocity. In addition collisions can cool the rotational and vibrational energies of the molecules in the expansion. With sufficient number of collisions the energy initially stored in the rotational and vibrational degrees of freedom can be converted into direct translational energy of the species [48]. The broadening of P2 especially at high pressures is because of high cooling by the helium gas which improves the clustering of molecular species.

4.3.4 Plume Dynamics

The presence of helium gas during the ablation process has dramatic consequences on the expansion dynamics. The present results show that laser irradiance and pressure of the ambient helium gas have opposite effects on the plasma expansion processes. As irradiance increases, time delay for P1 increases while time delay for P2 is more or less constant up to a threshold irradiance and then decreases. Similarly increase in helium gas pressure decreases the time delay for P1 and in the case of P2, time delay is being constant up to a particular pressure and then increases. This can be explained by assuming a simple adiabatic model.

The plume length L can be estimated if it is assumed that at the end of the laser pulse the ablation products occupy a volume V_i at high pressure and subsequently expand adiabatically. Assuming adiabatic expansion model [49-51], the ablated material pushes the gas species until the plasma and gas pressures equilibrate. Then the length of the plasma is given by [49]

$$L = A[(\gamma - 1)E]^{1/3\gamma} P_0^{-1/3\gamma} V_i^{(\gamma-1)/3\gamma} \quad (4.3)$$

where A is the geometric factor related to the shape of the laser spot at the target surface, γ is the specific heat ratio (C_p/C_v), E is the laser energy density, P_0 is ambient gas pressure, V_i is the initial volume of the plasma ($V_i = v_0 \tau_{laser} w$, v_0 being the initial species velocity, τ_{laser} is the laser pulse duration and w , the laser spot size at the target surface). The factor A depends on the expansion geometry and for a conical plume with a spherical tip (inset of fig. 4.16) and expansion angle θ (for circular laser spot)

$$A = (1 + 1/\tan \theta) \left(\frac{3 \tan \theta}{\pi + 2\pi \tan \theta} \right)^{1/3} \quad (4.4)$$

From eqn.(4.3), it is clear that E/P_0 is the parameter controlling the length of the plasma if the experimental geometry remains constant; therefore, E and P_0 have opposite effects as experimentally observed in the present work. According to this model, the length of the plasma L is expected to increase as the laser energy density is increased or ambient gas pressure is decreased. Considering the experimental parameters used in this work, evaluating eqn. 4.3 with $\theta = 35^\circ$ (then $A = 1.6$), $\gamma = 2.56$ [47], $E = 270$ mJ, $v_0 = 4.8 \times 10^6$ cm.s⁻¹, $\tau_{laser} \simeq 9$ ns, gives a straight line as shown in fig. 4.16 corresponding to the present experimental pressure range. In our experiments, the estimated length of the plasma at a helium pressure of 0.05 mbar is 25 mm. Both the predicted pressure dependence and absolute value of L are seen to be reasonably in good agreement with experiment. The small error occurring in these calculations is mainly due to uncertainties in the value of γ and θ . It must be noted that the deposition rate and kinetic energy of ablated species will fall into a very low value for substrates located beyond L because of the subsequent cooling which tends to pull the material back to the target [52]. The dimension of the plasma, which is closely related to density, the excitation temperature and the coupling of laser radiation, are influenced by the atmosphere through eqn. (4.3). The pressure of the ambient atmosphere is one of the controlling parameters of the

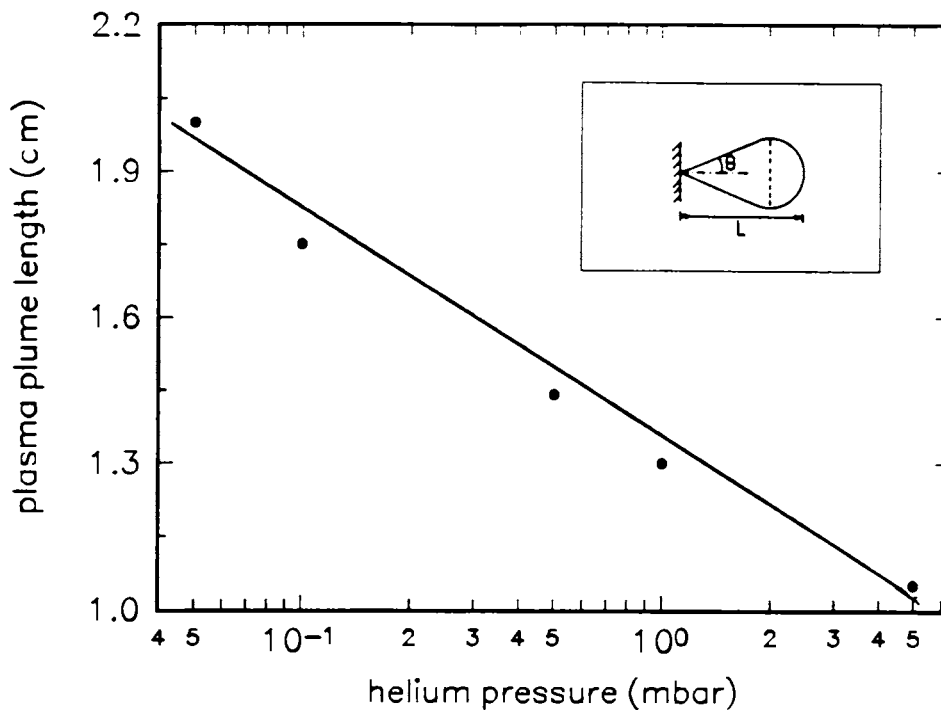


Figure 4.16: Estimated length of the ablation plume L as a function of helium pressure, laser irradiance 81.34 GW cm^{-2}

plasma characteristics, as well as factors related to the laser energy absorption [53].

4.3.5 Spatial Analysis at Greater Distances - Triple Peak Structure in TOF Distribution

In this section, a comprehensive study of spatial characteristic emission from C_2 using time resolved spectroscopy is given. In these experiments time resolved spectroscopic observations of the plasma plume from graphite under helium ambient atmosphere were carried out to determine the velocities of the ablated C_2 species. Such temporally and spatially resolved high resolution spectroscopic studies are helpful to optimize parameters of DLC film deposition and to correlate the carbon clusters with plasma dynamics. Our results show the existence of triple peak in the temporal history of C_2 emission from laser produced carbon plasma. It also indicates that the temporal profile of C_2 species produced during laser ablation of graphite exhibits a triple peak structure only beyond a certain spatial separation from the target (16 mm) and thereafter they propagate with three different expansion velocities.

The typical temporal profiles for emission from C_2 species (choosing $\lambda = 516.5 \text{ nm}$

corresponding to (0,0) band of Swan system) at a laser irradiance of 81 GW cm^{-2} for different axial distances from the target are shown in the figs. 4.17(a-f). The time resolved observation presented here characterizes the axial expansion of the plasma i.e, strictly along a direction perpendicular to the target surface. Figs. 4.17 (a) and (b) represent the oscilloscope traces of TOF distribution of C_2 molecules at distances 5 mm and 10 mm from the target. At these distances, there exists a double peak structure. The emergence of the new peak occurs only at distances greater than 16 mm from the target. Fig. 4.17 (c) shows the formation of the new peak in between the aforesaid twin peaks. Figs. 4.17 (d-f) show the triple fold TOF distribution of the C_2 species at distances 18 mm, 20 mm and 22 mm away from the target surface. The time evolution of the spectral emission obtained in the present work clearly reveals that the C_2 species ejected from graphite target has a twin peak distribution up to a certain distance from the target (16 mm) and at farther distances the TOF pattern shows a triple peak structure. It has also been found that there is a well defined threshold irradiance to observe this triple peak structure in the TOF distribution.

There are only a few reports which describe the triple fold TOF distribution in laser generated plasma from graphite target. Lowndes et al [6] recently observed three 'modes' of incident species in the TOF profile using ion probe method and they attributed it to scattered ions, ions that are slowed by gas phase collisions and slow moving clusters formed through collisions respectively. Tasaka et al [54, 55] observed triple fold plume structure during Nd:YAG laser ablation of graphite in helium ambient atmosphere. During optical emission studies using streak camera they found that, the fastest component is composed of carbon ions, second fastest component is due to compressed neutral molecules and the slowest component is the radial vapour from the graphite target. Bulgakov and Bulgakova [56] made a theoretical model for the plume expansion into ambient gas and have shown that the pulsating character in the velocity distribution can be explained using back and forth shock wave propagation and they also indicated that ionization and recombination processes have no significant effect on these pulsations. But they could not succeed in explaining the triple structure for BaO molecule during mass spectroscopic studies [51] using cloud ionization model.

TOF distributions give the time of arrival at a certain point in space with a known flight length and these can easily be transformed into velocity distribution. Variation of time delay with distance for P1 and P2 are given in figs. 4.18 and 4.19. It is seen from

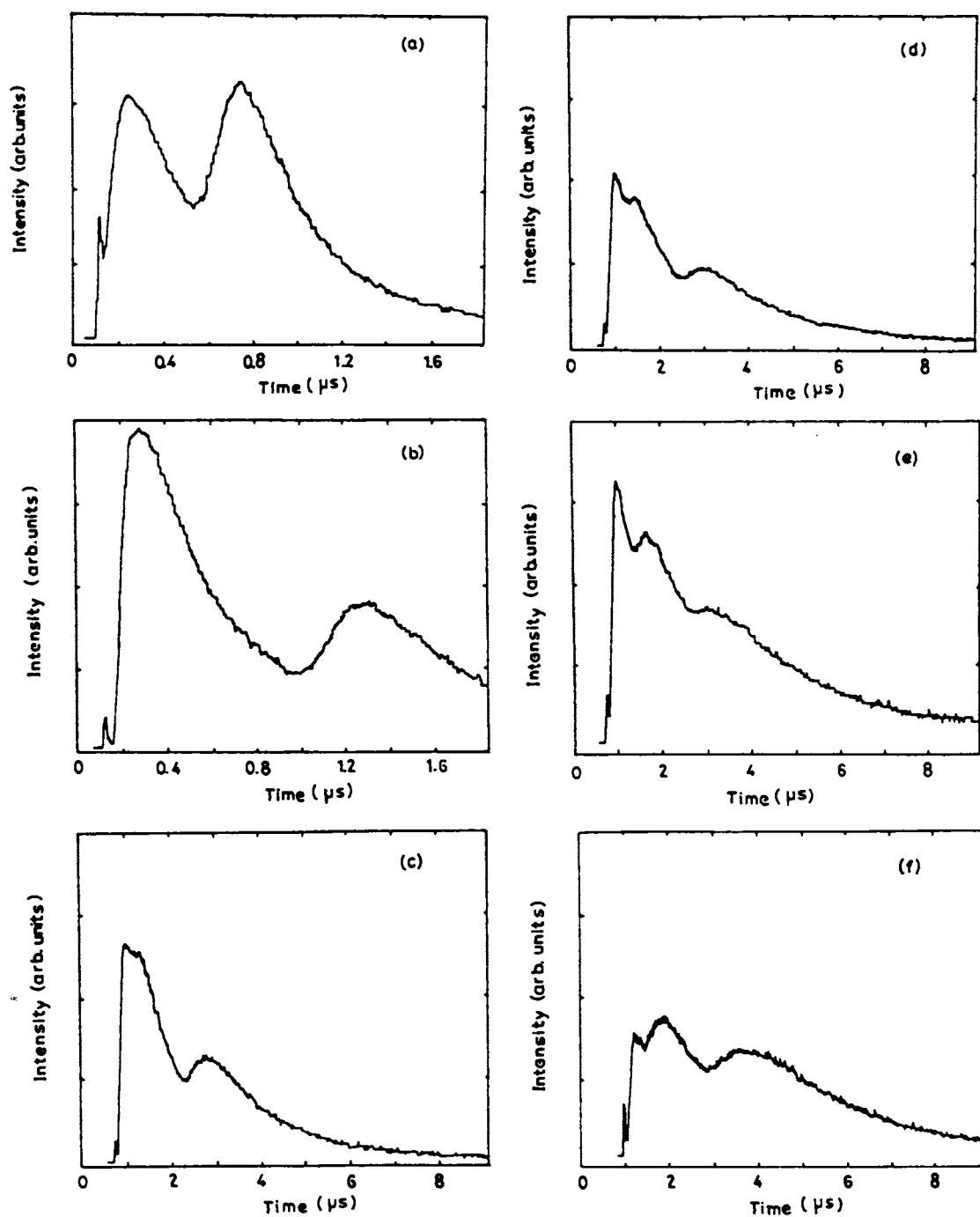


Figure 4.17: Intensity variation of spectral emission with time for C₂ species (516.5 nm) at different distances from the target. Distances are (a) 5 mm, (b) 10 mm, (c) 17 mm, (d) 18 mm, (e) 20 mm and (f) 22 mm. These TOF spectra are recorded at a laser irradiance 81.34 GW cm⁻².

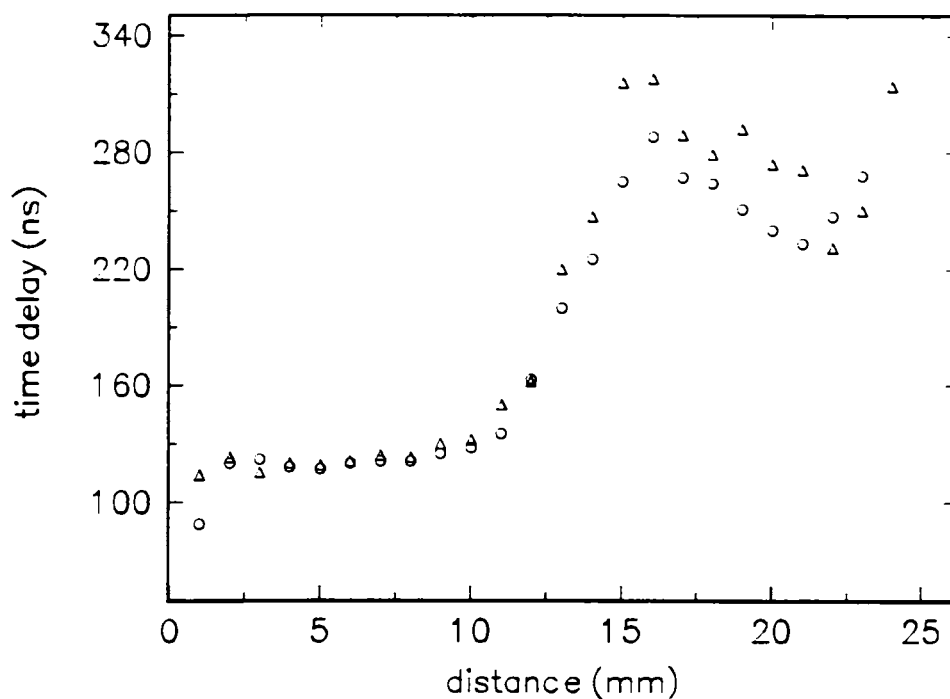


Figure 4.18: Variation of time delay in the peak intensities with distance for the P1 of C_2 at different laser irradiances. (\circ) 81.34 GW cm^{-2} and (Δ) 88.4 GW cm^{-2} .

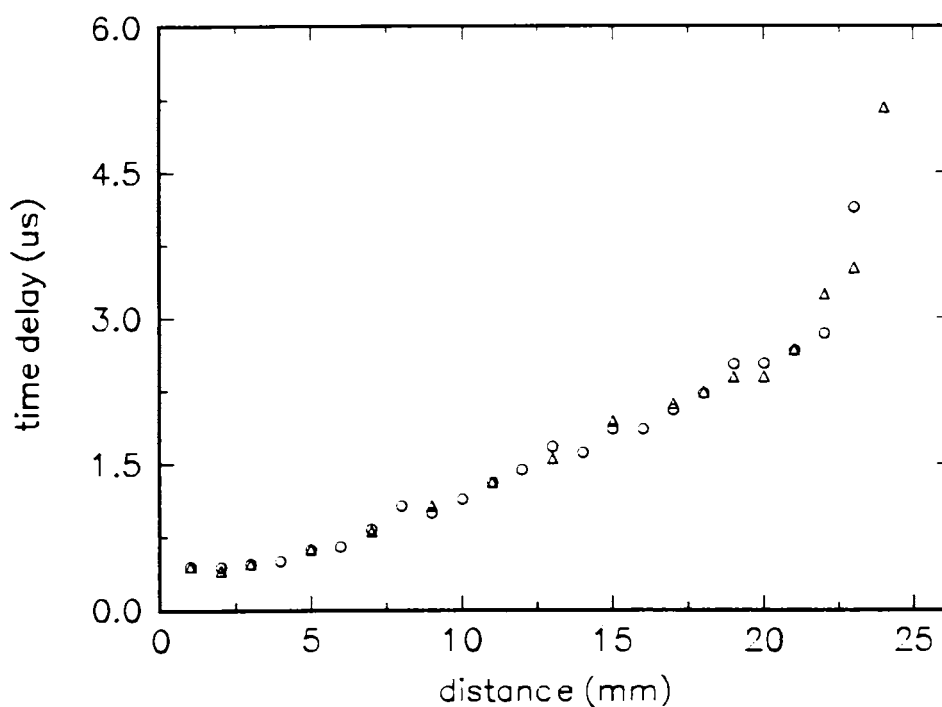


Figure 4.19: Variation of time delay in the peak intensities with distance for P2 of C_2 at different laser irradiances (\circ) 81.34 GW cm^{-2} and (Δ) 88.4 GW cm^{-2} .

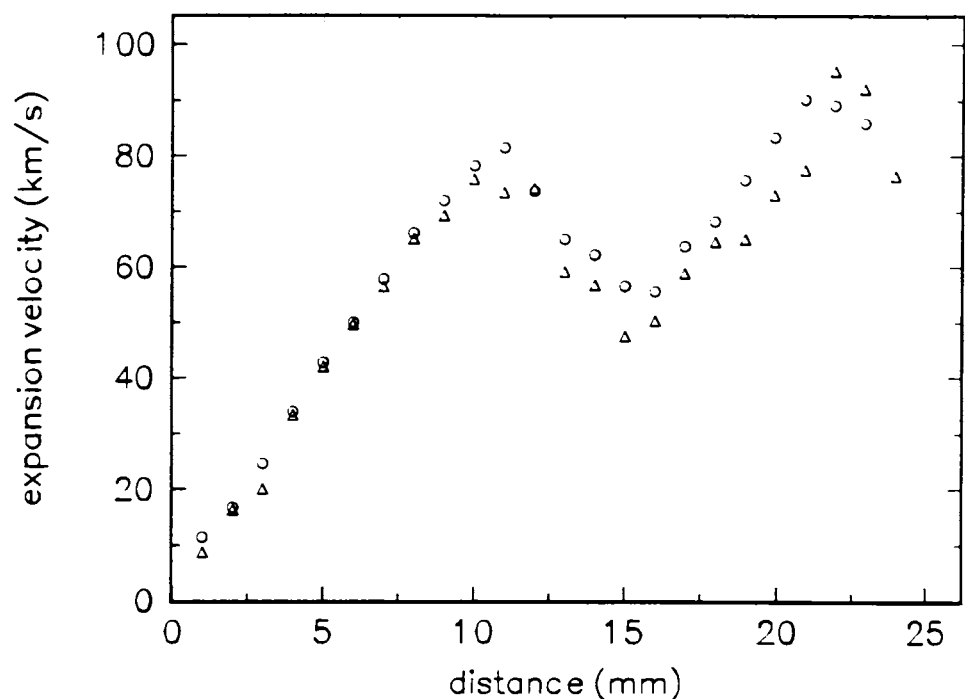


Figure 4.20: Expansion velocities as a function of distance for P1 of C₂ for laser irradiance (○) - 81.34 GW cm⁻² and (△) - 88.4 GW cm⁻².

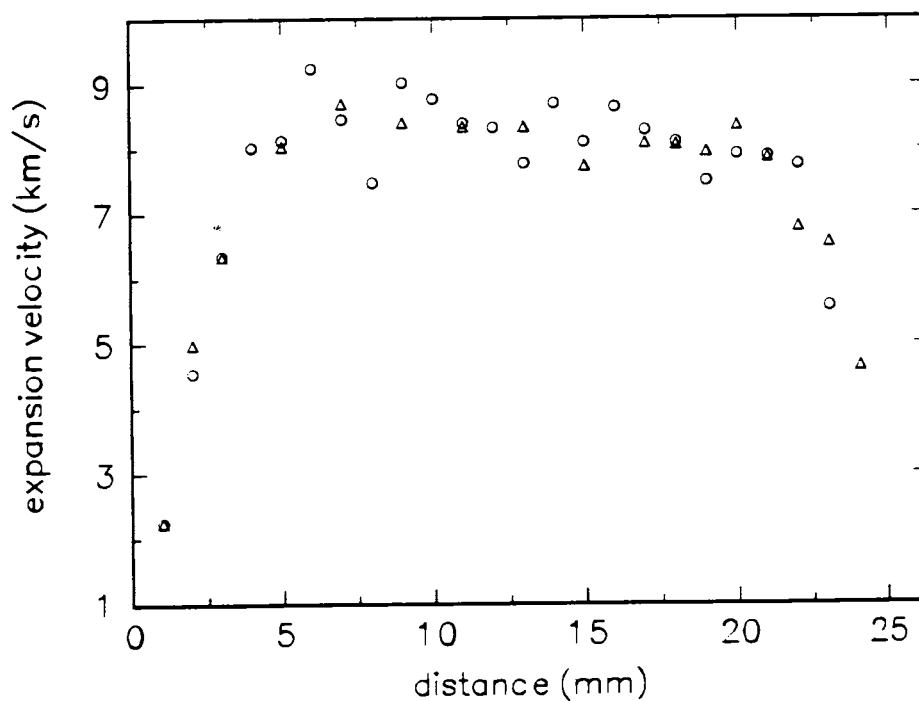


Figure 4.21: Expansion velocities as a function of distance for P2 of C₂ for laser irradiance (○) - 81.34 GW cm⁻² and (△) 88.4 GW cm⁻².

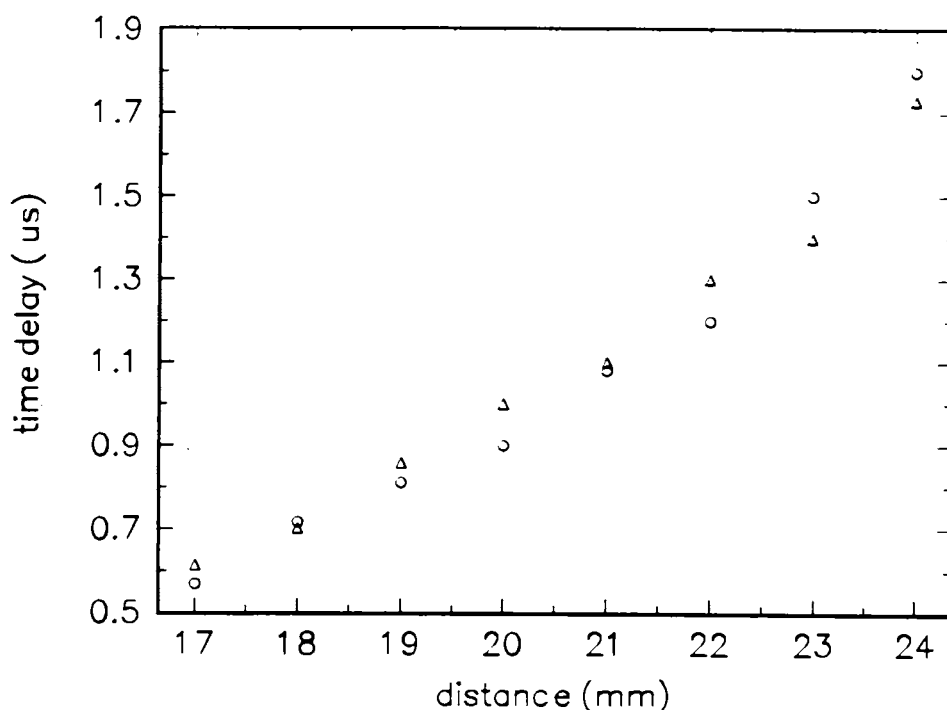


Figure 4.22: Variation of delay time with distance for newly generated peak of C_2 at different laser irradiances (\circ - 81.34 GW cm^{-2} and Δ - 88.4 GW cm^{-2})

fig. 4.18 that the time delay for the faster peak is constant up to 10 mm from the target and then increases. It is also noted that after 17 mm the delays for P1 decreases sharply. From the plots of delay time vs distance, one can obtain instantaneous velocities for C_2 molecules and these are given in figs. 4.20 and 4.21 respectively. It may be noted that the velocities are not constant and they vary with distance from the target. From the mean velocity distribution of these species it is clear that the velocity of P1 increases with spatial separation from the target up to $z = 10 \text{ mm}$. The sudden decrease in the velocity of these species after 10 mm shows the deceleration of the C_2 species. However at distances greater than $z = 15 \text{ mm}$, the velocity of the particles again gets enhanced. In the case of P2 (figure 4.21) the velocity increases with spatial separation from the target until it reaches 6 mm and then the expansion velocity is found to be somewhat constant (8 Km s^{-1}) up to $z = 20 \text{ mm}$ and then decreases. The intensity variation of these peaks with spatial separation shows different spatial maxima for faster ($z = 12 \text{ mm}$) and delayed peak (5 mm). The variation of time delay for newly generated peak beyond $z = 17 \text{ mm}$ is given in fig. 4.22 from which it is clear that the time delay is increasing with increasing distance in this case.

4.3.6 Time Resolved Studies of Ionized Species

In order to identify whether the multiply ionized carbon species have any role in this peculiar appearance of three peaks in the C_2 emission spectrum, optical emission analysis from carbon ions were also carried out. Emission originating from ionic species appears when the laser irradiance is sufficient to create a predominantly ionized plasma medium. Temporal profiles are recorded for the ionized carbon species, at 426.7 nm of C II ($3d^2D-4f^2F^0$), 569.5 nm of C III ($3p^1P^0-3d^1D$) and 580.1 nm of C IV ($3s^2S-3p^2P^0$) for different distances from the target. The ionic species are characterized by faster and narrower TOF distributions in comparison with atomic or molecular species. We observed a peculiar double peak structure for C^+ emission at 426.8 nm similar to the one observed by Abhilasha et al. [39]. They attributed it to stratification of plasma into fast and slow ion components occurring at the interface where fast component penetrates the ambient gas and slow one decelerate and consequently gives rise to a distinct double peak structure [57].

The time delays observed for different ionized species with respect to the axial distance from the target is given in the figure 4.23 at an irradiance of 70.7 GW cm^{-2} . The inverse slope of the curve drawn through the points gives their instantaneous velocities of these ionized species at a given time and distance. The expansion velocities of the ionized species are found to be increasing with degree of ionization. It is noted that the maximum expansion velocities of C II (taking the case of faster peak), C III and C IV are found to be at 40 Km/s, 58 Km/s and 80 Km/s respectively. The maximum spatial range for the ions were limited by the exponential drop in recorded intensity with distance (fig. 4.24) and the time. When ablation takes place in a gaseous environment at relatively high pressure ($\geq 0.05 \text{ mbar}$), the ablated material acts to sweep-up and drive the back ground gas at supersonic velocities as it expands outwards [58]. A shock wave is produced in the undisturbed gas, with the shock front being separated from the contact surface (boundary of the ablation products) by a layer of shock heated, compressed gas. In the early stages of expansion, the motion is unaffected by the gaseous background due to the high pressure of the ablation products [59]. However, as the plume expands and encompasses more gas, its velocity falls and, over a restricted range, the motion can be described by an ideal blast wave for which the shock boundary varies as [60, 61]

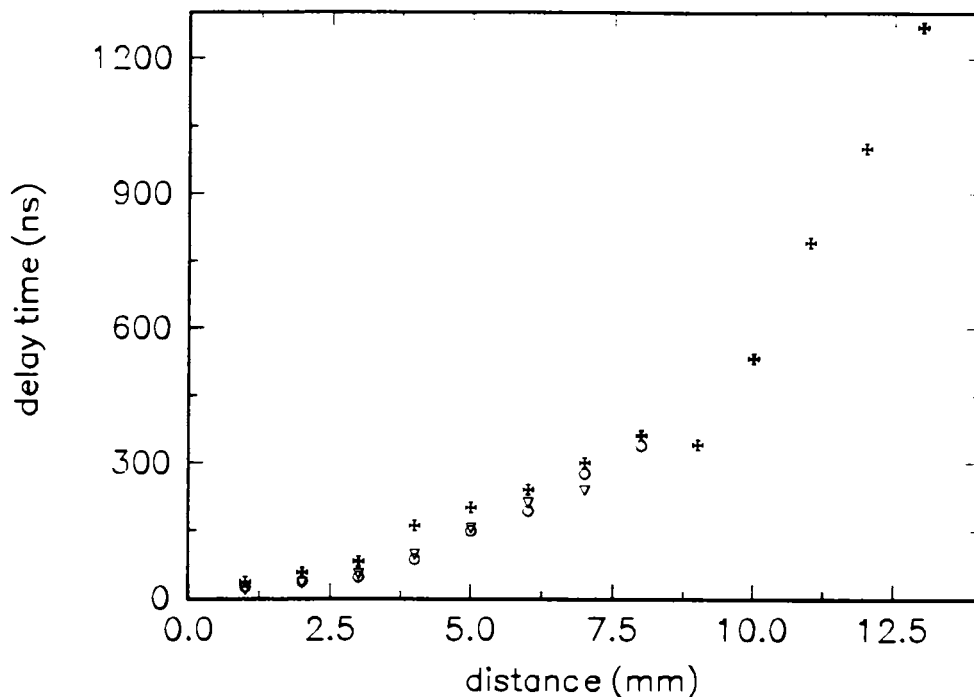


Figure 4.23: Variation of time delay in peak intensity with distance for different ionic species of carbon at a laser irradiance of 70.7 GW cm^{-2} . \oplus - C II transition ($3d^2D - 4f^2F^0$) at 426.7 nm , \circ - C III transition ($3p^1P^0 - 3d^1D$) at 580.1 nm and ∇ - C IV transition ($3s^2S - 3p^2P^0$) at 569.5 nm .

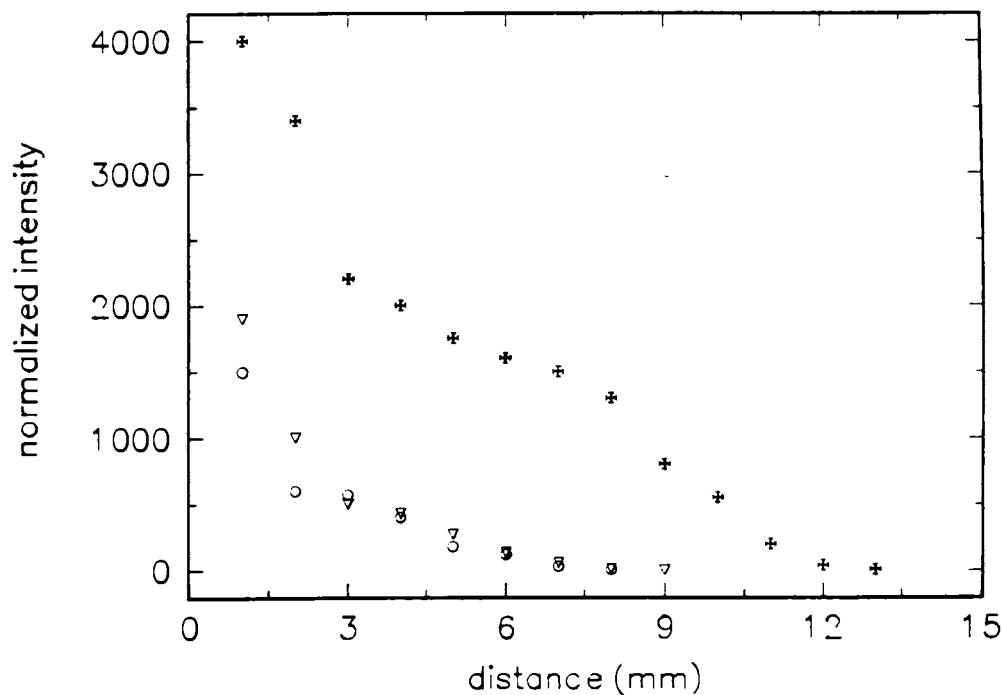


Figure 4.24: Change in intensity with distance for different ionic species of carbon. \oplus - C II transition ($3d^2D - 4f^2F^0$) at 426.7 nm , \circ - C III transition ($3p^1P^0 - 3d^1D$) at 580.1 nm and Δ - C IV transition ($3s^2S - 3p^2P^0$) at 569.5 nm .

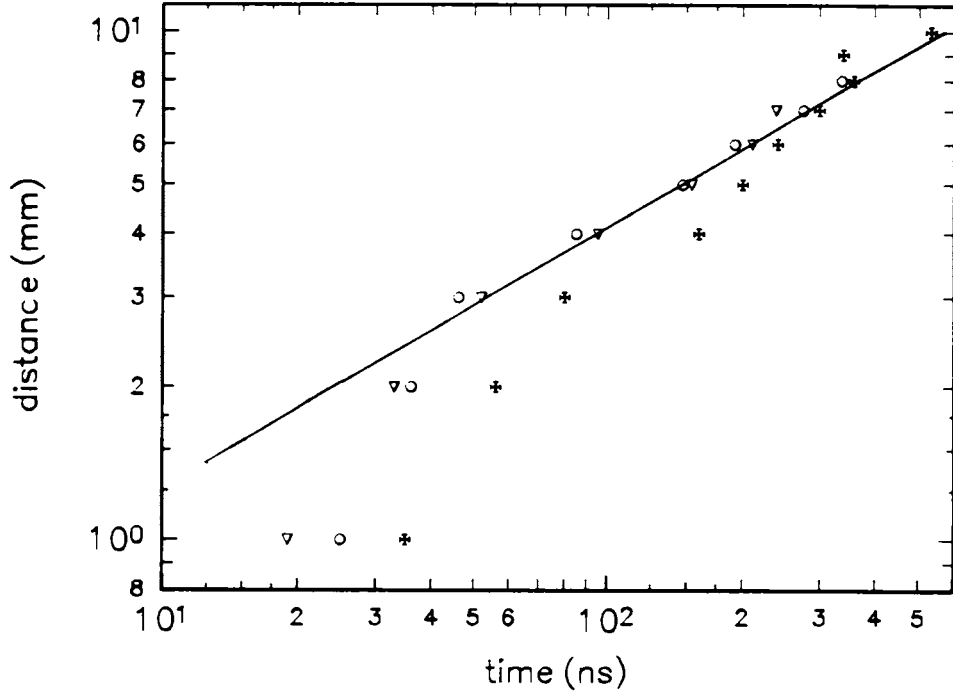


Figure 4.25: Distance (R) - time (t) plots for different ionic species. The solid line have the form $R \propto t^{0.4}$. \star - C II transition ($3d^2D - 4f^2F^0$) at 426.7 nm, \circ - C III transition ($3p^1P^0 - 3d^1D$) at 580.1 nm and ∇ - C IV transition ($3s^2S - 3p^2P^0$) at 569.5 nm.

$$z = \epsilon_0(E/P_0)^{1/5}t^{2/5} \quad (4.5)$$

where ϵ_0 is a constant of order unity, E is laser energy density absorbed and P_0 is the ambient gas pressure. This equation is valid only if, the pressure of the ablation products greatly exceeds the ambient pressure P_0 . Distance (z) - time (t) plots for different ionic species in the laser produced carbon plasma is given in fig. 4.25, these measurements are carried out at an irradiance of 70.7 GW cm^{-2} . Good agreement with $t^{0.4}$ dependence for R has been seen at the later times at a modest ambient gas pressure of 0.1 mbar. Therefore these results agree fairly well with the blast wave over most of the range observed. At distances close to the target, fits of the form $R = at^n$ suggest that exponent $n \geq 1$; not agreeing with this model. Blast wave interactions occurring in the presence of background gas may play an important role in multiple peak. But we do not observe such a $t^{0.4}$ dependence for the multiple peaks of the C_2 species. If it is assumed that the terminal stage of the plume can be modeled as a free expansion into the vacuum, the expansion velocity V can be written as [31, 47]

$$V = \sqrt{\frac{2\eta kT}{M}} \quad (4.6)$$

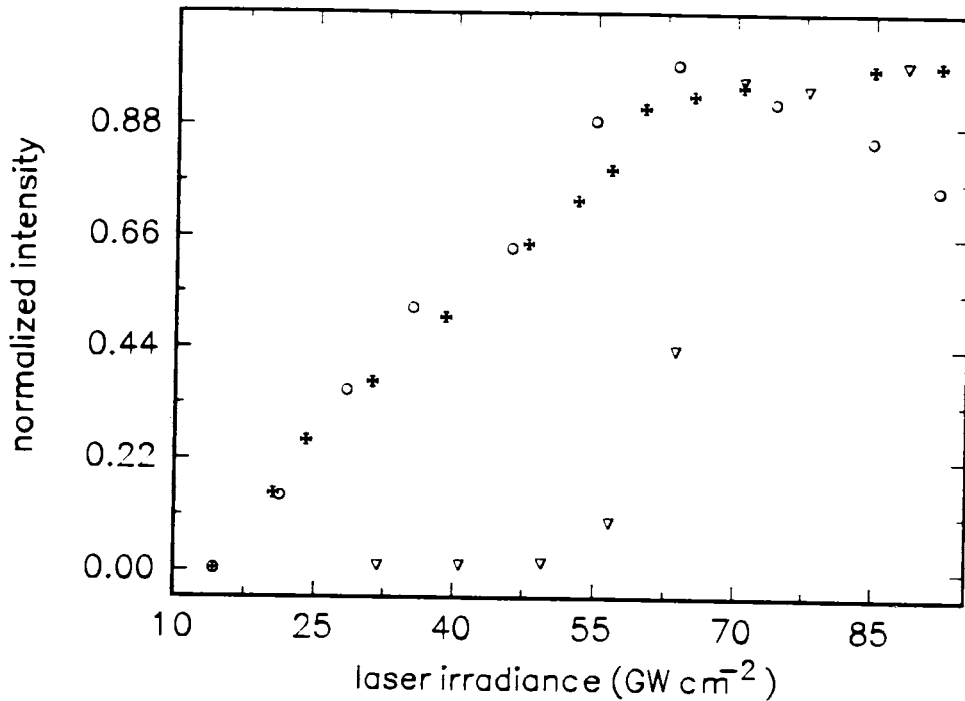


Figure 4.26: Change in intensity with laser irradiance for different ionic species. + - C II transition ($3d^2D - 4f^2F^0$) at 426.7 nm, o - C III transition ($3p^1P^0 - 3d^1D$) at 580.1 nm and ∇ - C IV transition ($3s^2S - 3p^2P^0$) at 569.5 nm.

where M is the mass of the species, η is the number of internal degrees of freedom which varies from 2.53 to 3.28 associated with ionization and excitation, T is the temperature of the plasma and k is the Boltzmann constant. The above equation shows that the time delay of the plasma species depends upon the temperature and dimensions of the plasma along with mass of the concerned species. According to eqn. (4.6), due to identical masses, different ionic species of carbon should have identical time delays. However, in actual practice, it is observed that the species with higher degree of ionization have higher velocities because of the Coulomb fields which are generated by negatively charged electrons escaping from the plume. These results are in consistent with our earlier observations suggesting the occurrence of faster peak in the temporal profile of C_2 above a certain threshold laser irradiance is caused by recombination of these ions. It is also supported by the fact that the molecules giving rise to these recombination peaks have almost identical kinetic energy distribution in comparison with highly energetic ions.

Another important observation is that the intensity of the ionized species increases with laser irradiances but get saturated at higher irradiance levels as is given in fig. 4.26. There is a laser intensity threshold for the appearance of multiply charged ions and this

threshold increases with degree of ionization. It is also noted that the expansion velocities of these ionic species increase with increasing laser irradiance. The exponential increase in the intensity of emission of positive ions with irradiance is in accordance with the Richardson-Saha laws [62]. The saturation in intensity at high laser intensities is due to a change in the efficiency of laser coupling to the target by increased absorption and/or reflection from the laser induced plasma, a process known as plasma shielding [63, 64]. The increase in ionization and intensity saturation with varying laser irradiance also seem to suggest strong interaction of the laser pulse with the dense plasma formed near the target within the pulse duration.

4.3.7 Expansion Dynamics

From fig. 4.17, it is seen that at higher spatial distance from the target (> 16 mm), the recombinational peak splits further into two forming a three fold TOF profile for the C_2 species. The reason for the occurrence of twin peak structure in the recombination emission intensity profile can be attributed to delays caused by different recombinational formation mechanism of C_2 species in the plasma. It is also seen from fig. 4.22 that the time delays for these newly generated C_2 species are increasing steadily with increasing distance from the target.

From fig. 4.20, one sees an anomalous variation of expansion velocity of the C_2 species with axial separation from the target. Gas dynamic effects are thought to play a major role in determining the spatial and velocity distribution of the vaporized material. The velocity at any point inside the plasma depends upon the spatial separation from the target surface. The atoms, molecules and ions undergo collisions in the high density region near the target forming the so called Knudsen layer, to create a highly directional expansion perpendicular to the target [65,66]. The density of the plasma will be maximum near the target due to collisions and hence the mean drift velocity normal to surface will be a minimum at very close to the target. The plasma expansion in a direction perpendicular to the target surface can be written as [24]

$$Z(t) \left[\frac{1}{2t} \frac{dZ}{dt} + \frac{d^2Z}{dt^2} \right] = \frac{6kT_0}{M} \quad (4.7)$$

where dZ/dt is the expansion velocity of the plasma in the Z direction, k , the Boltzmann constant, T_0 the isothermal temperature of the plasma and M is the molecular weight of the particle. The above equation evidently shows that the expansion velocities are

low and acceleration is very high during the initial stages of expansion. But when the expansion velocities increase, acceleration starts to decrease. The laser pulse being short, the plasma cloud within the pulse duration has a minimum size in the direction normal to the target surface. A dense plasma can absorb strongly the trailing part of the laser pulse. Thus the absorption of the laser radiation by the plasma increases the velocity of the species inside the plasma and the hydrodynamic expansion is directed right angles to the surface of the target. This is found to be true as seen in figs. 4.20 and 4.21 respectively at distances near the target where expansion velocities increase very rapidly with respect to the spatial separation from the target. During the initial stages of the plasma expansion, the velocity in the direction perpendicular to the target surface is very high as a result of the small dimension of the plasma in that direction. It is reported that [67,68] during shorter time intervals the expansion of the plume is one dimensional while for longer time scales the expansion is essentially three dimensional. This has also been supported by ultrafast photography of laser ablation plumes [69]. The dimensionality of the laser generated plasma, may deviate from these values depending several factors including laser irradiance, plasma temperature, irradiated spot shape, mass of the species etc.

After the termination of the laser pulse, adiabatic expansion of the plasma begins. During this process, the thermal energy is converted to kinetic energy with the plasma attaining high expansion velocities. The adiabatic expansion of the plasma in the Z direction can be written as [24]

$$Z(t) \left[\frac{d^2 Z}{dt^2} \right] = \frac{6kT_0}{M} \left[\frac{Z_0}{Z(t)} \right]^{\alpha-1} \quad (4.8)$$

where Z_0 is the edge of the plasma at which the laser pulse is terminated and α , the maximum attainable particle velocity. In the adiabatic expansion region, the acceleration depends on the initial temperature and the mass of the species.

From fig. 4.21 it is seen that, the velocity of P2 is constant (8 km/s) after the initial expansion of the plasma. The velocities of these are found to be decreased at the boundary of the plasma which is in accordance with drag model [70] which predicts that the plume eventually comes to rest due to resistance from collision with background gas. For low pressures, when the driven mass of the background gas is small compared with the driver mass of the expanding vapour, the drag force model can be applied. In this case the viscous force is proportional to the velocity of ejected material and the plasma propagation can thus be written as

$$Z(t) = Z_0 \left[1 - \exp\left(-\frac{u_0 t}{Z_0}\right) \right] \quad (4.9)$$

where u_0 is the initial expansion velocity and $Z_0 = u_0/\beta$ the so-called stopping distance.

Fig. 4.20 shows that between distances 10 mm to 15 mm from the target surface, the expansion velocity decreases for P1 while it increases again at farther distances. This peculiar velocity pulsations can be explained as follows. During the adiabatic expansions, the thermal energy is rapidly converted into kinetic energy, thereby attaining high expansion velocities. It has been reported that for spherical plasmas, temperature drops off as the square of its radius [71]. A rapid drop in temperature occurs when the spherical plasmas expand. This may be the reason for the decrease in kinetic energy for P1 in the region between 10 mm to 15 mm. However the temperature drop will not continue with respect to square of the radius of the spherical plasmas indefinitely, because cooling due to expansion will be balanced by the energy gained from the recombination processes of the ions.

4.4 Conclusions

A graphite target was ablated by 1.06 μm radiation from a Q-switched Nd:YAG laser in ambient helium atmosphere. Time resolved spectroscopic analysis of emission from C_2 species was carried out. The present work has differentiated the various mechanisms of the formation of C_2 species in the laser produced plasma from graphite in a helium gas atmosphere. Measurements of spatial dependence of the TOF emission intensities are made up to 25 mm away from the target. An oscillatory behavior is observed in the TOF distribution of C_2 species and this is observed only above a certain threshold value for irradiance. At distances greater than 16 mm from the target surface, a three fold TOF distribution is observed and the reason for the formation for these peaks is discussed. The peak due to low kinetic energy component which is observed at all levels of irradiance is formed as a result of dissociation of higher clusters. The departure of single peak velocity distribution at higher laser irradiances is due to processes like recombination of the high energetic particles. The energy released on recombination is converted into kinetic energy of the molecules, atoms and ions, which may give rise to a group of relatively faster C_2 species. It is found that at farther distances from the target the recombinational peak gets modified in to two due to inherent delays caused

by different recombination and excitation mechanisms. It is also found that these results are consistent with kinetic energy distribution of ionic species. The different expansion dynamics of C_2 species in the ambient gas are also discussed. The velocity pulsations in the faster peak during expansion into ambient gas are attributed to nonequilibrium kinetic energy transfer because of many body recombination.

A blast wave model appears to be in good agreement in considering the expansion dynamics of ionic species. But in the case of C_2 species, this model does not succeed. A simple adiabatic expansion model appears to provide a good description of the plume range and this may prove useful for scaling deposition experiments in terms of pressure, laser irradiance and deposition range.

Finally, the present work clearly points to the existence of the various mechanisms of the formation of C_2 species in the laser induced plasma. Analysis of these data provides a fairly clear picture of the evolution and dynamics of C_2 species in the laser induced plasma from graphite as well as the role of carbon clusters in the same.

4.5 References

- [1] H. W. Kroto, R. J. Heath, S. C. O'Brien, R. F. Curl and R. E. Smalley, *Nature* **318** 165 (1985).
- [2] E. A. Rohlfing, *J. Chem. Phys.* **93** 7851 (1990).
- [3] G. Meijer and D. S. Bethane, *J. Chem. Phys.* **93** 7800 (1990).
- [4] R. E. Smalley, *Acc. Chem. Res.* **25** 98 (1992).
- [5] D. B. Chrisey and G. K. Hubler (eds.) *Pulsed laser deposition of thin films* (John Wiley and sons, New York, 1994).
- [6] D. H. Lowndes, D. B. Geohegan, A. A. Puretzky, D. P. Norton and C. M. Rouleau, *Science* **273** 898 (1996).
- [7] D. R. Mckenzie, D. Muller, B. A. Palithorpe, *Phys. Rev. Letts.* **67** 773 (1991).
- [8] M. E. Kozlov, K. Yaze, N. Minami, P. Fons, H. A. Durand, A. N. Obraztsov, K. Nozaki and M. Tokumoto, *J. Phys. D* **29** 929 (1996).
- [9] D. L. Pappas, K. L. Saenger, J. Bruley, W. Krakow, J. J. Cuomo, T. Gu and R. W. Collins *J. Appl. Phys.* **71** 5675 (1992).
- [10] F. Davanloo, E. M. Juengerman, D. R. Jander, T. J. Lee and C. B. Collins, *J. Appl. Phys.* **67** 2081 (1990).
- [11] S. S. Wagal, E. M. Juengerman and C. B. Collins *Appl. Phys. Lett.* **53** 187 (1988).
- [12] G. Dollinger, C. M. Frey and P. Maier-Komor, *Nucl. Instr. and Meth.* **A334** 167 (1993).
- [13] C. L. Marquardt, R. T. Williams and D. J. Nagel, *Mat. Res. Soc. Sym. Proc.* **38** 325 (1985).
- [14] M. Mattioli, *Plasma Phys.* **13** 19 (1971).
- [15] F. E. Irons and N. J. Peacock, *J. Phys. B.* **15** 2084 (1974).
- [16] J. Stevefelt and C. B. Collins, *J. Phys. D* **24** 2149 (1991).

- [17] J. T. Cheung in *Pulsed laser deposition of thin films* D. B. Chrisey and G. K. Hubler (eds.)(John Wiley and sons, New York, 1994) Chapter 1.
- [18] J.A. Greer, in *Pulsed laser deposition of thin films* D. B. Chrisey and G. K. Hubler (eds.)(John Wiley and sons, New York, 1994) Chapter 11.
- [19] J. A. Greer and M. D. Tabat, *J. Vac. Sci. Technol.***A**, **13** 1175 (1995).
- [20] A. A. Voevodin, M. S. Donely, J. S. Zabinski and J .E. Bultman, *Surf. Coat. Technol.*, **77** 534 (1995).
- [21] M. S. Donely and J. S. Zabinski, in *Pulsed laser deposition of thin films* D. B. Chrisey and G. K. Hubler (eds.)(John Wiley and sons, New York, 1994) Chapter 18.
- [22] A. A. Voevodin and M. S. Donley, *Surf. Coat. Technol.*, **82** 199 (1996).
- [23] R. K. Singh and J. Narayan, *Phys. Rev. B* **41** 8843 (1990).
- [24] R. K. Singh, O. W. Holland and J. Narayan, *J. Appl. Phys.* **68** 233 (1990).
- [25] P. T. Murray and D. T. Peeler in *Laser Ablation : Mechanisms and Applications II* (American Institute of Physics, New York, 1994) p.359.
- [26] F. Amiranoff, R. Fabbro, E. Fabre, C. Garban, J. Virmont and M. Weinfeld, *Phy. Rev. Letts.* **43** 522 (1979).
- [27] Abhilasha and R. K. Thareja, *Phys. Letts. A* **184** 99 (1993).
- [28] M. B. Guseva, V. G. Babaev, V. V. Khvostov, Z.Kh. Valioullova, A.Yu. Bregadze, A. N. Obraztsov and A. E. Alexenko, *Diamond Rel. Mater.*, **3** 328 (1994).
- [29] N. Kikuchi, Y. Ohsawa and I. Suzuki, *Diamond Rel. Mater.*, **2** 190 (1993).
- [30] A. A. Voevodin, S. J. P. Laube, S. D. Walck, J. S. Solomon, M. S. Donley and J. S. Zabinski, *J. Appl. Phys.*, **78** 4123 (1995).
- [31] R. Kelly and A. Miotello in *Pulsed laser deposition of thin films* D. B. Chrisey and G. K. Hubler (eds.)(John Wiley and sons, New York, 1994) chap. 3.
- [32] R. Kelly and B. Braren, *Appl. Phys. B.* **53** 160 (1991).

- [33] R. Kelly, *Phys. Rev. A* **46** 860 (1992).
- [34] William Weltner Jr. and R. J. Van Zee, *Chem. Rev.* **89** 1713 (1989).
- [35] R. W. B. Pearse and A.G. Gaydon, *The Identification of Molecular Spectra*, (Chapman & Hall Ltd, London 1965) P94
- [36] G. Koren and J. T. C. Yeh, *J. Appl. Phys.* **56** 2120 (1984).
- [37] R. H. Dixon, R. C. Elton, and J. F. Seely, *Opt. Commun.*, **45** 397 (1983).
- [38] R. H. Dixon and R. C. Elton, *Phys. Rev. Letts.*, **38** 1072 (1977).
- [39] Abhilasha, P. S. R. Prasad, and R. K. Thareja *Phys. Rev. E* **48** 2929 (1993).
- [40] S. S. Harilal, P. Radhakrishnan, V. P. N. Nampoori and C. P. G. Vallabhan, *Appl. Phys. Letts.* **64** 3377 (1994).
- [41] A. Harano, J. Kinoshita, K. Itou, T. Kitamori, T. Sawada and S. Koda, *J. Spectrosc. Soc. Japan*, **42** 94 (1993).
- [42] H. W. Kroto, A. F. Allaf and S. P. Balm, *Chem. Rev.* **91** 1213 (1991).
- [43] Y. Iida and E. S. Yeung, *Appl. Spectros.* **48** 945 (1994).
- [44] D. L. Pappas, K. L. Saenger, J. J. Cuomo and R. W. Dreytus, *J. Appl. Phys.* **72** 3966 (1992).
- [45] See Chapter 3 of this thesis.
- [46] See Chapter 5 of this thesis.
- [47] R. W. Dreyfus, R. Kelly and R. E. Walkup, *Nucl. Instru. Meth. Res. B* **23** 557 (1987).
- [48] J. B. Anderson in *Molecular Beams and Low Density Gas Dynamics*, P. P. Wegener (ed.) (Marcel Dekker, New York 1974).
- [49] P. E. Dyer, A. Issa and P. H. Key, *Appl. Surf. Sci.* **46** 89 (1996).
- [50] P. E. Dyer, A. Issa, P. H. Key, *Appl. Phys. Letts.* **57** 186 (1990).

- [51] K. A. Kummuduni, Y. Nakayama, Y. Nakata, T. Okada and M. Maeda, *J. Appl. Phys.* **74** 7510 (1993).
- [52] G. Koren, *Appl. Phys. Letts.* **51** 569 (1987).
- [53] See Chapter 5.
- [54] Y. Tasaka, M. Tanaka and S. Usami, *Jpn. J. Appl. Phys.* **34** 1673 (1995).
- [55] Y. Tasaka, M. Tanaka and S. Usami, *Appl. Sur. Sci.* **79/80** 141 (1994).
- [56] A. V. Bulgakov and N. M. Bulgakova, *J. Phys. D* **28** 1710 (1995).
- [57] R. K. Thareja, Abhilasha and R. K. Dwivedi, *Laser and particle beams* **13** 481 (1995).
- [58] J. L. Bobin, Y. A. Durand, P. Langer and G. Tonon, *J. Appl. Phys.* **39** 4184 (1968).
- [59] D. A. Freiwald and R. A. Axford, *J. Appl. Phys.* **46** 1171 (1975).
- [60] T. P. Hughes, *Plasmas and Laser Light*, (John Wiley and Sons, Inc., New York 1975).
- [61] D. B. Geohegan in *Pulsed Laser Deposition of Thin Films* D. B. Chrisey and G. K. Hubler (eds.)(John Wiley and sons, New York, 1994) chap. 5.
- [62] E. N. Sobol in *Phase Transformation and Ablation in Laser Treated Solids* (John Wiley and sons, New York, 1994) chp.6
- [63] J. F. Ready, *Effects of High Power Radiation* (Academic Press, New York 1971).
- [64] See Chapter 5.
- [65] R. Kelly and R. W. Dreyfus, *Sur. Sci.* **198** 263 (1988).
- [66] R. Kelly, *Phys. J. Chem. Phys.* **92** 5047 (1990).
- [67] W. Pietsch, B. Dubreuil and A. Briand, *Appl. Phys. B* **61** 267 (1995).
- [68] J. C.S. Kools, T. S. Baller, S. T. Dezwart and J. Dielemen, *J. Appl. Phys.* **71** 4547 (1992).

- [69] A. Guptha, B. Baren, K. G. Casey, B. W. Husley and R. Kelly, *Appl. Phys. Letts.* **59** 1302 (1991).
- [70] D. B. Geohegan, *Thin Solid Films* **220** 138 (1992).
- [71] J. M. Dawson, *Phys. Fluids* **7** 981 (1964).

Chapter 5

Dynamics of Laser Produced Carbon Plasma

Plasma produced by fundamental radiation from a Nd:YAG laser focused onto a graphite target is studied spectroscopically. Measured line profiles of several ionic species were used to infer electron temperature and density at several sections located in front of the target surface. Line intensities of successive ionization states of carbon were used for electron temperature and electron density calculations. Stark broadened profiles of singly ionized species have been utilized for verifying electron density measurements. Electron density and temperatures were studied as functions of laser irradiance and time elapsed after the incidence of laser pulse. The effect of different background gases on the dynamics of laser produced plasma also have been studied in these investigations. The validity of the assumption of local thermodynamic equilibrium is discussed in the light of the results obtained.

5.1 Introduction

Pulsed laser induced plasma has a short temporal existence and is transient in its nature, with a fast evolution of the parameters that are heavily depend on the irradiation conditions such as incident laser intensity, irradiation spot size, ambient gas composition and pressure. It is also true that these parameters vary drastically with axial or radial distance from the target surface. Detailed investigation of the optical emission of the plasma plume gives the information on the spatial and temporal evolution of transient species produced during laser-target interaction, such as excited atoms, ions or molecules. The spectroscopic studies made on spatial volume elements in the neighbourhood of the target surface in the early stages of the plasma evolution give direct information about the laser-target interaction as well as laser-plasma interaction. Investigations on optical emission at comparatively larger distances from the target surface result in yielding information on the plasma species reactivity, which is an important quantity needed to maintain quality of thin films, prepared using pulsed laser deposition technique. It also reveals the dynamics of the ablated material before collision with a substrate surface [1,2].

Experimental studies show that pulsed laser evaporation of a solid target with intensities well above the vapourization threshold is generally accompanied by plasma formation. Actually the formation mechanism of this laser produced plasma is fully not understood yet [3-5]. The plasma initiation in the case of pulsed CO₂ laser irradiation of metals in an ambient gas at atmospheric pressure shows that an avalanche ionization can occur in the ambient gas even for laser intensities lower than the threshold for the bulk material vaporization [6]. Primary electrons coming from vaporization of surface defects were able to initiate the plasma formation in the surrounding gas. Due to the high absorption coefficient of infrared radiation in the plasma, it was not possible to couple laser energy efficiently to the target and the ablated vapour remained low even at high laser irradiance levels [7].

Pulsed laser deposition is increasingly being utilized for thin film preparation [8]. Among the parameters involved in pulsed laser deposition process, laser irradiance, laser wavelength, background gas pressure, distance at which the substrate is placed seem to be more relevant in order to the control the film growth. Spectral analysis of light emitted from the plasma produced in the process of target ablation and material transport in

laser deposition of thin films gives information about plasma composition, the energy content of ablation products and the dynamics of the different species in the plume [9-16]. In addition, the evolution of the plume can be theoretically predicted with models that refer to the initiation mechanism, kinetic processes and other important parameters like electron temperature, electron density, ionization stage etc. Richter [17] demonstrated the peculiarities of the pulsed laser plasma method for the deposition of thin films by estimating the evaporation threshold as well as the electron temperature and density of the absorbing laser plasma. The energy content of the plasma varies with the kind of laser light. The degree of vapourization of a plasma generated by a CO₂ laser is higher than that produced by an excimer laser [17].

The interaction of pulsed laser irradiation of nanosecond duration with a metal surface was studied by numerical stimulation by various authors [18-20]. During the stage of interaction between the incident laser beam pulse and the solid target, part of the laser beam is reflected back to the ambient and part of the energy is absorbed within a short penetration depth in the metal. The macroscopic picture at low laser intensities implies that skin depth absorption and surface heating eventually drive heat conduction into the material. The mechanisms of energy transfer from the laser beam to the metal were described in one of the earliest reports in the field by Ready [21]. The laser-plasma-target interactions may strongly affect the energy delivered to the target surface. The coupling of the laser radiation with the target may be substantially different from that due to surface absorption alone. This phenomenon, called, thermal coupling, has been observed by previous researchers [19,22]. The mechanism for enhanced thermal coupling are not fully understood yet, although it is believed that coupling is caused by high-temperature plasma formed in the vapour phase above the target surface. Therefore thermal coupling has been called plasma-enhanced coupling by some researchers. Energy can be transferred from the plasma to the target by one or combinations of the following mechanisms: (i) normal electron heat conduction; (ii) short-wavelength thermal plasma radiation which is absorbed by the target surface; and (iii) condensation of the vapour forced back to the target surface by the plasma pressure [18]. These three mechanisms provide additional heat flux contributions to the target surface, which may or may not exceed the loss of the incident light flux due to plasma absorption [23]. Singh and Narayan [24] proposed a theoretical model for simulating laser-plasma-solid interaction, assuming that the initially formed plasma undergoes a three dimensional

isothermal expansion followed by adiabatic expansion. Aden et al [25-27] dealt with the laser induced expansion of metal vapour against background pressure. The inverse bremsstrahlung mechanism was used to model the plasma laser light absorption. The thermal ionization was modeled by the Saha-Eggert equation [28]. Erpelding et al [29] calculated the radiation loss by the stationary plasma above the target surface and discussed the thermal coupling due to plasma absorption and heating. Further research is needed to understand the dynamic formation of plasma in the ejected vapour phase and its interaction with the incoming laser pulse.

Laser induced graphite plasma has got several applications. Carbon thin films have been attracting both intensive theoretical and experimental investigations due to their diamond-like properties. This technique is also utilized for fullerene synthesis in an ambient gas. It is potential method for many possible new, yet to be defined technological applications. While this strong interest leads to intense research work on the physical and chemical properties of these classes of carbon, the precise nature of its formation remains controversial.

Usually plasmas are characterized by their electron temperature (T_e) and electron density (n_e). There are several diagnostic techniques employed for the determination of electron density which includes, plasma spectroscopy [30, 31], Langmuir probe [32-34], microwave and laser interferometry [35-38], and Thomson scattering [39-42]. Thomson scattering is probably the most direct and least theory-dependent, while spectroscopy is the simplest as far as instrumentation is concerned. Plasma density determination using Stark broadening of spectral lines is a well established and reliable technique in the range of number density 10^{14} to 10^{18} cm^{-3} [43-45]. The electron temperature is an equally important plasma parameter. Knowledge of the electron temperature is vital to the understanding of the dissociation, atomization, ionization and excitation processes occurring in the plasma. It can be determined spectroscopically in a variety of ways: from the ratio of integrated line intensities, from the ratio of line intensity to underlying continuum, and from the shape of the continuum spectrum (bremsstrahlung) [30]. Irons and co-workers [46-48] have reported detailed studies on the temporal, spatial and spectral characteristics of ruby laser- produced carbon plasma. They deduced electron density by line intensity measurements and Stark broadened wavelength profiles of the carbon VI and carbon V lines in high density plasma produced by a 5 J Ruby laser irradiation of a polyethylene target in vacuum.

In this chapter, the studies on plasma parameters such as electron density and electron temperature and their dependence on factors like incident laser irradiance, time after the elapse of laser pulse, spatial separation from the target surface and pressure and nature of the ambient gas will be discussed. Temperature and density of the plasma have been evaluated using the relative line intensities of successive ionization states of carbon atom. The determination of electron density is also carried out using the Stark broadened profile of singly ionized carbon atom. The details of these are given in the following sections.

5.2 Experimental

Details of the experimental technique are given in chapter 2. Briefly, plasma was generated by laser ablation of the high purity polycrystalline graphite sample using 1064 nm radiation pulses from a Q-switched Nd:YAG laser with repetition rate 10 Hz. The target in the form of a disc (20 mm diameter and 5 mm thickness) was placed in a evacuated chamber provided with optical windows for laser irradiation and spectroscopic observation of the plasma produced from the target. The target was rotated about an axis parallel to the laser beam to avoid nonuniform pitting of the target surface. The bright plasma emission was viewed through a side window at right angles to the plasma expansion direction. The line-of-sight intensity of the plasma is collected from a cross section of area 0.01 cm^2 . The section of the plasma was imaged onto the slit of a 1 meter Spex monochromator (with entrance and exit slits are parallel to the target surface using appropriate collimating and focusing lenses so as to have one to one correspondence with the sampled area of the plasma and the image. The scan of the monochromator was controlled using Spex CD2A compudrive arrangement. The recording was done by using a thermoelectrically cooled PMT, which was coupled to a boxcar averager/gated integrator. The averaged output from the boxcar averager was fed to a chart recorder, which for the present study averaged out intensities from 10 pulses. For Stark broadening studies, the resolution of the monochromator was kept at its maximum by keeping the slit width at a minimum ($3 \mu\text{m}$, $6 \mu\text{m}$).

5.3 Relative line intensity measurements

One of the simplest methods for the determination of electron temperature is by using relative intensities of lines of the same element and ionization state. This is one of the

earliest method for the determination of temperatures in Local thermodynamic equilibrium (LTE) plasmas, which is based on the the fact that densities in various excited states are proportional to the product of statistical weights with the exponentials of the negative ratios of excitation energy and the thermal energy kT . The temperature is accordingly inversely proportional to the logarithm of the ratio of the total intensities of lines arising from different upper levels, provided that none of these lines is affected by self absorption. The electron temperature T_e can be determined using the eqn. [30]

$$kT = \frac{E' - E}{\ln(I\lambda^3 g' f' / I'\lambda'^3 g f)} \quad (5.1)$$

where I , λ , g and f are the intensity, wavelength, statistical weight of the lower state and oscillator strength of the one line and E its excitation energy. Primed quantities represent corresponding constants for the second line.

Relative line intensities from the same element and ionization state usually do not provide accurate temperatures. The principal reason for this is the relatively small separation between the upper levels of two lines. This renders the line intensity ratio rather insensitive to temperature changes. Considerable improvement in sensitivity can be obtained by selecting lines from successive ionization states of the same element, because the effective energy difference is now enhanced by the ionization energy, which is larger than the thermal energy. In LTE, the ratio of such line intensities is given by [30],

$$\frac{I'}{I} = \left[\frac{f' g' \lambda'^3}{f g \lambda^3} \right] \left[4\pi^{3/2} a_0^3 n_e \right]^{-1} \left[\frac{kT_e}{E_H} \right]^{3/2} \exp \left[-\frac{E' + E_\infty - E - \Delta E_\infty}{kT} \right] \quad (5.2)$$

where the primed symbols represent the line of the atom with higher ionization stage; f , is the oscillator strength; g , statistical weight; a_0 , Bohr radius; E_H , ionization energy of the hydrogen atom; E , excitation energy and ΔE_∞ is the reduction to the ionization energy E_∞ of the lower ionization stage.

The correction factor in the ionization energy is given by [30]

$$\Delta E_\infty = 3z \frac{e^2}{4\pi\epsilon_0} \left[\frac{4\pi n_e}{3} \right]^{1/3} \quad (5.3)$$

where $z = 2$ for the lower ionization state.

The correction factor in the ionization energy for different values of electron densities obtained in our studies are given below.

$$\text{For } N_e = 10^{18} \text{ cm}^{-3} \quad \Delta E_\infty = 1.3 \text{ eV}$$

$$\text{for } N_e = 10^{17} \text{ cm}^{-3} \quad \Delta E_\infty = 0.6 \text{ eV}$$

$$\text{for } N_e = 10^{16} \text{ cm}^{-3} \quad \Delta E_\infty = 0.3 \text{ eV}$$

During the spectral studies of laser produced carbon plasma, we have observed ionized species up to C IV along with molecular species like C₂. We have not observed any line of considerable intensity corresponding to excited carbon atom in the wavelength region studied. Intensities of the successive ionized lines of carbon *viz*, C II, (C⁺) and C III (C⁺⁺) are used for these calculations. There are two unknown quantities (T_e and n_e) in eqn. 5.2. We can have two equations by taking intensities corresponding to two lines each from the same ionization stage, from which T_e can be deduced.

For the given plasma temperature, we can qualitatively evaluate the variation of plasma density. The plasma density is related to the emission intensity and the plasma temperature by eqn.(5.2).

For the evaluation of T_e and n_e we make use of line intensities corresponding to the lines at 464.7 nm and 569.6 nm of C III and 392 nm and 407.4 nm lines of C II. The spectroscopic constants of these spectral lines are given in table 5.1.

Table 5.1. Spectroscopic data of the lines selected [30]

Lines	Wavelength (nm)	Excitation energy (eV)	g	f
CII	392.07	19.41	4	0.134
CII	407.49	27.30	2	0.797
CIII	464.74	32.05	3	0.423
CIII	569.60	34.13	3	0.407

5.3.1 Spatial dependence

It is possible to distinguish between two phases in the time and space evolution of the laser induced vapour plasma [5]. The first one is the ionizing phase characterized by laser heating of the target and the dense ionized vapour in the vicinity of the surface. The second one is the recombining phase of the expanding plasma. The first phase is not

accessible for optical emission spectroscopic observation because of the reduced dimension of the dense ionizing vapour layer and its high optical opacity. The only indicator of the ionizing phase is the continuum emission which is very intense in the vicinity of the target surface. Due to high density of particles in the initial stages of the plasma expansion, there are numerous collisions lead to free-free (bremsstrahlung) and free-bound (recombination) transitions and plasma behaves as a continuum of compressible fluid [24, 49]. This plasma represents a heated high pressure gas kept in a region of small dimensions which later on, is allowed sudden expansion into the surrounding vacuum. In a laser produced plasma the preferential vapourization of the evaporated material is always found to be in a direction perpendicular to the target surface, irrespective of the angle of incidence of laser beam. The estimations of electron temperature and density of the laser produced carbon plasma were carried out here for distances up to 12 mm from the target surface in a time integrated manner. When the laser is focused onto the carbon target [which is placed in a vacuum (2×10^{-5} mbar)], due to density gradients in the plasma a rapid expansion takes place.

The spatial dependence of electron temperature of the carbon plasma deduced from line intensity measurements is given in fig. 5.1. The spectra are charted at a pressure of 2×10^{-5} mbar and at an irradiance of 50 GW cm^{-2} . The temperature shows a steadily decreasing behaviour with distance. With increasing separation from the target surface, the electron temperature falls from 2.43 eV to 1.6 eV. The variation of electron temperature with distance (z) perpendicular to the target surface shows a $z^{-0.1}$ dependence. For these studies time integrated intensities were used and the value of T_e presented in different distances from the target should be regarded as indicative of the average conditions occurring in an Nd:YAG laser induced carbon plasma, rather than defining the conditions at a particular stage of its evolution.

The density of the plasma at a point z , at any time t can be expressed as [49]

$$n_e(z, t) = n_0(t) \frac{t}{\tau} \left(1 - \frac{z}{Z(t)} \right) \quad (t < \tau) \quad (5.4)$$

where n_0 is the density at the center of the laser irradiated spot ($z = 0$) at time t ; t/τ takes into account of the injection of particles into the plasma (τ , pulse width of the laser); the z coordinate is directed perpendicular to the target and $Z(t)$ refer the spatial coordinate of the leading edge of the plasma. The above equation shows that the number of particles of the plasma increases linearly with time (for $t < \tau$, isothermal expansion)

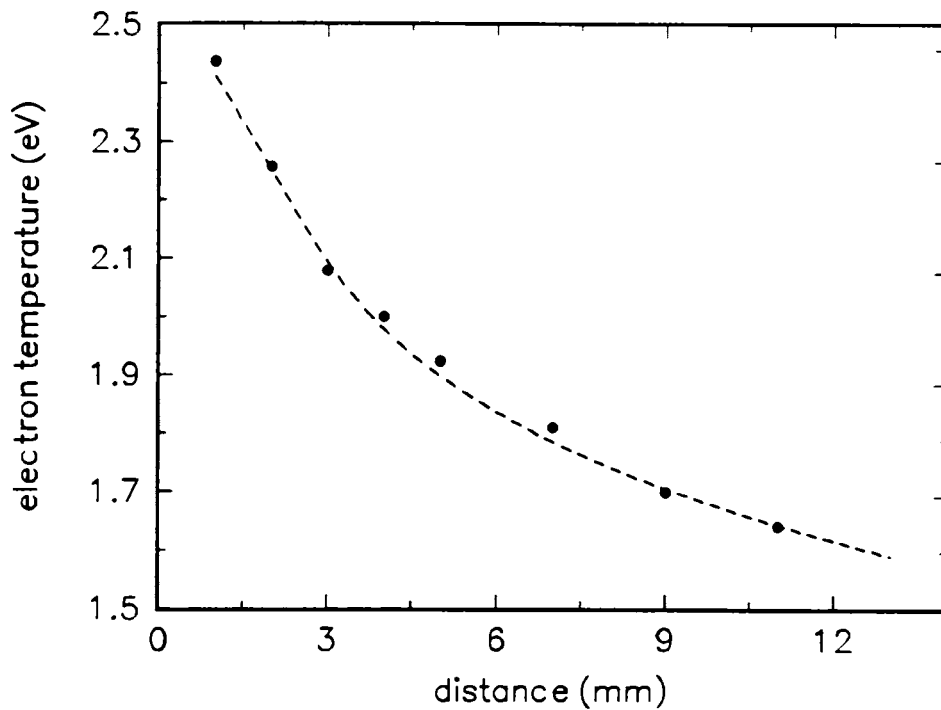


Figure 5.1: The variation of electron temperature as a function of distance from the target surface (laser irradiance used 50 GW cm^{-2} and pressure $2 \times 10^{-5} \text{ mbar}$)

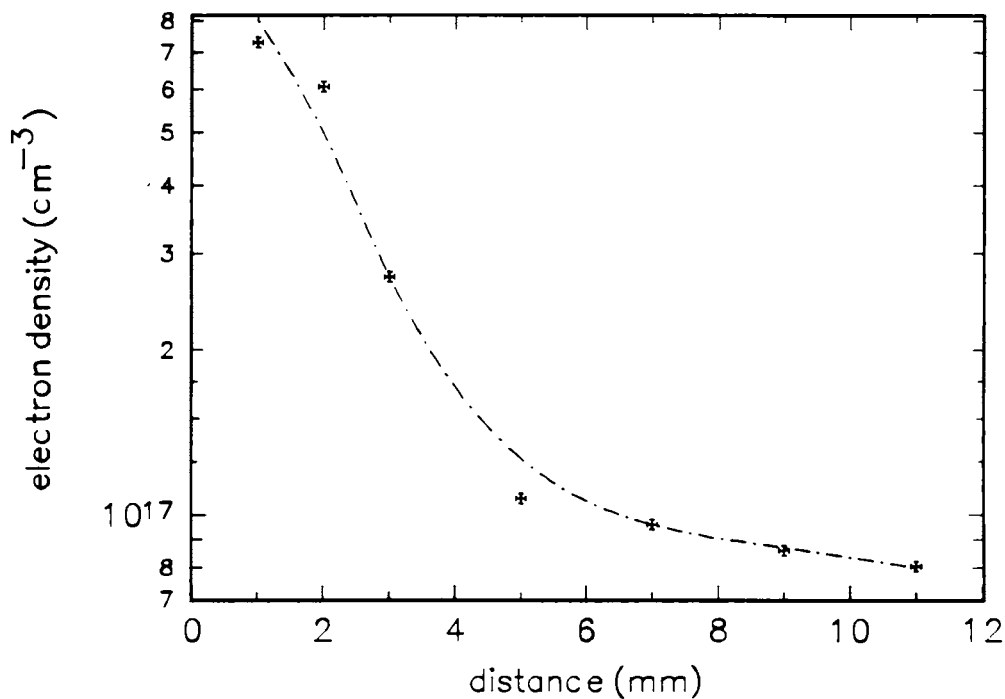


Figure 5.2: Electron density of the graphite plasma as a function of distance from the target surface (laser irradiance used 50 GW cm^{-2} and pressure $2 \times 10^{-5} \text{ mbar}$)

during the incidence of the laser pulse due to constant evaporation from the target. In the adiabatic expansion there is no increase in the number of particles ($t > \tau$), the density gradients can be expressed as [49]

$$n(z, t) = n_0(t) \left(1 - \frac{z}{Z(t)} \right) \quad (t > \tau) \quad (5.5)$$

According to eqns. 5.4 & 5.5, the density decreases linearly with distance from the target surface. The spatial dependence of electron density of the carbon plasma is given in fig. 5.2. With increase in separation from the target surface, the electron density decreases from $7 \times 10^{17} \text{cm}^{-3}$ at 1 mm to $3 \times 10^{16} \text{cm}^{-3}$ at 11 mm.

5.3.2 Time dependence

The temporal evolutions of electron temperature and electron density are of prime importance, since many kinetic reaction rates depend directly or indirectly on these parameters. The experimentally measured variations of temperature and density of the laser generated carbon plasma with time are given in figs. 5.3 and 5.4 respectively. For these studies the boxcar gate width was set at 10 ns. An initial electron temperature of about 3.6 eV and density of about $4 \times 10^{19} \text{cm}^{-3}$ were observed.

At shorter times (< 100 ns), the line to continuum ratio is so small and the temperature measurement is very sensitive to errors in setting the true continuum level. This problem is particularly acute for times up to 50 ns. For time interval > 100 ns, the line to continuum ratios are within reasonable limit, interference with the continuum measurement is not severe and the values of T_e shown in the figure should be reliable.

Initially the plasma expands isothermally within the time of the duration of the laser pulse. After the termination of the laser pulse, the plasma expands adiabatically. During this expansion the thermal energy is converted into kinetic energy and the plasma cools down rapidly. An adiabatic expansion of the plasma occurs, when the temperature can be related to the dimensions of the plasma by the adiabatic thermodynamic relation

$$T[X(t)Y(t)Z(t)]^{\gamma-1} = \text{constant} \quad (5.6)$$

where γ is the ratio of specific heat capacities at constant pressure and volume, $X(t)$, $Y(t)$ and $Z(t)$ are the dimension of the expanding plasma in the three mutually orthogonal directions.

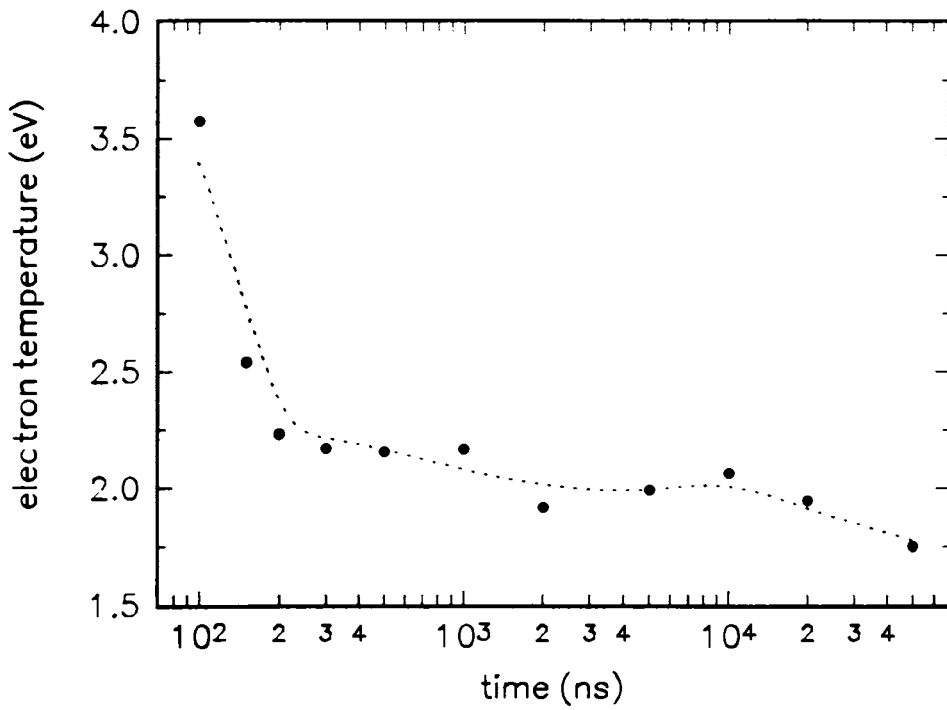


Figure 5.3: Electron temperature of the expanding plasma as a function of time (distance 3 mm; pressure 2×10^{-5} mbar, 50 GW cm^{-2})

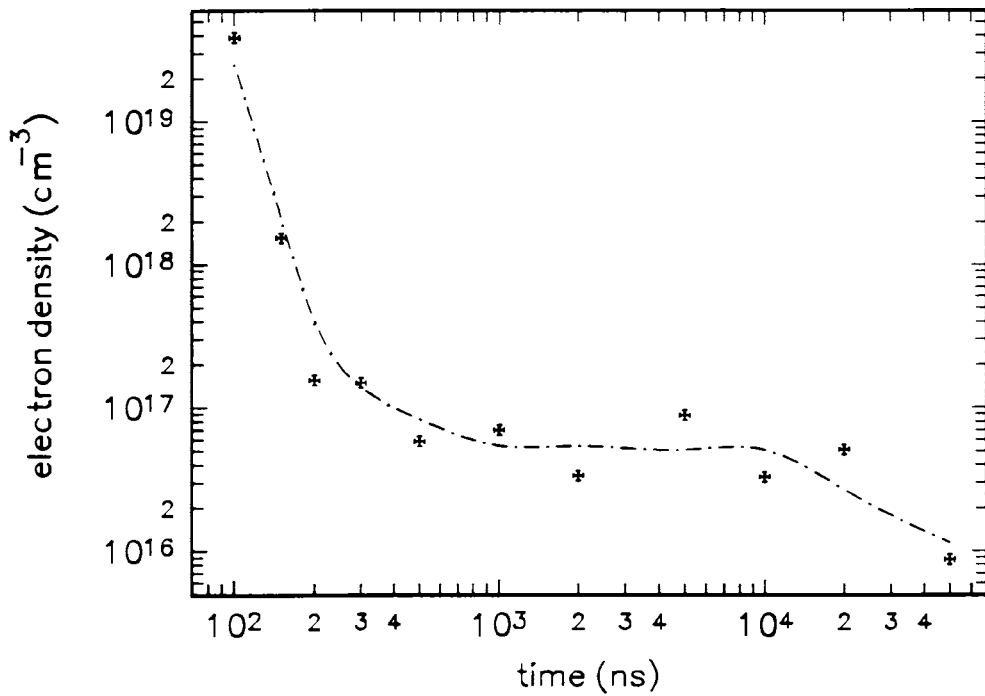


Figure 5.4: Electron density of the expanding plasma as a function of time (distance 3 mm; pressure 2×10^{-5} mbar, laser power density 50 GW cm^{-2})

It is noted that within 300 ns after the laser pulse the temperature drops from 3.6 eV to 2.1 eV while the density falls from $4 \times 10^{19} \text{cm}^{-3}$ to $1 \times 10^{17} \text{cm}^{-3}$. In the early stage of plasma evolution the electron temperature is high and it varies very rapidly. When the time is greater than 300 ns, the electron temperature (kT) of the plasma is reduced to about ~ 2 eV. But afterwards the temperature gets stabilized for a period up to ~ 2000 ns.

As seen from the adiabatic equation of state, the rate of decrease of temperature strongly depends on the specific heat ratio γ . However, in actual practice (as shown in fig. 5.3) the temperature decreases more slowly than predicted by the adiabatic equation due to preferential expansion of the plasma in one dimension during initial stages and due to recombination effects. But, 300 ns after the initiation of the plasma the temperature begins to decrease more slowly due to the energy released by the recombinations which compensate the cooling due expansion processes. The variation of electron temperature with time (t) for $1.06 \mu\text{m}$ radiation show t^{-2} dependence which is in accordance with the theoretical adiabatic expansion model by Rumsby and Paul [50].

The variation of n_e with time can be explained as follows. During initial times, when $t < \tau$, plasma expands isothermally and when $t > \tau$, it expands adiabatically. In the adiabatic regime, according to eqn. 5.5, the density decreases linearly with time. But in actual practice the density varies exponentially with time because of the high expansion velocities of the leading edge of the plasma which makes the plasma transparent the laser beam. The electron temperature has been found to decay with a dependence $T_e \propto t^{-2}$ rather than the reported theoretical $T_e \propto t^{-3}$ [50]. Such discrepancies from the t^{-3} has been noted by others also [50].

5.3.3 Dependence on Laser Irradiance

The nature and characteristics of the laser produced plasma strongly depend on the laser irradiance. Figs. 5.5 and 5.6 give variation of electron temperature and density of the laser produced graphite plasma with respect to laser irradiance (3 mm, 2×10^{-5} mbar). Time integrated line intensities were used for these calculations. As laser irradiance increases from 21 GW cm^{-2} to 64 GW cm^{-2} , the electron temperature increases from 1.29 eV to 2.15 eV, and saturates at higher irradiance levels while electron densities varies from $5 \times 10^{15} \text{cm}^{-3}$ to $2 \times 10^{17} \text{cm}^{-3}$ and then saturates. The saturation in T_e and n_e at higher irradiance conditions is expected to be due to plasma shielding, *ie.*,

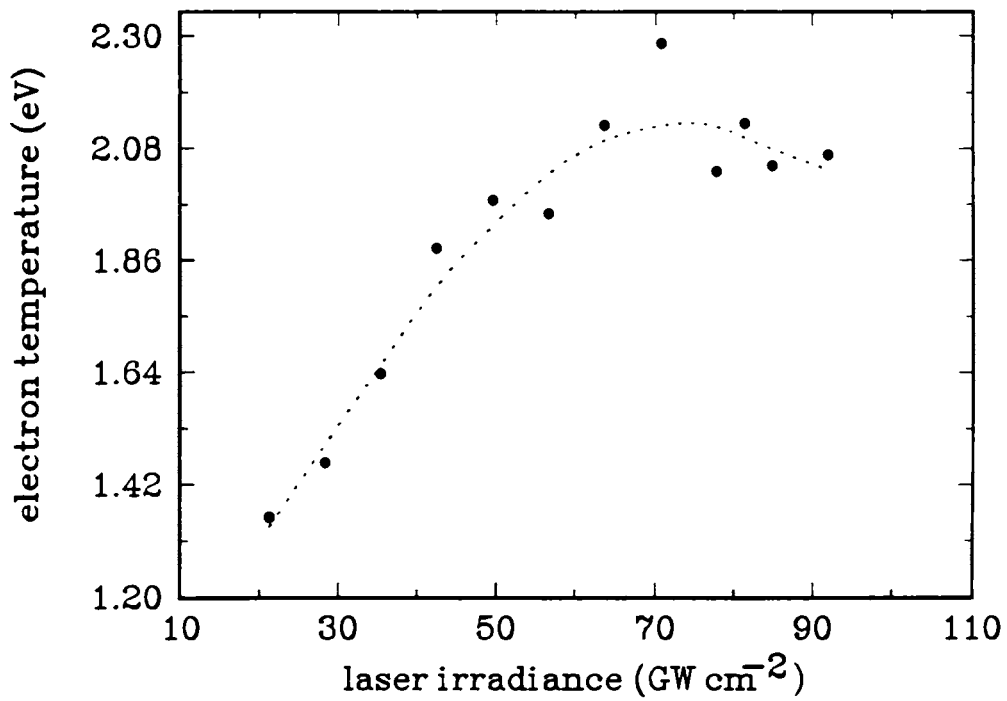


Figure 5.5: The variation of electron temperature with laser irradiance (distance 3 mm)

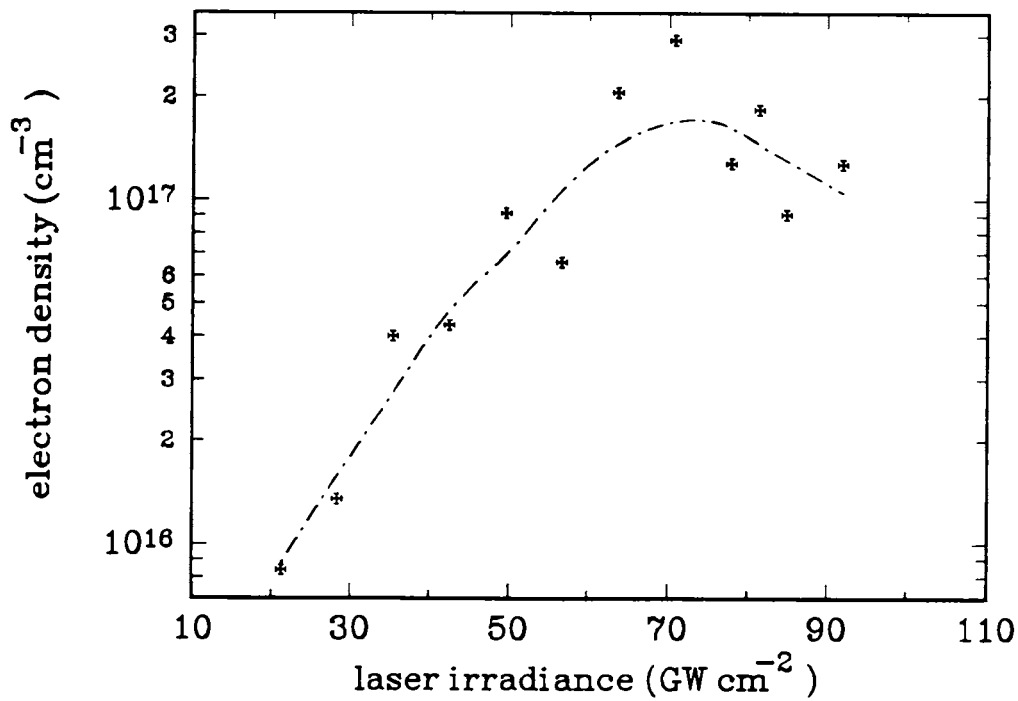


Figure 5.6: The variation of electron temperature with laser irradiance (distance 3 mm)

absorption and/or reflection of the laser photons by the plasma itself [51]. The reflection of the incident laser beam depends on the plasma frequency ν_p , which should be lower than the laser frequency. For Nd:YAG laser with its fundamental wavelength ($1.06 \mu m$) corresponds to a frequency $\nu_l = 2.828 \times 10^{14}$ Hz. The plasma frequency is given by $\nu_p = 8.9 \times 10^3 n_e^{0.5}$, where n_e is the electron density. Calculations show that, with $n_e \sim 10^{17} cm^{-3}$, $\nu_p = 6.5 \times 10^{12}$ Hz, which is much smaller than the laser frequency. So the energy losses due to reflection of Nd:YAG laser beam from the plasma can be assumed to be insignificant. An expression for the plasma absorption coefficient k_{pl} which depends on the plasma and laser light frequencies can be written as [52]

$$k_{pl} = \frac{2\nu_l}{c} Im \left[\left(1 - \frac{\nu_p^2}{\nu_l^2 [1 + (i/\tau_{ei})]} \right)^{1/2} \right] \quad (5.7)$$

where τ_{ei} is the electron-ion collision time. The above equation is derived considering electromagnetic wave propagation in plasma, and is valid when the quasistationary approximation is satisfied, ie, when the amplitude of the electric field varies slowly with time. Since, ν_l , in our case, is much larger than ν_p , this approximation is valid. From this expression it follows that the absorption coefficient for laser radiation is approximately proportional to the square of the electron density, the square of the light wavelength and to $T_e^{-3/2}$. Essentially the same result is obtained by treating absorption as due to inverse bremsstrahlung [53]. This expression also reveals that the plasma absorption coefficient has a pronounced maximum when the laser frequency is in the vicinity of the plasma frequency.

When the vapour initially becomes slightly ionized, it absorbs part of the incident laser radiation. The energy is converted into internal energy of the plasma. With increase in plasma temperature, the degree of ionization of the vapour is also increased, thereby further enhancing absorption of the incident laser radiation. As the plasma density and temperature rise, the vapour phase progressively behaves like an optically thick medium. The plasma effectively shields the target surface from the trailing part of the laser pulse. The energy in the plasma is then transferred away by thermal radiation or converted into hydrodynamic motion. Due to lateral expansion of the plasma, the energy radiated from the plasma to the target is often distributed over an area significantly larger than the laser beam spot.

A radiating gas may be composed of molecules, atoms, ions and electrons. These particles have various energy levels associated with them. In accordance with the gen-

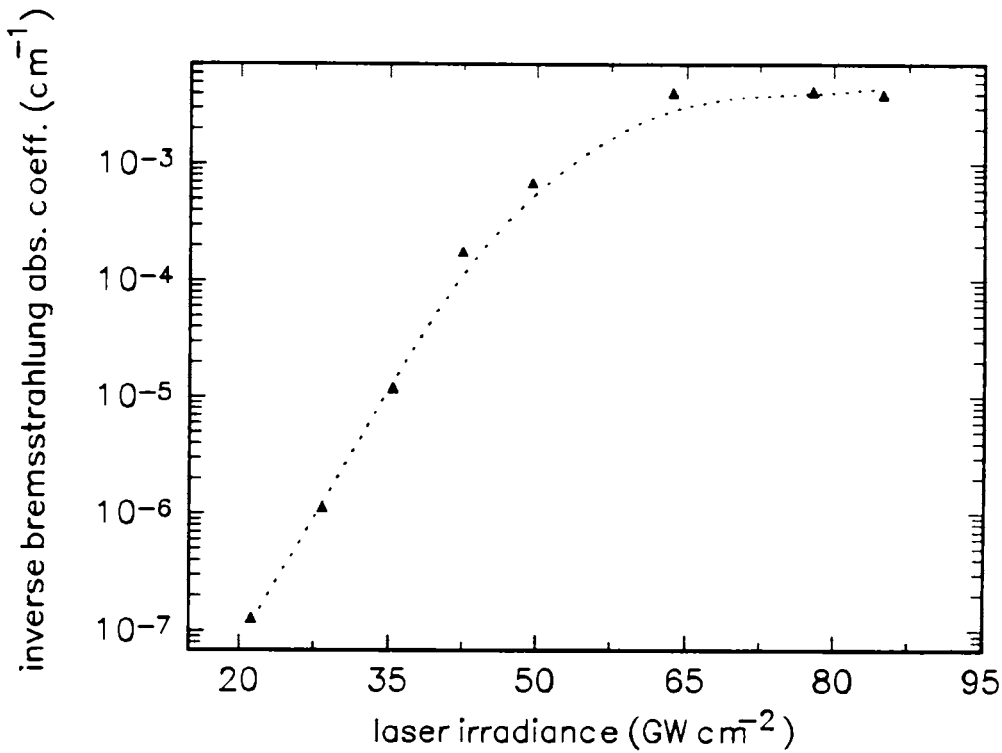


Figure 5.7: The estimated absorption depth (at $1.06 \mu\text{m}$) of graphite vapour plume for inverse Bremsstrahlung

eral scheme of allowed energy states of an atomic system, the electronic transitions accompanying absorption and emission of light are subdivided into three types: free-free, bound-free and bound-bound transitions. From an energy point of view on continuous spectra, bound-free and free-free transitions are of primary interest. The reason is that the radiant energy losses by distinct spectral lines usually represent small part of the continuous spectrum [53]. In this study it is assumed that the evaporated particles are either in atomic form or ionized states. The two dominant mechanisms responsible for plasma absorption at these laser irradiance levels used in our work are inverse bremsstrahlung and photoionization. Inverse bremsstrahlung absorption α_{ib} via free electrons is approximated by [53]

$$\alpha_{ib}(\text{cm}^{-1}) = 1.37 \times 10^{-35} \lambda^3 n_e^2 T_e^{1/2} \quad (5.8)$$

where λ is the wavelength of the laser photons in μm . The absorption due to inverse bremsstrahlung at different laser irradiance levels is shown in fig. 5.7. It is noted that the absorption due to inverse bremsstrahlung is negligibly small at low irradiance levels and increases with increasing laser irradiance.

Absorption via photoionization can be estimated with Kramer's formula and absorp-

tion coefficient [53, 54]

$$\alpha_{pi} = \sum_n 7.9 \times 10^{18} \left[\frac{E_n}{h\nu_l} \right]^3 \left[\frac{1}{E_n} \right]^{1/2} n_n \quad (5.9)$$

where E_n and n_n are the ionization energy and number density of the excited state n ; h , Plank's constant; ν_l , laser frequency; I , ionization potential of the ground state atom. The absorption coefficient of photo ionization is obtained by summing up all the excited states whose ionization energy are smaller than the laser photon energy. Since the excitation potentials of atomic transitions of carbon atoms are much greater than the photon energy of the pump used (1.17 eV), direct photoionization by the absorption of a laser photon is ruled out. The only possibility for this type of ionization to happen is by the simultaneous absorption of number of photons.

The ionization rate in the case of photoionization is given by [55]

$$W_n = \omega_0 n_e^{3/2} \left[\frac{\xi_{os}}{I_i} \right]^p \quad (5.10)$$

where $p = I_i/\hbar\omega_0$ is the number of photons absorbed and ξ_{os} is the electron oscillation energy which is given by

$$\xi_{os} = 0.093\lambda^2 I (eV) \quad (5.11)$$

where I is the power density used for the ablation ($W\text{ cm}^{-2}$). Since the ionization rate depends on number of absorbed quanta p and the laser irradiance through ξ_{os} , the slope of the log – log plot between laser irradiance and emission intensity will be a direct measure of number of photons involved in this process. Fig. 5.8 gives such a plot for C II and C III ionic species from the laser produced carbon plasma. One can see that the intensity of the line grows as I^p where $p = 10$ for C II and $p = 9$ for C III, which are in good agreement with the photon energy used in the present experiment and the first ionization potential of carbon atoms (11.3 eV). The mismatch observed in the case C III ions implies that along with photoionization, other processes like impact ionization and direct generation of the species at higher energy states also take place. At higher irradiance levels exponent is close to unity and obviously the multiphoton ionization is not a dominant process in this regime. Besides photoionization, other mechanisms especially impact ionization, thermal ionization etc. may also affect the absorption coefficient of the plasma.

The saturation in T_e and n_e at higher irradiances cannot be explained by considering only the prominent absorption mechanisms via, inverse bremsstrahlung and photoionization. Such temperature behaviour can be explained by assuming the formation of a

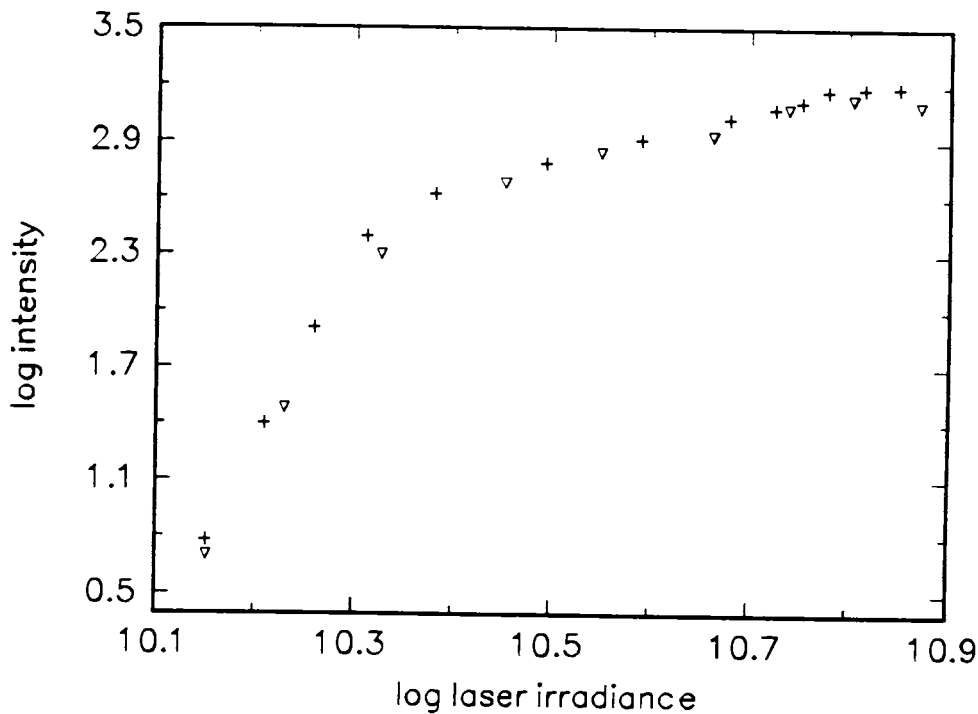


Figure 5.8: Variation of logarithm of the ion emission intensity of singly and doubly ionized species of carbon with laser irradiance (+ - C II, ∇ - C III)

self-regulating regime at higher irradiances. During the incidence of the laser pulse on the target surface, we can have four separate domains which include, (i). unaffected bulk target, (ii). evaporating target surface, (iii). area near the target absorbing the laser beam, and (iv). rapidly expanding outer edge of the plasma which is transparent to the laser beam. During isothermal expansion a dynamical equilibrium exists between the plasma absorption coefficient and rapid transfer of thermal energy into kinetic energy, which controls the isothermal temperature of the plasma. At high irradiance levels, when an appreciable amount of energy is absorbed by the plasma, a self-regulating regime may form near the target surface. If the absorption of the laser photons by the plasma becomes higher due to high plasma density, the evaporation of the species from the target becomes less, which in turn decreases density of the charged species. This consequently increases the absorption of the laser photons by the target, which in turn increases the temperature of the plasma. On the other hand, when the absorption of the laser energy is less, the process is reversed, with similar results. It has been theoretically proved that the density, temperature and dimensions of the plume adjust in such a manner that the plasma absorbs same amount of laser radiation to maintain a self-regulating

regime [56]. This assumption was found to be valid in laser generated plasma, where thermalization time is significantly less than the plasma expansion time, resulting in an establishment of uniform temperature in the plasma. The thermalization time τ_{ei} of energy exchange between electron and ions/neutrals during collision can be estimated from the relation [57]

$$\tau_{ei} = \frac{252MT_e^{8/2}}{\ln(\Lambda)n_e} \quad (5.12)$$

where

$$\Lambda = \frac{3(kT)^{3/2}}{4(\pi n_e)^{1/2}e^3} \quad (5.13)$$

where $\ln \Lambda$ stands for the Coulomb logarithm, which involves dynamical information about ion-electron collisions, M is atomic weight. With $n_e = 10^{17} \text{ cm}^{-3}$, $T_e \approx T$ (vapour temperature) = 22000 K, the relaxation time is ~ 3 fs, which is much smaller than the expansion time or pulse width of the laser beam which is of the order of few of nanoseconds.

5.3.4 Pressure dependence

The formation and role of a plasma resulting from the interaction between a laser beam and solid target in an ambient gas are reviewed extensively by various workers [7, 58-63]. Kagawa et al. [72] have studied the effect of surrounding gases like helium, argon, nitrogen and carbon dioxide on the emission characteristics of the nitrogen - laser induced plasma. Piemeir and Osten [73] have discussed the influence of the atmosphere on Q-switched laser sampling and the resulting plumes. They have also pointed out the importance of laser energy absorption by resulting plasmas. Laser induced fluorescence studies [74, 75] have indicated that the ambient atmosphere acted not only as a buffer to increase the residence time of the ablated atoms, but also helped to atomize ablated droplets. Some reports have also discussed the effect of ambient atmosphere on the improvement of the analytical performance of atomic emission spectrometry using laser induced plasmas [76, 77]. Iida [78] investigated the atmospheric effects on the laser vapourization process. Time-resolved spectroscopy and direct measurement of vapourized sample mass revealed that the atmosphere present during the vapourization phase was very important for both the effectiveness of the vapourization and the subsequent plasma emission measurement. Ownes and Majidi [79] studied the effects of increased pressure of buffer gas on the laser-induced plasma emission.

The three different laser intensity thresholds for plasma initiation in the presence of an ambient gas can be distinguished as the surface vapourization threshold, the target vapour plasma threshold and the ambient gas plasma threshold. These threshold values for vapourization, vapour plasma and gas breakdown strongly depend on experimental parameters like target material, wavelength of the laser radiation, nature of the ambient gas etc.

One of the important applications of laser produced plasma from graphite is the preparation of diamond-like carbon (DLC) films. Despite the considerable success that have been achieved in making DLC thin films by using laser ablated carbon plasma [64-66], dynamics of laser induced plume expansion into an ambient gas are not fully understood. Ablation into high pressure ambient gases results in shock waves and expansion fronts propagating through the background gas. With increase in background gas pressure, the fluorescence from all species increases as a result of increased collision rates on the leading edge of the expansion, slowing down of the plume boundary and the attenuation of the material penetrating the background gas [4]. Compared to the expansion into vacuum, the interaction of the plume with an ambient gas is a far more complicated gas dynamic process which involves deceleration, attenuation, thermalization of the ablated species, and the formation of the shock waves. Recent measurements performed over wide range of expansion durations have demonstrated a complicated gas dynamic picture of plume ambient gas interaction which is characterized by different propagation phases and is accompanied by plume oscillations at rather high background pressure [10-12,67]. Due to the complexity of the ablation dynamics, an appropriate theoretical description of plume expansion for a wide range of ablation conditions is lacking. In low gas pressure, the plume propagation could be described by Monte Carlo Simulation [68]. In moderate or high pressures, which is typical for thin film preparation, a blast wave model is found to describe accurately the plume propagation distance during the early expansion stages, whereas a shock layer model and an empirical drag model predict the maximum plume length with considerable accuracy [69-71].

We have studied the effects of atmosphere on the laser vapourization and excitation processes were investigated with spectral measurements. The spectral intensity measurements are carried out in a time integrated manner and these are used for the estimation of electron temperature and electron density. Studies were made by keeping the graphite target in three different atmospheres *viz.* air, helium and argon from 1 mbar to a pres-

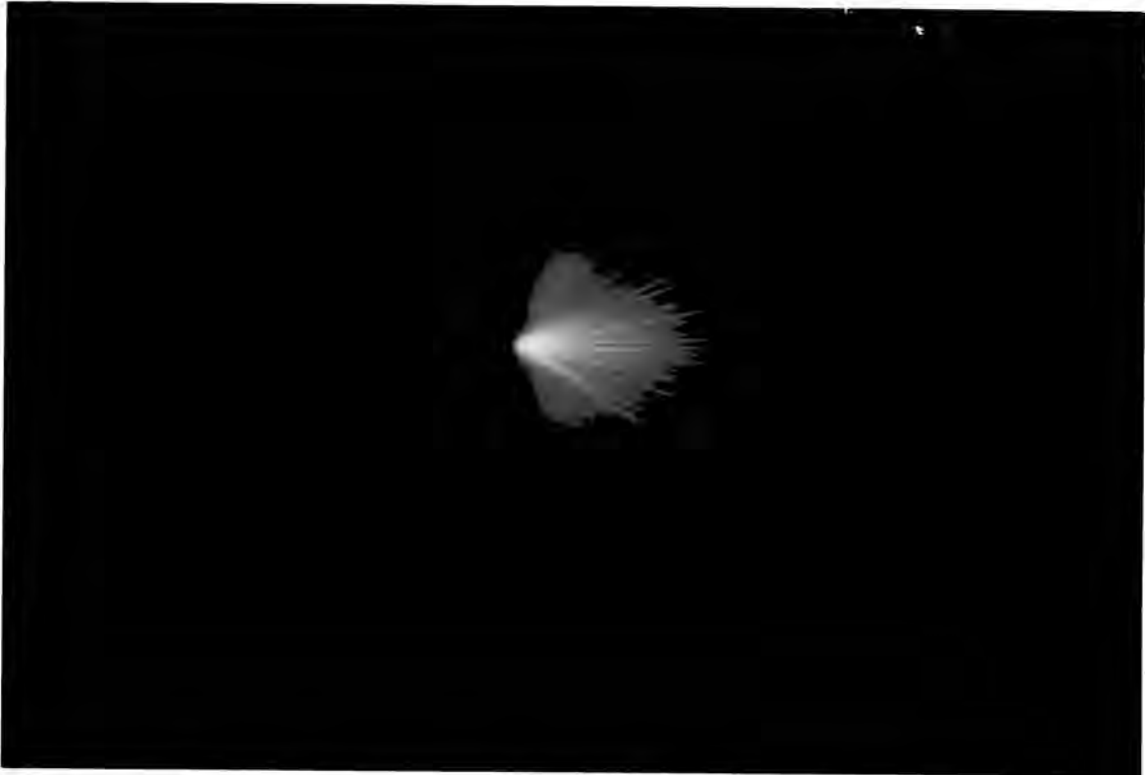


Figure 5.9: Photograph of the laser produced plasma emission from graphite target in helium atmosphere (0.1 mbar)

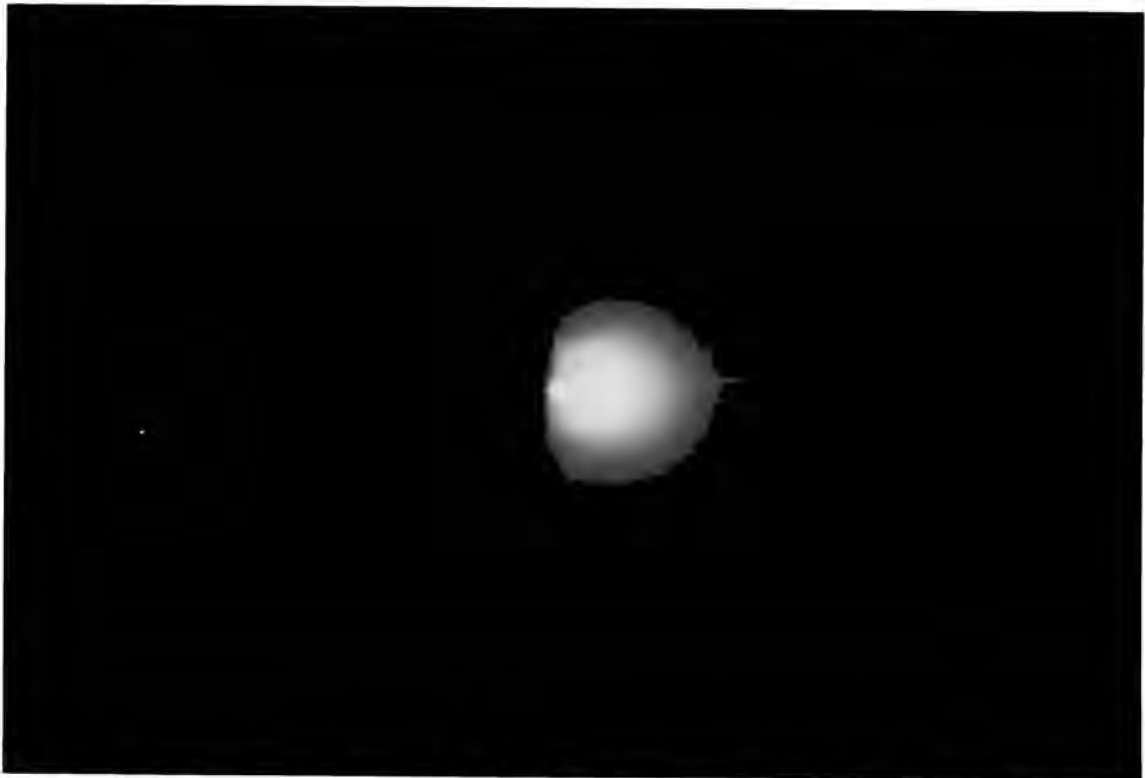


Figure 5.10: Photograph of the laser produced plasma emission from graphite target in argon atmosphere (0.1 mbar)

sure reduced to 10^{-5} mbar. Helium and argon gases are used as buffer gas for industrial applications such as welding. These rare gases avoid chemical reactions of ambient gas with targets.

The emission spectra, electron temperature and density are found to be significantly influenced by the ambient atmosphere. The addition of an ambient gas enhances the emission from all species. The relative enhancement depends on the gas pressure, the nature of the gas, and also the excitation energy of the electronic transition responsible of the line. The life time of all the transitions studied is of the order of few nanoseconds, while the observed increase of the emission occurs at a time in the order of few tens of nanoseconds [80], the increase in intensity should be due to species that have been excited during the plasma expansion. The two main processes invoked in the excitation are the particle collision excitation and electron impact excitation.

The shielding effect, ie. the absorption of the laser energy by the plasma strongly depends on nature of the background gas used. Ambient gas breakdown will profoundly influence the laser energy coupling to the target surface. If gas breakdown occurs before laser light reaches the sample surface, major part of the energy will be absorbed by the resulting plasma formed from the gas. The laser irradiance used in these studies is 50 GW cm^{-2} . The breakdown thresholds of helium and argon reported using Q-switched ruby laser are 3×10^{11} and $1 \times 10^{11} \text{ Wcm}^{-2}$ at atmospheric pressure and increase gradually with decrease in gas pressure [81]. In the present experimental work, the pressure range used for Ar and He are well below atmosphere pressure and one may safely predict that gas breakdown will not occur.

A cascade growth of the electron number density and absorption coefficient of the plasma will be greatly influenced by the nature of the background gas. A cascade like growth of electron density is an important process because of the absorption of the laser radiation by the plasma with increase in ambient gas pressure. The condition necessary for the development of cascade like growth is given by [82]

$$\frac{d\epsilon}{dt} = \frac{4\pi^2 e^2 I \nu_{eff}}{m_e c \omega^2} - \frac{2m_e \nu_{eff} E}{M} > 0 \quad (5.14)$$

where ϵ is the energy of the free electrons; e and m are the charge and mass of the electron; M , mass of the background gas neutral particle; E , the energy of the first ionization stage of the gas; ν_{eff} , the effective frequency of \bar{e} - neutral collision; I , radiation intensity and ω , the cyclic frequency of radiation. The first term on the right hand side of the eqn.

5.14 expresses the rate of growth of energy by the absorption of laser photons, and the second term gives the maximum rate of energy loss due to elastic and inelastic collisions with neutral gas particles.

According to the classical electrodynamics, the spectral absorption coefficient (k_{ib}) due to inverse bremsstrahlung is given by [83]

$$k_{ib} = [1 - \exp(-\hbar\omega/kT)] \left[\frac{16e^6\pi^2}{3\hbar cm_e\omega^3} \right] \left[\frac{2\pi}{3m_e kT} \right]^{1/2} n_e \sum_i Z_i^2 n_i g_i \quad (5.15)$$

where k is the Boltzmann constant, h , Planck's constant, T temperature, n_i and n_e represent the number of ions and electrons per unit volume, Z_i stands for the charge of ions and g_i , the Gaunt factor which corrects the semiclassical expression for quantum effects. In the above expression, the inverse bremsstrahlung contribution stemming from electron-neutral interaction has been neglected. This equation indicates that higher the electron density and degree of ionization, the more effectively the laser radiation is absorbed by the plasma.

When the plasma medium absorbs a significant fraction of laser energy, a laser supported detonation wave will be formed. Under this condition the length of the plasma can be written as [84]

$$z = \text{const} \left(\frac{E_F^2 \sigma (\gamma^2 - 1)}{\rho \beta} \right)^{1/5} t^{3/5} \quad (5.16)$$

where E_F is the electric field strength; γ , specific heat ratio; ρ , density of the ambient gas; β an absorption factor expressed partly by eqn. 5.15; and σ , the high frequency conductivity which is given by [83]

$$\sigma = \frac{e^2 n_e \nu}{m_e (\nu^2 + \omega^2)} \quad (5.17)$$

where ν is the electron collision frequency.

At moderately high pressures, the plasma expansion can be modeled as a blast wave, which is represented by [84]

$$z = \left(\frac{W}{\rho} \right)^{1/5} t^{2/5} \quad (5.18)$$

where W is the total energy absorbed. The dimension of the plasma, which is closely related to the density, temperature and coupling of laser radiation is influenced by the surrounding gas through eqns. 5.16 and 5.18. In our present work, the axial spread length of the plasma is considerably larger in helium atmosphere in comparison of argon and air, since density of helium is less than that of air and argon (fig. 5.11).

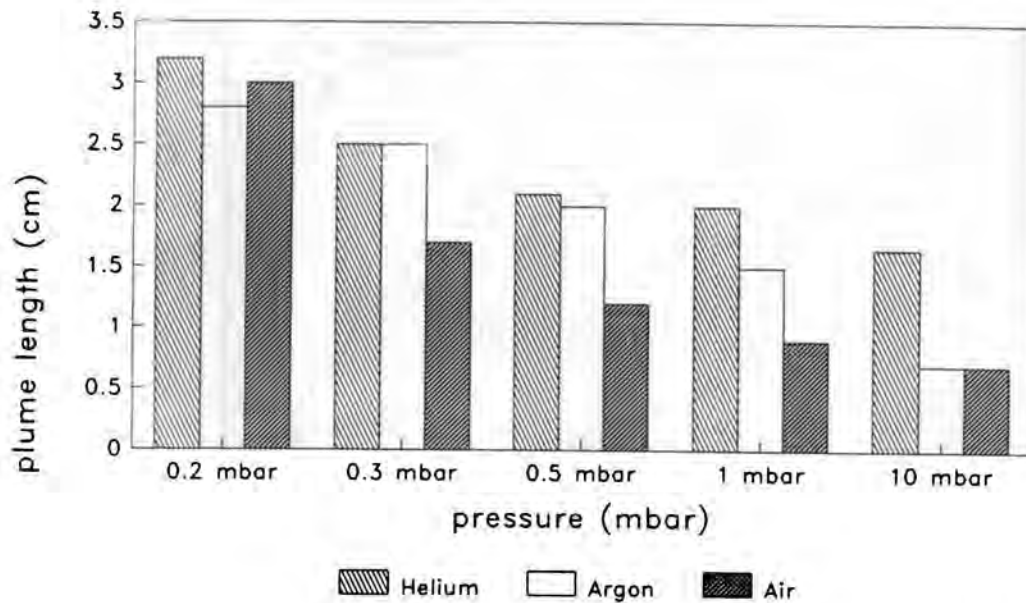


Figure 5.11: Approximate plume length of the laser produced graphite plasma at different background gas pressures

To get a clear idea about the background gas effect on the nature of the plasma, the physical processes of the ambient gases should be studied in detail. Some physical properties of the gases, which are related to plasma generation processes is given in the table 5.2.

Table. 5.2 : Physical properties of different ambient gases used [85]

	He	Ar	Air(N_2)
Atomic/molecular weight	4	40	28
Ionization energy (eV)	24.6	15.8	15.6
γ	1.67	1.67	1.40
Density (at 760 torr)(g/litre)	0.1785	1.784	1.251
Thermal conductivity ($10^{-6} cal s^{-1} deg^{-1} cm^{-1}$)	360.36	42.57	62.4

In comparing argon and helium atmospheres the cascade condition (eqn. 5.14) is more favoured for argon ($M = 40$, $E = 14.5$ eV) than He ($M = 4$, $E = 23.4$ eV). The plasma formed in Ar atmosphere are more absorptive than He atmosphere which directly influence the value of T_e and n_e . We have observed that the temperature and density of carbon plasma is higher in argon compared to the presence of helium or air. Further-

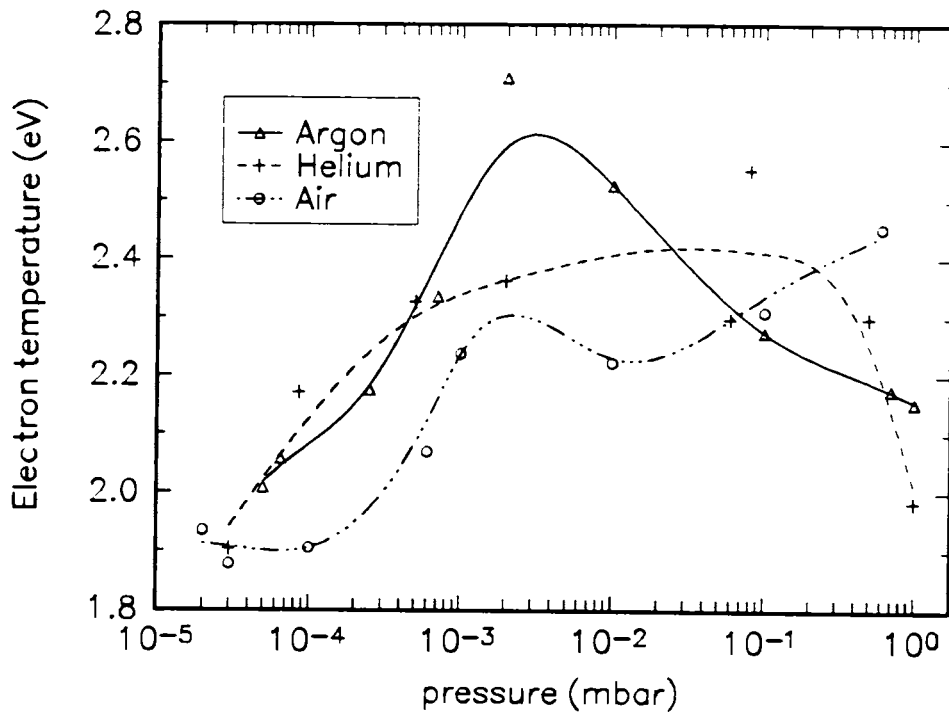


Figure 5.12: Variation of electron temperature as a function of pressure of the different ambient gas used

more, the pressure of the ambient gas is directly related to the plasma density so that the absorption coefficient increases with increase in ambient pressure.

Figs. 5.12 and 5.13 give the variation of time integrated electron temperature and electron density of the carbon plasma with pressure at different ambient atmosphere (Air, He and Ar). The plasma temperature T_e and density n_e show a somewhat similar behaviour for helium and argon ambient atmospheres. Despite the large difference in atomic mass between the two inert gases (≈ 4 for He and ≈ 40 for Ar) the temperature profiles in these two atmospheres are very similar. It can be seen that the electron temperature and density attains a maximum value at $\sim 10^{-2}$ mbar for argon and He ambient atmospheres, then decreases with change of pressure on either side. The decrease in electron temperature and density at pressures $< 10^{-2}$ mbar is presumably due to less efficient confinement of the plasma, so that plasma energy is distributed over a large volume. As the pressure of the ambient gas increases, confinement of the plasma takes place, which improves the elastic and inelastic collisions and thereby recombination processes. The increase in temperature with pressure is therefore due to the energy gained by the recombinations superseding the cooling due to increased intraplume colli-

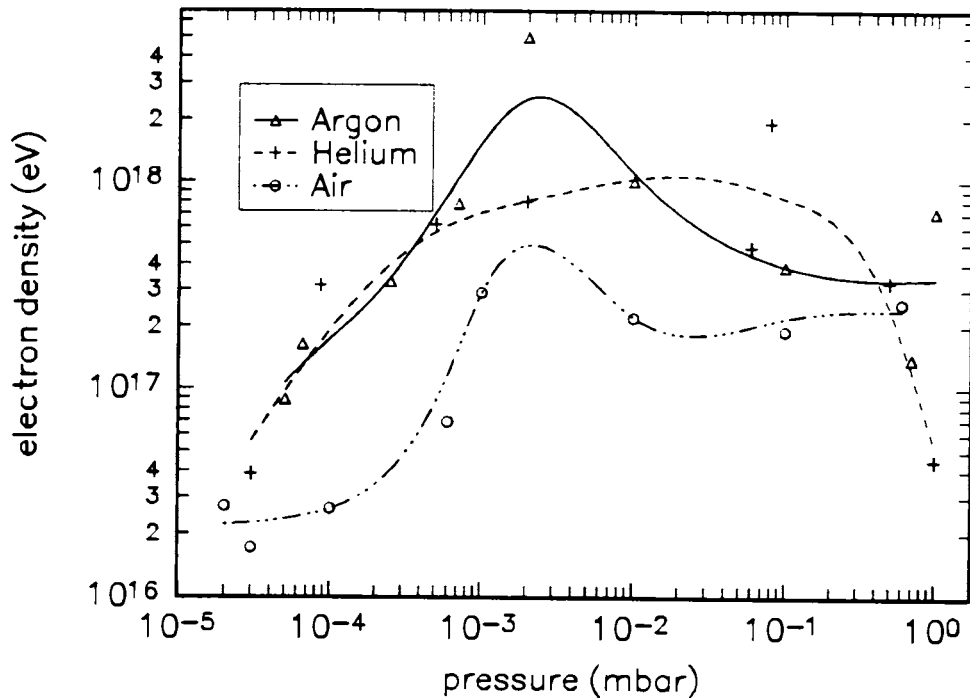


Figure 5.13: Variation of electron density as a function of pressure of the different ambient gas used

sions. At still higher pressures (pressures $> 10^{-2}$ mbar), the confinement of the plasma nearer to the target surface takes place, which in turn increases the effective frequency of electron collisions with background gas atoms. The cascade condition is not favoured at high pressures because of the energy loss due to elastic collision of the electrons with the neutral particles of the gas which supersedes the rate of growth of energy of free electrons via inverse bremsstrahlung and hence T_e and n_e decrease.

The temperature and density profiles in air is different from the profiles in helium and argon particularly at higher pressures ($\geq 10^{-2}$ mbar). T_e can be affected by chemical reactions in the plasma as well as by simple hydrodynamic expansion of the plasma. Higher temperature was obtained in 1 mbar air than was obtained with a similar argon and helium atmospheres. The nitrogen and oxygen present in air atmosphere influences the temperature through exothermic reactions [86].

The rate of change of electron temperature in the plasma is the sum of three terms *viz.*, elastic collision, electron heating due to collisional deexcitation of metastable ions and recombination of ions. The rate of loss of electron energy at short times is mainly

dominated by elastic collision term $Q_{\Delta t}$, given by [50]

$$Q_{\Delta t} = \frac{2m_e}{M_B} \sigma_{ea} n_B \left[\frac{8kT_e}{\pi m_e} \right]^{1/2} \quad (5.19)$$

where σ_{ea} represents elastic scattering cross-section between electrons and atoms; n_B and M_B are the density and mass of background gas atom. It is clear from the eqn. 5.19 that, the cooling is inversely proportional to M_B and hence lighter gases are efficient for rapid cooling. Helium being the lighter gas compared to argon or N_2 (air) gives rise to rapid cooling as is observed in the present experiment. The cooling effect by the high thermal conductivity of helium can suppress the background continuum.

5.4 Condition for LTE

The calculations of T_e and n_e were carried out under the assumption that the plasma is in LTE. In a transient system, such as the plasma formed by a pulsed laser beam, LTE is said to exist if the time between collisions of the particles in the plasma is small compared with the duration over which the plasma undergoes any significant change [8]. In LTE plasmas, the populations of atomic and ionic excited states are maintained by electron collisions. Since the collision frequency is proportional to the electron density, a lower limit for the electron density given in eqn. 5.20 has been determined that will maintain the populations to within 10

$$n_e \geq 1.4 \times 10^{14} T_e^{1/2} (\Delta E_{mn})^3 \text{ cm}^{-3} \quad (5.20)$$

ΔE_{mn} is the energy difference between the upper and lower states and T_e is the temperature. Using $\Delta E_{mn} = 3.16$ eV, corresponding to the largest energy gap of the four transitions (392 nm) used for temperature measurements, and the highest temperature 3.6 eV, the lower limit given by eqn. 5.20 is $8.4 \times 10^{15} \text{ cm}^{-3}$. Our observed values of n_e are always greater than this limit implying that LTE approximation assumed for our analysis is valid. However, it should be remembered that laser produced plasma is a transitory phenomenon, LTE applies only to a limited time interval and spatial positions.

5.5 Determination of Electron Density using Stark Broadening method

One of the most powerful spectroscopic techniques to determine the electron density is by the measurements the Stark broadened line profile of an isolated atom or singly charged ion with reasonable accuracy [30, 31, 87, 88]. The broadening of emission lines here is caused by the interactions of radiating atoms or ions with perturbing electrons or ions. In dense plasmas with temperatures in the 1-10 eV range, the dominant line broadening mechanism is Stark broadening. Stark broadening is principally a density effect and does not depend sensitively on the temperature or on the electron velocity distribution. Stark broadening is thus essentially independent of the assumption of LTE [89, 90]. It follows that the Stark broadening measurements will give reliable electron densities even in cases where the existence of LTE is doubtful, whereas some other methods would then become invalid.

In Stark broadening method absolute photon intensities are not required, and merely the relative line shapes and widths are sufficient to calculate electron density. Here, full widths at half maximum (FWHM), ie., wavelength differences between two points where the intensity has fallen by a factor of 2 from that at the maximum, should be used. Their measurements require some relative intensity calibration or test of linearity of the detector, but background corrections are not essential, as long as intensity maximum of the line is well above this background. In order to estimate the electron density, the Stark broadened profile of C II transition at 392 nm ($3p^2p^0 - 4s^2S$) is charted keeping the monochromator at its maximum resolution. The full width at half maximum (FWHM) of the lines $\Delta\lambda_{1/2}$ is related to the electron density by the expression [30]

$$\Delta\lambda_{1/2} = 2W\left[\frac{n_e}{10^{16}}\right] + 3.5A\left[\frac{n_e}{10^{16}}\right]^{1/4}\left[1 - \frac{3}{4}N_D^{-1/3}\right]W\left[\frac{n_e}{10^{16}}\right]A^0 \quad (5.21)$$

where W is the electron impact parameter which can be incorporated to different temperatures [30]; A , ion broadening parameter and N_D the number of particles in the Debye sphere defined as [88]

$$N_D = 1.72 \times 10^{12} \frac{[T(\text{eV})]^{3/2}}{[n_e(\text{m}^{-3})]^{1/2}} \quad (5.22)$$

The first term in the right side of eqn. 5.21 represents the broadening due to electron contribution and the second term is the ion correction factor. For nonhydrogenic ions Stark broadening is predominantly by electron impact. Since the perturbations caused by

ions is negligible compared to electrons, the ion correction factor can safely be neglected. Therefore eqn. 5.21 reduces to

$$\Delta\lambda_{1/2} = 2W\left[\frac{n_e}{10^{16}}\right]A^0 \quad (5.23)$$

Stark shift measurements can also yield electron density measurements. The shift in the Stark profile $\Delta\lambda_{shift}$ by the field contributed by electrons and ions and is given by the expression [30, 88]

$$\Delta\lambda_{shift} = D\left(\frac{n_e}{10^{16}}\right) \pm 2A\left(\frac{n_e}{10^{16}}\right)^{1/4}\left[1 - \frac{3}{4}N_D^{-1/3}\right]W\left(\frac{n_e}{10^{16}}\right)A^0 \quad (5.24)$$

where D is the electron impact shifts which can be incorporated to different temperatures [30]; The first term in the right side of eqn. 5.24 represents the shifts due to electron contribution and the second term is the ion correction factor. The minus sign in the shift formula applies to the high temperature range of those few lines that have a negative value of D/W at low temperatures. A comprehensive list of shift parameters D, A and N_D is given by Griem [30] for numerous lines of different atoms and singly ionized ions. But the shift measurements will yield electron densities with a precision that is, in general, inferior to that of width measurements [91, 92]. The major disadvantage of this method is that the calculated shifts, particularly the smaller ones, are not too reliable. Shifts measurements should be employed only if the cases in which the lines with ratios of shift to half-width of the order of 1 or larger [87].

The time integrated electron density measurements were made for C II transition at 392 nm. The Stark broadened line profile is approximately Lorentzian as shown in fig. 5.14 which fits fairly well with typical Lorentzian profile. Measurements were performed at different distances and various irradiance levels. Line shape analyses were repeated at different distances from the target surface which provide a direct indication of space evolution of electron density giving an insight into the basic ionization processes taking place in the pulsed laser ablation. Both emission and absorption spectroscopy measurements on plasma plumes yield spectral line widths [93-95] which are markedly wider than the corresponding natural line widths ($\sim 10^{-4} A^0$). The line shape of the absorption or emission lines are sensitive to local plasma conditions such as pressure and electron density, so line shape measurements has considerable diagnostic potential and provides a spectroscopic method for determination of local electron densities from the magnitude of the corresponding broadening. Three broadening mechanisms are likely to contribute

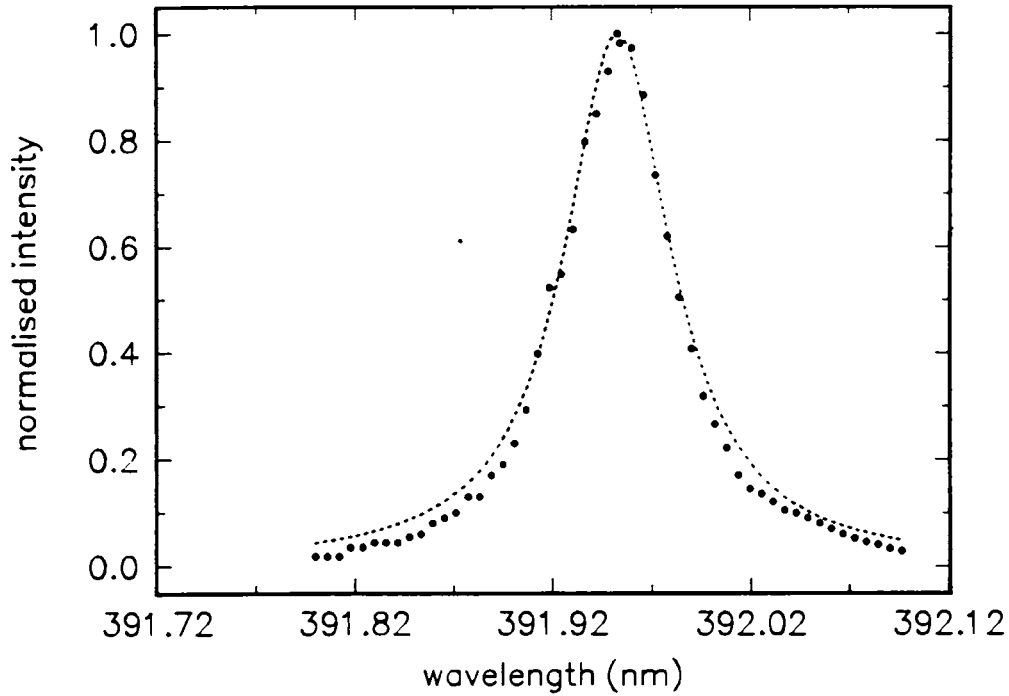


Figure 5.14: Stark broadened profile of C II at 392 nm along with fitted Lorentzian curve

significantly to UV/visible line widths observed in plasmas produced during pulsed laser deposition, *viz.*, Doppler broadening, resonance pressure broadening and Stark broadening. For ablation in vacuum, where ablated species exhibit high expansion velocities, one of the dominant contributions to spectral line broadening (particularly at distance > 5 mm from the target surface) is motional Doppler broadening which is due to different Doppler shifts (ie, $\Delta\lambda = \lambda v_z/c$) experienced by the species in different regions of the plume having different velocity components v_z in the observation direction. Typically for pulsed laser deposition plasmas the velocity component v_z are $\sim 10^6 \text{ cm s}^{-1}$ [96] which, for lines in the visible region, corresponds to Doppler line widths (FWHM) $\sim 0.13A^0$. The resonance pressure broadening interaction occurs on strong resonance lines of and atom/ion when excited atom/ion interacts with identical ground state atoms/ions. The resulting broadening is proportional to the ground state number density of the corresponding species and transition oscillator strength. Since the relatively small transition oscillator strength has been reported [97] for C II at 392 nm (0.134), the resonance broadening part can be safely neglected. Stark broadening of special lines in plasmas results from collisions with charged species which Stark shifts the energy levels of the atom/ion undergoing transition, resulting in both a broadening of the line width and a shift in the

line centre.

The half width of the Stark broadened profile is sensitive to plasma electron density even though the shape is a simple combination of Lorentz, Voigt or Stark shapes [91]. The dependence of the profile on the plasma conditions is complicated because it arises from the separate contributions of the Stark components of the radiative transition, each of which has an average position, width and intensity that varies with electron density and temperature. In addition, the amplitude shifts, and the presence or absence of fine structure and plasma induced forbidden components also contribute to the shape of the overall spectral profile. Each particular transition, therefore will have a shape with a specific dependence on the electron density that serves as the signature of the plasma conditions from which the line was emitted. It is this particular dependence of the environment of the radiating ion which enables the spectral profile to be used for diagnostic information.

5.5.1 Spatial dependence

The broadening close to the target, where the density is highest, is predominantly Stark, [46] and decreases rapidly with distances from the target, until at large distances only Doppler broadening (due to the ion streaming motions) is observed. To this end, in our work the observations have been made at a number of distances in the range 1-12 mm. Measurements could not be made at distances < 1 mm because of strong continuum emission. The spatial dependence of electron density of the carbon plasma is given in fig. 5.15 at laser irradiance of 50 GW cm^{-2} . Clearly the plasma expansion is characterised by a rapid decrease of density with distance from the target. According to the eqn 5.5, the electron density decrease linearly with distance from the target surface. With increasing separation from the target surface, the electron density decreases from $2.1 \times 10^{17} \text{ cm}^{-3}$ at 1 mm to $1 \times 10^{17} \text{ cm}^{-3}$ at 11 mm. The decrease of n_e as a function of distance is following approximately the $1/z$ law at short distances, indicating that the initial expansion of the electron gas is one dimensional, in good agreement with the predictions of the plume expansion model given by Singh and Narayan [49].

5.5.2 Dependence on Laser Irradiance

The nature and characteristics of the laser produced plasma strongly depends on the laser irradiance. Fig. 5.16 gives variation of electron density of the plasma with respect

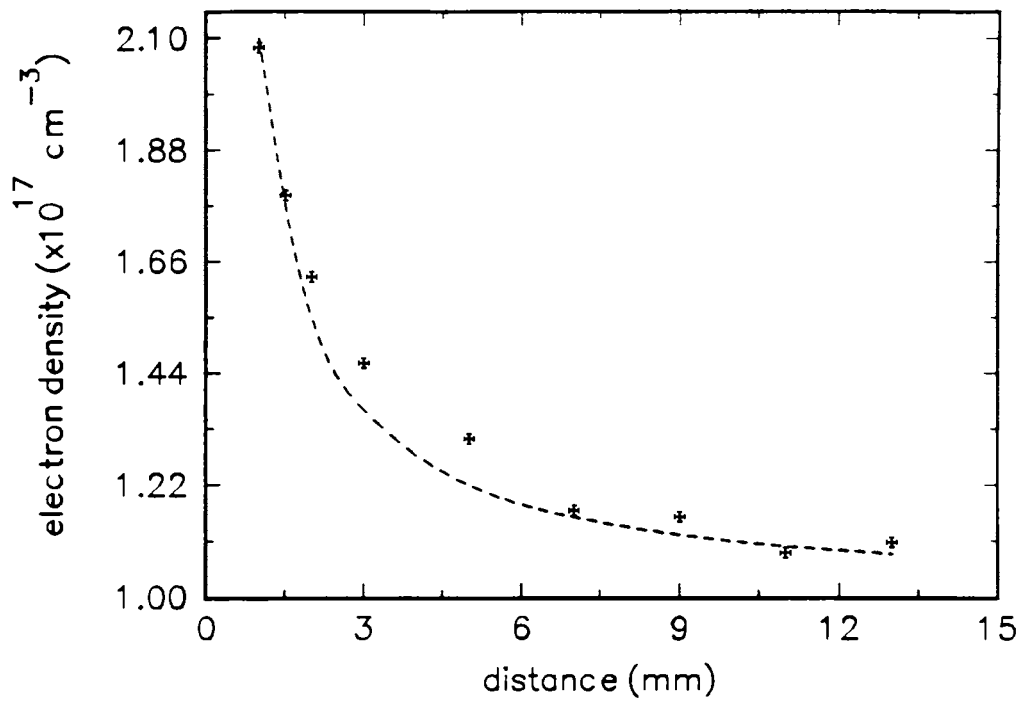


Figure 5.15: Electron density of the graphite plasma as a function of distance, the dotted line represents the $1/z$ curve

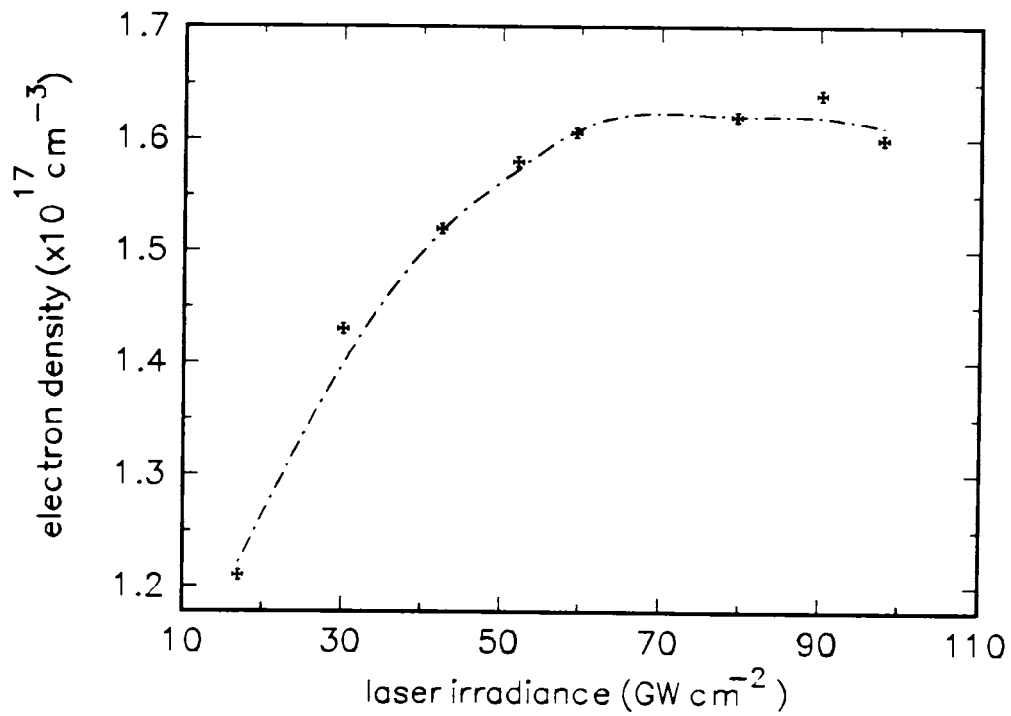


Figure 5.16: Variation of electron density with laser irradiance at a distance 3 mm from the target surface

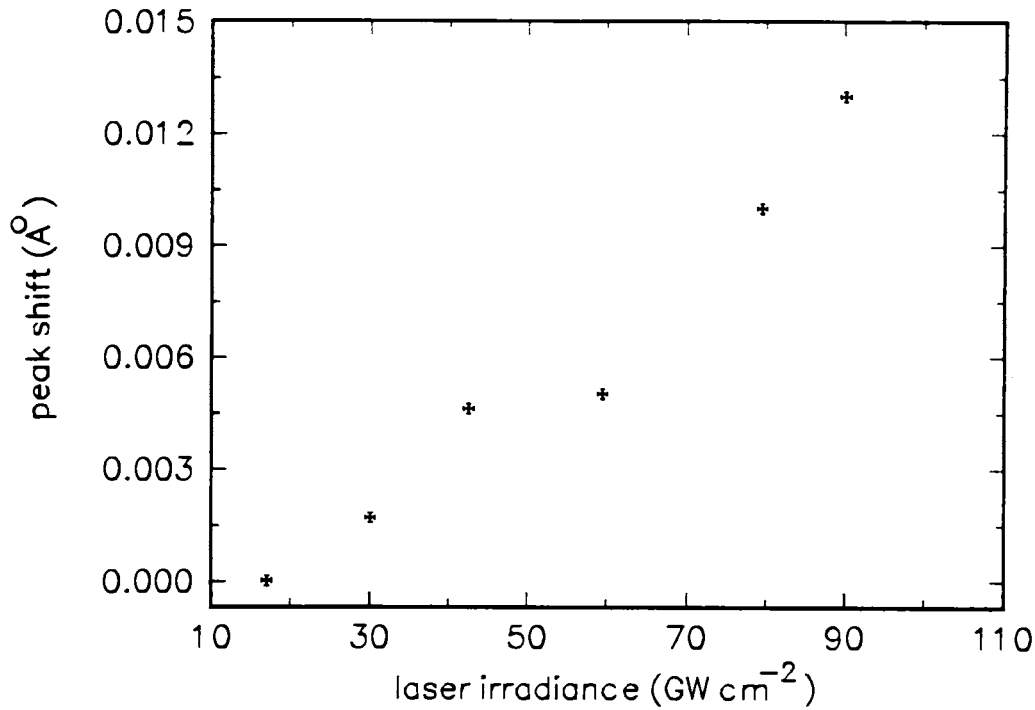


Figure 5.17: Peak shift observed in the profile at different irradiance levels (distance 3 mm). The dotted line represents the dotted Stark shift

to laser irradiance at distance 3 mm from the target surface. As laser irradiance increases from 18 GW cm^{-2} to 54 GW cm^{-2} , electron densities varies from $1.3 \times 10^{17} \text{ cm}^{-3}$ to $1.55 \times 10^{17} \text{ cm}^{-3}$ and then saturates. The saturation in n_e at high irradiance conditions are expected to be due to plasma shielding by the plasma, as discussed in the earlier sections.

It is observed that along with the broadening of the line, there is a shift of the peak towards the longer wavelength side (fig. 5.17). It is reported that this shift would be due to the inhomogeneities in the perturbing electric fields [97]. Usually elements other than hydrogen exhibit quadratic Stark effect and a line broadened by the quadratic effect tends to be asymmetric and shifted to longer wavelength side [87]. As the excitation energy increases, the crowding together of excited level increases, the excited levels on balance tend to be shifted down which results line shift towards longer wavelength side.

5.5.3 Time Dependence

The electron density during the initial duration of expansion ($< 100 \text{ ns}$) could not be properly determined by Stark broadening because of an intense background radiation.

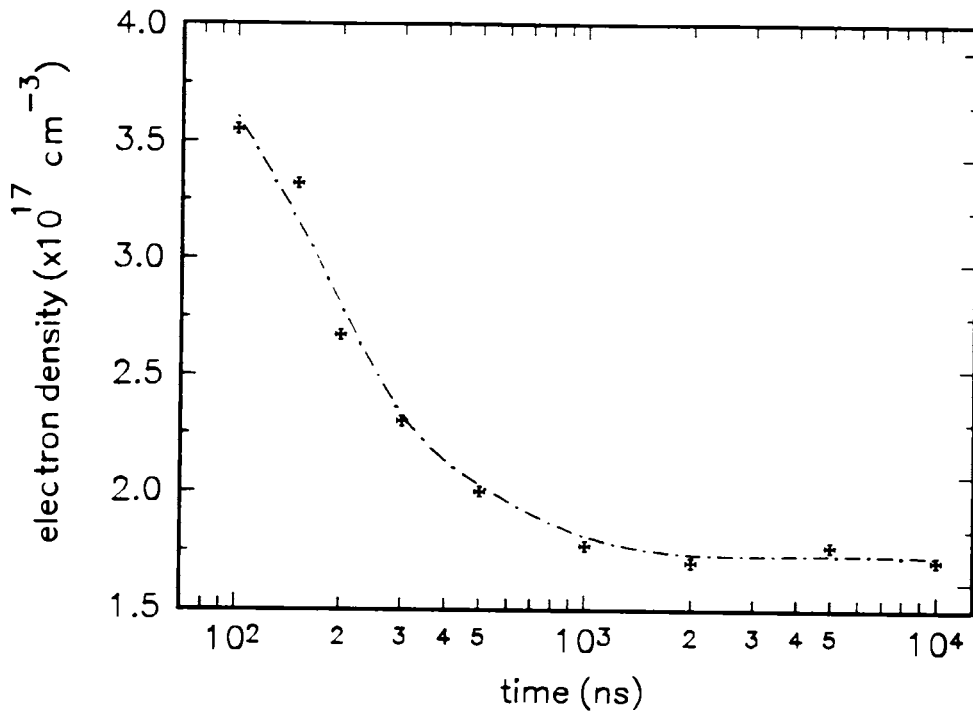


Figure 5.18: The variation of electron density with time after the initiation of plasma. (distance 3 mm, laser irradiance 50 GW cm^{-2})

The variation of electron density of carbon plasma with time is shown in fig. 5.18. The variation in electron density is similar to that of electron temperature. During the initial times electron density is around $3.5 \times 10^{17} \text{ cm}^{-3}$ which decreases to a value of $2 \times 10^{16} \text{ cm}^{-3}$ within 300 ns and then remains a constant value for about $10 \mu\text{s}$ after the elapse of laser pulse. The electron density variation with time shows a t^{-2} dependence on time, which is in accordance with the theoretical adiabatic expansion model developed by Rumsby [50].

5.6 Comparison between the two ways to determine the electron density

We have used two methods for the determination of electron density, viz., intensity ratios of successive ionization states of carbon and by Stark broadening. The existence of local thermodynamic equilibrium is not doubtful for the high electron densities ($n_e \sim 10^{17} \text{ cm}^{-3}$) and relatively low temperatures ($\sim 2 \text{ eV}$) in these experiments. It is noted that the behaviour of electron density profiles with different experimental parameters are more or less the same for these two methods. The electron density calculations show a

good agreement especially at distances ≥ 3 mm and at times later than 300 ns. The margins of error for the electron density measurements using two types of experiments are due to (a) plasma reproducibility errors (< 5 %), (b) calibration errors (< 10 %) and (c) uncertainties in the values of constant parameters such as oscillator strength, electron impact parameter etc. used for these calculations. The mismatch in the electron density calculations occurred at distances very near to the target surface and at shorter times are also expected to be due to the uncertainty in the condition for LTE at high temperatures and the error occurred in the spectral line intensity measurements where the plasma front is masked by continuum emission.

5.7 Conclusions

1.06 μm radiation from a Q-switched Nd:YAG laser was focused onto the graphite target where it produced a transient and elongated plasma. Electron density and temperature measurements were carried out by spectroscopic means. Line intensity ratios of the successive ionization stages of the carbon have been used for the determination of electron temperature and Stark broadened profile of first ionized carbon species is used for the electron density measurements. The dependence of electron density and electron temperature on different experimental parameters like distance from the target surface, time after the initiation of plasma, laser irradiance and pressure and nature of ambient gases used are also carried out. At very short distances and times the intense continuum radiation is emitted from the target surface. The line to continuum ratio improves as time evolves. An initial electron temperature of about 3.6 eV is observed and it decays rapidly to much lower values within 200 ns time. At greater times the electron temperature is more or less constant. The electron density exhibit an approximate $1/z$ dependence with spatial separation from the target surface.

With increase in laser irradiance, both electron temperature and density increase and saturate at higher irradiance levels. The saturation of electron density and temperature at these irradiance levels is expected to be due to plasma shielding. The absorption would occur by an inverse bremsstrahlung process, which involves the absorption of a photon by a free electron. Saturation phenomena of these fundamental parameters with laser irradiance can be explained by assuming the formation of self-regulating regime in the plume.

The electron temperature and density show an abrupt change with the addition of ambient gases and these parameters also depend on the nature and composition of the gas used. It is noted that hotter and denser plasmas are formed in Ar atmosphere compared to He and air as a result of difference in the efficiency of cascade-like growth of electron number density and plasma absorption coefficient. However, the differences between these parameter in Ar and He, and the profile in air, particularly at higher pressures, suggest that T_e and n_e may be affected by chemical reactions as well as simple hydrodynamic expansion of the plasma. Electron density measurements using two alternative spectroscopic methods show good agreement especially at distances ≥ 2 mm and times ≥ 300 ns. The drawback occurred in these measurements at short distances and short times are also discussed.

5.8 References

- [1] J. C. Miller and R. F. Haglund (eds). *Laser Ablation : Mechanisms and Applications* (Springer-Verlag, Heidelberg 1991).
- [2] J. C. Miller and D. B. Geohegan (eds). *Laser Ablation : Mechanisms and Applications II* (American Institute of Physics, New York, 1994).
- [3] R. W. Dreyfus, *J. Appl. Phys.*, **69** 1721 (1991).
- [4] D. B. Geohegan, *Thin Solid Films*, **220** 138 (1990).
- [5] J. Hermann, A. L. Thomann, C. Boulmer-Leborgne, B. Dubreuil, M. L. De Giorgi, A. Perrone, A. Luches and I. N. Mihailescu, *J. Appl. Phys.*, **77** 2928 (1995).
- [6] J. Hermann, C. Boulmer-Leborgne, I. N. Mihailescu and B. Dubreuil, *J. Appl. Phys.*, **73** 1091 (1993).
- [7] Y. Iida, *Spectrochimica Acta*, **45B** 1353 (1990).
- [8] D. B. Chrisey and G. K. Hubler (eds.) *Pulsed Laser Deposition of Thin Films* (John Wiley and sons, New York, 1994).
- [9] S. S. Harilal, P. Radhakrishnan, V. P. N. Nampoore and C. P. G. Vallabhan, *Appl. Phy. Letts.* **64** 3377 (1994).
- [10] S. S. Harilal, R. C. Issac, C. V. Bindhu, V. P. N. Nampoore and C. P. G. Vallabhan, *J. Appl. Phys.* **80** 3561 (1996).
- [11] S. S. Harilal, R. C. Issac, C. V. Bindhu, V. P. N. Nampoore and C. P. G. Vallabhan, *J. Appl. Phys.* **81** (in press) (1997).
- [12] S. S. Harilal, R. C. Issac, C. V. Bindhu, V. P. N. Nampoore and C. P. G. Vallabhan, *Jpn. Jour. Appl. Phys.* **36** 134 (1997).
- [13] S. S. Harilal, R. C. Issac, C. V. Bindhu, V. P. N. Nampoore and C. P. G. Vallabhan, *Spectrochimi. Acta A* (in press) (1997).
- [14] S. S. Harilal, R. C. Issac, C. V. Bindhu, V. P. N. Nampoore and C. P. G. Vallabhan, *J. Phys. D* (in press) (1997).

- [15] S. S. Harilal, R. C. Issac, C. V. Bindhu, V. P. N. Nampoori and C. P. G. Vallabhan, *Plasma Sour. Sci. Technol.* (in press) (1997).
- [16] S. S. Harilal, R. C. Issac, C. V. Bindhu, V. P. N. Nampoori and C. P. G. Vallabhan, *Pramana - J. Phys.* **46** 145 (1996).
- [17] A. Richter, *Thin Solid Films*, **188** 275 (1990).
- [18] M. Von Allmen, *Laser Beam Interactions with Materials* (Springer, Heidelberg, 1987).
- [19] M. Von Allmen, *J. Appl. Phys.*, **47** 5460 (1976).
- [20] J. R. Ho, C. P. Grigoropoulos and J. A. C. Humphrey, *J. Appl. Phys.*, **79** 7205 (1995).
- [21] J. F. Ready, *J. Appl. Phys.*, **36** 462 (1965).
- [22] J. A. McKay and J. T. Schriempf, *Appl. Phys. Lett.*, **35** 433 (1979).
- [23] W. E. Maher and R. B. Hall, *J. Appl. Phys.*, **51** 1338 (1980).
- [24] R. K. Singh and J. Narayan, *Phys. Rev. B*, **41** 8843 (1990).
- [25] M. Aden, E. Beyer and G. Herziger, *J. Phys.D*, **23** 655 (1990).
- [26] M. Aden, E. Beyer and G. Herziger, and H. Kunze, *J. Phys. D*, **25** 57 (1992).
- [27] M. Aden, E. W. Kreutz, and A. Voss, *J. Phys. D*, **25** 57 (1993).
- [28] S. Eliezer, A. Ghatak, H. Hora and E. Teller, *An Introduction to Equations of State : Theory and Applications* (Cambridge University Press, Cambridge, 1986).
- [29] P. Erpelding, A. Minardi and P. J. Bishop, *J. Heat. Trans.*, **113** 939 (1991).
- [30] H. R. Griem, *Plasma spectroscopy* (McGraw-Hill Book Company, New York, 1964).
- [31] H. R. Griem, *Spectral Line Broadening by Plasmas* (Academic Press, New York, 1974).
- [32] R. H. Huddelstone and S. L. Leonard, *Plasma Diagnostic Techniques* (Academic press, London, 1965).

- [33] D. B. Geohegan *Pulsed Laser Deposition of Thin Films* D. B. Chrisey and G. K. Hubler (eds.) (John Wiley and sons, New York, 1994).
- [34] G. Padmaja, Ph.D thesis, Cochin University of Science & Technology (1994).
- [35] M. A. Heald and C. B. Wharton, *Plasma diagnostics with microwaves* (Wiley, New York, 1965).
- [36] G. K. Varier, S. S. Harilal, R. C. Issac, C. V. Bindhu, V. P. N. Nampoori and C. P. G. Vallabhan, *Mod. Phys. Letts.B* **10** 235 (1996).
- [37] G. K. Varier, R. C. Issac, S. S. Harilal, C. V. Bindhu, V. P. N. Nampoori and C. P. G. Vallabhan, *Spectrochimica Acta B* (in press) (1997).
- [38] T. Mochizuki, K. Hirata, H. Ninomiya, K. Nakamura, K. Maeda, S. Horiguchi and Y. Fujiwara, *Opt. Commn.*, **72** 302 (1989).
- [39] M. C. M. Van de Sanden, J. M. de Regt, G. M. Janssen, J. A. M. Van der Mullen, D. C. Schram and B. Van der Sijde, *Rev. Sci. Instrum.*, **63** 3369 (1992).
- [40] S. B. Cameron, M. D. Tracy and J. F. Camacho, *IEEE Trans. Plas. Sci.*, **24** 45 (1996).
- [41] J. M. de Regt, J. A. M Van de Mullen and D. C. Schram, *Phy. Rev. E*, **52** (1995).
- [42] R. F. G. Meulenbroeks, M. F. M. Steenbakkens, Z. QIng, M. C. M. van de Sanden and D. C. Schram, *Phy. Rev. E*, **49** 2272 (1994)
- [43] Y. W. Huang, J. S. Wang, J. C. Moreno and H. R. Griem, *Phy. Rev. Lett.*, **65** 1757 (1990).
- [44] H. R. Griem, *Phy. Rev.*, **128** 515 (1962).
- [45] M. A. Gigisos, S. Mar, C. Perez and I de la Rosa, *Phy. Rev. E*, **49** 1575 (1994).
- [46] F. E. Irons, *J. Phys. B*, **6** 1562 (1973)
- [47] B. C. Boland, F. E. Irons and R. W. P. McWhirter, *J.Phys.B.*, **1** 1180 (1968).
- [48] M. Galanti and N. J. Peacock, *J. Phys. B* **8** 2427 (1975).

- [49] R. K. Singh, O. W. Holland and J. Narayan, *J. Appl. Phys.* **68**, 233 (1990).
- [50] P. T. Rumsby and J. W. M. Paul, *Plasma Phys.*, **16** 247 (1974).
- [51] J. F. Ready, *Effects of High Power Laser Radiation* (Academic, London 1971).
- [52] P. Mulser, R. Sigel and S. Witkowski, *Phys. Rep.*, **6** 187 (1973).
- [53] Ya. B. Zel'dovich and Yu. P. Reizer, *Physics of Shock Waves and High Temperature Dynamics Phenomena* (Academic, London 1968).
- [54] J. J. Chang and B. E. Warner, *Appl. Phys. Lett.*, **69** 473 (1996).
- [55] E. G. Gamaly, *Laser and Particle Beams*, **12** 185 (1994).
- [56] A. Caruso and R. Gratton, *Plasma Phys.*, **10** 867 (1968).
- [57] L. Spitzer, *Physics of Fully Ionized Gases* (Wiley-Interscience, New York, 1962).
- [58] A. V. Bulgakov and N. M. Bulgakova, *J. Phys. D*, **28** 1710 (1995).
- [59] C. Boulmer-Leborgne, J. Hermann and B. Dubreuil, *Plasma Sour. Sci. Tech.*, **2** 219 (1993).
- [60] J. Hermann, C. Boulmer-Leborgne, B. Dubreuil and I. N. Mihailescu, *J. Appl. Phys.*, **73** 1091 (1993).
- [61] M. R. Joseph, N. Xu and V. Majidi, *Spectrochimica Acta*, **49B** 89 (1994).
- [62] C. Timmer, S. K. Srivastava, T. E. Hall and A. F. Fucaloro, *J. Appl. Phys.*, **70** 1888 (1991).
- [63] M. Owens and V. Majidi, *Appl. Spectrosc.*, **45** 1463 (1991)
- [64] S. S. Wagal, E. M. Juengerman and C. B. Collins *Appl. Phys. Lett.* **53** 187 (1988).
- [65] F. Davanloo, E. M. Juengerman, D. R. Jander, T. J. Lee and C. B. Collins, *J. Appl. Phys.* **67** 2081 (1990).
- [66] R. K. Dwivedi and R. K. Thareja, *Surf. Coat. Technol.*, **73** 170 (1995).
- [67] D. H. Lowndes, D. B. Geohegan, A. A. Puretzky, D. P. Norton and C. M. Rouleau, *Science* **273** 898 (1996).

- [68] J. C. S. Kools, *J. Appl. Phys.*, **74** 6401 (1993).
- [69] D. B. Geohegan, *Appl. Phys. Lett.*, **60** 2732 (1992).
- [70] M. R. Pretechensky and A. P. Mayokov, *Appl. Superconductivity*, **1** 2011 (1993).
- [71] D. B. Geohegan in *Laser Ablation : Mechanisms and Applications* J. C. Miller and R. F. Haglund (eds) (Springer-Verlag, Heidelberg 1991).
- [72] K. Kagawa, M. Ohtani, S. Yokoi and S. Nakajima, *Spectrochimica Acta*, **39B** 525 (1984).
- [73] E. H. Piemeier and D. E. Osten, *Appl. Spectrosc.*, **25** 642 (1971).
- [74] A. L. Lewis and E. H. Piepmeier, *Appl. Spectrosc.*, **37** 523 (1983).
- [75] W. Sdorra and K. Niemax, *Spectrochimica Acta*, **45B** 917 (1990).
- [76] W. J. Treytz, K. W. Marich, J. B. Orenberg, P. W. Carr, D. C. Miller and D. Glick, *Anal. Chem.*, **43** 1452 (1971).
- [77] F. Leis, W. Sdorra, J. B. Ko and K. Neimar, *Mikrochimica Acta*, **II**, 185 (1989).
- [78] Y. Iida, *Appl. Spectrosc.* **43** 229 (1989).
- [79] M. Ownes and V. Majidi, *Appl. Spectrosc.*, **45** 1463 (1991)
- [80] See Chapter 4 of this thesis.
- [81] Young and Hercher, *J. Appl. Phys.*, **38** 4393 (1967).
- [82] G. M. Weyl in *Laser-induced Plasmas and Applications*, L. J. Radziemski and D. A. Cremers (eds), (Marcel Dekker, Inc., New York, 1989) Chapter 1.
- [83] R. G. Root in *Laser-induced Plasmas and Applications*, L. J. Radziemski and D. A. Cremers (eds), (Marcel Dekker, Inc., New York, 1989) Chapter 2.
- [84] T. P. Hughes, *Plasmas and Laser Light* (Adam Hilger, England 1975).
- [85] R. C. Weast, *CRC Handbook of Chemistry and Physics* (CRC press, Inc., Florida, 1988).

- [86] Y. Lee, T.L. Thiem, Gi-Ho Kim, Ye-Yung Teng and J. Sneddon, *Appl. Spectrosc.*, **46** 1597 (1992)
- [87] A.P.Thorne, *Spectrophysics* (Chapman and Hall, London, 1974).
- [88] G. Bekfi, *Principles of Laser Plasmas* (John Wiley & Sons, New York, 1976).
- [89] W. L. Wiese, *Plasma Diagnostic Techniques*, R. H. Huddlestone and S. L. Leonard (eds), (Academic Press, New York, 1965)
- [90] G. V. Marr, *Plasma Spectroscopy*, (Elsevier pub. company, New York, 1968).
- [91] H. F. Berg, A. W. Ali, R. Lincke and H. R. Griem, *Phys. Rev.*, **125** 199 (1962).
- [92] H. R. Griem, M. Baranger, A. C. Kolb and G. Oertel, *Phys. Rev.*, **125** 177 (1962).
- [93] R. Tambay, R. Singh and R. K Thareja, *J. Appl. Phys.*, **72** 1197 (1992).
- [94] A. H. El-Astal and T. Morrow, *J. Appl. Phys.*, **80** 1156 (1996).
- [95] F. Fuso, L. N. Vyacheslavov, G. Masciarelli and E. Arimontz, *J. Appl. Phys.*, **76** 8088 (1994).
- [96] See Chapter 4 of this Thesis.
- [97] R. M. Herman, *Bull. Ame. Phys. Soc.*, **5** 234 (1960).

Chapter 6

Spectroscopic Studies on Cyanogen Bands from Laser Produced Carbon Plasma

Time and space resolved studies of emission from CN molecules have been carried out in the plasma produced from graphite target by 1.06 μm pulses from a Q-switched Nd:YAG laser. Depending on the laser pulse energy, time of observation and position of the sampled volume of the plasma, the features of the emission spectrum are found to change drastically. The vibrational temperature and population distribution in the different vibrational levels have been studied as functions of distance, time, laser irradiance and ambient gas pressure. Evidences for nonlinear effects of the plasma medium like self-focusing which exhibits threshold-like behaviour are also obtained. The translational temperature calculated from time of flight is found to be higher than the observed vibrational temperature for CN molecules and the reason for this is explained.

Chapter 6

Spectroscopic Studies on Cyanogen Bands from Laser Produced Carbon Plasma

Time and space resolved studies of emission from CN molecules have been carried out in the plasma produced from graphite target by 1.06 μm pulses from a Q-switched Nd:YAG laser. Depending on the laser pulse energy, time of observation and position of the sampled volume of the plasma, the features of the emission spectrum are found to change drastically. The vibrational temperature and population distribution in the different vibrational levels have been studied as functions of distance, time, laser irradiance and ambient gas pressure. Evidences for nonlinear effects of the plasma medium like self-focusing which exhibits threshold-like behaviour are also obtained. The translational temperature calculated from time of flight is found to be higher than the observed vibrational temperature for CN molecules and the reason for this is explained.

6.1 Introduction

The Cyanogen (CN) system is of considerable astrophysical interest because of its use in determining the nitrogen abundance in stellar atmospheres [1]. The CN radical occurs in a wide variety of sources. It can be observed through either the red ($A^2\Pi \rightarrow X^2\Sigma^+$) or violet ($B^2\Sigma^+ \rightarrow X^2\Sigma^+$) emission systems [2]. In the laboratory, CN is abundant in flames, electrical discharges of all types, plasma produced during laser ablation of any carbon containing material in air or under partial vacuum conditions etc. CN is also detected in a wide variety of extraterrestrial sources including sun, stellar atmosphere, comets, red giants, interstellar clouds by techniques of microwave, infrared and ultraviolet spectroscopy [3-7]. In principle the two CN band systems should be an excellent probe of the chemistry under these conditions, where direct measurements are difficult or impossible. If the dissociation energy and transition probability of CN were known, the observed emission intensity in the stellar atmosphere could be converted into elemental abundance. Theoretical studies of the dissociation energy of the red and violet band systems of CN were carried out by Bauschlicher et al [8]. They reported that dissociation energy of CN molecules to be 7.65 ± 0.1 eV and the life time of the $v' = 0$ level of the violet system to be 62.4 ns. Fluorescence from the CN radical in both the $A^2\Pi$ and $B^2\Sigma^+$ states has been extensively studied [9, 10] as a probe of primary photochemical processes in cyanide-containing polyatomic molecules such as HCN, CH_3CN and ICN. This has led to detailed information of final energy distributions in the photofragments [9]. Much effort has therefore been devoted to determine reliable radiative transition probabilities and life times for the CN system. Knowels et al [11] reported Einstein coefficients of spontaneous emission and oscillator strengths for CN molecules.

CN molecules have been the subject of numerous laboratory investigations. It is reported that CN molecules produced by ablation using excimer laser are due to photochemical processes whereas if they are obtained by NIR (Nd:YAG) laser, thermal processes might be expected to be more relevant [12]. Rotational and vibrational temperatures of CN molecules produced during laser ablation of graphite target in air have been reported by Hatem et al [13]. Atoms or ions of carbon ejected during laser ablation of graphite target combine with the ambient nitrogen inside the plasma chamber producing the excited CN molecules through recombination processes. Characteristic spectral emission of CN bands were obtained due to $B^2\Sigma^+ \rightarrow X^2\Sigma^+$ for violet system

and $A^2\Pi \rightarrow X^2\Sigma^+$ for red system.

Irradiation of a target material with a high power laser pulse generates intense plasma emission from the target surface. Such laser generated plasma is a rich source for atomic, ionic and molecular species in various states of excitations [14, 15]. The abundance of molecular, atomic and ionic species in the plasma will depend on various parameters like nature of the target, laser power and pressure of the residual gas in the plasma chamber [16-18]. Laser induced plasma (LIP) from graphite target will contain, in addition to different clusters, atomic and ionic species of carbon and transient species like CN in a partially evacuated plasma chamber [19-21].

Depending on the time of observation and position of the sampled volume the features of the plasma emission change as the plasma expands. In the case of LIP from graphite target, the emission contain molecular band systems from different species like C_2 , CN etc.. It has been pointed out that the excited diatomic species, which are sources of band emission in the different regions of plasma, may be formed by a secondary photolysis of the initial products. The CN violet system ($B^2\Sigma^+ \rightarrow X^2\Sigma^+$) has been studied by a variety of techniques [22-24] since it is an important free radical occurring in many emission sources. Even though a few studies are available in the literature related to CN species in the plasma, a systematic investigation of spatial and temporal variations of the characteristics of the plasma has not been reported yet. This chapter describes the spatial, temporal, laser irradiance and ambient gas pressure dependence of the CN species generated in graphite plasma by $1.06 \mu m$ pulsed laser irradiation under partial vacuum using optical emission diagnostics technique. Optical spectroscopy is an effective as well as convenient tool to detect various transient species such as excited atoms, ions and diatomic/polyatomic molecules, all of which are produced during laser ablation. The vibrational temperature and its variations under different conditions have been evaluated from the emission spectrum of CN violet band.

6.2 Experimental Details

The schematic experimental set-up is shown in chapter 2. Plasma was produced by the irradiation of a high purity graphite target with $1.06 \mu m$ laser radiation from a Q-switched Nd:YAG laser at a pulse repetition frequency of 10 Hz. The target was placed in a partially evacuated chamber (0.05 mbar) with quartz windows. The target was

mechanically rotated so as to minimize the surface etching and after every five minutes' scan the focal spot was laterally shifted to different positions on the target surface in order to provide fresh surface for ablation. In the absence of this arrangement, emission line intensities tend to fade due to etching of the target surface.

The emission spectrum from the plasma was viewed normal to its expansion direction by imaging the plasma plume using appropriate collimating and focusing lenses onto the slit of a one meter Spex monochromator. The recording was done by a thermoelectrically cooled PMT which was coupled to a boxcar averager/gated integrator. The total extension of the plasma in the present set-up was about 25 mm beyond which the light emission became very weak for effective detection. For spatially resolved observations, different regions of the plume was focused on to the monochromator slit. In these studies, accuracy in spatial dimensions was better than 0.2 mm. The output from the gated integrator (gate width 100 ns), which averaged out emission intensities from ten consecutive pulses, was fed to a chart recorder. For temporal studies the PMT output was fed to a 200 MHz digital storage oscilloscope with 50 Ω input impedance.

6.3 Results and Discussion

6.3.1 Emission Spectra

The CN emission spectra of the LIP from graphite target were recorded in the region $\lambda\lambda$ 355 - 475 nm. All the emission intensities are corrected for the detector spectral response which was predetermined through use of a standard lamp. The emission spectrum is found to contain different vibrational bands of CN molecules in addition to atomic and ionized species of carbon. The intensities of the band emission has been found to depend on the delay time and distance from the target surface. Near the target surface atomic as well as ionic species predominate while in regions away from the target, molecular species like CN and C₂ dominate. In the present experiment the emission from the CN system arises from the outer region of the plasma that surrounds the laser beam. The atomic, ionic and molecular carbon ejected from the target due to laser ablation combines with the ambient nitrogen resulting in the formation of CN molecules. Characteristic spectral emission of CN molecule in the violet region is obtained due to $B^2\Sigma^+ \rightarrow X^2\Sigma^+$ transition. Well defined bands in sequences $\Delta v = 1, 0, -1, -2$ are recorded, where $\Delta v = v' - v''$ is the difference between the vibrational quantum numbers of the upper ($B^2\Sigma^+$)

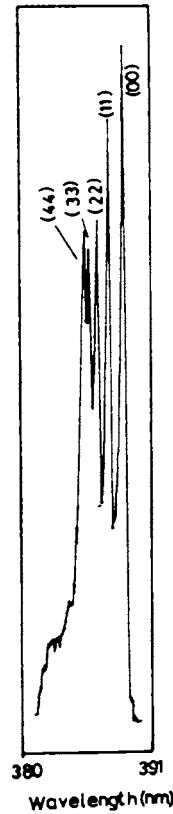


Figure 6.1: Spectrum of the resolved CN violet band emission for $\Delta v = 0$

and lower ($X^2\Sigma^+$) electronic states. The CN ($B \rightarrow X$) $\Delta v = 0$ violet band sequence (fig. 6.1) consisted of band heads (0-0) at 388.3 nm, (1-1) at 387.1 nm, (2-2) at 386.2 nm, (3-3) at 385.5 nm and (4-4) at 385.1 nm. For $\Delta v = -1$ (fig. 6.2) band heads from (0-1) at 421.6 nm to (5-6) at 415.2 nm are found to be predominant. We also observed the $\Delta v = 1$ CN violet sequence (fig. 6.3) with band heads of (1-0) at 359 nm, (2-1) at 358.6 nm and (3-2) at 358.4 nm. Fig. 6.4 shows the $\Delta v = -2$ violet band system with band heads of (0-2) at 460.6 nm, (1-3) at 457.8, (2-4) at 455.3nm, (3-5) at 453.2 nm, (4-6) 451.5 nm and (5-7) at 450.2 nm.

6.3.2 Spatial Dependence

One of the results in the present series of studies is that the spectral features are distinctly different for the emission from different sections of the plasma plume. For spatial studies, different parts of the plasma were imaged onto the slit of the monochromator. Fig. 6.5 gives the typical CN violet band ($\Delta v = 0$) for different distances along the plasma expansion direction at a laser power density of 35 GW cm^{-2} (pressure 0.05 mbar). The continuum emission intensity in the plasma emission is greatest in the region close to the

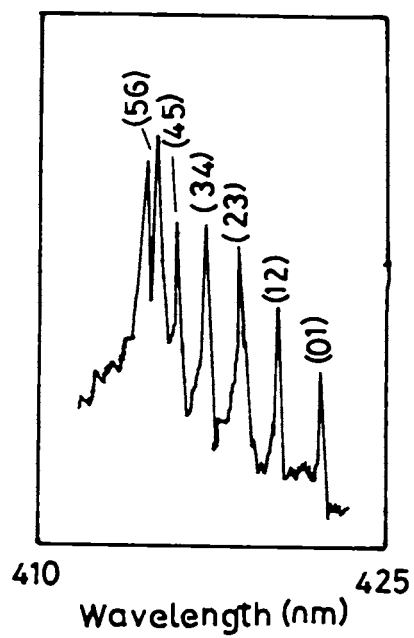


Figure 6.2: Spectrum of the resolved CN violet band emission for $\Delta v = -1$

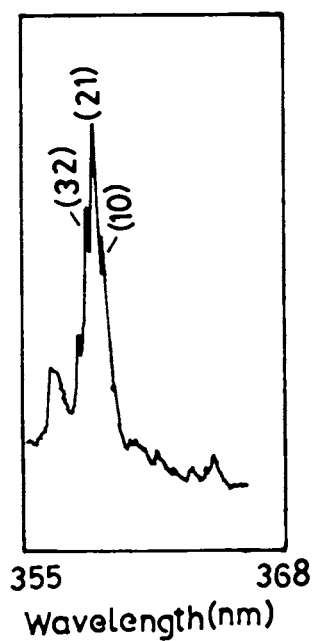


Figure 6.3: Spectrum of the resolved CN violet band emission for $\Delta v = 1$

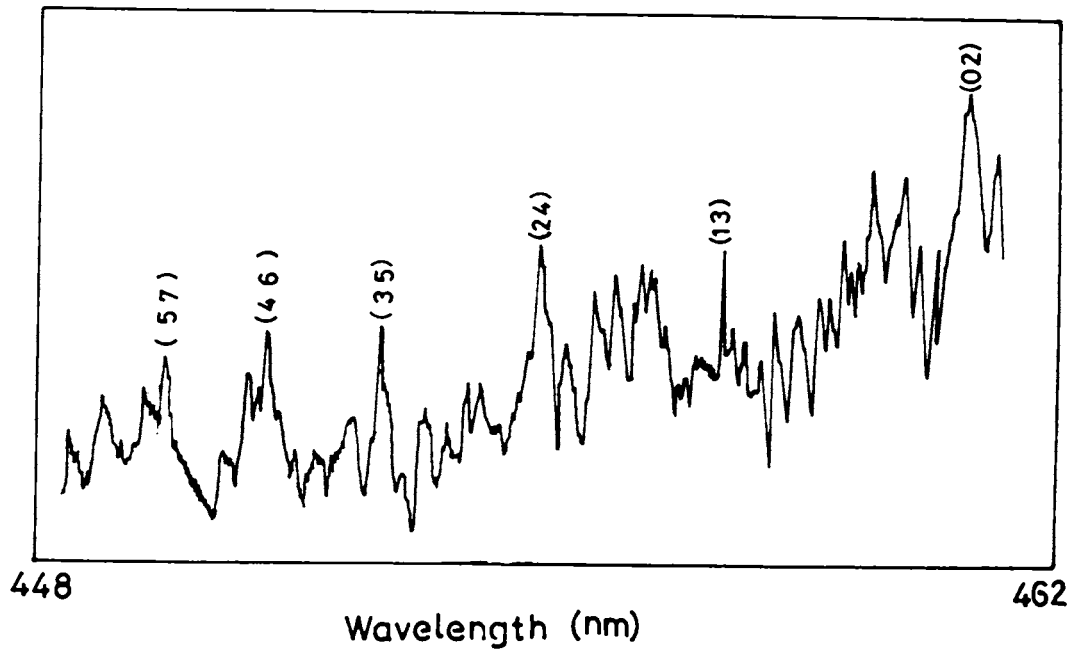


Figure 6.4: Spectrum of the resolved CN violet band emission for $\Delta v = -2$

target surface and decreases sharply within a few millimeters from the target surface. The spectral emission intensity is very bright during the initial stages (up to ~ 100 ns) of plume expansion due to Bremsstrahlung emission (free-free transition) from the hot plasma. In the region very close to the target surface, density in the plasma core is so high that much of the broadened line emission cannot be separated from the background. Farther away from the target surface, in the case of excited carbon species, the lines become narrower and weaker with increasing separation from the target. Spectrum show a gradual increase in the CN emission intensity up to a distance 10 mm away from the target and beyond this distance the intensity decreases rapidly. Contrary to this, the singly ionized carbon (C II) line intensity decreases continuously as we move away from the target. From this it can be inferred that CN emission arises from the outer region of the plasma as was already mentioned. For these studies the gate width was set at 100 ns. The average velocity being $6 \times 10^5 \text{ cm/sec}$ [25], for an integration time of 100 ns, the spatial distance travelled by CN molecules is 0.6 mm, which is smaller than the successive spatial steps of 1 mm. In our present work the spatial resolution was better than 0.2 mm. Hence there will not be any significant mixing of spatial and temporal aspects of plasma. The vibrational distribution in the excited states of CN molecules at distance

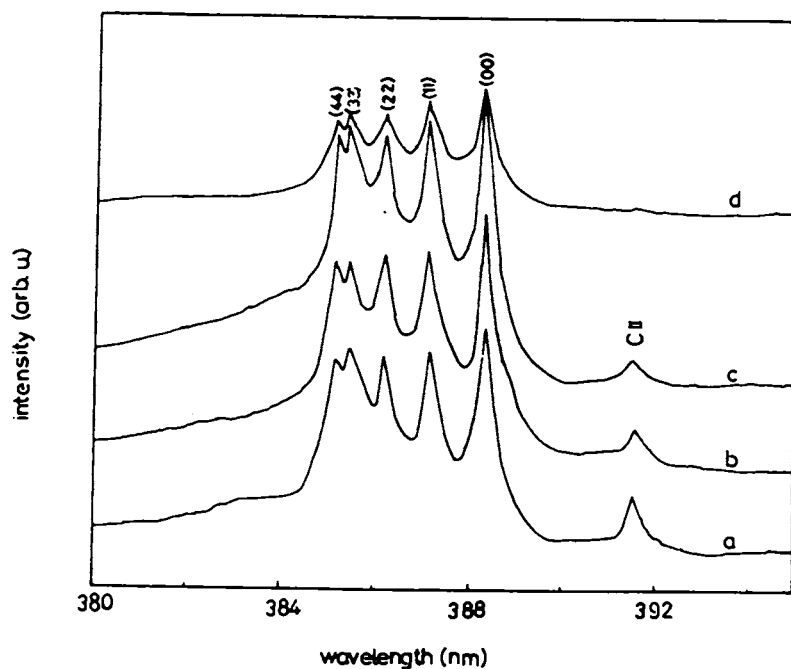


Figure 6.5: CN violet band for $\Delta v = 0$ sequence at different spatial distances from the target (laser irradiance 7.3 GW cm^{-2} , time delay $5 \mu\text{s}$) (a) 2 mm, (b) 6 mm, (c) 10 mm, (d) 14 mm

10 mm away from the target is shown in fig. 6.6 at a laser irradiance 73 GW cm^{-2} . The inverse distribution observed for $v < 1$ is in accordance with the Frank-Condon principle. Similar inverse distributions were also observed in certain other molecules [27,28].

The band emission intensities were used to calculate molecular vibrational temperature T_{vib} , details of which are given in section (3.3.1) [26]. The vibrational temperature is obtained from the slope of the Boltzmann plot between $\ln \sum_{v'} (\lambda^4 I_{v'})$ and $G(v')$. Typical Boltzmann plot of the band intensities against vibrational energy are given in fig. 6.7 for various distances from the target surface. The spatial variation of the vibrational temperature for $2 \mu\text{s}$ and $5 \mu\text{s}$ delay times after the onset of the plasma is given in fig. 6.8. It was found that at a particular laser irradiance, depending on the time of observation and the position of the sampled volume, the vibrational temperature of CN molecules varies. Spatial variation of vibrational temperature after $2 \mu\text{s}$ from the onset of plasma formation was found to peak ($2.05 \times 10^4 \text{ K}$) at a distance 3 mm away from the target. For $5 \mu\text{s}$ delay time, the vibrational temperature was maximum ($1.96 \times 10^4 \text{ K}$) at 8 mm from the target surface. The expected experimental error was $\pm 10\%$. These results are also consistent with earlier reports on vibrational temperature of CN species [13,29,30].

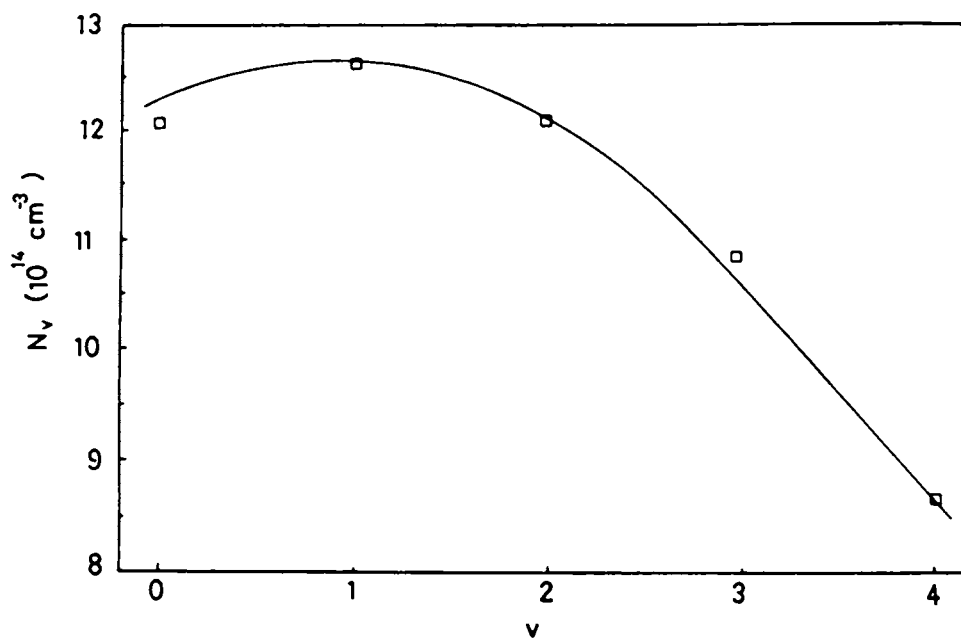


Figure 6.6: The vibrational distribution of CN violet band (distance 10 mm, laser fluence 73 W cm^{-2})

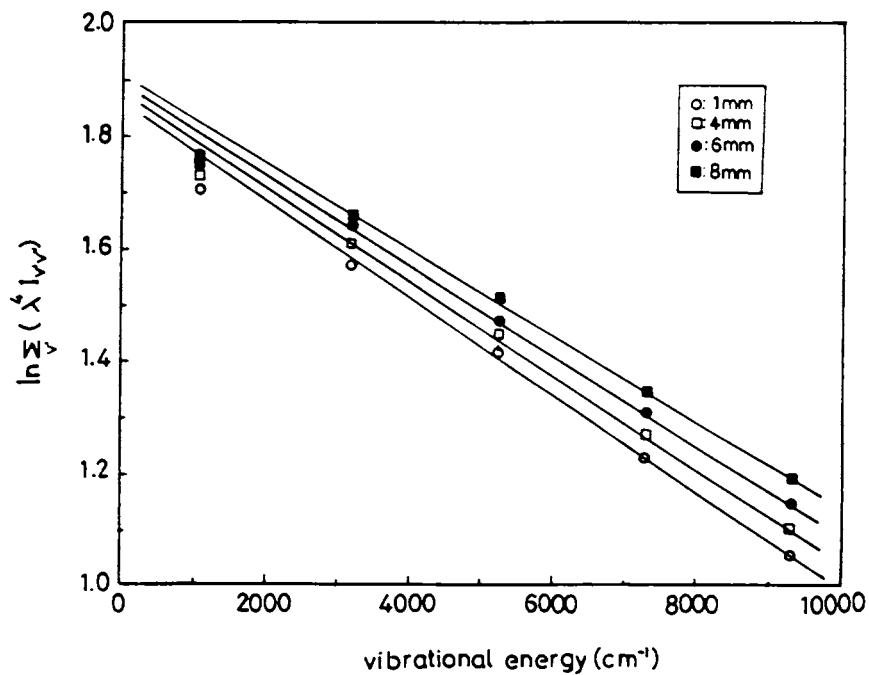


Figure 6.7: Typical Boltzmann plots of vibrational band intensity vs vibrational energy for different distances from the target

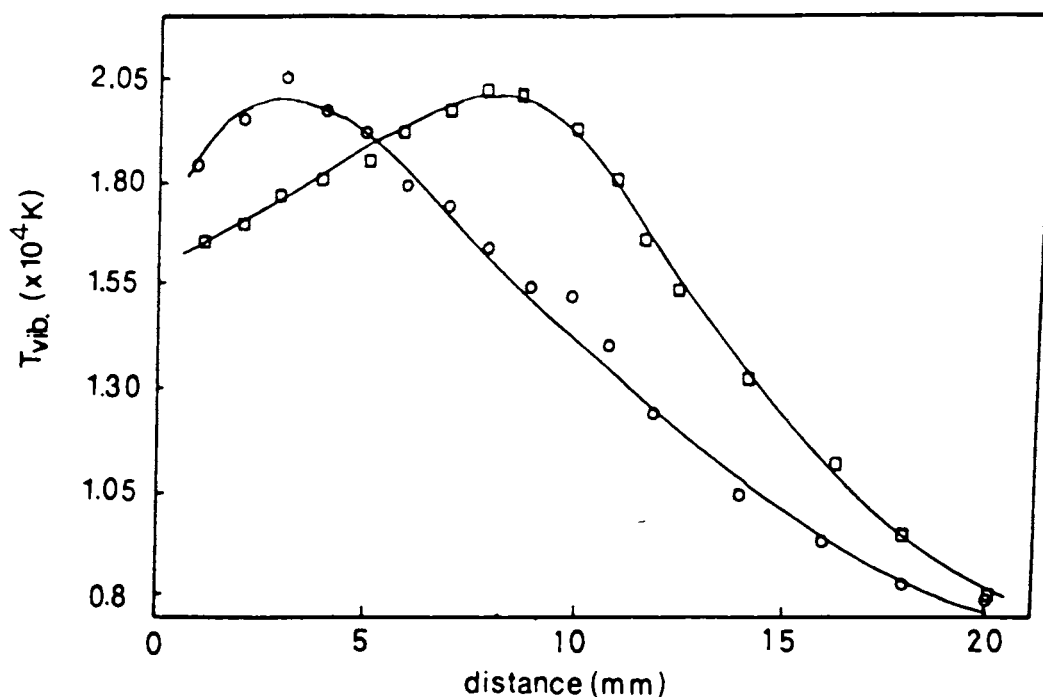


Figure 6.8: The variation of vibrational temperature of the CN violet band with distance from the target for $2 \mu\text{s}$ (○) and $5 \mu\text{s}$ (□) delay time

The observed spatial variation of vibrational temperature can be explained as follows. Near the target surface the temperature is so high that collisional dissociation predominates and this causes a net decrease of de-excitation of the higher vibrational levels with corresponding reduction in band intensity. As we move away from the target, the collisional effects are reduced so that effectively the vibrational temperature is found to be high. At distances beyond an optimal value the decrease in plasma temperature [31] will cause a reduction in vibrational temperature. The location at which maximum occurs for vibrational temperature was different for $2 \mu\text{s}$ and $5 \mu\text{s}$ delays (for $2 \mu\text{s}$ maximum is at 3 mm and for $5 \mu\text{s}$ at 8 mm). Such an effect takes place because different physical processes like collision between neutrals, ions or electron capture by CN^- etc. predominate at different times within the plasma and the evolutionary history of CN is fairly complex. This causes the CN number densities to vary with respect to time as well as space in the laser generated plasma from graphite.

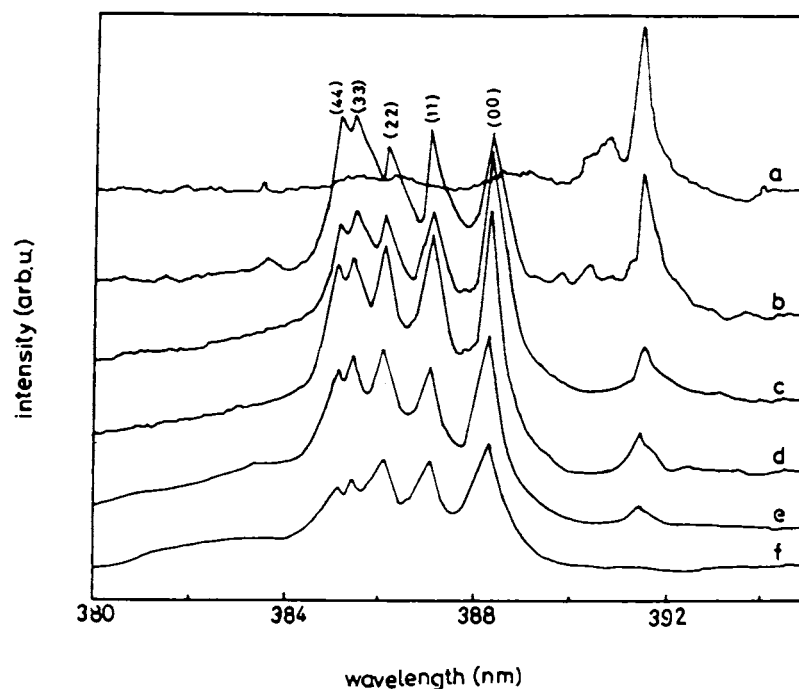


Figure 6.9: CN violet band for $\Delta v = 0$ sequence at different time delays after the onset of plasma (laser irradiance 35 W cm^{-2} , distance 7 mm) Time delays (a) $20 \mu\text{s}$, (b) $10 \mu\text{s}$, (c) $4 \mu\text{s}$, (d) $2 \mu\text{s}$ (e) $1 \mu\text{s}$ and (f) 500 ns

6.3.3 Time Dependence

For the time dependence studies, emission spectra were recorded by varying delay times with respect to the laser pulse in the range 100 ns to $40 \mu\text{s}$ with the gate width of the boxcar averager fixed at 100 ns . All the spectra were recorded at a distance of 7 mm away from the target. Fig. 6.9 gives the change in band head intensity of CN molecules ($\Delta v = 0$) at different time delays for a laser power density of 35 GW cm^{-2} . The emission characteristics of the plasma varied with time as illustrated in fig. 6.9. Shortly after the plasma initiation, the dominant radiation was a continuum mixed with ionic lines. The continuum emission is due to Bremsstrahlung radiation and radiative recombination. Between $0.1 \mu\text{s}$ to $1 \mu\text{s}$, both of these contributions decayed, leaving neutral lines and molecular bands which were seen up to $40 \mu\text{s}$ or longer. It has been observed that the individual emission lines from different atomic and ionic species are highly stark broadened [31] during the the initial stages of the plasma due to high plasma electron densities. At later times greater than $2 \mu\text{s}$, the spectrum is found to be dominated by CN violet system. It is to be noted that CN molecules are formed as a result of recombination

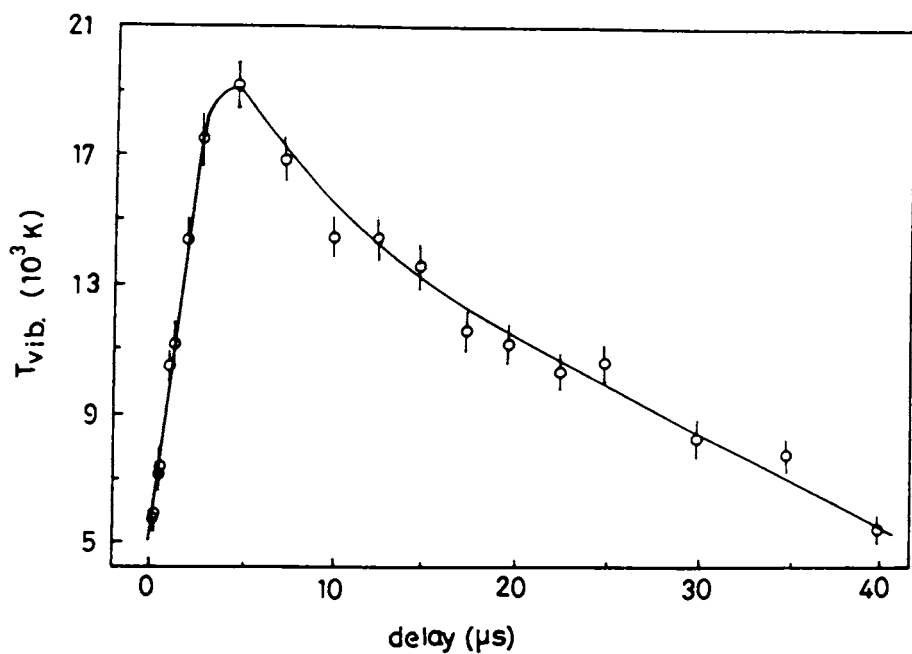


Figure 6.10: Time dependence of vibrational temperature of CN molecule (laser irradiance 35 GW cm^{-2} , distance 7 mm)

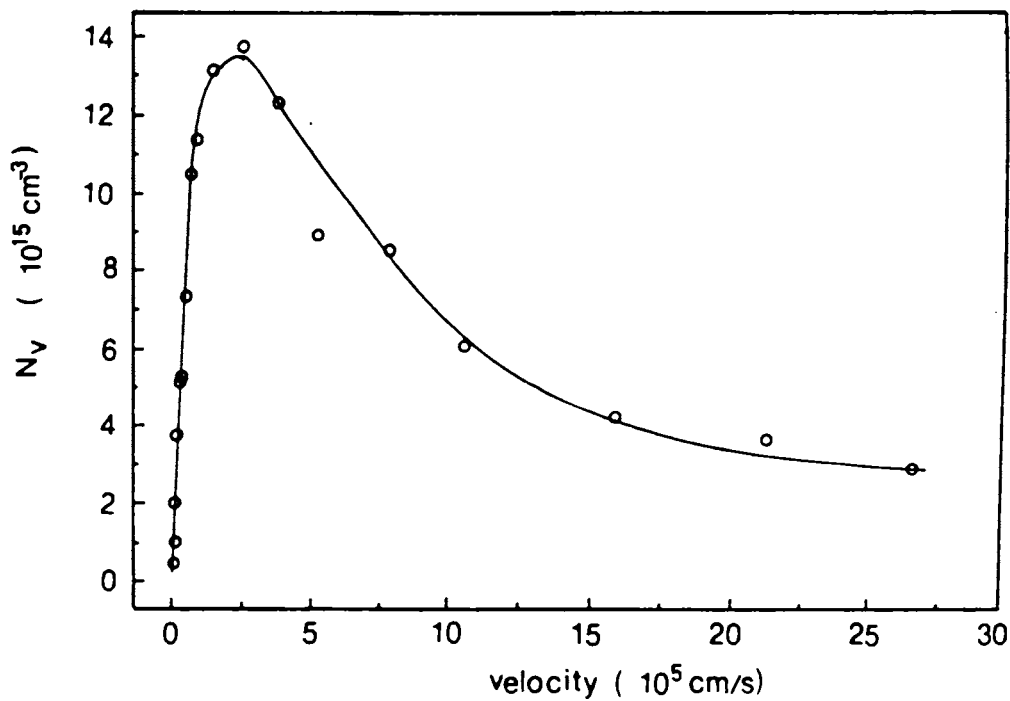


Figure 6.11: Velocity distribution of CN molecules for $v = 0$ (N_v , number density)

of excited carbon species with ambient nitrogen present in the chamber as the hot plasma expands and cools. The time dependence of vibrational temperature is shown in fig. 6.10. As it is clear from the figure there is a maximum vibrational temperature (19×10^3 K) after an elapse of $5 \mu s$ at a distance of 7 mm away from the target. For time intervals from 1 to $5 \mu s$ the intensity of the CN band are found to be increasing and thereafter the intensity of the same decreases. Assuming that average temperature is proportional to vibrational temperature one can evaluate velocity distribution of CN molecules from fig. 6.11. The result of this calculation is given in fig. 6.11 which shows the variation in number density of CN molecules with velocity.

6.3.4 Effect of Laser Irradiance

The variation of vibrational temperature of CN molecules with laser irradiance at distances 5 and 10 mm from the target surface is given in fig. 6.12. Such variation of vibrational temperature with laser power density occurs essentially due to the fact that comparatively large number of molecules are excited into higher vibrational levels with increasing laser irradiance. At 5 mm axial distance from the target surface, the vibrational temperature increases rapidly till laser power density reaches 60 GW cm^{-2} and after that it shows saturation behaviour. The saturation in vibrational temperature at higher irradiance may be due to following reasons. At higher laser irradiance the plasma temperature is so high that collisional dissociation/ionization predominates over recombination causing a net decrease in de-excitation rate of population in the higher vibrational levels and by plasma shielding which is due to the change in efficiency of laser coupling to the target by increased absorption and/or reflection by the plasma itself [31, 32]. At 10 mm distance from the target surface, a knee is found to occur in the curve showing variation of vibrational temperature at 42 GW cm^{-2} . This suggests the onset of possible nonlinear interactions such as self-focusing of the laser beam within the plasma medium.

The self-focusing phenomenon of laser beams in plasma will occur if the Debye length (λ_D) is less than the laser beam diameter. The Debye length which is the characteristic screening length of the plasma is given by [33, 34],

$$\lambda_D = \left[\frac{k_B T_e \epsilon_0}{n_e e^2} \right]^{1/2} \quad (6.1)$$

where k_B is the Boltzmann constant, T_e is the equilibrium plasma temperature, n_e is the

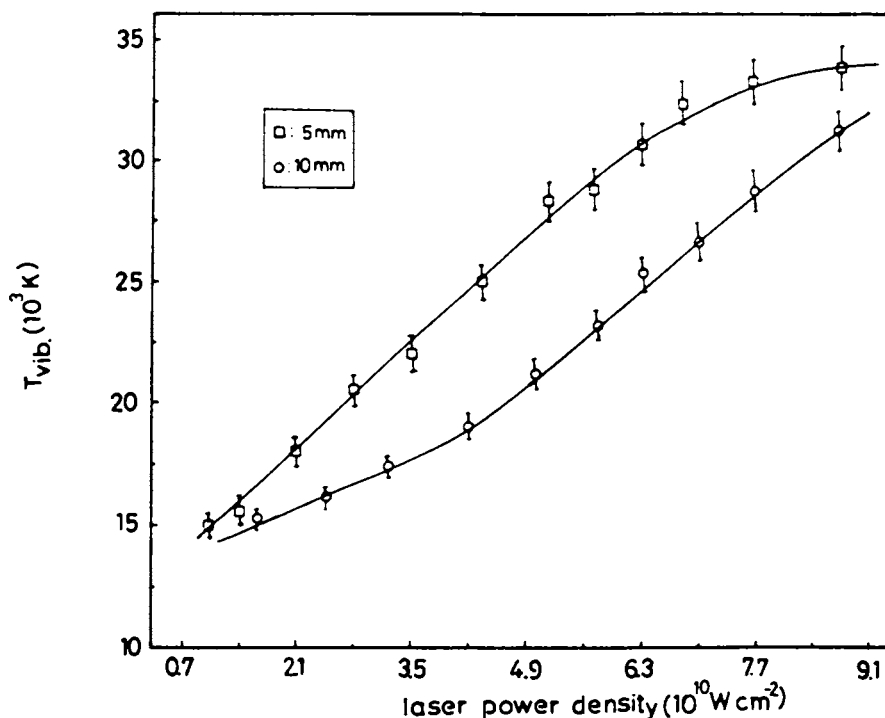


Figure 6.12: The variation of vibrational temperature of the CN molecule with laser energy at distances (\square) 5 mm, (\circ) 10 mm from the target

equilibrium concentration, ϵ_0 is the permittivity and e is the electron charge. At 10 mm radial distance from the target surface, using the relative line intensity measurements of the successive ionization stages of the carbon species (as mentioned in chapter 5), the estimated T_e and n_e are 19700 K and $9.6 \times 10^{16} \text{ cm}^{-3}$. Using these data, the Debye length is found to $\lambda_D = 0.03 \mu\text{m}$ which is much less than the estimated beam diameter ($200 \mu\text{m}$). Such self-focusing in the plasma leads to a higher effective power density resulting in an enhanced emission. Similar threshold like phenomenon is not perceptible at 5 mm radial distance from the target. Apparently this is due to the fact that a greater laser power density resulting from self-focusing due to large plasma density and temperature lead to a much lower value for this threshold.

6.3.5 Effect of Ambient Nitrogen

The emission characteristics of laser produced plasma are influenced to a large extent by the nature and composition of the surrounding atmosphere. A quantitative study of the effect of pressure on the relative intensities of the lines in the CN bands gives insight into the mechanism of formation of CN in its excited states and the mechanism

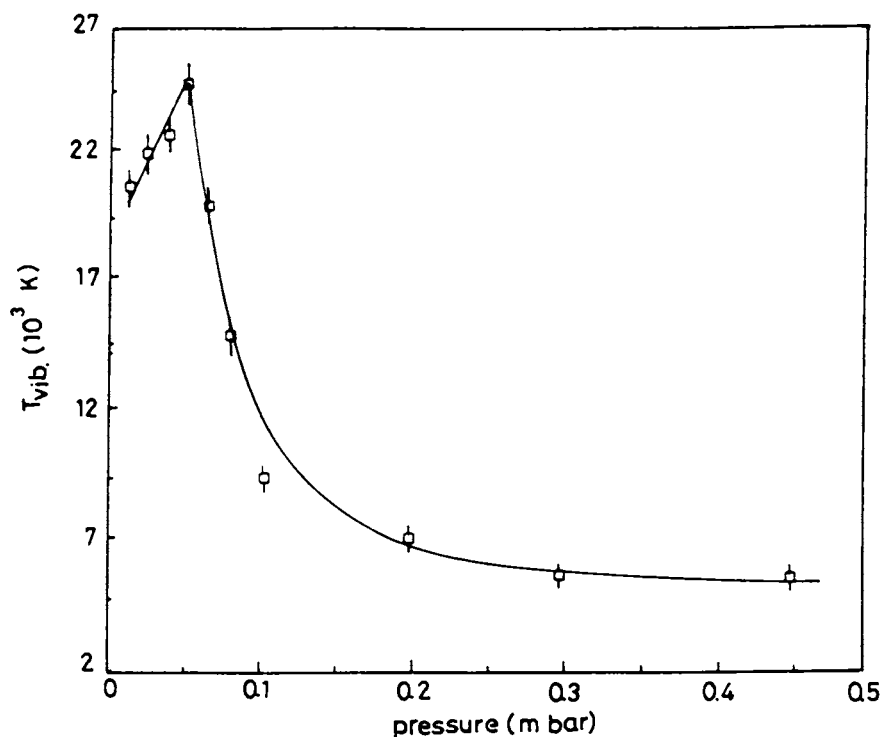


Figure 6.13: The change in vibrational temperature for CN molecules with respect to ambient nitrogen gas pressure inside the plasma chamber (distance 3 mm, 35 GW cm^{-2})

of collisional energy transfer [35-37]. The change in vibrational temperature for CN molecules with respect to ambient nitrogen gas pressure inside the plasma chamber is given in fig. 6.13 at a radial distance 3 mm away from the target and $3 \mu\text{s}$ after the irradiation at 35 GW cm^{-2} . The vibrational temperature peaks at 0.08 mbar and then falls quickly with increase in pressure and finally levels off at slightly lower value for T_{vib} . Highest rate of formation of excited CN molecules occur at 0.08 mbar pressure under the above conditions. It can be noted that at higher nitrogen pressure the confinement of the plasma takes place. There can be competing nonradiative de-excitation processes which will be predominant at higher pressure of nitrogen gas in the chamber. Thus competition with collisional de-excitation results in reduced vibrational temperature as seen in fig. 6.13.

6.3.6 Time of Flight Analysis

Time resolved studies on CN molecules were also made. In order to study the time evolution of a particular species produced by laser ablation, the characteristic lines were selected using the monochromator, and the PMT output with 50Ω termination was fed

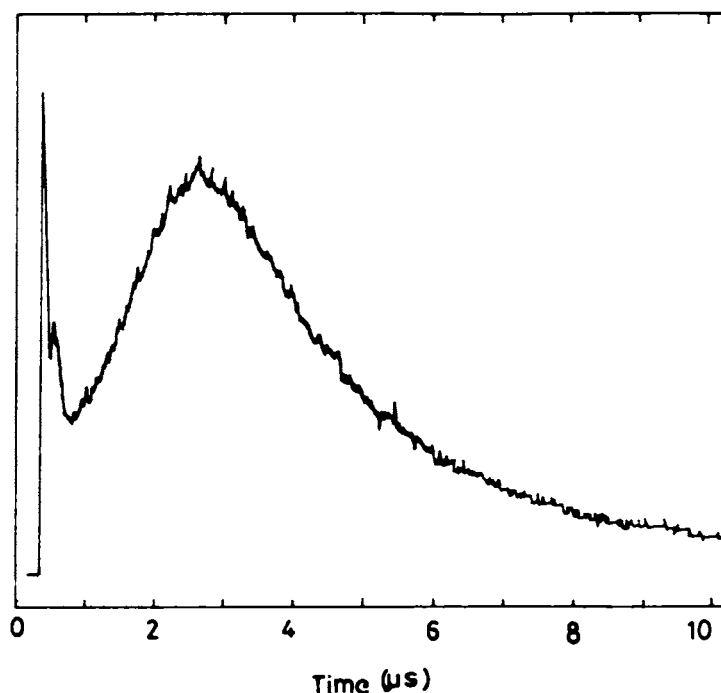


Figure 6.14: Typical CRO plot of the intensity distribution of CN molecules (388 nm, 0-0 transition)

to a 200 MHz digital storage oscilloscope. The experimental details of the time resolved studies are described in chapter 2. Typical time of flight pattern for CN molecules (selecting 388.3 nm corresponding to (0-0) transition of the CN violet system) is given in fig. 6.14. The CRO trace shows a sharp prompt emission and delayed emission peaking after few nanoseconds. The variation of measured time delay with distance from the target surface is given in fig. 6.15. These time delays can directly be converted into expansion velocities of these transient species and that is given in the right axis of fig. 6.15. From the figure it is clear that the time delays are found to increase with increase in distance from the target surface, while expansion velocities of CN molecules increasing up to a certain distances from the target surface and thereafter they slow down rapidly attaining a much smaller expansion velocity, which corresponds to plasma cooling. The maximum molecular vibrational temperature for CN molecules was found to be around 2.14×10^4 K, which is much higher than the melting point of graphite (4×10^3 K) [38]. This large vibrational temperature may arise due to the direct heating of the plasma plume. This is supported by the measurement of the temperature equivalent of translational energy which varies from 2×10^4 K to 7×10^4 K at a laser irradiance

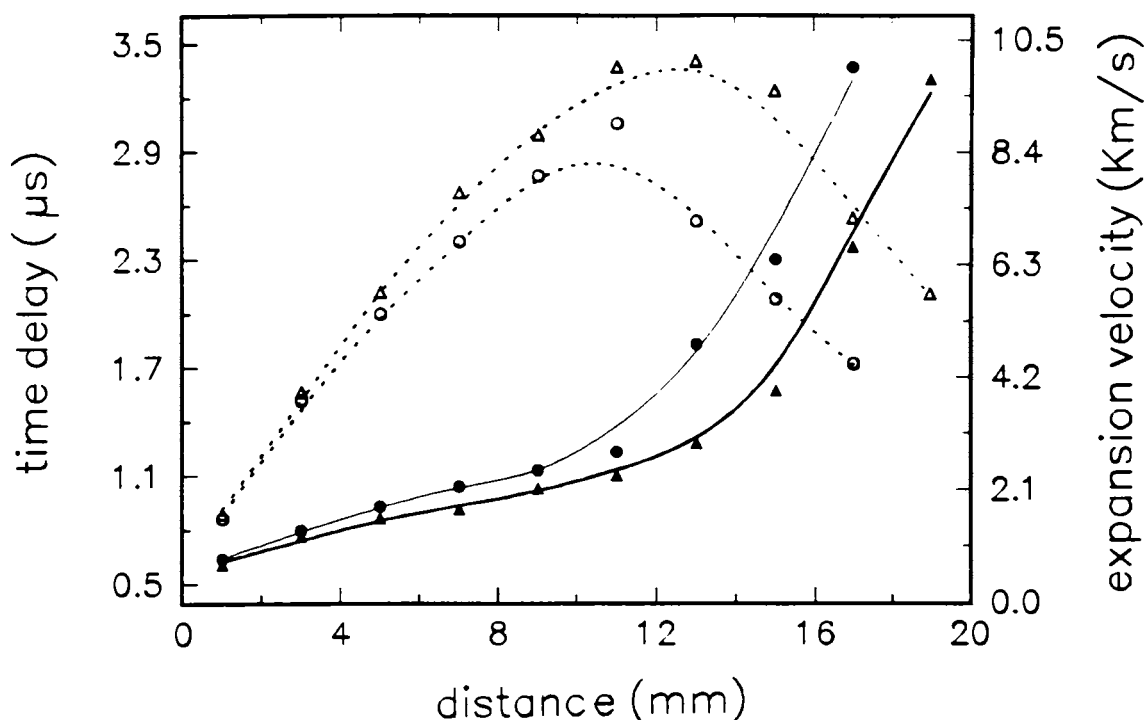


Figure 6.15: The change in the time delay and expansion velocity of CN molecules (388.3 nm) as a function of distance from the target (\circ - 73 GW cm^{-2}) and Δ - 35 GW cm^{-2} . The darkened symbols correspond to expansion velocity

of 73 GW cm^{-2} . The large variation in the translational temperature implies that, the observed time delays are not only due to time of flight (TOF) phenomenon alone but also due to those arising from other processes like recombination/dissociation of the species, collisional excitation process etc. Further experiments like mass spectral measurements may shed some light on these aspects.

6.4 Conclusions

Q-switched Nd:YAG laser ablation of graphite target in partial vacuum conditions generates plasma containing CN molecules. From the spectroscopic studies of the emission bands of the CN molecules, the population distribution and vibrational temperature at different regions of the plasma plume have been obtained. Extensive studies on the time and space resolved emission characteristics have been carried out. These investigations demonstrate that the emission intensities from CN species are sensitive to laser power density, pressure of the background gas, time after the elapse of laser pulse and spatial separation from the target. At low laser irradiance the emission bands due to C_2 and

CN predominates while at higher irradiance the multiply ionized species up to C IV have been observed along with CN and C₂ species.

The vibrational temperature is found to increase with increase in laser power density and saturates at higher power levels. The saturation of vibrational temperature at higher power density is due to depletion of excited state population of CN molecules and by plasma shielding. The nonlinear interactions between the laser and the plasma give rise to phenomenon such as self-focusing which exhibit threshold-like behaviour. It is noted that the vibrational temperature of the CN molecules varies with the position of the sampled volume within the plasma plume, integration time after the elapse of laser pulse and ambient gas pressure inside the plasma chamber.

6.5 References

- [1] M. R. Combi, *Astrophys. J.* **241** 830 (1980).
- [2] R. W. B. Pearse and A. G. Gaydon, *The Identification of Molecular Spectra* (Chapman & Hall Ltd., 1965).
- [3] C. Sneden and D. L. Lambert, *Astrophys. J.*, **259** 381 (1982).
- [4] D. L. Lambert, J. A. Brown, K. H. Hinkle and H. R. Johnson, *Astrophys. J.*, **284** 223 (1984).
- [5] J. R. Johnson, U. Fink and H. P. Larson, *Astrophys. J.*, **270** 769 (1983).
- [6] B. E. Turner and R. H. Gammon, *Astrophys. J.*, **198** 71 (1975).
- [7] D. M. Meyer and M. Jura, *Astrophys. J.*, **297** 119 (1984).
- [8] C. W. Bauschlicher, S. R. Langhoff and P. R. Taylor, *Astrophys. J.*, **332** 531 (1988).
- [9] A. Mele and H. Okabe, *J. Chem. Phys.*, **51** 4798 (1969)
- [10] G. A. West and M. J. Berry, *J. Chem. Phys.*, **61** 4700 (1974).
- [11] P. J. Knowles, H. Werner, P. J. Hay and D. C. Cartwright, *J. Chem. Phys.* **89** 7334 (1988).
- [12] R. W. Dreyfus, R. Kelly and R. E. Walkup, *Nucl. Inst. Meth B*, **23** 557 (1987).
- [13] G. Hatem, C. Colon and J. E. Campos, *Spectrochimica Acta*, **49A** 509 (1993).
- [14] S. S. Harilal, P. Radhakrishnan, V. P. N. Nampoori and C. P. G. Vallabhan, *Appl. Phys. Letts.*, **63** 3377 (1994).
- [15] G. Padmaja, A. V. Ravi Kumar, P. Radhakrishnan, V. P. N. Nampoori and C P. G. Vallabhan, *J. Phys. D*, **22** 1558 (1989).
- [16] Y. Iida and E. S. Yeung, *Appl. Spectroc.* **48** 945 (1994).
- [17] R. K. Dwivedi and R. K. Thareja, *Surf. Coat. Tech.* **73** 170 (1995).
- [18] R. K. Thareja and Abhilasha, *J. Chem. Phys.*, **100** 4019 (1994).

- [19] G. Padmaja, A. V. R. Kumar, P. Radhakrishnan, V. P. N. Nampoori and C. P. G. Vallabhan, *J. Phys. D*, **26** 35 (1993).
- [20] S. S. Harilal, R. C. Issac, C. V. Bindhu, V. P. N. Nampoori and C. P. G. Vallabhan, *J. Phys. D*, (in press) (1997).
- [21] S. S. Harilal, R. C. Issac, C. V. Bindhu, V. P. N. Nampoori and C. P. G. Vallabhan, *Plasma Sour. Sci. Tech.*, (in press) (1997).
- [22] R. Engleman Jr, *J. Mol. Spectroc.* **49** 106 (1974).
- [23] C. V. V. Prasad, P. F. Bernath, C. Frum and R. Engleman Jr *J. Mol. Spectroc.* **159** 473 (1992).
- [24] F. A. Jenkins, *Phys. Rev.*, **31** 539 (1928).
- [25] S.S. Harilal, R. C. Issac, C. V. Bindhu, V. P. N. Nampoori and C. P. G Vallabhan, *Pramana - J. Phys.* **46** 145 (1996).
- [26] G. Herzberg, *Spectra of Diatomic Molecules (Molecular Spectra and Molecular Structure I)* 2nd edn. (VanNostrand: New York, 1950).
- [27] M. A. MacDonald, S. J. David and R. D. Coombe, *J. Chem. Phys.* **84** 5513 (1986).
- [28] R. L. Stephen, W. B. Charles, P. R. Alistair, *J. Chem. Phys.* **92** 300 (1990).
- [29] X. Chen, J. Mazumder and A Purohit, *Appl. Phys A* **52** 328 (1991).
- [30] J. A. Howe, *J. Chem. Phys.* **39** 1362 (1963).
- [31] See Chapter 5.
- [32] D. B. Geohegan in *Laser Ablation Mechanisms and Applications*, Miller J.C. and R. F. Haglund (eds) **389** 28 (1991).
- [33] G. Bekfi, *Principles of Laser Plasmas* (John Wiley & sons, New York, 1976).
- [34] T. P. Hughes, *Plasmas and Laser Light* (The institute of Physics, England, 1975).
- [35] N. H. Kiess and H. P. Broida, *J. Mole. Spectroc.* **7** 194 (1961).
- [36] A.T. Wager, *Phys.Rev.* **64** 18 (1943).

[37] H. T. Byck, *Phys.Rev.* **34** 453 (1927).

[38] R. C. Weast *CRC handbook of Chemistry and Physics*, (CRC press Inc., Florida 1988).

Chapter 7

Dynamics of laser produced plasma from $\text{YBa}_2\text{Cu}_3\text{O}_7$

Spectroscopic studies of Nd:YAG laser ablated high temperature superconducting material viz. $\text{YBa}_2\text{Cu}_3\text{O}_7$ (YBCO) plasma have been carried out. Electron temperature and electron density measurements are made from spectral data. The Stark broadening of emission lines has been used to determine the electron density and the ratio of line intensities has been exploited for the determination of electron temperature. The dependence of electron temperature and density on different experimental parameters like distance from the target surface, delay time after the initiation of the plasma and nature of ambient gas is also discussed. Finally, the LTE condition is discussed.

7.1 Introduction

Following the discovery of superconductivity in a Ba-La-Cu-O system [1], the compound $\text{YBa}_2\text{Cu}_3\text{O}_7$ with a high transition temperature ($T_c = 92 \text{ K}$) was synthesized [2]. Immediately after this, extensive investigations were undertaken in various laboratories all over the world aimed at improving the process of its preparation and for utilizing it in practical devices. Most of these rare earth based ceramics are superconducting above liquid nitrogen temperature and are expected to have tremendous applications in various devices and systems. The superconducting phase $\text{YBa}_2\text{Cu}_3\text{O}_{7-\delta}$ (where $\delta \leq 1$ is the deficit in oxygen), labeled as 123 compound, has a perovskite type crystal lattice comprising of Cu-O layers between which there are located Y, Ba and O atoms arranged in a certain order (fig. 7.1). The Cu-O layers form the base for many high temperature superconductors (HTSC) and are known to contain metals other than Cu (eg K) [3], but oxygen is apparently a necessary element. Thin films of HTSC materials were attempted

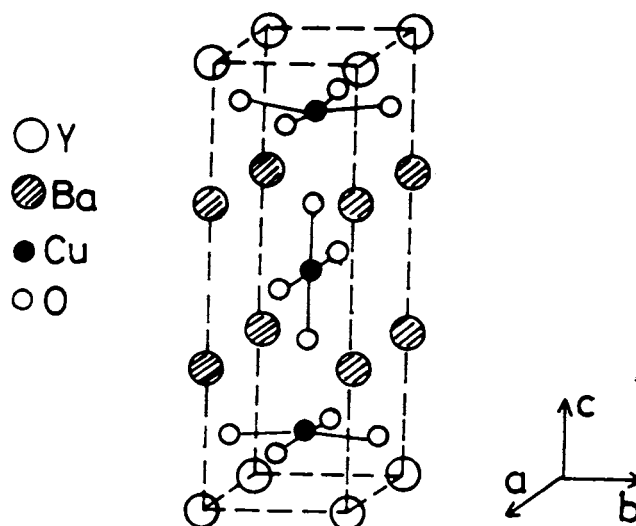


Figure 7.1: Unit cell of orthorhombic $\text{YBa}_2\text{Cu}_3\text{O}_7$ superconducting sample

very soon after the materials were discovered. For many of the device applications, it is necessary to fabricate HTSC materials in thin film form. HTSC films have been grown by both physical and chemical deposition techniques. Physical deposition involves the production of a vapour which includes only the species to be deposited (some combination of atoms, molecules and radicals), possibly mixed with an inert ambient (e.g. argon). Chemical Vapour Deposition (CVD) involves passing a vapour of molecules con-

taining the elements to be deposited (in addition to other elements, notably hydrogen and carbon). Physical deposition offers the advantage of having no extraneous elements present during film growth. Among the different successful techniques already developed for producing HTSC films, including evaporation [4-6], sputtering [7, 8], molecular beam epitaxy [9], the laser ablation of superconducting targets appears to be one of the most promising method. In this process, a laser pulse impinges upon the surface of a target material. The surface of the target is heated and vapourized. The vapourized material expands away from the target surface. Some of this material impinges upon an appropriately positioned substrate surface where a film of the ablated material deposits. Because of the success of this process in growing HTSC thin films, work has been undertaken to characterise and model the process [10-13]. The laser ablation method for growing epitaxial superconducting films is the only method where complex molecular structures are transferred from a ceramic target onto a substrate. These structures are transferred either intact or as a result of disintegration-recombination process. The technique is advantageous because of its highly directed and local nature and is capable of giving a flexible control over the process parameters and the film composition, structure and properties [14-22]. Its relatively low production rate (compared to that of chemical vapour deposition or magnetron deposition) is offset by the high quality of the films it produces, the new possibilities it offers for laser treatment, and comparative simplicity and cost effectiveness of its equipment as compared to that of molecular epitaxy process. Laser radiation is being successfully used not only to deposit thin films on to the specially prepared substrates, but also to effect some modification and structerization of the deposited layer, to analyze the molecular composition and velocity distribution of the particles encountering the substrate [23,24]. Numerous experimental investigations have shown that the threshold laser energy for ablation, and the kinetics of ablated particles depend on the wavelength of the laser irradiation and pulse duration [25,26].

The laser ablation of HTSC target is accompanied by the formation of brilliant elongated plasma located over the target surface extending outward. The length of the laser ablated plasma plume depends on the laser irradiance employed and the nature of the ambient gas used [27-29]. Research into the ablation products of YBCO superconductor shows that there exist four types of particles: neutral atoms and oxide molecules, ions and ionized molecules, micro clusters and macro particles [30-34]. Analysis of the optical emission spectrum from the plasma plume has been used to identify vapourized and

ejected atoms, ionized atoms and diatomic molecules, while mass spectroscopic studies can be successfully used for the study of micro clusters and macro particles. Identification of these species is important in understanding the complicated ablation, transport and deposition processes. It is also reported that the size and velocity of the particles have a material effect on the film deposition processes [35]. The velocity of the particles depends on the laser irradiance and varies with distance z from the target surface.

An analysis of optical emission produced by laser ablation of YBCO targets using wide range of wavelengths showed that 193 nm (ArF) radiation produced neutral atomic species and 1.06 μm and 532 nm radiation produced mostly ionic species [36, 37]. An excimer laser with very high photon energy may causes an internal electronic excitation. It was observed earlier that YBCO has got smaller absorption coefficient for the IR radiation compared to that for excimer laser so that more thermal effects can be expected in the latter case. An important difference between the excimer and YAG lasers is the much greater coherence of the YAG output leading to vastly different far field characteristics of the light source. Consequently, the YAG laser excitation of the target occurs in a far more localized manner.

Many laser applications such as laser cutting, laser structuring, laser engraving or pulsed laser deposition are based on the effect of a normal absorption via laser plasma. It allows an effective energy coupling of laser energy into the target. The other mechanism of laser plasma interaction is the inverse bremsstrahlung [38]. The absorption coefficient based on Drude theory and Coulomb interaction is a function of collisional frequency and plasma frequency [39]. On the other hand these frequencies depend on electron temperature and electron density. Many of the published works have concentrated mainly on identification of plasma species and on parametric studies of the velocity distributions of the species in the expanding plume [40-50]. Several authors have described the plume expansion in terms of analytical models [51-57]. Spectral analysis of plasma- emitted light in the process of target erosion and material transport for laser deposition of thin films gives information about plasma composition, the energy content of ablation products, and the dynamics of plume species. Investigation of the optical emission of plasma plume gives information about the spatial and temporal evolution of transient species produced during laser target interaction, such as excited atoms, ions and molecules. However, relatively little quantitative information is available on either the fundamental plasma parameters, like electron temperature, electron density, composition etc., on the nature

of the dominant plume excitation processes in different spatial and temporal regions of the expanding plasma. Such data are required in order to develop and test models of plasma processes [58-60] and these enable us to evaluate the energy transport into the plasma with regard to temporal and local behaviour as well as its effectiveness.

Accurate knowledge of the electron density, n_e is very important when one is confronted with problems of plasmas through laser irradiation of solid targets. In a sense, the study of plasmas begins with measuring the electron density. It constitutes one of the most fundamental parameters for plasmas. The electron temperature is an equally important plasma parameter whose value is much needed. The various spectroscopic techniques of determining the electron temperature T_e are predicted on the stringent condition that the plasma be in Local Thermodynamic Equilibrium (LTE).

Because of the highly transitory behaviour of laser produced plasma (LPP), it is most important to characterize the LPP in a time- and space- resolved way. In the present chapter, an attempt is made to characterize the YBCO plasma produced by $1.06 \mu\text{m}$, 9 ns laser pulses delivered from a Nd:YAG laser. Under the assumption of LTE, the electron temperature was deduced from line intensity measurements. Stark broadening method was employed to calculate the electron number density in the plasma. Also spatiotemporal dependence of electron temperature and electron density is discussed. Effect of different ambient gases, *viz.* He, Ar and air on the electron temperature of the plasma is also given. Finally, the LTE condition is discussed.

7.2 Experimental

The schematic diagram and details of the experimental set-up are given in chapter 2. Briefly, high purity $\text{YBa}_2\text{Cu}_3\text{O}_7$ pressed and sintered into a 25 mm diameter \times 3 mm thick cylindrical pellet, was placed in a vacuum chamber equipped with windows for laser irradiation and light collection. Light from a Nd:YAG laser with its fundamental frequency (repetition rate 10 Hz) was focused on to the target surface. Emission was detected through a quartz window at 90° to the laser beam axis. The light collected by the 1 meter Spex monochromator - PMT assembly is coupled to a boxcar averager. For the time resolved studies the gate width of the boxcar was set at 10 ns. For the Stark broadening measurements the resolution of the monochromator is set at its maximum by keeping the entrance and exit slit widths at $3\mu\text{m}$ and $6\mu\text{m}$ respectively.

7.3 Results and Discussion

7.3.1 Time Resolved Spectra

To understand the detailed aspects of laser beam interaction with the target material and recombination processes following the laser ablation, the time resolved studies of the emission spectra from the plasma offer the most convenient approach. The nonvasive nature of detection suggests that using the emission as a signal source for a process monitoring in laser ablation technique would be ideally suited for designing an automated laser ablation superconducting thin film deposition apparatus. The well defined highly luminous plasma plume is observed during Nd:YAG laser ablation of YBCO and this extended normal to the target surface up to a distance ~ 3 cm from the sample. Time resolved spectra were recorded by setting the gate width of the Boxcar averager to 10 ns and choosing a section at a distance 1 mm away from the target. Typical spectra, as recorded under different regimes of the plasma expansion, are shown in figs. 7.2 and 7.3. Each spectrum corresponds to the average accumulated data over 10 laser shots and it corresponds to a distance 1 mm from the target surface. For these studies the chamber pressure was maintained at an air pressure of 10^{-2} torr. Prominent emission lines observed with corresponding literature values and assignments are also shown in these figures.

Laser ablation process can be classified into three regimes: evaporation of the target material, interaction of the evaporated cloud with incident laser beam resulting in cloud heating and plasma formation and finally expansion and rapid cooling of the plasma [41]. During the initial stages, (< 100 ns), the continuum emission dominates over line emission. As time evolves, the line to continuum ratio improves. The continuum radiation or Bremsstrahlung occurs when a free electron collide with another particle and make a transition to another free state of low energy, with the emission of a photon. Electron-electron collisions do not produce radiation except at relativistic velocities [61, 62]. In a plasma which is sufficiently hot, most of the atoms are stripped of all their orbital electrons and hence electron-ion recombination and bremsstrahlung are the dominant emission mechanisms. The situation occurs typically at electron temperatures of few eV. In general the main sources of continuum are Bremsstrahlung radiation and radiative recombination [63].

Beyond 100 ns, the line to continuum ratio improves and finally the spectrum consists

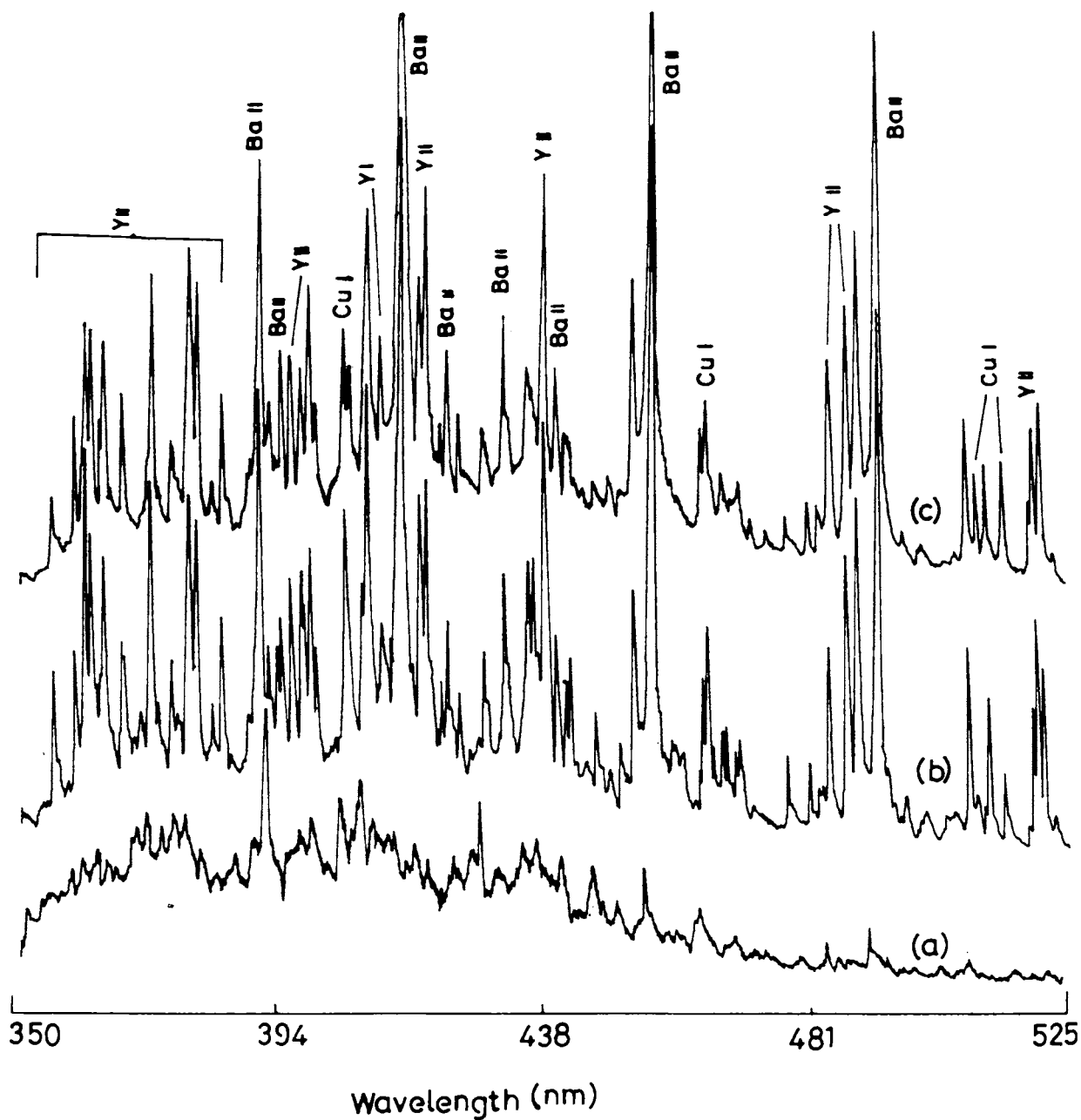


Figure 7.2: Plasma emission spectra in the wavelength range $\lambda\lambda 350 - 525\text{nm}$ at different time delays. The spectra are charted at a distance 1 mm away from the target surface and at a laser irradiance of 40 GWcm^{-2} . (a) 100 ns, (b) 500 ns and (c) $5\ \mu\text{s}$

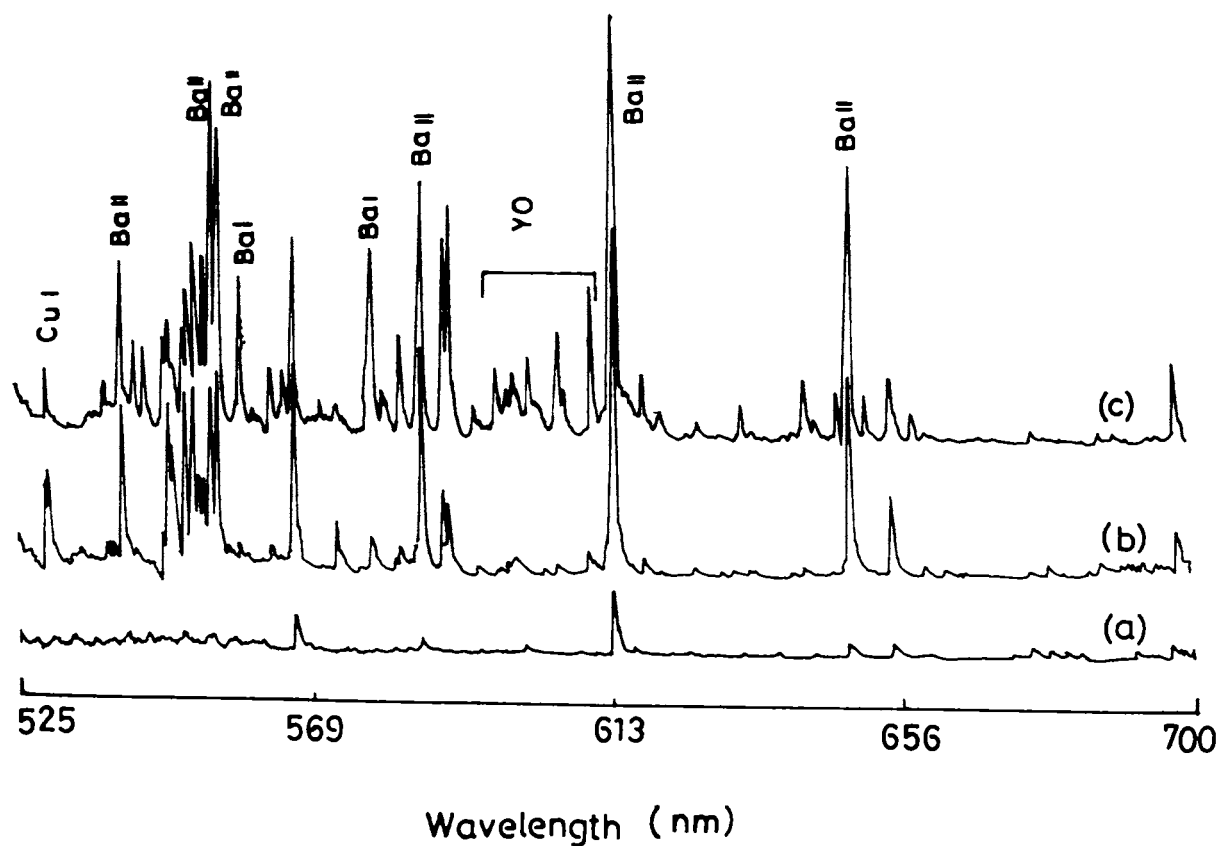


Figure 7.3: Time resolved $\text{YBa}_2\text{Cu}_3\text{O}_7$ plasma emission spectra in the wavelength range $\lambda\lambda 525 - 700$ nm. The spectra are charted at a distance 1mm away from the target surface and at a laser irradiance of 40 GW cm^{-2} . (a) 200 ns , (b) 500 ns and (c) $5\ \mu\text{s}$

of mainly ionic and atomic lines. At shorter time delays ionic species are predominant while at time delays > 500 ns, molecular species are also observed along with ionic and atomic species. From these studies, it is presumed that the electronically excited states are not produced immediately after laser irradiation. This interpretation is consistent with the report that no excited clusters or molecules are formed at the surface of YBCO because of the absence of the corresponding emission [3]. Generally the densities of the particles in the laser produced plasma with similar irradiance ranges are $\sim 10^{17} \text{cm}^{-3}$ and which is enough to justify the collisional processes among the particles in the plasma. As the velocity of the particles in the expanding plume has been found to be high of the order of 10^6cms^{-1} [23], the collision between particles which have high kinetic energy may lead to electronic excitation of component atoms, ions or molecules. It is also noted that the plasma emission lasts for more than $100 \mu\text{s}$.

Although, at least qualitatively, the results confirm the presence of strong emission lines from Y I, Y II, Ba I, Ba II, Cu I and YO (A \rightarrow X) in the plasma, features corresponding to Cu II, BaO and CuO, may be present, but are very weak. Since these spectra are recorded at a distance very close to the target surface (1 mm), it is obvious that the emission intensities due to oxide species are very weak, since they are expected to be formed only by the recombination processes [49]. Relatively weak intensity observed for the Cu II emission lines is due to higher ionization potential of Cu I (7.726 eV) compared to Ba I (5.211 eV) and Y I (6.378 eV) [64]. Since the ionization potential of these lines are much greater than the excitation energy of the laser photons (1.16 eV), the mechanism of ionization is possibly by multiphoton ionization [65].

7.3.2 Electron Density Measurements

The Stark broadening of spectral lines by interactions of radiating atoms or ions with perturbing electrons and ions affords a sensitive method for determining plasma densities. Stark broadening is the dominant broadening mechanism in laser produced plasmas. When Stark broadening dominates the Doppler broadening, the line profiles do not depend critically on the electron and ion velocity distributions or the temperature, hence electron densities can be inferred from line profiles without knowing plasma temperature precisely [66]. In this technique, no assumptions are necessary as to the distribution of atoms or ions among the various quantum states so that measurements are independent of LTE considerations [67, 68]. Determination of electron density is by measuring the

broadening of a suitable emission line of the laser plasma spectrum. In practice the electron density can be deduced from the full width at half maximum (FWHM) of a line. The observed line profile is approximate Lorentzian. The FWHM $\Delta\lambda_{1/2}$ of a Stark broadened line without ionic contribution is given by the simple relation [66,69]

$$\Delta\lambda_{1/2} = 2W\left(\frac{n_e}{10^{16}}\right) \quad (7.1)$$

where W is the electron impact parameter which is a slowly varying function of temperature.

We have selected line broadened profile of Ba I at 553.5 nm transition for the electron density measurements. There are three types of mechanisms that can broaden an emission line *viz*, resonance broadening, Doppler broadening and Stark broadening. The effect of resonance broadening is proportional to the ground state number density and the transition oscillator strength. Since the reported value for resonance broadening for Ba I at 553.5 nm is relatively small [70], the contribution due to this type of broadening can be neglected. Doppler broadening can also be ruled out in our experimental conditions, since the expansion velocities of the Ba atoms are $\sim 5 \times 10^5 \text{ cm s}^{-1}$ [71] which contribute a broadening factor $\sim 0.1 A^0$. Under these conditions Stark broadening, due to collisions with plasma electrons, is the dominant broadening process. The electron impact parameter (W) values for the Ba I 553.5 nm transition are not available in literature, but values are available for the corresponding $nsnp^1P_1^0 \rightarrow ns^21S_0$ transitions of the elements Mg, Be and Ca from the same periodic group [72]. The latter values increase approximately linearly with n^2 and this dependence was extrapolated to yield a W value of $\sim 1.6 \times 10^{-2}$ for Ba I 553.5 nm transition at a temperature of 10000 K. Since W values are weak functions of temperature and vary by a factor less than 2 over the temperature range 10000 K - 80000 K, the determination of electron density deduced using this W value is reliable [69].

We have measured electron density variation using Stark broadening method as function of distance of separation from the target, time after the elapse of laser pulse and laser irradiance. Typical Stark broadened profile of Ba I at 553.5 nm line with theoretically fitted Lorentzian curve is given in fig. 7.4.

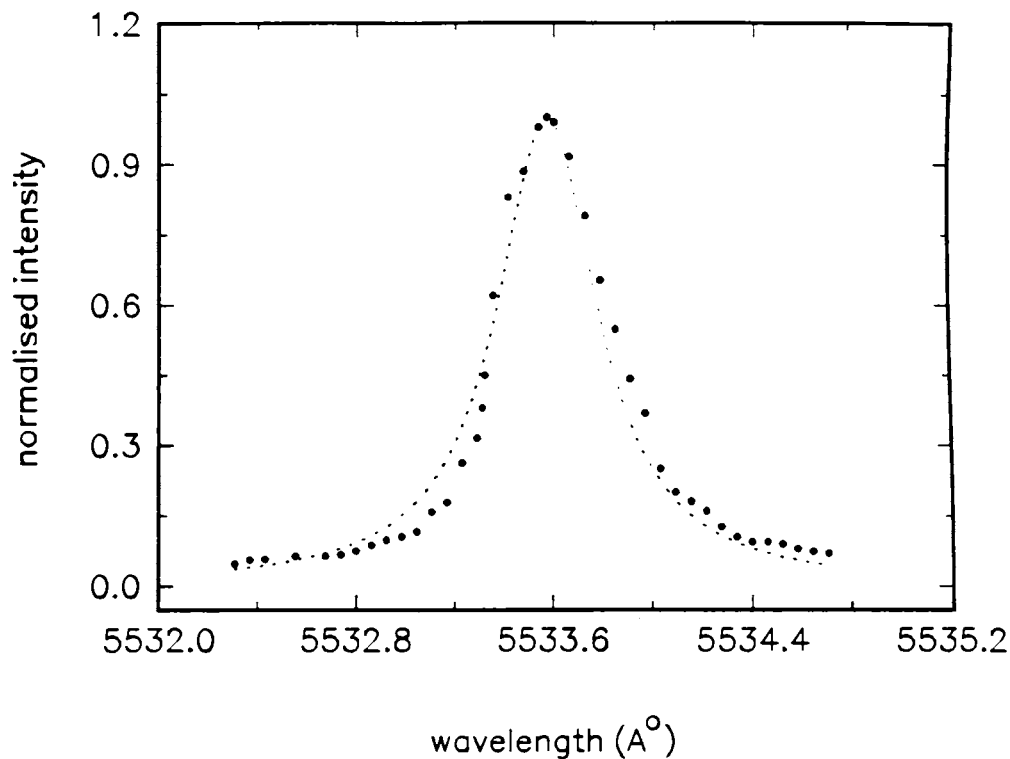


Figure 7.4: Typical Stark broadened profile of Ba I transition at 553.5 nm. The FWHM of this line is used to infer electron density. The dotted line in the figure represents fitted Lorentzian curve

7.3.2.1 Spatial Dependence

Analysis of the plasma emission provides the electron temperature and density. At distances of < 1 mm, the emission lines are so broad that they are not discernable from the continuum emission of the hot target. Fig. 7.5 represents a plot of electron density as a function of distance. The time integrated Stark broadened profile of Ba I transition at 553.5 nm is used for these calculations. All results are obtained in a direction of the expanding plasma axis at different distances from the target surface at a chamber pressure of 2×10^5 mbar and at a laser irradiance of 42 GW cm^{-2} . The electron density is found to decrease rapidly from $2.4 \times 10^{17} \text{ cm}^{-3}$ at 1 mm to $1.55 \times 10^{17} \text{ cm}^{-3}$ at 3 mm and levels off at higher distances. The electron density in the plasma core decreases with distance because of the expansion of the plasma, and also due to recombination and diffusion within the plasma volume. The much faster decrease near the target surface may be caused by plasma cooling due to condensation and recombination. The decrease of electron density as a function of distance shows a z^{-1} dependence.

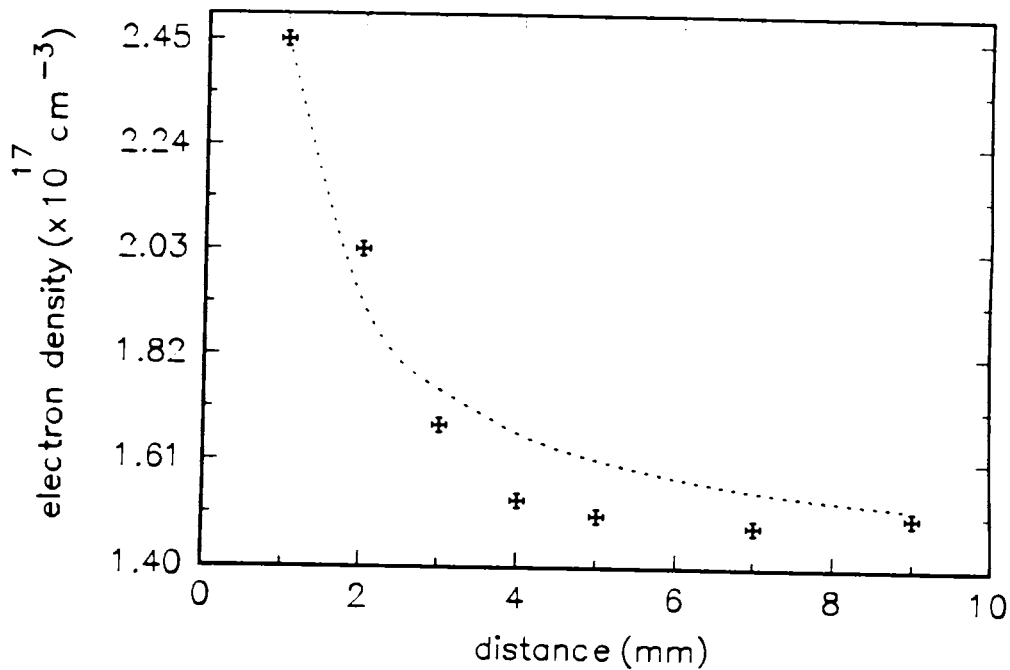


Figure 7.5: Electron density as a function of distance. Laser irradiance used 42 GW cm^{-2}

7.3.2.2 Effect of Laser Irradiance

The electron densities derived from the 553.5 nm linewidth (at 3 mm distance from the target surface) as a function of laser intensity are shown in fig. 7.6. The Stark broadened spectra are recorded in a time integrated manner in which the plasma plume is sampled at a distance 3 mm from the target surface (pressure of $2 \times 10^{-5} \text{ mbar}$). As laser irradiance increases from 28 GW cm^{-2} to 55 GW cm^{-2} electron density varies rapidly from $1.42 \times 10^{17} \text{ cm}^{-3}$ to $1.8 \times 10^{17} \text{ cm}^{-3}$ and then it remains at a more or less constant value. As the laser irradiance increases the number of free electrons increases and consequently the electron density too. The electron densities are essentially constant over the laser intensity range of $55 - 90 \text{ GW cm}^{-2}$. This peculiar behaviour was also observed by Knudson et.al in laser produced aluminium plasma [73]. The saturation in electron density at high irradiance levels is presumably due to plasma shielding. The absorbing plasma prevents light from reaching the surface. Therefore, most of the energy in the laser pulse will be absorbed by material in front of the surface. The surface is effectively cut off from the trailing edge of the incoming laser pulse. Thus the given amount of energy delivered at high power is less effective in causing vapourization than the energy delivered at lower powers. We have also observed a peak shift in the line center

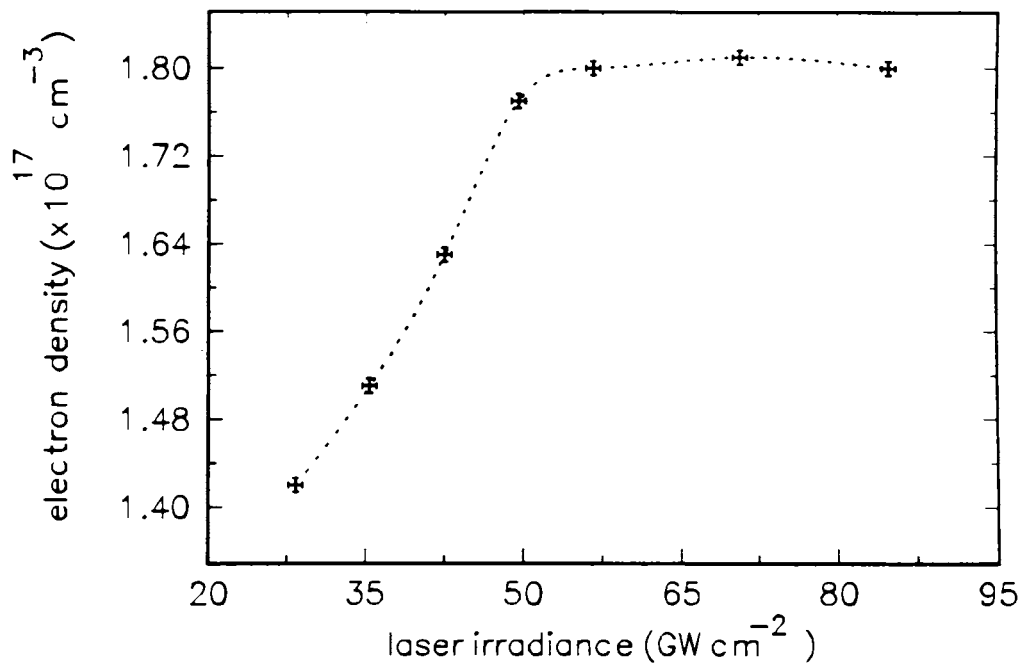


Figure 7.6: Electron density as a function of laser irradiance. The spectra were sampled at a distance 3 mm from the target surface

with increasing irradiance. The observed asymmetry of our time integrated emission line shapes is consistent with what would be expected for a convolution of various Stark shifts towards the red which will arise from differing electron densities within the plume volume sampled, caused by different irradiance levels.

7.3.2.3 Time dependence

The temporal evolution of electron density deduced from Stark broadening of Ba I 553.5 nm transition is shown in fig. 7.7 (distance 3 mm, laser irradiance 42 GW cm⁻² and pressure 2 × 10⁻⁵ mbar). For these studies the gate width of the boxcar is set at 10 ns. Because of the spectral line emission front is masked by the continuum emission, the electron density for time < 200 ns could not be measured by this method. Nevertheless, we can characterize the temporal evolution of n_e which diminishes rapidly with time up to 500 ns and then levels off. The fast decay rate can be attributed to the plasma propagation while the slowing and leveling off at larger times are probably due to recombination. It may also be noted that electron density shows a t⁻² dependence on time.

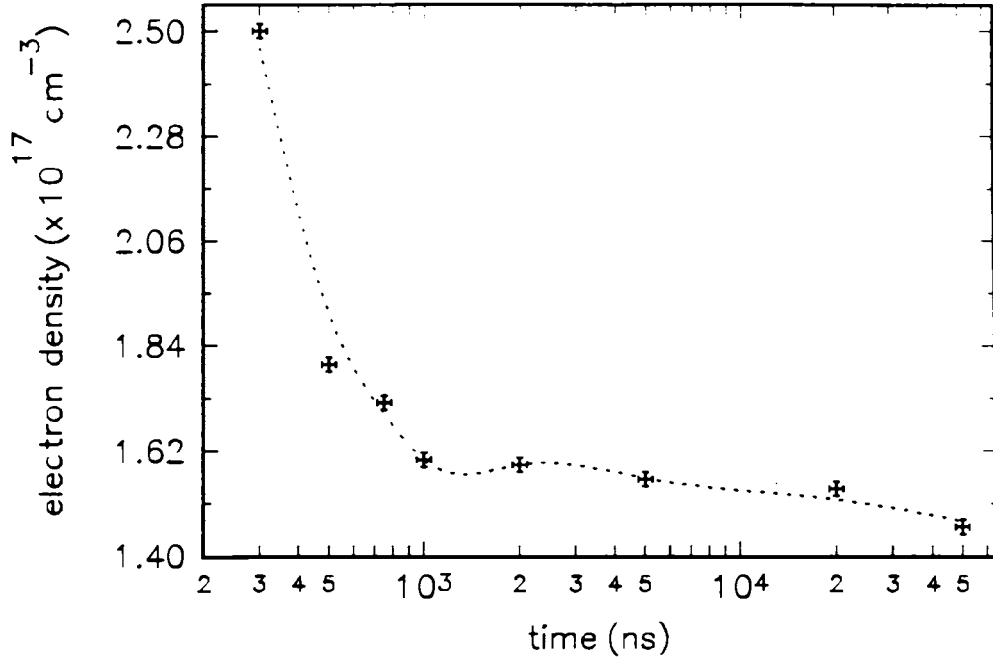


Figure 7.7: Temporal evolution of electron density at a distance 3mm from the target surface. Laser irradiance used 42GWcm^{-2}

7.3.3 Electron Temperature Measurements

Electron temperature was determined from relative intensities of barium spectral lines. We have used spectral lines of successive ionization states since in this case the energy difference between the upper levels of the lines is increased by the ionization energy of the lower ionization state [69, 74]. Electron temperature measurements were made using the eqn.

$$\frac{I'}{I} = \left[\frac{f'g'\lambda'^3}{fg\lambda^3} \right] \left[4\pi^{3/2} a_0^3 n_e \right]^{-1} \left[\frac{kT_e}{E_H} \right]^{3/2} e^{\Delta E/kT} \quad (7.2)$$

where $\Delta E = (E' - E + E_\infty - \Delta E_\infty)$, the primed quantities in the above equation represents relevant data for the spectral line emitted by the species with higher ionization stage, E_H is the ionization energy of the hydrogen atom (13.6 eV), E_∞ is the ionization energy of the atom/ion in the lower ionization state and ΔE_∞ is the correction factor of the energy due to plasma interaction, details of which are given in chapter 5. The estimated correction in the ionization energy ΔE_∞ for an electron density of 10^{17}cm^{-3} is used (0.6 eV) for these calculations.

For temperature calculations, we make use of recorded intensities for Ba II 614 nm and 649.8 nm lines and Ba I, 577.7 nm and 553.5 nm lines. Details of the spectroscopic

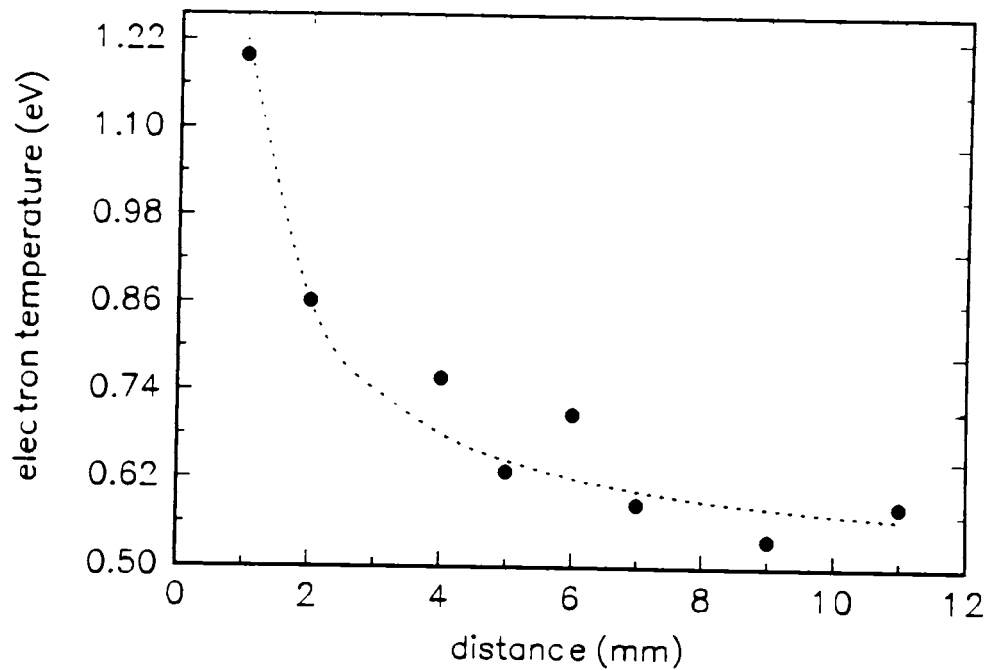


Figure 7.8: The variation of electron temperature with distance from the target surface at a laser irradiance of 35 GW cm^{-2}

constants of these lines were taken from ref. [69].

7.3.3.1 Spatial dependence

The emission spectrum of YBCO plasma was recorded in the visible region at different distances from the target. This was done by moving the collimating lens in a horizontal plane in a direction parallel to the axis of the expansion of the plasma. The time integrated spectrum of the plasma produced by $1.06 \mu\text{m}$ radiation at various distances from the target was recorded with increments of 1 mm. The uncertainty in the determination of position was about ± 0.2 mm. The recorded spectra were intensity normalized using the frequency response curve of the monochromator - PMT assembly. Fig. 7.8 shows the variation of electron temperature in space normal to the target surface. These data were taken with a laser irradiance of 35 GW cm^2 and a pressure of 2×10^{-5} mbar. The electron temperature close to the target is about 1.2 eV and it decreases with increasing separation from the target surface and at 5 mm distance, the electron temperature drops to 0.6 eV. At distances greater than 5 mm from the target surface, the electron temperature is almost constant. At distances close to the target the thermal energy is rapidly

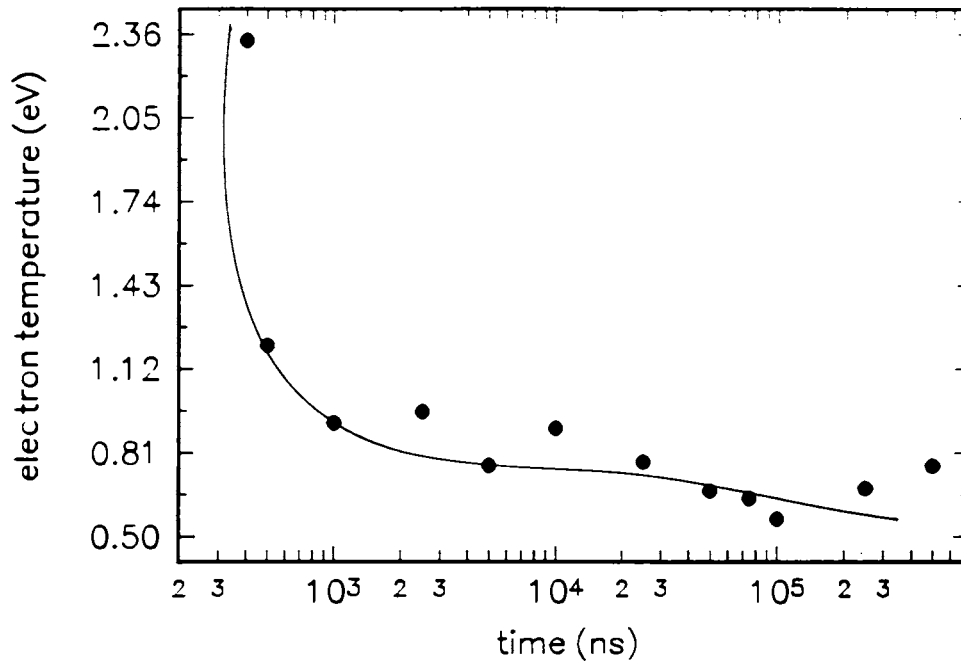


Figure 7.9: The variation of electron temperature with time. These spectra were recorded at distance 3 mm and at a laser irradiance of 35 GW cm^{-2}

converted into the kinetic energy, with plasma attaining maximum expansion velocities and thereby causing the temperature to drop off rapidly as the plasma expands. But at greater distances, the temperature drop is smaller and levels off because energy is gained in the recombination of ions. The variation of electron temperature shows a $z^{-0.8}$ dependence with distance.

7.3.3.2 Time dependence

The electron temperature calculations were made at different instants during the plasma evolution by keeping the gate width of the boxcar averager at 10 ns but by varying the delays. At shorter time delays, the continuum emission occurs and the line intensity detection is rather difficult under these conditions. The continuum emission is produced by both the free-free Bremsstrahlung and electron-ion recombination radiation. The intensity of the continuum decreases with increasing delay time. The calculated plasma temperature and its variation as a function of time after the initiation of the plasma are shown in fig. 7.9. In the early stage of plasma evolution, the electron temperature is very high and is changing very rapidly. However, at greater duration times $\geq 1 \mu\text{s}$, the plasma

is found to be cooled to much lower temperatures and thereafter temperature continues to remain very stable, around 0.6 - 0.7 eV for a long period. The electron temperature was found to decay with a t^{-2} dependence on time during the initial periods up to $\sim 1\mu\text{s}$.

7.3.3.3 Dependence on laser irradiance

To know more about the interaction between the plasma and the laser radiation, the irradiance of the laser beam, which directly influence the fundamental plasma parameters, was varied. The temperature and dynamics of the ablated species from the irradiated target depend on the nature of the interactions between gas dynamic processes and radiative heat transfer in plasma. The laser wavelength is one of the main governing factors that determines the conditions for volume energy release in laser produced plasma. Laser radiation is free to propagate in a cold gas along the z axis and is absorbed in the high temperature region near the surface. Laser radiation absorption results in raising temperature, pressure and ionization of the medium. Under the pushing-out action of hot layers in the cold gas there appears a shock wave, whose intensity is determined by the state of the high temperature region. The strong dependence of the absorption coefficient on the density, temperature and frequency of radiation leads to the variations of the optical density under the action of the gas-dynamic flow.

The dependence of electron density on laser irradiance is given in fig. 7.10 at a distance 3 mm away from the target surface. With increase in laser irradiance, the electron temperature is also found to increase up to a threshold irradiance and then saturates. The saturation in electron temperature at high irradiance levels is expected to be due to the absorption of the laser beam by the plasma medium. Details of plasma shielding are given in chapter 5. The saturation in electron temperature can be explained by assuming the formation of a self-regulating regime.

7.3.3.4 Pressure dependence

Pulsed laser vapourization of the target has been shown to be a powerful technique for depositing a wide variety of thin films. In general, these films are deposited either in vacuum or in a modest partial pressure of a background gas, viz., O_2 , N_2 , He, Ar etc. [70]. Of the many parameters which affect the quality of the thin films, the pressure of the ambient gas plays a key role. The gas may provide either a reactive or an inert buffer to

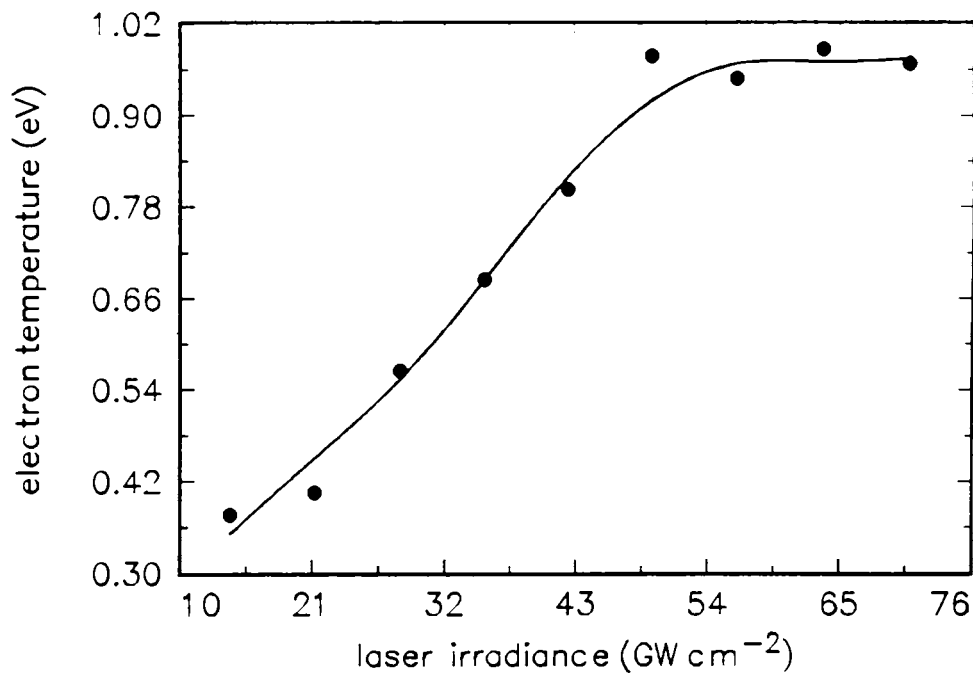


Figure 7.10: Electron temperature as a function of laser irradiance (distance 3 mm)

the laser produced plasma. In each case significant partial pressures lead to collisional processes between the plasma species and intervening gas. This is a clear example of modifying the energetics of the nascent ablation plasma by gas dynamic phenomena. The absorption characteristics of gases are responsible for the creation and propagation of plasma. The ambient gas is transparent to the laser radiation, whereas the ionized gas can absorb the laser energy strongly. The absorption of the gases increases rapidly as they are heated. These changes result from the creation of free electrons. Laser ablation experiments have shown that the plume propagation in background gas can lead to the stopping of the ablated materials. In some cases the material can even move backward, and several reflected shocks within the plume are apparent [76]. Fig. 7.13 shows the variation of electron temperature with the pressure of the ambient gas. These data were taken with a laser irradiance of 35 GW cm^{-2} and a distance 3 mm from the target surface. The variation of electron temperature with different ambient gas pressures show somewhat similar behaviour. Similar to the case of graphite plasma, compared to air and He, the electron temperature is maximum in argon ambient atmosphere. These results might indicate that the characteristics of plasma depends heavily on the



Figure 7.11: Photograph of the YBCO plasma in helium ambient atmosphere (pressure 0.1 mbar)

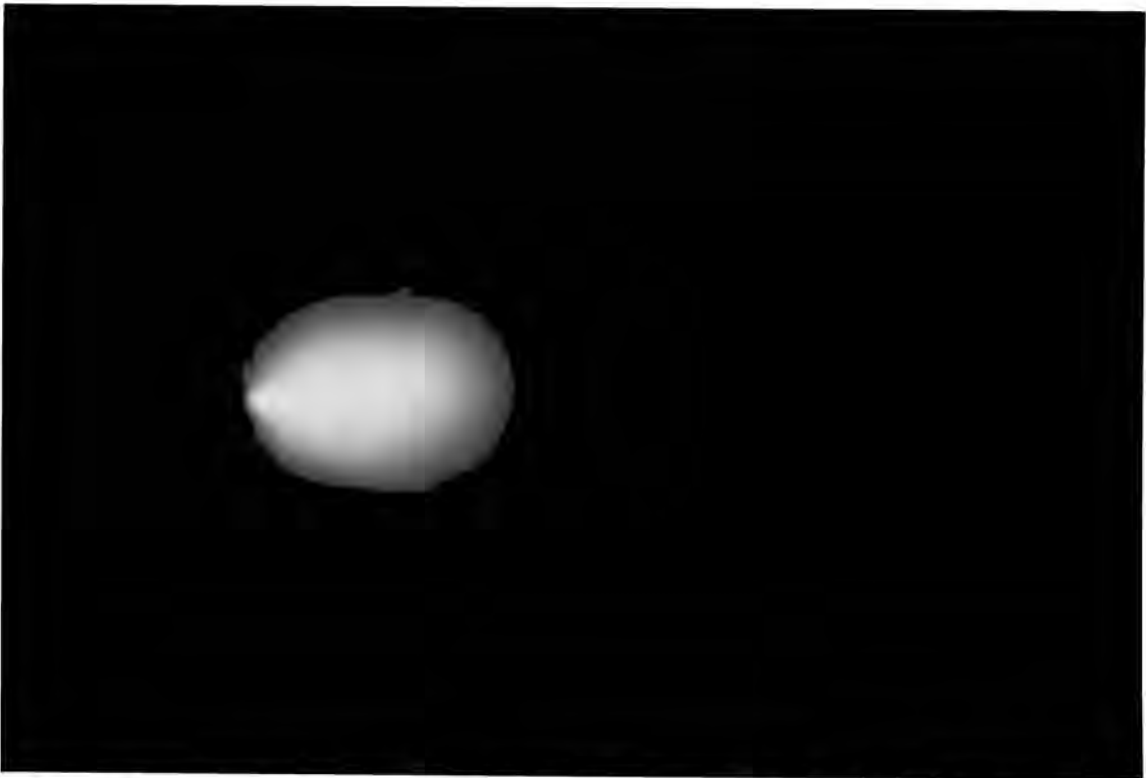


Figure 7.12: Photograph of the YBCO plasma in argon ambient atmosphere (pressure 0.1 mbar)

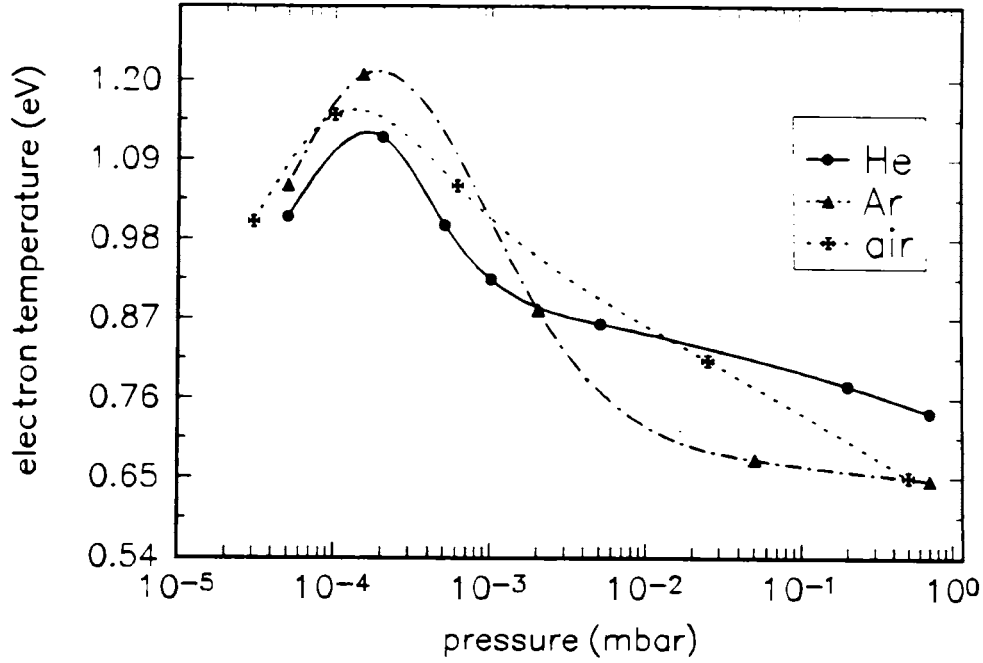


Figure 7.13: The effect of different ambient gases on electron temperature of the expanding plasma. These spectra were recorded at a distance 3 mm from the target surface and at a laser irradiance of 35 GW cm^{-2}

nature of the ambient gas environment used. The electron temperatures increase with increasing pressure up to a threshold value and then decreases. The cooling of the plasma at pressures greater than $\sim 10^{-4}$ mbar is due to recombination. At these pressures a considerable part of the ionization energy is converted into hydrodynamic flow via recombination. The decrease in electron temperature at low pressures is mainly due to reduced confinement of the plasma.

7.3.4 Local Thermodynamic Equilibrium

The calculations of T_e was carried out under the assumption that the plasma is in LTE. In a transient system, such as the plasma formed by a pulsed laser beam, LTE is said to exist if the time between collisions of the particles in the plasma is small compared with the duration over which the plasma undergoes any significant change [69]. LTE will be approached only at sufficiently large particle densities. A necessary criterion for LTE is that [66]

$$n_e \geq 1.4 \times 10^{14} T_e^{1/2} (\Delta E_{mn})^3 \text{ cm}^{-3} \quad (7.3)$$

For transition with largest gap (553.5 nm) $\Delta E = 2.24$ eV and highest temperature 2.5 eV, the lower limit for n_e is $2.5 \times 10^{15} \text{ cm}^{-3}$. Our observed values of n_e are always greater than this limit implying that LTE approximation assumed for our analysis is valid.

7.4 Conclusions

Spectral analysis of Nd:YAG laser-ablated plasma on YBCO target was carried out. The present work has identified the major luminescent species in the plasma plume of Nd:YAG laser ablated YBCO superconducting samples as neutral and ionized atoms along with diatomic molecules. Stark broadened profile of Ba I transition at 553.5 nm was used for the determination of electron density and its variation with distance from the target surface, time after the initiation of plasma and laser irradiance. The electron density variation shows z^{-1} dependence on distance from the target surface while a t^{-2} type variation is found to hold good in the case of time elapsed after the laser pulse. At higher irradiance levels, a saturation effect on electron density was also observed due to plasma shielding.

We have estimated electron temperature of the plasma by spectroscopic means. Line intensities of the successive ionization states were used for the determination of the electron temperature. The relative line intensities of the emission lines of the laser induced YBCO plasma plume depend on the incident laser intensity. Measurement of line intensities of electronically excited Ba atoms and Ba ions were used to infer electron temperature at several positions located away from the target surface and its variation as a function of time elapsed after the initiation of plasma. The electron temperature has got $z^{-0.8}$ and t^{-2} dependence on distance and time respectively. The variation of electron temperature with laser irradiance shows a saturation at high irradiance levels and this can be explained by assuming the formation of a self regulating regime. Irrespective of the nature of the gaseous environment, the plasma temperature shows somewhat similar behaviour. The temperature of the plasma is maximum in Ar atmosphere compared to He or air.

7.5 References

- [1] J. G. Bednorz, and K. A. Muller, *Zeitschrift für Physik B*, **64** 189 (1986).
- [2] M. K. Wu, J. R. Ashburn, C. J. Torng, P. H. Hor, R. L. Meng, L. Gao, Z. J. Huang, Y. Q. Wang and C. W. Chu, *Phys. Rev. Lett.*, **58** 908 (1987).
- [3] E. N. Sobol, *Phase Transformations and Ablation in Laser Treated Solids* (John Wiley & Sons, New York, 1995).
- [4] B. Oh, M. Naito, S. Arnason, P. Rosenthal, R. Barton, M.R. Beasley, T. H. Geballe, R. H. Hammond and A. Kapitulnik, *Appl. Phys. Letts.*, **51** 90 (1990).
- [5] B.C.W. Yuan and A. L. de Lozanne, *Appl. Phys. Letts.*, **57** 90 (1990).
- [6] M. P. Siegal, J. M. Phillips, Y. F. Hsieh and J. H. Marshall, *Physica C*, **172** 282 (1990).
- [7] M. Kawasaki, S. Nagata, Y. Sato, M. Funabashi, T. Hasegawa, K. Kishio, K. Kitazawa, K. Fueki and H. Koinuma, *Jpn. J. Appl. Phys.*, **26** L736 (1987).
- [8] H. Adachi, K. Hirochi, K. Setsune, M. Kitabatake and K. Wasa, *Appl. Phys. Letts.*, **51** 2263 (1989).
- [9] J. N. Eckstein, I. Bozovic, K. E. von Dessionneck, D. G. Scholm, J. S. Harris, Jr. and S. M. Baumann, *Appl. Phys. Letts.*, **57** 933 (1990).
- [10] R. A. Neifeld, S. Gunapala, G. Liang, S. A. Shaheen, M. Croft, J. Price, D. Simmons and W. T. Hill III, *Appl. Phys. Letts.*, **57** 933 (1990).
- [11] T. Venkatesan, X. D. Wu, A. Inam and J. B. Wachtman, *Appl. Phys. Letts.*, **52** 1193 (1988).
- [12] P. E. Dyer, R. D. Greenough, A. Issa and P. H. Key, *Appl. Phys. Letts.*, **53** 534 (1988).
- [13] R. E. Muenchausen, K.M. Hubbard, S. Foltyn, R. C. Estler, N. S. Nogar and C. Jenkins, *Appl. Phys. Letts.*, **56** 578 (1990).
- [14] P. Tiwari, S. Sharan and J. Narayan, *Appl. Phys. Lett.*, **59** 357 (1991).

- [15] D. K. Fork, F. A. Ponce, J. C. Tramontana and T. H. Geballe, *Appl. Phys. Lett.*, **58** 2294 (1991).
- [16] W. P. Shen, C. Lehane, J. P. Zheng and H. S. Kwok, *Appl. Phys. Lett.*, **64** 3175 (1994).
- [17] A. Kühle, J. L. Skov, S. Hjorth, I. Rasmussen and J. B. Hansen, *Appl. Phys. Lett.*, **64** 3178 (1994).
- [18] R. P. Reade, X. L. Mao and R. E. Russo, *Appl. Phys. Lett.*, **59** 739 (1991).
- [19] J. Wild, P. Engst, S. Civivs, J. Pochyly and J. Pracharova, *Appl. Phys. Lett.*, **60** 1747 (1992).
- [20] D. S. Misra and S. B. Palmer, *J. Appl. Phys.*, **68** 1403 (1990).
- [21] R. K. Singh, D. Bhattacharya, P. Tiwari, J. Narayan and C. B. Lee, *Appl. Phys. Lett.*, **60** 255 (1992).
- [22] S. Witanachchi, H. S. Kwok, X. W. Wang and D. T. Shaw, *Appl. Phys. Lett.*, **53** 234 (1988).
- [23] S. S. Harilal, P. Radhakrishnan, V. P. N. Nampoori and C. P. G. Vallabhan, *Appl. Phys. Lett.*, **64** 3377 (1994).
- [24] Y. Nakata, W. K. A. Kumuduni, T. Okada and M. Maeda, *Appl. Phys. Lett.*, **64** 2599 (1994).
- [25] P. T. Murray and D. T. Peeler in *Laser Ablation: Mechanisms and Applications II* (American Institute of Physics, New York, 1994).
- [26] S. Metev, M. Ozegowski, G. Sepold and S. Burmester, *Appl. Sur. Sci.* **96-98**, 122 (1996).
- [27] See Chapter 5 of this thesis
- [28] A. Mele, A. G. Guidoni, R. Kelly, A. Miotello, S. Orlando and R. Teghill, *Appl. Sur. Sci.* **96-98** 102 (1996).
- [29] S. I. Anisimov, B. S. Lukyanchuk and A. Luches, *Appl. Sur. Sci.* **96-98** 96 (1996).

- [30] G. Padmaja, A. V. Ravikumar, V. P. N. Nampoori and C. P. G. Vallabhan, *Bull. Mat. Sci.* **14** 545 (1991).
- [31] H. Chiba, K. Murakami, O. Eryu, K. Shihoyama and K. Masuda, *Jpn. J. Appl. Phys.* **30** L732 (1991).
- [32] O. Eryu, K. Murakami, K. Masuda, K. Shihoyama and T. Mochizuki, *Jpn. J. Appl. Phys.* **31** L86 (1992).
- [33] T. Venkateshan, X. D. Wu, A. Inam, Y. Jeon, M. Croft, E. W. Chase, C. C. Chang and J. Wachtman, *Appl. Phys. Lett.*, **53** 1431 (1988).
- [34] A. V. Bulgakov, M. R. Predtechensky and A. P. Mayorov, *Appl. Sur. Sci.* **96-98** 159 (1996).
- [35] R. A. Al-Wazzan, J. M. Hendron and T. Morrow, *Appl. Sur. Sci.* **96-98** 170 (1996).
- [36] L. Lynds, B. R. Weinberger, B. M. Potrepka, G. G. Peterson and M. P. Lindsay, *Physica C*, **159** 61 (1989).
- [37] H. S. Kwok, P. Mattocks, L. Shi, X. W. Wang, S. Witanachchi, Q. Y. Ying, J. P. Zheng and D. T. Shaw, *Appl. Phys. Lett.*, **52** 1825 (1988).
- [38] J. F. Ready, *Effect of High Power Laser Radiation* (Academic Press, New York, 1971).
- [39] H. Hora, *Nonlinear Plasma Dynamics at Laser Irradiation - Lecture notes in Physics* (Springer, Berlin, 1979).
- [40] D. B. Geohegan, *Appl. Phys. Lett.*, **60** 2732 (1992).
- [41] W. K. A. Kumudini, Y. Nakata, T. Okada and M. Maeda, *Appl. Phys. B*, **58** 289 (1994).
- [42] J. Gonzalo, C. N. Afonso and J. Perrière, *J. Appl. Phys.*, **79**, 8042 (1996).
- [43] W. Marine, M. Gerri, J. M. S. d'Aniello, M. Sentis, Ph. Delaporte, B. Forestier and B. Fontaine, *Appl. Sur. Sci.*, **54** 264 (1992).
- [44] D. B. Geohegan, *Thin Solid Films*, **220** 138 (1992).

- [45] J. Gonzalo, C. N. Afonso, F. Vega, D. Martínez García, J. Perrière, *Appl. Sur. Sci.* **86** 40 (1995).
- [46] C. E. Otis, P. M. Goodwin, *J. Appl. Phys.*, **73** 1957 (1993).
- [47] W. A. Weimer, *Appl. Phys. Lett.*, **52** 2171 (1988).
- [48] A. Giardini-Guidoni, R. Teghill and A. Mele, *Spectrochimica Acta*, **46A**, 503 (1990).
- [49] O. Auciello, S. Athavale, O. E. Hankins, M. Sito, A. F. Schreiner and N. Biunno, *Appl. Phys. Lett.*, **53** 72 (1988).
- [50] D. B. Geohegan and D. N. Mashburn, *Appl. Phys. Lett.*, **55** 2345 (1989).
- [51] R. K. Singh and J. Narayan, *Phys. Rev. B*, **41** 8843 (1990).
- [52] K. Singh, O. W. Holland and J. Narayan, *J. Appl. Phys.* **68** 233 (1990).
- [53] J. C. S.Kools, T. S. Baller, S. T. De Zwart and J. Dieleman, *J. Appl. Phys.*, **71** 4547 (1992).
- [54] R. Kelly, *Phy. Rev. A*, **46** 860 (1992).
- [55] J. N. Leboeuf, K. R. Chen, J. M. Donato, D. B. Geohegan, C. L. Liu, A. A. Poretzky and R. F. Wood, *Appl. Sur. Sci.* **96-98** 14 (1996).
- [56] A. D. Boardman, B. Cresswell and J. Anderson, *Appl. Sur. Sci.* **96-98** 55 (1996).
- [57] S. Fähler and H. Krebs, *Appl. Sur. Sci.* **96-98** 61 (1996).
- [58] H. C. Le, J. Vuillon, D. Zeitoun, W. Marine, M. Sentis and R. W. Dreyfus, *Appl. Sur. Sci.* **96-98** 76 (1996).
- [59] V. I. Mazhukin, I. Smurov and G. Flamant, *Appl. Sur. Sci.* **96-98** 89 (1996).
- [60] G. Granse, S. Völlmar, A.Lenk, A. Rupp and K. Rohr, *Appl. Sur. Sci.* **96-98** 97 (1996).
- [61] T. P. Hughes, *Plasmas and Laser Light* (Adam Hilger, England 1975).

- [62] L. J. Radziemski and D. A. Cremers, *Laser-induced Plasmas and Applications* (Marcel Dekker, Inc., New York, 1989).
- [63] Y. B. Zeldovich and Y. P. Raizer, *Physics of Shock Waves and High-Temperature Hydrodynamic Phenomena* (Academic Press, 1966).
- [64] R. C. Weast, *CRC Handbook of Chemistry and Physics* (CRC press, Inc., Florida, 1988).
- [65] See Chapter 5 of this thesis.
- [66] G. Bekefi, *Principles of Laser Plasmas*, (John Wiley & Sons, New York, 1976).
- [67] Geoffrey V. Marr, *Plasma Spectroscopy*, (Elsevier Publishing Company, New York, 1968).
- [68] W. L. Wiese, in *Plasma Diagnostics*, (R.H. Huddlestone and S. L. Leonard) (eds), (Academic Press, New York, 1965), Chapter 6.
- [69] H. R. Griem, *Plasma Spectroscopy* (McGraw-Hill book company, New York, 1964).
- [70] D. B. Geohegan in *Pulsed LASer Deposition of THin Films*, D. B. Chrisey and G. K. Hubler (eds) (Wiley, New York, 1994), Chapter 5.
- [71] See Chapter 8 of this thesis.
- [72] A. H. El-Astal and T. Morrow, *J. Appl. Phys.* **80** 1156 (1996)
- [73] J. T. Knudsen, W. B. Green and D. G. Sutton, *J. Appl. Phys.*, **61** 4771 (1987).
- [74] R. H. Huddlestone and S. L. Leonard, *Plasma Diagnostic Techniques* (Academic press, London, 1965).
- [75] P. T. Rumsby and J. W. M. Paul, *Plasma Physics*, **16** 247 (1974).
- [76] D. B. Geohegan and A. A. Puretzky, *Appl. Sur. Sci.* **96-98** 131 (1996).

Chapter 8

Temporal and spatial evolution of laser ablated plasma $\text{YBa}_2\text{Cu}_3\text{O}_7$

Abstract

$\text{YBa}_2\text{Cu}_3\text{O}_7$ target was laser ablated, and the time of flight (TOF) distributions of different species in the resultant plasma were investigated as functions of distance from the target and laser power density using emission spectroscopy. Up to a short distance from the target ($\simeq 1.5$ cm), TOF distributions show twin peaks for atomic and molecular species, while only single peak distribution is observed for ionic species. At greater distances (> 1.5 cm) all of them exhibit single peak distribution. The twin peaks are assigned to species corresponding to those generated directly/in the vicinity of target surface and to those generated from collisional/recombination process.

8.1 Introduction

Since the successful deposition of ceramic materials like high T_c superconducting films using pulsed laser ablation [1-9], there has been intensive interest in the studies on composition and transport properties of laser induced plasma (LIP) [10-18]. In this technique thin films are formed by condensing material ablated from the surface of a $YBa_2Cu_3O_7$ target onto a solid substrate. Ablation of the target is accompanied by the formation of brilliantly elongated plasma located in front of the target surface and extending outward to about 3 cm from the target surface. The pulsed laser high temperature superconducting (HTSC) film deposition can be subdivided into the following stages (i) absorption of radiation by the target (ii) preablation processes like heating and thermochemical reactions, (iii) ablation of the target, (iv) formation of a plasma cloud and interaction of laser radiation with the ablation products, (v) expansion of the plasma cloud and scattering of ablation products following the laser pulse and (vi) deposition. Laser deposition differs from other thermal film deposition techniques by the non-equilibrium character of plasma jet (non-Maxwellian velocity distribution of the particles), the directivity of ablation products (90 % of the material is contained within an angle of $\pm 30^\circ$, and cosine law is invalid), and a large number of ionized particles [19-21].

It is of fundamental importance to identify the different atomic, ionic and molecular species generated from laser induced plasma and to relate the quality and rate of thin film growth with species present and with various transport processes occurring in plasma plume. A full understanding of the plasma processes open up the possibility of reliable control of the deposition processes. Some of the techniques reported by various authors for characterizing LIP from different targets include optical emission spectroscopy [22-27], optical absorption spectroscopy [28-30], mass spectroscopy [31-33], ion probe method [34, 35], streak or high-speed photography [27, 36, 37] and laser induced fluorescence [38, 39].

The nature and characterization of laser produced plasma depends very much on the irradiance levels used. At low irradiance levels, the ablation process is analogous to the application of a thermal pulse, of several nanosecond duration, to the surface of the target. A Knudsen layer is formed near the surface where the density of desorbed particles is high [40]. In this region thermal energy is converted directly into translational energy. Further from the target the plume becomes a free expansion into vacuum. This is

the same principle of the nozzle beam expansion used to generate supersonic beams [41]. Kelly and co-workers [42-46] have described the theoretical details of this model. At high irradiance levels, typically used for deposition, a different model must be used. At these irradiance levels explosive dissociation of the target material takes place. The local pressure close to the target rises to several atmospheres and a shock wave propagates out from the target [47]. In vacuum the shock wave rapidly becomes a free expansion. But at moderate pressures, the shock wave acts as a piston that compresses the background gas, building up density at the shock front, leaving a rarefied region of the gas in its wake. At the shock front the temperature and the pressure significantly get elevated which enhances ionization, dissociation and electronic excitation. At sufficiently large pressures a blast wave is produced [48-50]. A blast wave is a shock wave produced by the strong explosion. The blast wave is powerful enough to produce a luminous shock front. A second luminous pulse is observed in the laser ablation of $\text{YBa}_2\text{Cu}_3\text{O}_7$ [27] and the ablation of polymers [49] at low pressures. At these low pressures reactive collisions probably account for strong emission, *ie*, from the chemiluminescent reactions of the background gas atomic species in the plume.

In spite of the large number of reports available in the literature, studies on LIP from solid targets have not yet yielded conclusive results and this is essentially due to the complexity of the phenomena involved. In this chapter, some new results of time and space resolved analysis of the spectral emission due to various excited atomic (Y I and Ba I), ionic (Y II and Ba II) and molecular species (YO) in the LIP from high T_c superconductor $\text{YBa}_2\text{Cu}_3\text{O}_7$ ($T_c = 90\text{K}$, here after YBCO) using $1.06 \mu\text{m}$ radiation from a Nd:YAG laser.

8.2 Experimental

The details of the experimental set-up is given in chapter 2. The YBCO target having diameter 15 mm and thickness 3 mm was mounted in a stainless steel vacuum chamber (~ 0.05 mbar) equipped with quartz windows such that the target surface could be irradiated at normal incidence using $1.06 \mu\text{m}$ laser beam from a Q-switched Nd:YAG laser having repetition rate 10 Hz. To avoid errors due to local heating and drilling, the sample was rotated about an axis parallel to the laser beam. Laser irradiance was varied by attenuating the simmer current of the flash lamp. The plasma emission spec-

trum for YBCO sample was viewed normal to its expansion direction and imaged using appropriate focusing lenses and apertures onto the slit of a monochromator (Jarrell-Ash 0.5 m) which is coupled to a PMT (S20 cathode). The monochromator allowed the measurements of individual species of atoms, ions or molecules by tuning the particular emission wavelengths. For spatially resolved studies, the plasma plume from different regions was focused on to the monochromator slit. The characteristic lines were selected by the monochromator and the PMT output was fed to a 200 MHz digital storage Oscilloscope (Iwatsu model DS 8621) with 50Ω termination to record the emission pulse shapes. This set-up essentially provides delay as well as decay times for emission from constituent species at a specific point within the plasma and these are extremely important parameters related to the evolution of laser ablated materials in a direction normal to the target surface.

8.3 Results and Discussion

The time resolved studies of emission lines from various species were made from the oscilloscope traces which showed definite time delays for emission with respect to the laser pulse. The time evolution of the constituent emission from the plasma determines the subsequent expansion and should provide the best observation for our understanding of the plasma dynamics. Typical time of flight distributions of Y I (558.1 nm), Y II (508.47 nm), and YO (601.9 nm) at a distance 1 cm from the target surface are given in fig. 8.1. The initial spike (prompt emission) in the figures can be used as a time marker. The prompt emission probably results from the laser excitation of the evaporated species. Following are the new significant observations made from the present studies: (1) The time evolution of the spectral emission profiles obtained in the present work clearly reveals that the species ejected by YBCO target exhibit twin peaks for the time of flight (TOF) distribution. (2) The twin peak distribution exists only for neutral atoms (like Y I, Ba I) and molecular species (like YO) while this feature is absent in the case of ionized species (like Y II, Ba II). (3) The twin peak distribution was observed only up to a certain distance from the target (up to $\simeq 1.5$ cm). At farther distances only the component corresponding to the first peaks occurs. (4) The intensity of the ionized species drastically decreases with increasing separation from the target surface. (5) The variation of delay time with distance is almost a linear behaviour for the delayed peak

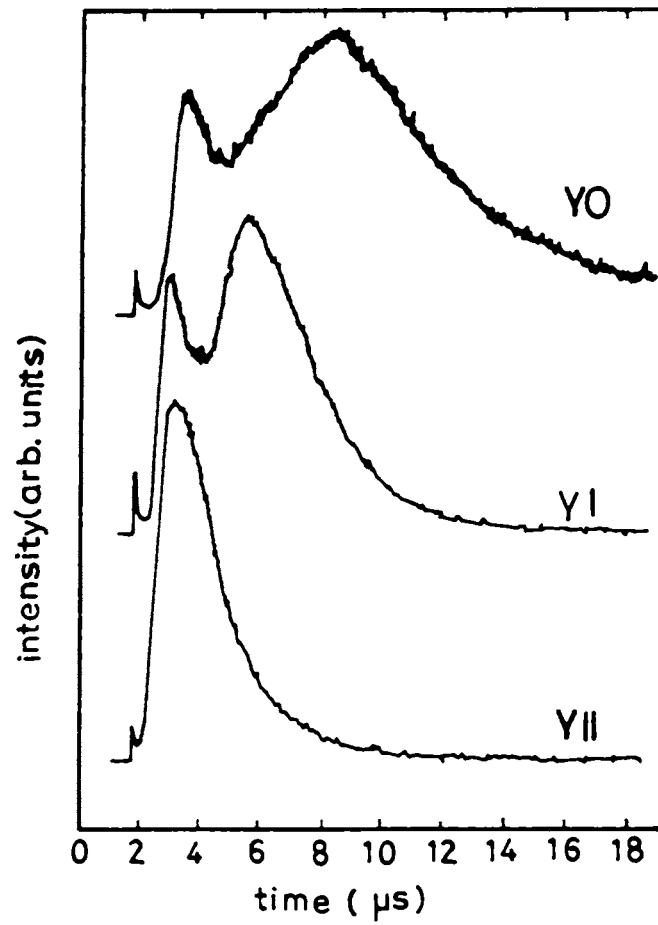


Figure 8.1: Intensity variation of spectral emission with time for Y II (508.5 nm), Y I (558.1 nm) and YO (601.9 nm) observed at the 1 cm away from the target at a laser irradiance of 62 GW cm^{-2} .

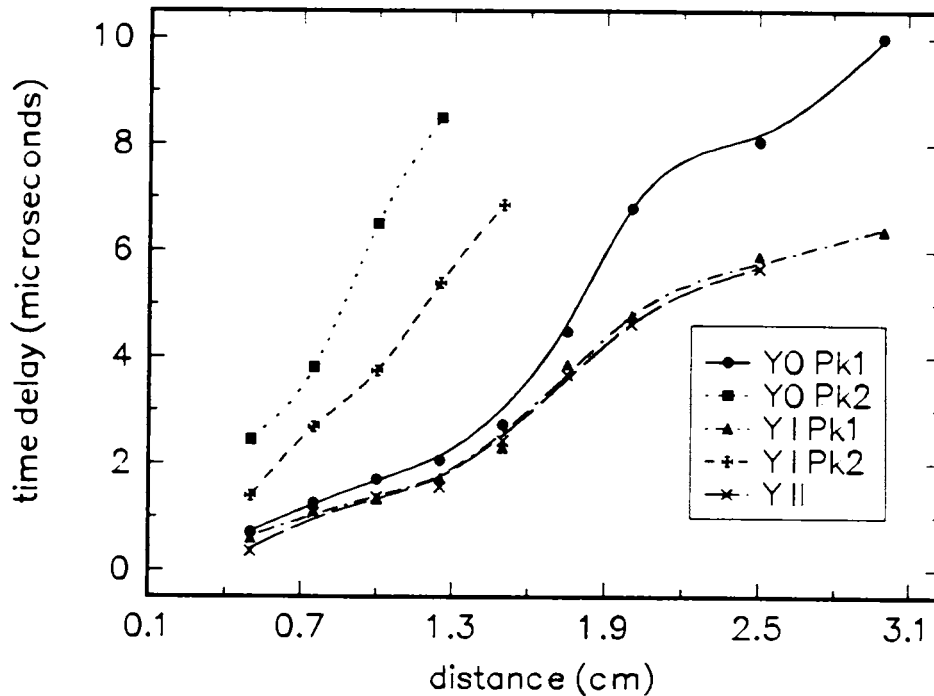


Figure 8.2: Variation of time delay vs distance for the intensity peaks I and II in the case of Y II, Y I and YO at constant laser irradiance of 62 GW cm^{-2} .

while a nonlinearity is observed in the case of first peak (figs. 8.2 and 8.3). (6) The time delay corresponding to first peak decreases with respect to irradiance. However, the time delay corresponding to second peak is constant at lower irradiances and decreases with increasing irradiance above a threshold (fig. 8.4 and 8.5).

Similar reports available in literature describe twin peak time of flight distribution in laser generated plasma from YBCO using optical absorption spectroscopy [28] and fluorescence technique [38]. However, using plasma emission studies, this is the first observation of a twin peak distribution.

It is seen that, as shown in fig. 8.6, the intensity of emission from ionic species like Y II and Ba II is very high near the target surface and decreases drastically beyond 1.5 cm and becomes below the detection limit at distances greater than 1.75 cm. The disappearance of ionic species with distance from the target surface is probably as a result of recombination. With reference to the twin peaks shown in fig. 8.1, the peak I corresponding to Y I, Ba I and YO grows in intensity up to an optimal distances ($\approx 1 \text{ cm}$) and then diminishes (figs. 8.7 and 8.8). Here the intensities of the faster peaks of these species increases with distance at shorter distances indicating it is being generated

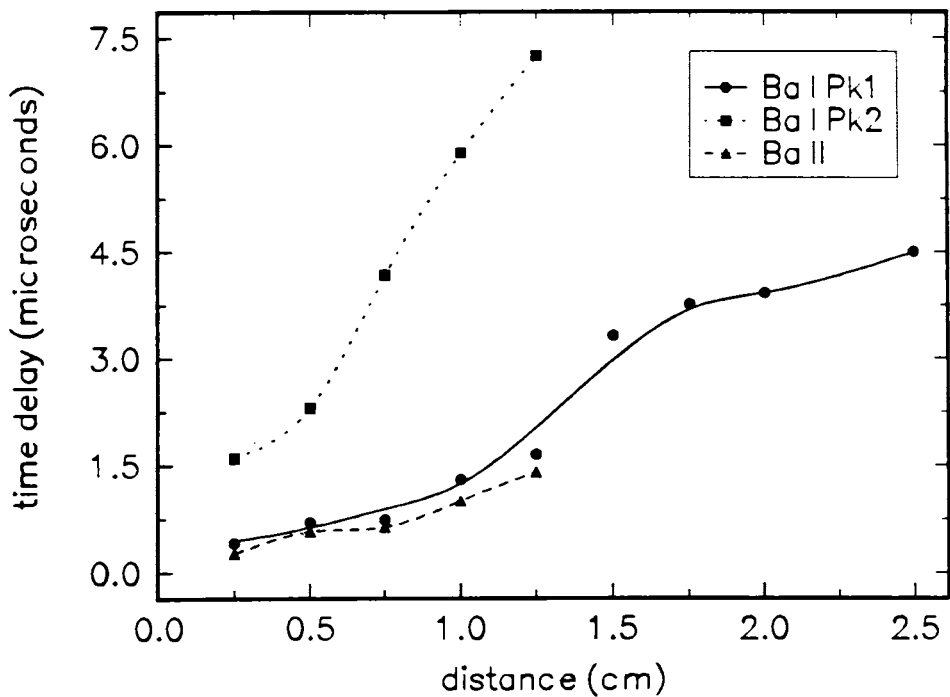


Figure 8.3: Variation of time delay vs distance for the intensity peaks I and II in the case of Ba I (606.3 nm) and Ba II (585.4) at constant laser irradiance of 62 GW cm^{-2} .

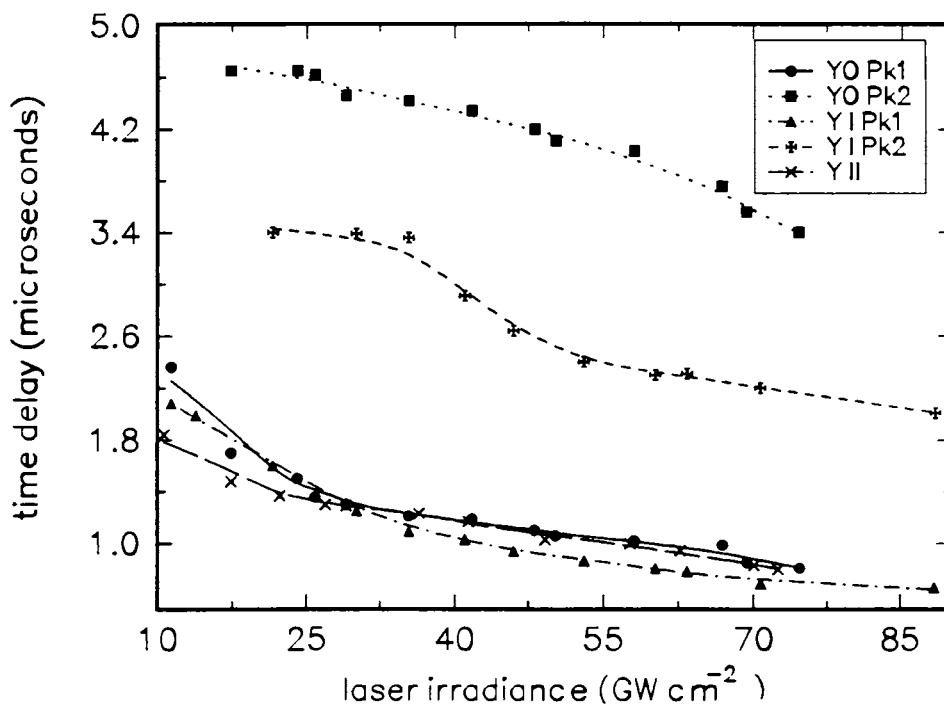


Figure 8.4: Variation of time delay of intensity peaks with laser irradiance for Y II, Y I, YO at a distance of 1 cm from the target.

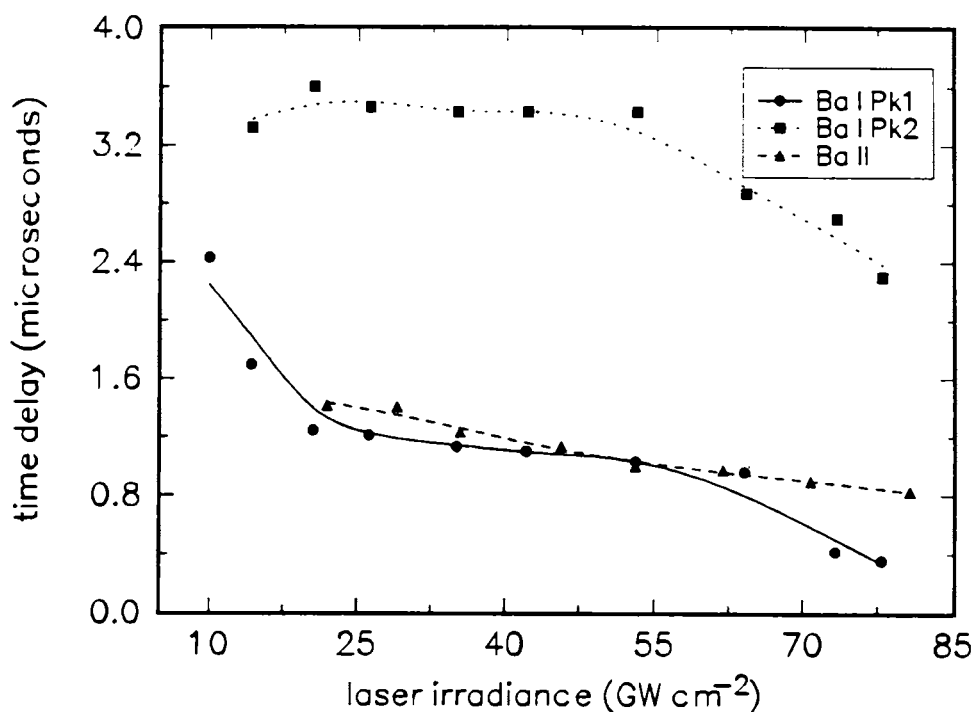


Figure 8.5: Variation of time delay of intensity peaks with laser irradiance for Ba I and Ba II at a distance of 1 cm from the target.

at some distance from the target surface. The delayed peaks (peak II) of Y I, Ba I and YO go down in intensity through out the plasma region and its range is limited up to 1.5 cm. It may be noted that the time delay for peak I of Y I is almost same as that of Y II. The variation of time delays as a function of distance and laser irradiance for Y based species are shown in figs. 8.2 and 8.4 respectively. The variation of time delays as a function of distance is linear for second peak of Y I and YO, while that for first peaks of the Y I and YO and for the single peak of Y II are slightly nonlinear showing a saturation effect farther from target surface. Results obtained during the time resolved study of excited neutral and singly ionized Ba species are in good agreement with the above studies on Y based species. The variation of time delays for these species with respect to distance from the target surface and laser irradiance are given in fig. 8.3 and 8.5. We have not studied the emission intensity from excited BaO molecules because of very weak intensity.

Measurements of time delays yield the plasma front axial velocity defined as the expansion velocity of the ablated species perpendicular to the target surface. A plot of delay time as a function of position (fig. 8.2) shows that the first peak of Y I and YO

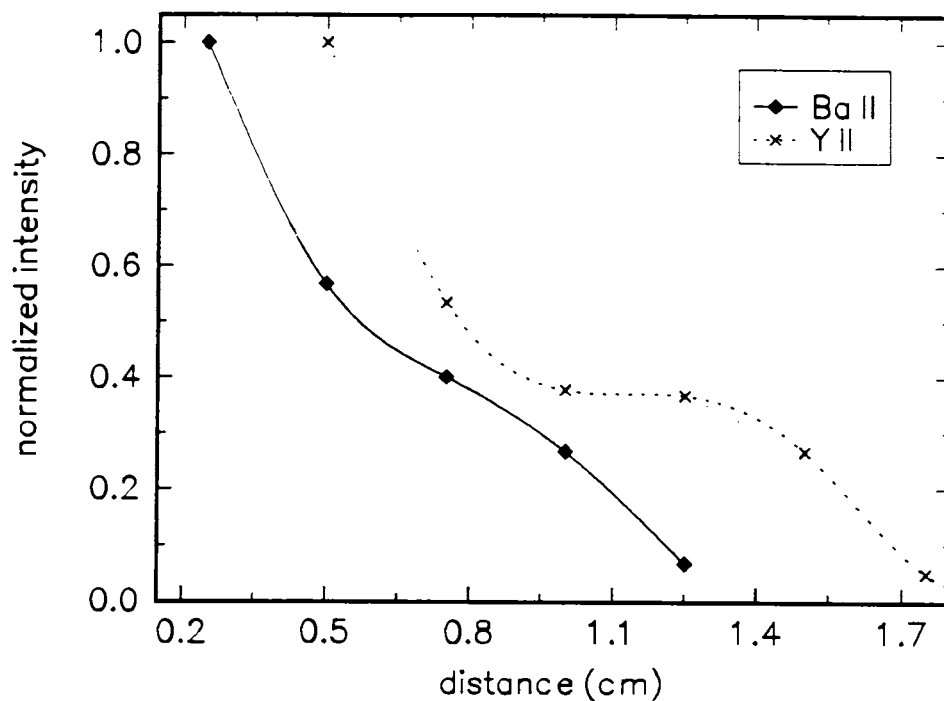


Figure 8.6: Variation of emission intensity with distance from the target surface for Y II and Ba II (laser irradiance 62 GW cm^{-2})

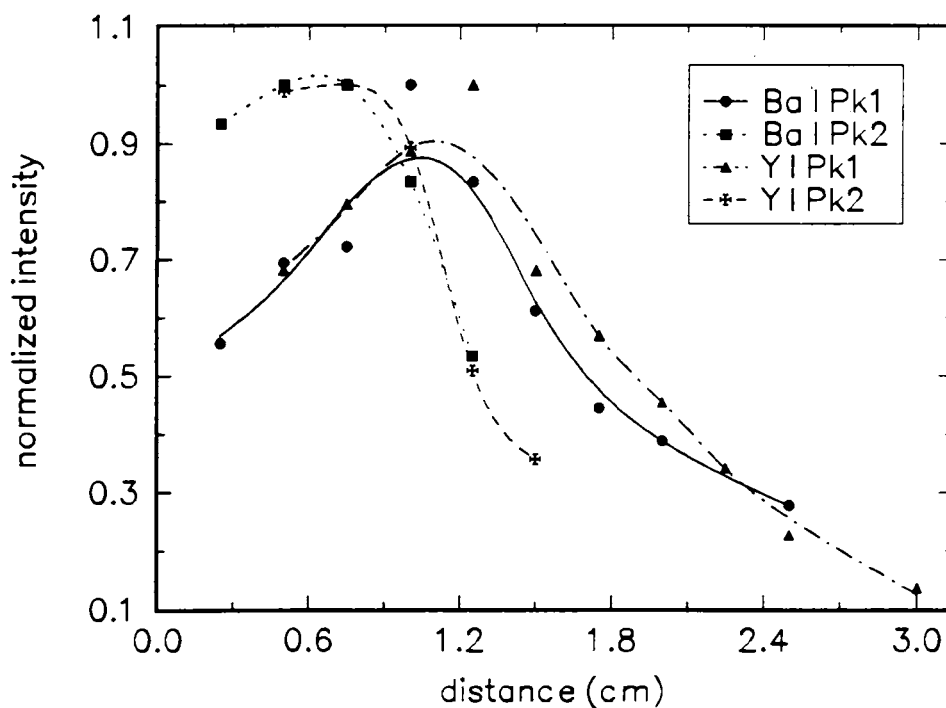


Figure 8.7: Change in intensity of Pk1 and Pk2 of atomic species with distance from the target surface. Laser irradiance used 62 GW cm^{-2}

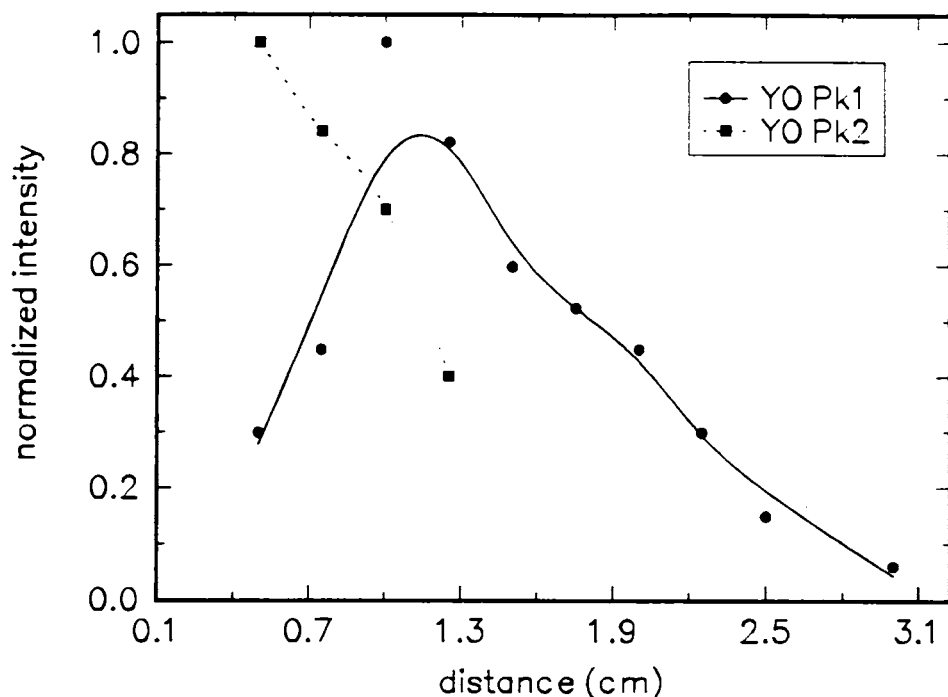


Figure 8.8: Intensity variation of YO emission for Pk1 and Pk2 with distance. Laser irradiance used 62 GW cm^{-2} .

gives a constant velocity ($V_{yo} \simeq (7 - 6) \times 10^5 \text{ cm s}^{-1}$, $V_y \simeq (8 - 7) \times 10^5 \text{ cm s}^{-1}$) until it reaches $\simeq 1.5 \text{ cm}$ from the target surface after which they slow down rapidly to a much smaller expansion velocity ($V_{yo} \simeq (3 - 2) \times 10^5 \text{ cm s}^{-1}$, $V_y \simeq (5 - 4) \times 10^5 \text{ cm s}^{-1}$). The time of flight (TOF) analysis is strictly valid for free flight (collisionless) from a pulsed source. In the laser ablation experiments, the plume of gas expanding from the surface is very dense at earlier times, *ie*, particles undergo many collisions. Thus the velocity should be regarded as an effective stream velocity in the direction normal to the target surface. The effective stream velocity may not, however, be identical to the actual particle stream velocity. For eg., if optical emission arises from electron impact excitation of species in the laser produced plasma, the excitation rate is proportional to the electron and species densities. Thus the time dependence of the emission intensity would be affected by the motion of electrons as well as that of particles.

The possibility of twin peak structure for Y I and YO due to radiation trapping or self absorption [51,52] is unlikely due to the fact that the time delays between the peaks vary with respect to distance from the target and they are of the order of microseconds. Radiation trapping effects are expected to be more important as the plume density

increases (*ie.*, closer to the target), and for strong emission lines terminating on the ground state, since the level has the highest population of potential absorbers. Geohegan et al [53] observed a peculiar double peak structure during ion probe studies of Y plasma. They regarded this as due to the momentum transfer between the plume and background gas which result into a slowed component only for a limited range and distance. Sakeek et.al [28] also observed a double peak structure for YO molecules using laser induced absorption spectroscopy and explained it as due to evaporation from the target is possible for the delayed slower component of the plume. Okada et.al [38] attributed the time delays solely to TOF arising from different velocities of the species. They assigned the observation of twin peak to the presence of faster and slower components of same species. If it is assumed that the terminal stage of the plume can be modeled as a free expansion into vacuum, the expansion velocity v can be written as [50]

$$v = \frac{2}{\gamma - 1} \sqrt{\frac{\gamma kT}{M}} \quad (8.1)$$

where M is the mass of the species, γ is the specific heat ratio the value of which varies from 1.2-1.3 to account for the degree of freedom associated with ionization and excitation, and k is the Boltzmann's constant. However at a given point, using above equation, since velocities depend only on mass of the species and plasma temperature, it is not possible to have two different velocity distributions for the same species. The most plausible explanation is as follows. The twin peak distribution arises as due to different origins for the same species occurring in the plasma. Species like Y I and YO are generated directly from the target, while ionic species are produced mainly just outside the target due to electron impact. In the vicinity of target surface, temperature is so high that ionization of Y I and Ba I by electron collision is highly probable [54]. As time evolves plasma temperature drops so that Y II generation decreases and collisional recombinations of Y II with electrons result into enhanced spectral emission from Y I apart from those directly coming from the target. At slightly later times YO is generated from collisional recombination of Y I and O. Thus we have two types of same species in plasma. (i) Those coming directly/generated in the vicinity of the target surface and having larger TOF delays giving rise to second peak. (ii) Those generated away from the target surface due to collisions and recombination process which occur earlier at the point of observation giving rise to first peak.

It must be noted that there is only one kind of Y II viz. that generated in the vicinity

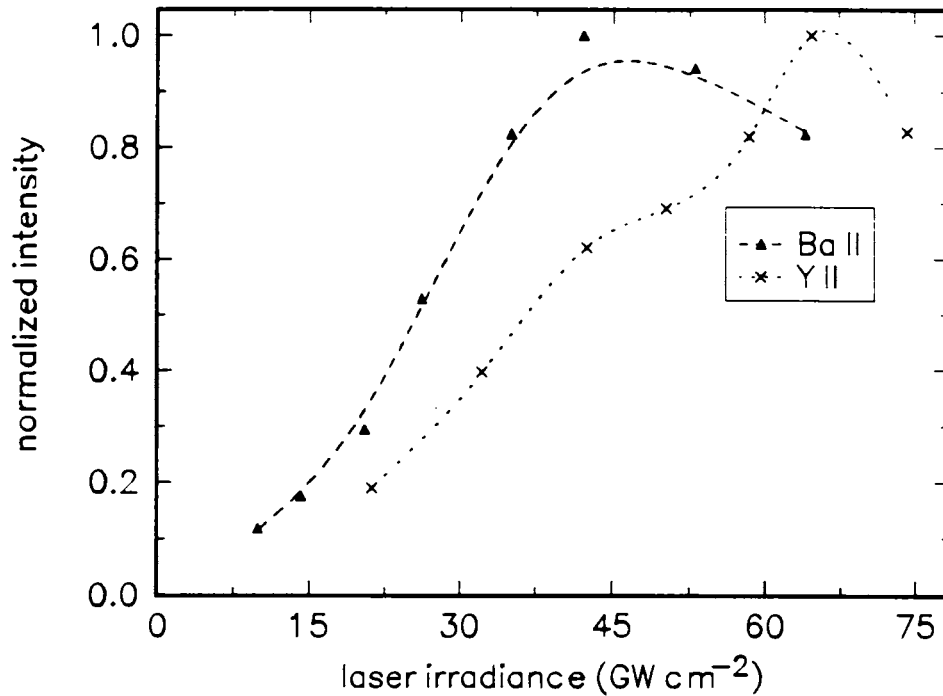


Figure 8.9: Intensity of ionic species as a function of laser irradiance for 1 cm distance from the target surface.

of target surface due to collisional impact in the plasma. According to eqn. (8.1), since the masses are the same, both Y I and Y II should have identical time delays which implies that peak of Y II should coincide with peak II of Y I. However peak of Y II is observed earlier (coinciding with peak I of Y I) due to the fact that the velocity of Y II is larger than that observed for Y I, because of the ambipolar diffusion process due to space charge effect produced by ion and electron densities near the target surface [55]. In this type of diffusion processes the charge separation and fields adjust to each other that the field restrains the run-away electrons and pulls forward the heavy ions, making them diffuse only as a team.

When the laser irradiance is increased, the emission from all species show a drastic increase in intensity, especially at low irradiance levels, but their time history is not significantly changed. The intensity increase with laser irradiance is more pronounced for the ionic lines. A plot of normalized intensity vs laser irradiance (fig. 8.9) for Y II and Ba II species show an increase in intensity with respect to irradiance and a decrease in population at higher irradiance levels. The decrease in intensity of ionic lines at higher irradiance levels is mainly due to two reasons. At higher irradiance levels, because of

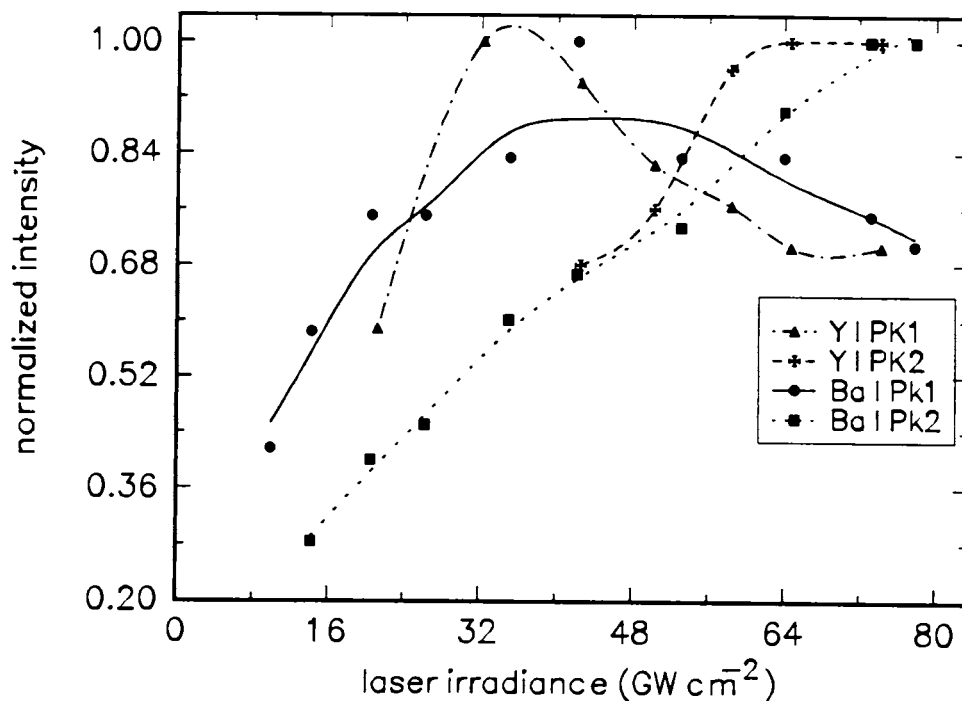


Figure 8.10: Normalized intensity vs laser irradiance for Pk1 and Pk2 of neutral Y II and Ba II (distance 1 cm).

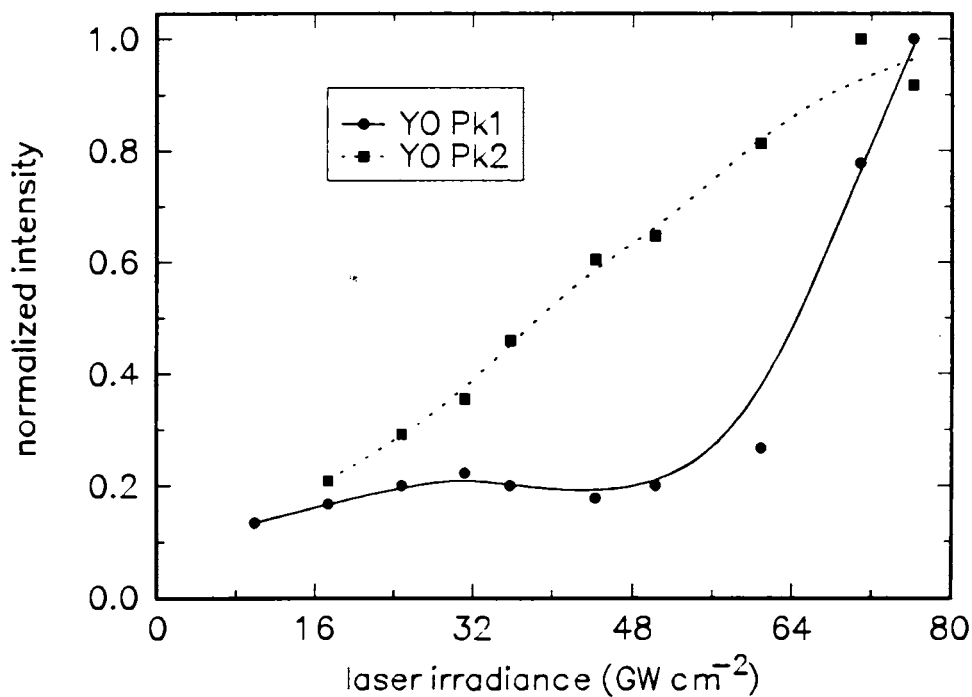


Figure 8.11: Variation of emission intensity with laser irradiance for the Pk1 and Pk2 of YO at a distance 1 cm from the target surface.

high plasma density, absorption of the laser beam by the plasmas takes place, so called plasma shielding, and by collisional excitation. However, the intensity variation with laser irradiance of the double peaks of atomic and molecular species show somewhat different peculiarities (fig. 8.10 and 8.11). The intensity of first peak of Y I and Ba I increases up to a threshold laser irradiances and then decreases while in the case of the first peak of YO, it is more or less constant at low irradiance levels and increases rapidly at higher irradiance levels. Emission intensities from the delayed peaks of Y I, Ba I and YO show continuous increase with increasing laser irradiance indicating that, as the laser irradiance increased more material gets ablated from the target and emit. However the faster emission peaks corresponding to Y I and Ba I in the vapour plume decreases relative to Pk2 of these species as the irradiance is increased.

From fig. 8.3 one can see that the delay time for the first peak of species for Y I and YO decreases with respect to increasing laser irradiance, while the time delay corresponding to second peak is constant at lower irradiance levels and decreases at higher irradiances. This implies that the kinetic energy of the species coming directly/from the vicinity of the target surface do not vary much at lower irradiance, while above a certain threshold sudden enhancement in kinetic energy take place due to the initiation of nonlinear process in laser-matter interaction. The nonequilibrium character of the laser plasma and also the departure of particles from the Maxwellian velocity distribution are expected to be associated with the mutually reversible processes of ionization and recombination. The energy released on recombination is converted into the kinetic energy of atoms and ions which may give rise to a relatively faster neutral/molecular particles as observed in the case of Ba I, Y I and YO.

On closer inspection, it can be seen that the species with same status, irrespective of their atomic weight show the same properties with space and time. The delayed component observed for atomic and molecular species, which is dominant at short distances (≤ 1.5 cm) is attributed to electron impact excitation of these species ejected directly from the target during ablation. The faster component which becomes stronger at certain distance from the target surface is identified as produced during recombination of cool ionic/atomic species in the outer contact front of the expanding plasma.

8.4 Conclusion

YBa₂Cu₃O₇ target was laser ablated using 1.06 μ m Q-switched Nd:YAG laser. The time of flight (TOF) distributions of different species in the resultant plasma were investigated as functions of distance from the target and laser power density using emission spectroscopy. The present work has differentiated the type of species directly coming from the target surface and those due to recombination process. We have observed the twin peak structure for atomic and molecular species such as Y I, Ba I and YO at short distances. Evaporation from the target/expansion of those generated in the vicinity of the target leads to the appearance of the delayed component and those created by collisional or recombination process apparently give rise to first peak. The complicated interplay between laser irradiance and distance from the target surface is not yet completely understood, but data and discussion presented here do provide a good picture regarding the YBCO plasma dynamics.

8.5 References

- [1] D.Dijkkamp, T.Venkatesan, X.D.Wu, S.A.Shaheen, N.Jisrawi, Y.H.Min-Lee, W.L.McLean, and M.Croft, *Appl. Phys. Lett.* **51** 619 (1987).
- [2] L.Lynds, B.R.Weinberger, G.G.Peterson, and H.A.Krasinski, *Appl. Phys. Lett.* **52** 320 (1988).
- [3] C. Champeaux, P. Marchet, J. Aubreton, J. P. Mercucio and A. Catherinot, *Appl. Sur. Sci.*, **69** 335 (1993).
- [4] Y. Mei, H. L. Luo and R. Hu, *Appl. Phys. Letts.*, **56** 581 (1990).
- [5] H. F. Sakeek, M. Higgins, W. G. Graham, T. Morrow, R. J. Turner, D. G. Walmley, *J. Appl. Phys.*, **70**, 2455 (1991).
- [6] H. Jiang, A. J. Drehman, R. J. Andrews and J. A. Horrigan, *Appl. Phys. Letts.*, **65** 3132 (1994)
- [7] Q. Li *Pulsed Laser Deposition of Thin Films* D. B. Chrisey and G. K. Hubler (eds.)(John Wiley and sons, New York, 1994) Chapter 23.
- [8] E. N. Sobol, *Phase Transformation and Ablation in Laser Treated Solids* (John Wiley and sons, New York, 1994) Chapter 6.
- [9] K. L. Saegner in *Pulsed Laser Deposition of Thin Films* D. B. Chrisey and G. K. Hubler (eds.)(John Wiley and sons, New York, 1994) Chapter 7.
- [10] J.P.Zheng, Z.Q.Huang, D.T.Shaw, and H.S.Kwok, *Appl. Phys. Lett.* **54** 280 (1989).
- [11] X.D.Wu, B.Dutta, M.S.Hegde, A.Inam, T.Venkatesan, E.W.Chase, C.C.Chang, and R.Howard, *Appl. Phys. Lett.* **54** 179 (1989).
- [12] P.E.Dyer, R.D.Greenough, A.Issa, and P.H.Key, *Appl. Phys. Lett.*, **53** 534 (1988).
- [13] N.H.Cheung, Q.Y.Ying, J.P.Zheng, and H.S.Kwok, *J. Appl. Phys.*, **69** 6349 (1991).
- [14] S. Deshmukh, E. W. Rothe, G. P. Reek, T. Kushida and Z. G. Xu, *Supercond. Sci. & Technol.*, **1** 319 (1989).

- [15] O. Aucliello, S. Athavale, O. E. Hankins, M. Sito, A. F. Schreiner and N. Biunno, *Appl. Phys. Letts.*, **53** 72 (1988)
- [16] D. B. Geohegan and D. N. Mashburn, *Appl. Phys. Letts.*, **55** 2345 (1989)
- [17] D. B. Geohegan in *Pulsed Laser Deposition of Thin Films* D. B. Chrisey and G. K. Hubler (eds.)(John Wiley and sons, New York, 1994).
- [18] J. G. Lunney, J. F. Lawler and R. Aratari, *J. Appl. Phys.*, **74** 4277 (1993).
- [19] R. K. Singh, O. W. Holland and J. Narayan, *J. Appl. Phys.* **68** 233 (1990).
- [20] C. E. Otis and P. M. Goodwin, *J. Appl. Phys.*, **73** 1957 (1993).
- [21] R. K. Singh and J. Narayan, *Phys. Rev. B*, **41** 8843 (1990).
- [22] W. A. Weimer, *Appl. Phys. Letts.*, **52** 2171 (1988).
- [23] S. Pramanik, A. Kumar and J. Narayanan, *Jpn. J. Appl. Phys.*, **32** 789 (1993).
- [24] C. Girault, D. Damiani, J. Aubreton and A. Catherinot, *Appl. Phys. Letts.*, **54** 2035 (1989).
- [25] H. Izumi, K. Ohata, T. Sawada, T. Morishita and S. Tanaka, *Jpn. J. Appl. Phys.*, **30** 1956 (1991).
- [26] P. Engst, P. Kubat, P. Bahacek and J. Wild, *Appl. Phys. Letts.*, **64** 2025 (1994).
- [27] P. E. Dyer, A. Issa and P. H. Key, *Appl. Phys. Letts.*, **57** 186 (1990).
- [28] H. F. Sakeek, T. Morrow, W. G. Graham and D. G. Walmsley, *Appl. Phys. Letts.*, **59** 3631 (1991).
- [29] T. Ohyanagi, A. Miyashita, K. Murakami and O. Yoda, *Jpn. J. Appl. Phys.*, **35** 3436 (1996).
- [30] T. Morrow, H. F. Sakeek, A. E. Astal, W. G. Graham and D. G. Walmsley, *J. Superconductivity* **7** 823 (1994).
- [31] A. G. Guidoni, R. Teghill and A. Mele, *Spectrochim. Acta*, **46A** 503 (1990)

- [32] H. Izumi, K. Ohata, T. Sawada, T. Morishita and S. Tanaka, *Appl. Phys. Letts.*, **59** 597 (1991).
- [33] R. C. Estler and N. S. Nogar, *J. Appl. Phys.* **69** 1654 (1991)
- [34] P. E. Dyer, R. D. Greenough, A. Issa and P. H. Key, *Appl. Phys. Letts.*, **53** 534 (1988).
- [35] G. Padmaja, A. V. R Kumar, V. P. N. Nampoori and C. P. G. Vallabhan, *J. Phys. D*, **22** 1558 (1989).
- [36] K. Scott, J. M. Huntley, W. A. Phillips, J. Clarke and J. E. Field, *Appl. Phys. Letts.* **57** 922 (1990).
- [37] D. B. Geohegan, *Appl. Phys. Letts.*, **60** 2732 (1992).
- [38] T. Okada, N. Shibamaru, Y. Nakayama, and M. Maeda, *Appl. Phys. Lett.*, **60** 941 (1992).
- [39] Y. Nakata, W. K. A. Kumudini, T. Okada and M. Maeda, *Appl. Phys. Lett.*, **66** 3206 (1995).
- [40] J. L. Robin, Y. A. Durand, P. H. Langer and G. Tonons, *J. Appl. Phys.*, **39** 4184 (1968).
- [41] J. B. Anderson, R. P. Andres and J. B. Fenn, *Adv. Chem. Phys.*, **10** 275 (1966).
- [42] R. Kelly and A. Miotello in *Pulsed Laser Deposition of Thin Films* D. B. Chrisey and G. K. Hubler (eds.) (John Wiley and sons, New York, 1994) chap. 3.
- [43] R. Kelly and R. W. Dreyfus, *Surf. Sci.*, **198** 263 (1988).
- [44] R. Kelly and B. Braren, *Appl. Phys. B.*, **53** 160 (1991).
- [45] R. Kelly, *Phys. Rev. A*, **46** 860 (1992).
- [46] R. Kelly, *J. Chem. Phys.*, **92** 5047 (1990).
- [47] T. P. Hughes, *Plasmas and Laser Light*, (John Wiley and Sons, Inc., New York 1975).

- [48] P. E. Dyer, A. Issa and P. H. Key, *Appl. Surf. Sci.*, **46** 89 (1990).
- [49] P. E. Dyer and J. Sidhu, *J. Appl. Phys.*, **64** 4663 (1988).
- [50] Ya.B.Zel'dovich and Yu.P.Reizer, *Physics of Shock Waves and High Temperature Dynamics Phenomena* (Academic, London 1968).
- [51] K.L.Saenger, *J. Appl. Phys.*, **66** 4435 (1989).[50] J.F.Ready, *Effects of High Power Laser Radiation* (Academic, London 1971).
- [52] R. C. Issac, S. S. Harilal, C. V. Bindhu, V. P. N. Nampoori and C. P. G. Vallabhan, *Spectrochim. Acta B* (submitted).
- [53] D.B.Geohegan and A. A. Puretzky, *Appl. Phys. Lett.*, **67** 197 (1995).
- [54] Q.Y.Ying, D.T.Shaw, and H.S.Kwok, *Appl. Phys. Lett.*, **53** 1762 (1988).
- [55] Yuri P.Raizer, *Gas Discharge Physics* (Springer-Verlag Berlin Heidelberg 1991).

- [48] P. E. Dyer, A. Issa and P. H. Key, *Appl. Surf. Sci.*, **46** 89 (1990).
- [49] P. E. Dyer and J. Sidhu, *J. Appl. Phys.*, **64** 4663 (1988).
- [50] Ya.B.Zel'dovich and Yu.P.Reizer, *Physics of Shock Waves and High Temperature Dynamics Phenomena* (Academic, London 1968).
- [51] K.L.Saenger, *J. Appl. Phys.*, **66** 4435 (1989).[50] J.F.Ready, *Effects of High Power Laser Radiation* (Academic, London 1971).
- [52] R. C. Issac, S. S. Harilal, C. V. Bindhu, V. P. N. Nampoori and C. P. G. Vallabhan, *Spectrochim. Acta B* (submitted).
- [53] D.B.Geohegan and A. A. Puretzky, *Appl. Phys. Lett.*, **67** 197 (1995).
- [54] Q.Y.Ying, D.T.Shaw, and H.S.Kwok, *Appl. Phys. Lett.*, **53** 1762 (1988).
- [55] Yuri P.Raizer, *Gas Discharge Physics* (Springer-Verlag Berlin Heidelberg 1991).

Chapter 9

Summary and Conclusions

Laser ablation of solid materials has become an important technique in several scientific disciplines including physics, material science, chemistry and biology. The interaction of light with matter leads to electronic excitation by the absorption of photons. It is well established that the absorption of laser light leads to very rapid heating of opaque materials to very high temperatures. Melting, evaporation and high temperature and density plasma formation may occur. The high temperature conditions may be quite localized in space and time.

Pulsed laser induced plasma has a very short temporal existence and is transient in its nature, with a fast evolution of the characteristic parameters that are heavily dependent on the irradiation conditions such as incident laser intensity, irradiation spot size, ambient gas composition and pressure. It is also true that these parameters vary drastically with axial or radial distance from the target surface under the same irradiation conditions. Detailed investigation of the optical emission of the plasma plume gives the information on the spatial and temporal evolution of transient species produced during laser-target interaction, such as excited atoms, ions or molecules. The spectroscopic studies made on spatial volume elements in the neighbourhood of the target surface in the early stages of the plasma evolution give direct information about the laser-target interaction as well as laser-plasma interaction. Investigations of optical emission at comparatively larger distances from the target surface result in providing information on the plasma species reactivity, which is an important quantity needed to maintain quality of thin films prepared using pulsed laser deposition technique. It also reveals the dynamics of the ablated material before collision with a substrate surface. The investigation made here are centered around the characterization and dynamics of plasma generated during Nd:YAG laser ablation of graphite and $\text{YBa}_2\text{Cu}_3\text{O}_7$ targets.

The discovery of new allotrope of carbon, viz., fullerenes, has initiated substantial

research into the formation, characteristics and possible applications of the graphite plasma. While carbon is known to exist as either diamond or graphite, the third form consists of even numbered carbon clusters which exists in hollow spheres. Laser ablation of graphite target in the presence of an inert gas is an established method for the production of these carbon clusters. Although considerable progress has been achieved in studies involving ablation of carbon clusters C_n ($n > 10$), including fullerenes, relatively little effort has been expended to study the production and characterization of C_n with $n < 10$. Here, we mainly focus into the formation, vibrational distribution and expansion dynamics of the C_2 species produced during laser ablation of graphite target. The band head intensities of the C_2 molecules were used to evaluate the vibrational temperature. These investigations demonstrate that the vibrational distribution of C_2 species are sensitive to laser irradiance, pressure of the background gas, time after the elapse of the laser pulse and spatial separation from the target. It also demonstrates different possible routes for the formation of C_2 molecules. The formation of C_2 emission could be observed at low irradiance due to plasma excitation and at high irradiance due to recombination processes. The presence of helium ambient atmosphere causes the line emission enhancement of the band heads of the C_2 species. This enhancement in the emission intensity from C_2 is due to collisions on the expansion front and subsequent intraplume collisions. It is also confirmed that vibrational temperature of the C_2 molecules decreases with increase in helium pressure. The addition of helium apparently cools and confines the plasma causing reduction in the vibrational temperature.

Time resolved spectroscopic analysis of emission from C_2 species has differentiated the various mechanisms of the formation of these species in the laser produced plasma from graphite in a helium gas atmosphere. Measurements of spatial dependence of the TOF emission intensities are made up to 25 mm away from the target. An oscillatory behavior is observed in the time of flight distribution of C_2 species and this is observed only above a certain threshold value for irradiance. At distances greater than 16 mm from the target, a three fold TOF distribution is observed. The departure of single peak velocity distribution at higher laser irradiances is due to processes like recombination of the high energetic particles. It is found that at farther distances from the target the recombinational peak gets modified into two distinct peaks due to inherent delays caused by different recombination and excitation mechanisms. The different expansion dynamics of C_2 species in the ambient gas are also discussed. The velocity pulsations

in the faster peak during expansion into ambient gas are attributed to nonequilibrium kinetic energy transfer because of many body recombination.

In summary, the present work throws some light on the production and kinetics of C₂ molecules in a laser generated plasma from graphite target. Analysis of these data provides a fairly clear picture of the evolution and dynamics of C₂ species in the laser induced plasma from graphite and the role of carbon clusters in the same.

Electron density and temperature measurements of the graphite were carried out by spectroscopic means. Line intensity ratios of the successive ionization stages of the carbon have been used for the determination of electron temperature and density and Stark broadened profile of first ionized carbon species is used for verifying electron density measurements. The dependence of electron density and electron temperature on different experimental parameters like distance from the target surface, time after the initiation of plasma, laser irradiance and pressure and nature of ambient gases used are also carried out. An initial electron temperature of about 3.6 eV and density $1 \times 10^{19} \text{ cm}^{-3}$ is observed and it decays rapidly to much lower values within 300 ns time. At greater times the electron temperature is more or less constant. The electron density exhibits an approximate $1/z$ dependence with spatial separation from the target surface which is in accordance with the adiabatic expansion model.

With increase in laser irradiance, both electron temperature and density increase and saturate at higher irradiance levels. The saturation of electron density and temperature at these irradiance levels is expected to be due to plasma shielding. The prominent absorption mechanisms occur in a plasma such as inverse Bremsstrahlung and photoionization are discussed. Saturation phenomena of these fundamental parameters with laser irradiance can be explained by assuming the formation of self-regulating regime in the plume.

The electron temperature and density show an abrupt change with the addition of ambient gases and these parameters also depend on the nature and composition of the gas used. It is noted that hotter and denser plasmas are formed in Ar atmosphere compared to He and air as a result of difference in the efficiency of cascade-like growth of electron number density and plasma absorption coefficient. However, the differences between these parameter in Ar and He, and the profile in air, particularly at higher pressures, suggest that T_e and n_e may be affected by chemical reactions as well as simple hydrodynamic expansion of the plasma. It is also noted that the length of the plasma

plume along the expansion axis is greater in helium atmosphere compared to argon or air atmosphere and this is presumably due to higher thermal conductivity of the helium gas. Electron density measurements using two alternative spectroscopic methods show good agreement especially at distances > 2 mm and times > 300 ns. The drawback occurring in these measurements at short distances and short times are also discussed.

Laser irradiation of graphite target in partial vacuum conditions generates plasma containing CN molecules. From the spectroscopic studies of the emission bands of the CN molecules, the population distribution and vibrational temperature at different regions of the plasma plume have been obtained. These investigations demonstrate that the emission intensities from CN species are sensitive to laser irradiance, pressure of the background gas, time after the elapse of laser pulse and spatial separation from the target. At low laser irradiance the emission bands due to C_2 and CN predominates while at higher irradiance the multiply ionized species up to C IV have been observed along with CN and C_2 species. The band head intensities of the different vibrational sequences of the CN molecules were used to evaluate the vibrational temperature using Boltzmann plot. The vibrational temperature is found to increase with increase in laser irradiance and saturates at higher power levels. The saturation of vibrational temperature at higher power density is due to depletion of excited state population of CN molecules and by plasma shielding. The nonlinear interactions between the laser and the plasma give rise to phenomenon such as self-focusing which exhibit a threshold-like behaviour. It is noted that the vibrational temperature of the CN molecules varies with the position of the sampled volume within the plasma plume, integration time after the elapse of laser pulse and ambient gas pressure inside the plasma chamber.

Laser ablation and deposition of high temperature superconducting (HTSC) material like $YBa_2Cu_3O_7$ has recently attracted interest among researchers. The laser ablation of HTSC target is accompanied by the formation of brilliant elongated plasma located over the target surface extending outward. Analysis of the optical emission spectrum from the plasma plume has been used to identify vapourized and ejected atoms, ionized atoms and diatomic molecules. Identification of these species is important in understanding the complicated ablation, transport and deposition processes. Most of the published works have concentrated mainly on identification of plasma species and on parametric studies of the velocity distributions of the species in the expanding plume. However, relatively little quantitative information is available on either the fundamental plasma parameters, like

electron temperature, electron density, composition etc., or the nature of the dominant plume excitation processes in different spatial and temporal regions of the expanding plasma. We have estimated electron temperature of the plasma by spectroscopic means. Line intensities of the successive ionization states were used for the determination of the electron temperature and Stark broadened profile of Ba I transition at 553.5 nm was used for the measurement of electron density. The electron temperature has got $z^{-0.8}$ and t^{-2} dependence on distance and time respectively. The variation of electron temperature with laser irradiance shows a saturation at high irradiance levels and this can be explained by assuming the formation of a self-regulating regime. Irrespective of the nature of the gaseous environment, the plasma temperature shows somewhat similar behaviour. The temperature of the plasma is maximum in Ar atmosphere compared to He or air.

A comparative study is made between the electron temperature of the graphite and $\text{YBa}_2\text{Cu}_3\text{O}_7$ plasmas. Studies show that the fundamental parameters of the plasma varies largely with the nature and composition of the target. Compared to $\text{YBa}_2\text{Cu}_2\text{O}_7$ plasmas, graphite plasmas are more hotter. The large difference in temperature may be due to the variation in its excitation energy levels. For eg. first ionization energy for carbon atom is 11.3 eV, while the ionization energies for Y, Ba and Cu are 6.37, 5.2 and 7.7 eV respectively. We have seen ionic species up to C IV in the case of graphite plasma, while only singly ionic species have been observed in $\text{YBa}_2\text{Cu}_2\text{O}_7$ plasma.

Time resolved studies of $\text{YBa}_2\text{Cu}_2\text{O}_7$ plasma are also made. The present work has differentiated the type of species directly coming from the target surface and those due to recombination process. We have observed the twin peak structure for atomic and molecular species at short distances. Evaporation from the target/expansion of those generated in the vicinity of the target leads to the appearance of the delayed component and those created by collisional or recombination process apparently give rise to first peak. The complicated interplay between laser irradiance and distance from the target surface is not yet completely understood, but data and discussion presented here do provide a good picture regarding the $\text{YBa}_2\text{Cu}_2\text{O}_7$ plasma dynamics.

The present investigations clearly indicate the scope and nature of future work required to get a complete understanding of laser produced plasmas. Use of Langmuir probe will provide considerable information especially regarding the density and temperature in the plasma. Mass spectroscopic measurements will form another type of

work which can throw much light on the nature and number of ablated species including clusters. Use of CCD cameras can provide frame by frame imaging of plasma evolution as a whole. All these indicate that laser induced plasma will continue to receive major attention in recent years to come from the side of scientists and technologists.